

# **Development of a Hybrid Sounding Rocket Motor**

Bernard Geneviève

Submitted in fulfillment of the academic requirements for the degree of Master of Science in  
Mechanical Engineering, College of Agriculture, Engineering and Science,  
University of KwaZulu-Natal

March, 2013

Supervisor: Mr. Jean-François Philippe Pitot de la Beaujardiere

Co-Supervisor: Mr. Michael Brooks

Co-Supervisor: Professor Lance Roberts

## ABSTRACT

This work describes the development of a hybrid rocket propulsion system for a reusable sounding rocket, as part of the first phase of the UKZN Phoenix Hybrid Sounding Rocket Programme. The programme objective is to produce a series of low-to-medium altitude sounding rockets to cater for the needs of the African scientific community and local universities, starting with the 10 km apogee Phoenix-1A vehicle. In particular, this dissertation details the development of the Hybrid Rocket Performance Code (HRPC) together with the design, manufacture and testing of Phoenix-1A's propulsion system.

The Phoenix-1A hybrid propulsion system, generally referred to as the hybrid rocket motor (HRM), utilises SASOL 0907 paraffin wax and nitrous oxide as the solid fuel and liquid oxidiser, respectively. The HRPC software tool is based upon a one-dimensional, unsteady flow mathematical model, and is capable of analysing the combustion of a number of propellant combinations to predict overall hybrid rocket motor performance. The code is based on a two-phase (liquid oxidiser and solid fuel) numerical solution and was programmed in MATLAB. HRPC links with the NASA-CEA equilibrium chemistry programme to determine the thermodynamic properties of the combustion products necessary for solving the governing ordinary differential equations, which are derived from first principle gas dynamics. The combustion modelling is coupled to a nitrous oxide tank pressurization and blowdown model obtained from literature to provide a realistic decay in motor performance with burn time. HRPC has been validated against experimental data obtained during hot-fire testing of a laboratory-scale hybrid rocket motor, in addition to predictions made by reported performance modelling data.

Development of the Phoenix-1A propulsion system consisted of the manufacture of the solid fuel grain and incorporated finite element and computational fluid dynamics analyses of various components of the system. A novel casting method for the fabrication of the system's cylindrical single-port paraffin fuel grain is described. Detailed finite element analyses were performed on the combustion chamber casing, injector bulkhead and nozzle retainer to verify structural integrity under worst case loading conditions. In addition, thermal and pressure loading distributions on the motor's nozzle and its subsequent response were estimated by conducting fluid-structure interaction analyses.

A targeted total impulse of 75 kNs for the Phoenix-1A motor was obtained through iterative implementation of the HRPC application. This yielded an optimised propulsion system configuration and motor thrust curve.

## **DECLARATION 1 – PLAGIARISM**

I, Bernard Geneviève, declare that

1. The research reported in this thesis, except where otherwise indicated, is my original research.
2. This thesis has not been submitted for any degree or examination at any other university.
3. This thesis does not contain other persons' data, pictures, graphs or other information, unless specifically acknowledged as being sourced from other persons.
4. This thesis does not contain other persons' writing, unless specifically acknowledged as being sourced from other researchers. Where other written sources have been quoted, then:
  - a. Their words have been re-written but the general information attributed to them has been referenced.
  - b. Where their exact words have been used, then their writing has been placed in italics and inside quotation marks, and referenced.
5. This thesis does not contain text, graphics or tables copied and pasted from the Internet, unless specifically acknowledged, and the source being detailed in the thesis and in the References sections.

Signed \_\_\_\_\_ Date \_\_\_\_\_

Bernard Geneviève

As the candidate's supervisor, I agree/do not agree to the submission of this thesis.

Signed \_\_\_\_\_ Date \_\_\_\_\_

Mr. Jean-Francois Pitot de la Beaujardiere

As the candidate's co-supervisor, I agree/do not agree to the submission of this thesis.

Signed \_\_\_\_\_ Date \_\_\_\_\_

Mr. Michael Brooks

As the candidate's co-supervisor, I agree/do not agree to the submission of this thesis.

Signed \_\_\_\_\_ Date \_\_\_\_\_

Prof. Lance Roberts

## **DECLARATION 2 – PUBLICATIONS**

Brooks, M. J., Pitot de la Beaujardiere, J. P., Chowdhury, S. M., Genevieve, B. and Roberts, L., “Introduction to the UKZN Hybrid Sounding Rocket Program”, Proceedings of the 46<sup>th</sup> AIAA/ASME/SAE/ASEE Joint Propulsion Conference & Exhibit, Nashville, TN, United States of America, 25-28 July 2010.

Pitot de la Beaujardiere, J. P., Brooks, M. J., Genevieve, B., Chowdhury, S., M. and Roberts, L., W., “Sounding Rockets for Africa”, Proceedings of the 1st South African Space Association Congress, Cape Town, South Africa, 7-9 October 2010.

Genevieve, B., Brooks, M. J., Pitot de la Beaujardiere, J. F. and Roberts, L. W., “Performance Modelling of a Paraffin Wax / Nitrous Oxide Hybrid Rocket Motor”, Proceedings of the 49th AIAA Aerospace Sciences Meeting, Orlando, Florida, United States of America, 4-7 January 2011.

Pitot de la Beaujardiere, J. P., Brooks, M. J., Chowdhury, S. M., Genevieve, B. and Roberts, L.W., “The Phoenix Hybrid Sounding Rocket Program: A Progress Report”, Proceedings of the 47th AIAA/ASME/SAE/ASEE Joint Propulsion Conference & Exhibit, San Diego, CA, United States of America, 2011.

Genevieve, B., Chowdhury, S. M., Brooks, M. J., Pitot de la Beaujardiere, J. P., Veale, K. And Roberts, L. W., “The Phoenix Sounding Rocket Program: A Progress Report 2012”, Proceedings of the 48<sup>th</sup> Annual AIAA/ASME/SAE/ASEE Joint Propulsion Conference and Exhibit and 10th Annual International Energy Conversion Engineering Conference, Atlanta, GA, United States of America, 29 July – 1 August 2012.

Signed \_\_\_\_\_ Date \_\_\_\_\_

Bernard Genevièvre

## **ACKNOWLEDGEMENTS**

I would like to express my most sincere gratitude to my supervisor, Mr. Jean-François Pitot de la Beaujardiere and co-supervisors, Mr. Michael Brooks and Professor Lance Roberts for their continuous advice, encouragement, and motivation throughout the course of this research project. Indeed, without their mentorship, this work would not have been possible.

Special thanks go to my colleague and friend, Seffat Chowdhury for his immense knowledge and help in computer programming and insightful comments. In addition, I wish to thank the entire UKZN Aerospace Systems Research Group (ASReG) Fiona Leverone, Kirsty Veale, Jonathan Smyth, and Luke Philogene for their incredible assistance during the project. I give my sincere thanks to Mr. Markus Nowotny from Check IT Systems for his valuable help in LabVIEW programming.

I acknowledge my gratitude to the UKZN Innovation Company (Pty) Ltd for their funding support, SASOL for provision of the paraffin wax, and the Denel Overberg Test Range for their valued cooperation.

Je dédie cette thèse à mes parents qui m'ont éclairé le chemin de la vie.

## TABLE OF CONTENTS

ABSTRACT.....	ii
DECLARATIONS.....	iii
ACKNOWLEDGEMENTS .....	v
NOMENCLATURE .....	x
LIST OF FIGURES .....	xvii
LIST OF TABLES.....	xxi
CHAPTER 1: Introduction .....	1
CHAPTER 2: Literature Review .....	7
2.1 Survey of Hybrid Rocket Motors .....	7
2.2 Fundamentals of Hybrid Propulsion.....	11
2.2.1 Hybrid Rocket Motor Functionality .....	11
2.2.2 Combustion Instabilities.....	13
2.3 Propellants .....	15
2.3.1 Typical Oxidisers and Fuels.....	15
2.3.2 Properties of Nitrous Oxide .....	17
2.3.3 Properties of SASOL 0907 Paraffin Wax .....	21
2.3.4 Fuel Grain Configurations .....	24
CHAPTER 3: Hybrid Rocket Motor Performance Modelling.....	26
3.1 Description of the Hybrid Rocket Motor Physical and Chemical Models .....	26
3.2 Oxidiser Tank Pressurisation and Blowdown Process .....	27
3.2.1 Liquid Nitrous Oxide Blowdown Modelling .....	28
3.2.2 Gaseous Nitrous Oxide Blowdown Modelling .....	32
3.2.3 Initial Conditions and Thermodynamic Properties .....	33
3.3 Solid Fuel Regression Rate Modelling.....	34
3.3.1 Classical Regression Rate Theory.....	35
3.3.2 Non-Classical Regression Rate Theory .....	39
3.4 Gas Dynamics Modelling .....	42
3.4.1 Rocket Fundamental Formulae .....	42

3.4.2 Zero-Dimensional Combustion Chamber Gas Model.....	45
3.4.3 One-Dimensional Nozzle Gas Flow Model .....	49
3.4.3.1 Subsonic Flow Modelling.....	53
3.4.3.2 Supersonic Flow Modelling.....	55
3.4.3.3 Normal Shock Wave Flow Modelling .....	56
 CHAPTER 4: Hybrid Rocket Performance Code.....	59
4.1 Scope and Specifications .....	59
4.2 NASA-CEA.....	59
4.3 HRPC Motor Design .....	61
4.3.1 Fuel Grain and Nozzle Designs .....	61
4.3.2 Motor Performance Analysis .....	65
4.3.3 Nozzle Contour Design.....	67
4.4 HRPC.....	71
4.4.1 Data Processing and Numerical Solution.....	71
4.4.2 Code Validation .....	76
4.4.3 Implementation into the UKZN HYROPS Software .....	79
 CHAPTER 5: PV-1 Flight Motor Design and Manufacture.....	82
5.1 Specifications and Design Goals .....	82
5.2 Phoenix-1A Propulsion System Design .....	82
5.2.1 Nitrous Oxide/Paraffin Wax Performance Analysis .....	82
5.2.2 PV-1 Motor Design .....	85
5.3 PV-1 Motor Structural Design and Manufacture.....	88
5.3.1 Combustion Chamber Casing.....	90
5.3.2 Injector Bulkhead .....	93
5.3.3 Nozzle .....	96
5.3.4 Nozzle Retainer .....	98
5.3.5 Feed System and Injector .....	99
5.4 Fuel Grain Cartridge Development .....	102
5.4.1 Fuel Grain.....	102
5.4.2 Thermal Liner.....	106

CHAPTER 6: PL-1 and PV-1 Static Motor Tests.....	109
6.1    PL-1 Laboratory-Scale Motor .....	109
6.2    Phoenix-1A Mobile Rocket Launch Platform .....	111
6.3    PL-1 Motor Tests and Post-Analysis.....	113
6.4    PV-1 Motor Tests and Post-Analyses.....	119
6.4.1  Igniter and Cold Flow Tests .....	119
6.4.2  Hot-fire Tests .....	120
CHAPTER 7: Conclusion .....	124
REFERENCES .....	128
APPENDICES .....	134
A      Phoenix-1A Hybrid Sounding Rocket.....	134
B      Air Liquide: Nitrous Oxide Material Compatibility.....	137
C      Oxidiser Tank Blowdown Process: Thermodynamic Properties.....	140
D      HRPC Fuel Grain Standard Geometries .....	143
E      HRPC Motor Design Application.....	157
F      Phoenix-1A Propulsion System Design .....	163
G      PV-1 Motor Drawings .....	173
H      PV-1 Motor Structural Design.....	187

## NOMENCLATURE

### Symbols

$a$	Regression rate ballistic coefficient
$a_e$	Nozzle exit velocity of sound
$a_{ent}$	Entrainment coefficient
$A_b$	Burnt cross-sectional area
$A_e$	Nozzle exit area
$A_{inj}$	Injector orifice cross-sectional area
$A_p$	Grain port cross-sectional area
$A_t$	Nozzle throat area
$c_P$	Specific heat capacity at constant pressure
$c_V$	Specific heat capacity at constant volume
$c^*$	Characteristic velocity
$C_d$	Discharge coefficient
$C_F$	Thrust coefficient
$C_r$	Contraction ratio
$\bar{C}_P$	Molar heat capacity at constant pressure
$\bar{C}_V$	Molar heat capacity at constant volume
$C_H/C_{H0}$	Blocking factor
$D$	Diameter
$D_{p,f}$	Final port diameter
$D_{p,i}$	Initial port diameter
$E$	Young's modulus
$F$	Thrust
$F_r$	Roughness parameter
$G$	Mass flux rate
$G_{ox,p}$	Oxidiser mass flux rate per port
$G_{ox,t}$	Total oxidiser mass flux rate
$h$	Specific Enthalpy
$h_e$	Total heat of entrainment

$h_m$	Total heat of melting
$H$	Enthalpy
$H_{cx}$	Contraction angle point to throat plane radius
$He_v$	Helium vapour
$\overline{H}$	Molar enthalpy
$I_{sp}$	Specific impulse
$I_t$	Total impulse
$I_{vac}$	Vacuum specific impulse
$k$	Specific heat ratio
$k_c$	Chamber specific heat ratio
$k_e$	Nozzle exit specific heat ratio
$L_c$	Bell-shaped parabolic length
$L_c$	Conical-shaped nozzle cone length
$L_{cx}$	Contraction angle point to throat plane length
$L_f$	Bell-shaped nozzle fractional length
$L_g$	Grain length
$L_{ne}$	Nozzle throat to exit plane total length
$L_{ni}$	Nozzle inlet to throat plane length
$L_v$	Latent heat of vaporization
$m$	Mass
$\dot{m}$	Mass flow rate
$\dot{m}_{f,p}$	Fuel mass flow rate per port
$\dot{m}_{f,t}$	Total fuel mass flow rate
$\dot{m}_{ox,p}$	Oxidiser mass flow rate per port
$\dot{m}_{ox,t}$	Total oxidiser mass flow rate
$\dot{m}_{noz}$	Nozzle mass flow rate
$M_{fc}$	Fuel mass storage in chamber
$M_{f,f}$	Final fuel grain mass
$M_{f,i}$	Initial fuel grain mass
$M_e$	Nozzle exit Mach number
$M_{He}$	Helium mass in tank
$M_{N_2O}$	Nitrous oxide mass in tank

$M_{oc}$	Oxidiser mass storage in chamber
$M_{ot,i}$	Initial oxidiser mass loaded into tank
$M_{pt}$	Total propellant mass in tank
$M_t$	Nozzle throat Mach number
$M_1$	Mach number before shock
$M_2$	Mach number after shock
$MW$	Molecular weight
$n$	Number of moles
$n_{ox,t}$	Total number of moles of nitrous oxide
$\dot{n}$	Number of moles of fluid flow rate
$N_{inj}$	Number of injector orifices
$N_p$	Number of ports
$OF$	Oxidiser-to-fuel ratio
$P$	Pressure
$P_a$	Atmospheric pressure
$P_c$	Chamber pressure
$P_d$	Design pressure
$P_e$	Nozzle exit pressure
$P_{inj}$	Pre-Combustion Chamber Pressure
$P_{losses}$	Pressure drop in feed line
$P_{ox}^*$	Saturated vapour pressure of nitrous oxide
$P_{per}$	Burnt perimeter
$P_{o,c}$	Chamber stagnation pressure
$P_{o,e}$	Nozzle exit stagnation pressure
$P_{o,1}$	Stagnation pressure before shock
$P_{o,2}$	Stagnation pressure after shock
$P_1$	Static pressure before shock
$P_2$	Static pressure after shock
$P_{1st}$	Nozzle first critical pressure ratio
$P_{2nd}$	Nozzle second critical pressure ratio
$P_{3rd}$	Nozzle third critical pressure ratio
$Q$	Heat transfer energy

$\dot{Q}_c$	Convective heat transfer
$\dot{Q}_r$	Radiative heat transfer
$r_i$	Inner radius
$r_o$	Outer radius
$\dot{r}$	Regression rate
$\dot{r}_{cl}$	Classical regression rate
$\dot{r}_{ent}$	Entrainment regression rate
$\dot{r}_v$	Vaporisation regression rate
$R$	Gas constant, Radius
$R_c$	Chamber gas constant
$R_d$	Nozzle downstream arc radius
$R_e$	Nozzle exit gas constant
$R_{he}$	Nondimensional energy parameter for entrainment
$R_{hv}$	Nondimensional energy parameter for vaporisation
$R_{ni}$	Combustion chamber radius
$R_p$	Port radius
$R_u$	Universal gas constant
$R_{up}$	Nozzle upstream arc radius
$s$	Specific entropy
$S_f$	Safety factor
$t_b$	Burn time
$T$	Temperature
$T_c$	Chamber static temperature
$T_e$	Nozzle exit static temperature
$T_m$	Melting temperature
$T_{o,c}$	Chamber stagnation temperature
$T_{o,e}$	Nozzle exit stagnation temperature
$T_{T,i}$	Initial tank temperature
$u$	Specific internal energy
$U$	Internal energy
$\overline{U}$	Molar internal energy
$v_e$	Nozzle exit velocity
$v_{in}$	Nozzle inlet velocity

$V$	Volume
$V_{exh}$	Exhaust gas velocity
$V_{fc}$	Pre + Post combustion chamber volumes
$V_{f,f}$	Final fuel grain volume
$V_{f,i}$	Initial fuel grain volume
$V_{post}$	Post-combustion chamber volume
$V_{pre}$	Pre-combustion chamber volume
$\bar{V}$	Molar volume
$w_a$	Additional allowable web thickness
$w_b$	Burnt web thickness
$w_t$	Total web thickness
$W$	Work done
$x$	Axial port distance
$\Delta\bar{H}$	Molar heat of vaporization
$\Delta s$	Entropy change
$\alpha$	Coefficient of thermal expansion
$\alpha_c$	Conical nozzle diverging cone half-angle
$\beta$	Blowing coefficient
$\varepsilon_r$	Nozzle expansion ratio
$\lambda$	Nozzle exit angle correction factor
$\eta_{eff}$	Combustion efficiency
$\theta_c$	Nozzle contraction angle
$\theta_e$	Bell-shaped nozzle parabola exit angle
$\theta_n$	Bell-shaped nozzle parabola inlet angle
$\kappa$	Thermal conductivity
$\lambda_c$	Conical-shaped nozzle correction factor
$\mu$	Combustion gas viscosity
$\nu$	Poisson's ratio
$\rho$	Density
$\rho_e$	Nozzle exit density
$\sigma_a$	Axial stress
$\sigma_c$	Compressive strength

$\sigma_f$	Flexural strength
$\sigma_h$	Hoop stress
$\sigma_r$	Radial stress
$\sigma_s$	Shear strength
$\sigma_t$	Tensile strength
$\sigma_y$	Yield Strength

## Subscripts

<i>a</i>	Atmospheric
<i>Al</i>	Aluminium
<i>ATJ</i>	Graphite
<i>c</i>	Combustion chamber
<i>e</i>	Exit
<i>exp</i>	Experiment
<i>f</i>	Fuel
<i>g</i>	Gas, Grain
<i>in</i>	Inflow
<i>l</i>	Liquid
<i>noz</i>	Nozzle
<i>opt</i>	optimum
<i>out</i>	Outflow
<i>ox</i>	Oxidiser
<i>ox,d</i>	Oxidiser discharge
<i>ox,l</i>	Liquid oxidiser
<i>ox,v</i>	Vapour oxidiser
<i>sp,v</i>	Supercharge gas
<i>st</i>	Steel
<i>t</i>	Total, Throat
<i>the</i>	Theoretical
<i>T</i>	Tank
<i>v</i>	Vapour
<i>vac</i>	Vacuum

## **Abbreviations**

ASReG	Aerospace Systems Research Group
CEA	Chemical Equilibrium with Applications
GSE	Ground Support Equipment
HRM	Hybrid Rocket Motor
HRPC	Hybrid Rocket Performance Code
HYROPS	Hybrid Rocket Performance Simulator
MRLP	Mobile Rocket Launch Platform
ONERA	Office National d'Études et de Recherches Aérospatiales
PFS	Propellant Filling System
UKZN	University of KwaZulu-Natal

## LIST OF FIGURES

### CHAPTER 1

- Figure 1.1** Different configurations of chemical rocket engines (Chiaverini and Kuo, 2006). 2

### CHAPTER 2

- Figure 2.1** Conceptual design of a hybrid strap-on booster for NASA Space Shuttle (Sutton and Biblarz, 2001). 10
- Figure 2.2** Classical hybrid rocket motor schematic (Greatrix, 2012). 11
- Figure 2.3** Difference between injector configurations on combustion stability: (a) Conical injector, and (b) Axial injector (Sutton and Biblarz, 2001). 14
- Figure 2.4** Frequency analysis of the unstable motor static test (Sutton and Biblarz, 2001). 14
- Figure 2.5** Decomposition process of nitrous oxide (Zakirov, 2000). 19
- Figure 2.6** Vacuum specific impulse of various oxidisers with SASOL 0907 paraffin wax calculated at a chamber pressure of 40 bars and nozzle expansion ratio of 5.99. 21
- Figure 2.7** Characteristic velocity of typical paraffin waxes with nitrous oxide. 24
- Figure 2.8** Typical hybrid fuel grain configurations (Humble et al., 1995). 24

### CHAPTER 3

- Figure 3.1** Hybrid propulsion system control volumes modelling (Geneviève et al., 2011). 26
- Figure 3.2** Control volume 1 blowdown process (Fernandez, 2009). 28
- Figure 3.3** Classical diffusion limited theory of hybrid rocket propellants (Sutton and Biblarz, 2001) 35
- Figure 3.4** Effects of pressure on regression rate (Humble et al., 1995). 36
- Figure 3.5** Entrainment mass transfer mechanism (Karabeyoglu et al., 2001). 39
- Figure 3.6** Combustion chamber model (Geneviève et al., 2011). 45
- Figure 3.7** 1D nozzle gas flow model (Geneviève et al., 2011). 49
- Figure 3.8** Nozzle operating modes (Zucker and Biblarz, 2002). 50

### CHAPTER 4

- Figure 4.1** Flowchart of HRPC Motor Design. 61
- Figure 4.2** Flowchart of fuel grain and nozzle designs model. 63
- Figure 4.3** Flowchart of the motor performance analysis model. 66

<b>Figure 4.4</b>	Example of the output graphs of the code: (a) Constant atmospheric pressure, and (b) Constant expansion ratio.	67
<b>Figure 4.5</b>	Nozzle configuration: (a) Bell-shaped, and (b) Conical-shaped.	68
<b>Figure 4.6</b>	Flowchart of HRPC application.	72
<b>Figure 4.7</b>	Difference between explicit Euler and 4 <sup>th</sup> order Runge Kutta methods in the calculation of chamber pressure.	75
<b>Figure 4.8</b>	Motor performance validation of HRPC.	78
<b>Figure 4.9</b>	Coupling of motor performance and flight dynamics models to form HYROPS software.	79
<b>Figure 4.10</b>	Screenshot of the HYROPS's user interface where the HRPC parameters are inputted.	81
<b>Figure 4.11</b>	Screenshot of the HYROPS three dimensional trajectory visualisation window (Chowdhury, 2012).	81

## CHAPTER 5

<b>Figure 5.1</b>	Nitrous Oxide/Paraffin wax performance analyses for PV-1 hybrid rocket motor: (a) Characteristic velocity, (b) Specific impulse, and (c) Optimum nozzle expansion ratio.	83
<b>Figure 5.2</b>	PV-1 motor manual performance optimization.	86
<b>Figure 5.3</b>	Thrust curves of PV-1 motor selected design 2 operating at sea-level ( $P_a = 1.01325$ bar) and 3000 m ( $P_a = 0.7009$ bar).	87
<b>Figure 5.4</b>	Complete thrust curve of PV-1 motor design 2 operating at 3000 m ( $P_a = 0.7009$ bar).	87
<b>Figure 5.5</b>	Sectional views of PV-1 motor.	89
<b>Figure 5.6</b>	FEA von Mises stress distributions in combustion chamber casing.	92
<b>Figure 5.7</b>	Combustion chamber casing.	93
<b>Figure 5.8</b>	PV-1 motor in hydrostatic test configuration.	93
<b>Figure 5.9</b>	Torispherical head design guideline.	94
<b>Figure 5.10</b>	FEA von Mises stress distributions in injector bulkhead.	95
<b>Figure 5.11</b>	PV-1 motor injector bulkhead.	95
<b>Figure 5.12</b>	Equivalent stress distributions in bell-shaped nozzle.	97
<b>Figure 5.13</b>	PV-1 graphite nozzle.	97
<b>Figure 5.14</b>	Clearance between nozzle and its retainer.	98

<b>Figure 5.15</b>	FEA von Mises stress distributions in nozzle retainer.	99
<b>Figure 5.16</b>	PV-1 nozzle retainer.	99
<b>Figure 5.17</b>	Sectional views of PV-1 motor injectors: (a) Axial/straight showerhead, and (b) Impinging.	100
<b>Figure 5.18</b>	PV-1 motor injectors: (a) Axial/straight showerhead, and (b) Impinging.	101
<b>Figure 5.19</b>	Feed system schematic (Pitot de la Beaujardiere et al., 2011).	101
<b>Figure 5.20</b>	Feed system assembly.	102
<b>Figure 5.21</b>	Fuel grain manufacture.	104
<b>Figure 5.22</b>	Inherent characteristics of paraffin wax: (a) Shrinkage level, and (b) Void formation.	106
<b>Figure 5.23</b>	Development of the complete fuel grain cartridge.	107
CHAPTER 6		
<b>Figure 6.1</b>	UKZN hybrid rocket motor test cell (Geneviève et al., 2011).	109
<b>Figure 6.2</b>	PL-1 (top) and PV-1 (bottom) fuel grain cartridges.	110
<b>Figure 6.3</b>	Mobile Rocket Launch Platform (MRLP) and a mock-up of Phoenix-1A hybrid rocket.	112
<b>Figure 6.4</b>	Propellant Feed System (PFS) and control box (Geneviève et al., 2012).	113
<b>Figure 6.5</b>	PL-1 motor hot-fire test 1.	114
<b>Figure 6.6</b>	PL-1 motor hot-fire test 2.	114
<b>Figure 6.7</b>	Hot-fire test 1 experimental time history and theoretical output from HRPC: (a) Chamber pressure, and (b) Thrust.	115
<b>Figure 6.8</b>	Figure 6.8 Hot-fire test 2 experimental time history and theoretical output from HRPC: (a) Chamber pressure, and (b) Thrust.	117
<b>Figure 6.9</b>	Post analysis of test 2 fuel grain cartridge.	118
<b>Figure 6.10</b>	Igniter system development: (a) Igniter A, (b) Igniter B, and (c) Igniter C.	120
<b>Figure 6.11</b>	PV-1 motor cold flow test (Geneviève et al., 2012).	121
<b>Figure 6.12</b>	PV-1 motor static test 3 ignition failure.	122
<b>Figure 6.13</b>	Fuel grain post analysis of static motor test 3, pre-combustion chamber end.	123
APPENDIX A		
<b>Figure A.1</b>	Sectional view of Phoenix-1A hybrid sounding rocket (Pitot de la Beaujardiere et al., 2011).	136

## APPENDIX D

<b>Figure D.1</b>	HRPC fuel grains graphical output.	144
-------------------	------------------------------------	-----

## APPENDIX E

<b>Figure E.1</b>	Selected output graphs for both test runs.	159
<b>Figure E.2</b>	Graphical output of test run (a) Bell-shaped, and (b) Conical-shaped.	162

## APPENDIX F

<b>Figure F.1</b>	PV-1 hybrid rocket motor performance at atmospheric pressure of 0.7009 bar (mid-altitude), including gaseous blowdown: (a) Port radius, (b) Oxidiser-to-fuel ratio, (c) Oxidiser mass flux, (d) Regression rate, (e) Mass flow rate, (f) Chamber pressure, (g) Thrust, (h) Impulse, (i) Characteristic velocity, (j) Nozzle exit pressure, (k) Tank and chamber pressures, (l) Tank pressures, (m) Nozzle gas velocity, (n) Chamber gaseous mass storage, (o) Propellant masses, and (p) Fuel grain 2D representation.	169
-------------------	--	-----

## APPENDIX H

<b>Figure H.1</b>	FEA of chamber casing: (a) Hoop stress, and (b) Radial stress.	189
-------------------	--	-----

## LIST OF TABLES

### CHAPTER 2

<b>Table 2.1</b>	Typical hybrid rocket propellant combinations, $P_c = 34.5$ bar and $P_a = 1.01325$ bar (Chiaverini and Kuo, 2006).	16
<b>Table 2.2</b>	Chemical properties of nitrous oxide (Karabeyoglu et al., 2008).	17
<b>Table 2.3</b>	Physical and chemical properties of $C_{31}H_{64}$ and $C_{50}H_{102}$ paraffin waxes.	23

### CHAPTER 3

<b>Table 3.1</b>	Typical values of ballistic coefficients $a$ and $n$ , for $[r] = \text{m/s}$ and $[G_{ox}] = \text{kg}/(\text{m}^2\text{s})$ .	37
------------------	---	----

### CHAPTER 4

<b>Table 4.1</b>	Input and output parameters for fuel grain and nozzle designs model.	62
<b>Table 4.2</b>	Input and output parameters for motor performance analysis model.	65
<b>Table 4.3</b>	Input and output parameters for nozzle contour design model.	69
<b>Table 4.4</b>	Stanford Sounding Rocket Programme phase 2 propulsion system specifications.	77

### CHAPTER 5

<b>Table 5.1</b>	Phoenix-1A PV-1 propulsion system final design.	88
<b>Table 5.2</b>	Mechanical properties of 6082-T6 aluminium (MatWeb, 2012).	90
<b>Table 5.3</b>	Mechanical properties of 431 stainless steel (Kotecki and Armao, 2003).	94
<b>Table 5.4</b>	Mechanical properties of ATJ graphite.	96

### CHAPTER 6

<b>Table 6.1</b>	PL-1 lab-scale motor specifications.	111
<b>Table 6.2</b>	PV-1 motor hot-fire test outcomes.	122

### APPENDIX B

<b>Table B.1</b>	Nitrous oxide material compatibility.	138
------------------	---------------------------------------	-----

### APPENDIX D

<b>Table D.1</b>	Fuel grain diameter and port angle formulae.	146
------------------	--	-----

## APPENDIX E

<b>Table E.1</b>	Input parameters for the two typical runs.	158
<b>Table E.2</b>	Selected output parameters for both test runs.	158

## APPENDIX F

<b>Table F.1</b>	PV-1 motor fuel grain and nozzle designs for various altitudes.	164
<b>Table F.2</b>	PV-1 motor selected design 2 for optimum nozzle expansion at 1000 m altitude.	166

## APPENDIX H

<b>Table H.1</b>	Finite element analysis of chamber casing.	188
<b>Table H.2</b>	Failure modes of chamber casing at bolt joints for a 6 mm wall-thickness.	190

# **CHAPTER 1**

## **Introduction**

Rockets provide the technological means to deliver scientific and non-scientific payloads to a range of pre-determined altitudes or objectives. These payloads include, among others, artificial satellites, deep-space observatory telescopes, scientific instruments and robotic space probes such as the Mars rovers (Covault, 2012). The type of launch vehicle employed depends on the rocket onboard payload system and mission. For lower mesosphere and sub-orbital flights, the typical altitude between weather balloon and satellite operating regions, sounding rockets are uniquely utilised due to their inherent benefits.

Sounding rockets are specially developed rockets with experimental instruments housed in the designated payload bay. Depending on the task, individual instruments take specific measurements during the course of a flight. Sounding rockets follow a parabolic trajectory with a nearly vertical ascension that exerts significant acceleration loading on the payload system. As a result, the payload and its sub-systems must be designed to withstand these external forces for the success of the mission. The considerable advantages of sounding rockets are low-cost, design simplicity, and ease of manufacturing when compared to orbital launch vehicles. In addition, the general design concept remains relatively similar, and with reusable parts such as the propulsion system, sounding rocket programmes are effectively achieved within reasonable time schedules.

The basic difference between a rocket motor and air-breathing engine is that the former stores the inert oxidiser propellant in a tank or combustion chamber (Gordon, 1997). Rocket propulsion systems are commonly classified as chemical or non-chemical powered vehicles. Chemical rocket motors generate the required thermal energy from the combustion process of the propellants whereas non-chemical rocket motors use an external energy source such as a nuclear reactor or a solar concentrator to heat the propellant. For sub-orbital and orbital launch vehicles, a chemical rocket motor is more suitable due to the high level of thrust produced. Chemical rocket motors can be classified by the state of the propellants; liquid-, solid- and hybrid-propellant as depicted in Fig 1.1.

As mentioned above, a chemical rocket motor does not require an external energy source subsequent to the ignition phase. A chemical rocket motor uses the internal energy released from the exothermic chemical reaction of the propellants in the combustion chamber to produce useful thrust. In particular, the

conversion of thermal to kinetic energy is achieved through a nozzle as the hot pressurised gaseous products are expanded to high exhaust velocities. This conversion of energy forms the basis for generating thrust, which propels the vehicle (Hill and Peterson, 1992).

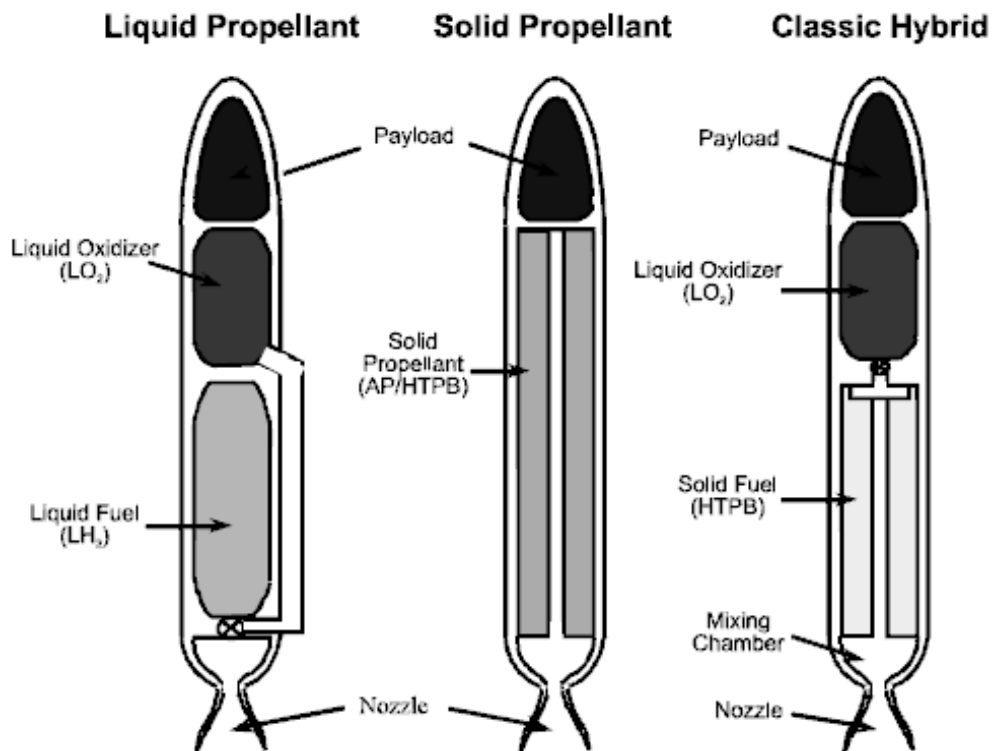


Figure 1.1 Different configurations of chemical rocket engines (Chiaverini and Kuo, 2006).

In liquid rocket motors both the fuel and oxidiser propellants are in the liquid phase, usually at cryogenic temperatures and low pressures. The highly energetic propellants are stored in separate thin-walled tanks prior to injection into the combustion chamber by means of turbine-driven pumps. For solid rocket motors, fuel and oxidiser propellants are premixed into a heterogeneous solid grain which resides in the combustion chamber. In contrast, hybrid rocket motors always store the propellants in two distinct states before undergoing the burning reaction. With classical hybrid motors, the fuel and oxidiser are in the solid and liquid phases, respectively. Conversely, interchanging the phases previously mentioned results in a reverse hybrid motor that reacts a solid oxidiser with a liquid fuel. Classical hybrid motors are more common than reverse hybrids due to the characteristic difficulties in manufacturing the solid oxidiser. Hybrid rocket motors offer attractive advantages over liquid and solid rocket motors. These advantages are described below, followed by some notable disadvantages (Humble et al., 1995, and Chiaverini and Kuo, 2006):

1. Safety – The solid fuel is inert under normal conditions and can safely be transported, handled and stored. In addition, as the propellants are kept in different phases, the system is generally non-explosive.
2. Throttling – The liquid oxidiser flow rate can be controlled to stop, start and restart the engine.
3. Grain robustness – Fuel grain cracks are not catastrophic as in solid rocket motors because the oxidant flows only through the centre ports.
4. Propellant versatility – A wide range of fuel and oxidiser propellant combinations is available compared to liquid or solid motors. Also, metal additives can be added to the solid grain to enhance rocket performance.
5. Low cost – Hybrid rockets are relatively cheaper than liquid rocket motors due to the ease of manufacturing and the overall design simplicity as less feed system plumbing is required.

The disadvantages of hybrid rocket motors are:

1. Low regression rate – Most conventional fuel propellants burn slowly compared to solid rocket propellants. Low fuel regression rate affects the rocket performance. One method to improve performance is to increase the burning surface area by using multiple ports.
2. Combustion efficiency – Due to the relatively large boundary diffusion flame, incomplete mixing occurs, which lowers the impulse efficiency by 1-2% more than in liquid or solid motors.
3. Oxidiser-to-fuel ratio shift – The optimum oxidiser-to-fuel ratio shifts with burn time due to the increase in port diameter. This shift lowers the performance of the rocket.
4. Slow transients - There is a time delay in motor ignition and thrust throttling.

With the recent advancements made in developing high burning rate fuel propellants, as discussed in Chapter 2, hybrid rocket motors have regained their popularity as power-plants for low-cost sounding rocket missions. To date, there has been a lack of sub-orbital launch capable vehicles to meet the demands of various South African and African scientific communities. Potential South African customers for launch services include the Hermanus Magnetic Observatory, the South African Weather Service, the CSIR and local universities. Furthermore, the development of a local sounding rocket programme eliminates the need to employ expensive foreign agencies for rocket launches. In response to the lack of local sounding rocket capacity, the Phoenix Hybrid Sounding Rocket Programme (Brooks et al., 2010) was initiated in 2010 at the University of KwaZulu-Natal as a project of the School of Engineering's Aerospace Systems Research Group (ASReG).

The UKZN Phoenix Hybrid Sounding Rocket Programme's long-term objective is to develop a series of sub-orbital sounding rockets powered by hybrid propulsion systems, due to the beneficial advantages described above, for customers engaged in atmospheric and space physics research. Phase I of the programme is to develop a sounding rocket capable of launching a 1 kg payload to 10 km altitude. This first vehicle, named Phoenix-1A, aims to demonstrate the functionality and feasibility of hybrid sounding rockets. A brief overview of the Phoenix-1A hybrid sounding rocket design is provided in Appendix A. The vehicle's motor utilises SASOL 0907 solid paraffin wax and liquid nitrous oxide as its fuel and oxidiser, respectively. This dissertation mainly describes the development of a motor performance prediction tool, called the Hybrid Rocket Performance Code (HRPC), together with the design and manufacture of the hybrid rocket PV-1 motor.

In particular, the research objectives of this study consisted of the following:

1. Overseeing the design and manufacture of a laboratory-scale hybrid rocket motor and static test-bench facility.
2. Developing a hybrid rocket motor performance code.
3. Validating the model against the experimental data obtained from the laboratory-scale hot-fire tests.
4. Designing and manufacturing PV-1 hybrid rocket motor.
5. Overseeing the design and manufacture of a mobile rocket launch platform.
6. Hot-fire testing the PV-1 motor and comparing data against HRPC predicted thrust curve.
7. Integrating the PV-1 hybrid rocket motor into the Phoenix-1A vehicle.

Chapter 2 of this dissertation is devoted to the literature review of hybrid rocket motor technology. In particular, a brief history of hybrid rocket motors and current developments in the field are given. The general functionalities of crucial components of a hybrid motor are described together with the fundamental causes of combustion instabilities and their mitigation measures. In addition, Chapter 2 contains a list of typical oxidiser/fuel propellant combinations with a focus on the properties of nitrous oxide and paraffin wax.

Chapter 3 is dedicated to the description of hybrid rocket motor physical and chemical models. In this study, the hybrid propulsion system is divided into three control volumes to facilitate the development of the fundamental governing formulae. The three control volumes are: 1) nitrous oxide self-pressurising delivery system modelling, 2) solid-fuel regression rate modelling, and 3) gas dynamics modelling within

the combustion chamber and nozzle. The self-pressurising delivery system model describes a blowdown process whereby the nitrous oxide properties in the oxidiser tank are constantly changing as the tank is discharged with time. Two solid-fuel regression rate theories are briefly discussed, namely the classical diffusion limited theory by Marxman et al. (1964), and the non-classical liquefying entrainment mass-transfer theory by Karabeyoglu et al. (2002). A zero-dimensional model is employed to capture the transient behaviour of the filling/emptying gas dynamics of the combustion chamber. This is coupled to a one-dimensional nozzle gas flow model which determines the motor performance from the rocket fundamental propulsion equations. Furthermore, a normal shock flow model is presented for off design gas flow operations.

Chapter 4 is focused on the development of two computer codes, namely a preliminary motor design code and a predictive performance code which were programmed in MATLAB. The derived equations of Chapter 3 form the core of the two codes. The first, referred to as HRPC Motor Design, is the preliminary motor design code which determines critical motor parameters for a series of specified inputs such as the thrust, the chamber and atmospheric pressures, and the oxidiser-to-fuel ratio. The predictive performance code, referred as HRPC, uses part of the output parameters generated from the HRPC Motor Design application to compute the theoretical motor performance. Both applications are linked to the NASA-CEA equilibrium chemistry code (Gordon and McBride, 1994) which provides the gas thermodynamic properties throughout the simulation. In addition, agreement between the HRPC application and reported performance model data from Karabeyoglu et al. (2003) is investigated for validation purposes.

Chapter 5 is devoted to the design and manufacture of Phoenix-1A's PV-1 motor. The codes developed in Chapter 4 provided the means to optimise the PV-1 motor for a targeted apogee of 10 km. The final PV-1 motor design specifications are given following the optimisation process. Moreover, Chapter 5 includes the finite element analysis and computational fluid dynamics analysis of the PV-1 motor components for the worst case pressure and thermal loading conditions. The mechanical properties of each selected material are tabulated. The casting of the paraffin wax grain is achieved through a novel technique developed at the University, and is presented at the end of the chapter.

In Chapter 6, an overview of the fabricated laboratory-scale PL-1 motor and its test rig is given, followed by the two successful hot-fire tests of the motor. The laboratory-scale PL-1 motor and test facility were developed by undergraduate project teams (Smyth et al., 2010 and Reddy et al., 2010) with the collaboration of the author. The experimental thrust data obtained from the two hot-fire tests are compared with the theoretical thrust predicted by the HRPC application. In addition, Chapter 6 reviews

the fabricated launch platform which was designed by an undergraduate project team (Giovanni et al., 2011 and Gopal et al., 2011), also in collaboration with the author. The purpose of the launch platform, referred to as Mobile Rocket Launch Platform (MRLP), is to launch the Phoenix-1A hybrid rocket as well as to hot-fire test the PV-1 motor. Before the concluding remarks and possible future work presented in Chapter 7, the development of the ignition system and the hot-fire test attempts of the PV-1 motor are also discussed in Chapter 6.

## CHAPTER 2

### Literature Review

#### 2.1 Survey of Hybrid Rocket Motors

In the 1930s, hybrid rocket motor development contributed to the early established liquid and solid rocket research in the field of chemical propulsion. During this period, numerous hot-fire tests were conducted to study the general characteristics of the motor with different propellant combinations. Although there was a lack of experimental flights to demonstrate its valuable advantages, engineers continued extensive research throughout the years to enhance the motor's capabilities. With recent advancements, such as the increase in solid-fuel regression rate, HRMs emerged as potential candidates for sub-orbital and orbital rocket propulsion. Typical applications of hybrid motors now include low-to-medium range altitude rockets and commercial space-tourism vehicle demonstrators. Based on the survey of Humble et al. (1995) and Chiaverini and Kuo (2006) a brief history of HRMs and current developments in the field is now presented.

Preliminary experiments on HRMs were performed at I. G. Farben in Germany by L. Andrussov, O. Lutz, and W. Noeggerath (Green, 1963). They designed a 10 kN hybrid motor constituting of coal as the solid fuel and nitrous oxide as the gaseous oxidiser. However, their attempted hot-fire motor test was unsuccessful due to the significant heat required to vaporise the fuel. This high heat of coal sublimation resulted in an undesirable low burning rate. Similar research was conducted in Germany by Hermann Oberth coinciding with the same period as Andrussov et al.'s hybrid motor programme. Oberth experimented on a system core of graphite and liquid oxygen propellant configuration. Following a series of hot-fire tests the results were disappointing, also due to graphite's high heat of sublimation.

The first documented flight attempt of a hybrid rocket was achieved by the Pacific Rocket Society in the mid-1940s subsequent to several motor static tests using liquid oxygen coupled with different fuels such as wood, solid wax with carbon-black additive, and rubber-based fuel. After a prolonged evaluation of motor prototypes and propellant combinations, the programme produced the XDF-23 hybrid motor which employed liquid oxygen and rubber-based fuel with an aluminium alloy nozzle. In June 1951, the XDF-23 hybrid motor successfully propelled its vehicle to an altitude of approximately 9 km.

From the late 1940s to mid-1950s, the General Electric Company in New York investigated the prospective use of hypergolic propellants. The research, spearheaded by G. Moore and K. Berman (Altman, 1991), involved the burning of 90% hydrogen peroxide and polyethylene as oxidiser and fuel, respectively. A silver screen catalyst bed was incorporated in the pre-combustion chamber to decompose the hydrogen peroxide, which in turn spontaneously ignited the polyethylene fuel. Employing a unique rod and tube grain design configuration, over 300 motor static tests were performed to characterise the combustion reaction. Moore and Berman reported uniform surface burning, combustion insensitivity caused by grain cracks, stable combustion, and high combustion efficiency. The main shortcoming observed by the authors was the low fuel regression rate and insignificant response to the oxidiser flow rate.

The Applied Physics Laboratory of Johns Hopkins University, Thiokol Propulsion, and the United Technology Centre all worked on reverse hybrid propulsion systems (Humble et al., 1995, and Chiaverini and Kuo, 2006). William Avery at Applied Physics Laboratory tested benzene and jet propellant (JP) as the liquid fuel with potassium perchlorate, ammonium perchlorate, and ammonium nitrate as solid oxidisers. He focused his investigations on the JP and ammonium nitrate propellant combination to maintain the lowest development motor cost. This reverse hybrid resulted in poor motor performance due to the reluctant burn feature of the solid oxidiser. In the mid-1960s, both Thiokol Propulsion and the United Technology Centre pursued research on hybrazine-based liquid fuel with ammonium perchlorate, hydrazinium diperchlorate, and nitronium perchlorate as solid oxidisers. Both programmes were ineffective because of poor motor thrust and high complexity in grain manufacturing.

Various military groups explored the possibility of powering target drones with hybrid motors in the late 1960s. A requirement was set for air launch drones that could reach targets up to 90 km. The United Technology Centre and Beech Aircraft developed three series of supersonic hybrid drones as possible contenders for the aforementioned application. Unrecoverable Sandpiper drones, the first series of hybrid drones developed, were boosted by MON-25 (25% NO, 75% N<sub>2</sub>O<sub>4</sub>) oxidiser and polymethyl methacrylate (PMM)-Mg fuel. After six test flights, the drones attained an overall range of 160 km with a maximum speed of Mach 4. Two more versions followed the Sandpiper: HAST and Firebolt. Both were recoverable, powered by inhibited red-fuming nitric acid (IRFNA) and PMM/PB (plexiglass/polybutadiene) propellants, oxidiser pressurized by a ram air turbine, and designed to deliver a heavier payload.

Flight tests of the earliest hybrid sounding rockets were accomplished by the French Aerospace research centre ONERA (Office National d'Études et de Recherches Aérospatiales) and Volvo-Flygmotor in Sweden. The propellants used in ONERA's sounding rockets were a combination of liquid nitric acid and solid amine fuel consisting of metatoluene diamine/nylon. Over the testing period, from April 1964 to November 1967, ONERA launched eight sounding rocket vehicles with recorded apogees of more than 100 km. Like the former programme, Volvo-Flygmotor experimented on a hypergolic propellant configuration of nitric acid as liquid oxidiser and Tagaform (polybutadiene with aromatic amine additive) as solid fuel. This 20 kg payload capability hybrid vehicle was flown in 1969 to an altitude of 80 km.

A decade ago, Lockheed Martin Corporation developed and launched a large scale hybrid sounding rocket based on liquid oxygen and hydroxyl-terminated polybutadiene (Chiaverini and Kuo, 2006). It was part of a hybrid sounding rocket programme initiated in 1999 to demonstrate single-stage hybrid propulsion system capability. A multiport grain configuration was manufactured with dimensions of 0.61 m diameter by 17.4 m long. The motor was specifically designed to reach an apogee of 100 km and produce an approximate average thrust of 267 kN. Launched from NASA Wallops Flight Facility in December 2002, the sounding rocket accomplished its flight with an apogee of 71 km. Similar projects, previously carried out by Starstruck and AMROC in the 1980s, were unsuccessful due to oxidiser valve malfunctions; they were frozen by the low temperature liquid oxygen.

Another feasible application of hybrid motors is a strap-on booster concept for liquid rockets. Subsequently to the Challenger Space Shuttle disaster in 1986, NASA investigated the use of hybrid boosters as replacement for the standard solid rocket boosters (SRBs) on their space shuttles. A typical example of a hybrid strap-on booster is shown in Fig 2.1. This booster integrates a pressurisation system which forces liquid oxygen into the combustion chamber occupied by an inert HTPB. Other conceptual designs, pursued by AMROC and Lockheed Martin, incorporated hybrid boosters into the Delta and Atlas family of launch vehicles.

Currently, universities worldwide are contributing to hybrid technology and there is a variety of ongoing research and development projects in the field. This is attributed to the relatively low cost, inherent safety and benefits of hybrid rocket propulsion. Mostly due to funding limitations, the programmes are restricted to low and medium flight missions. The Peregrine Sounding Rocket Programme is a collaborative effort between the NASA Ames Research Centre, NASA Wallops, Stanford University, and the Space Propulsion Group (SPG) in an attempt to flight test a liquefying fuel hybrid sounding rocket to an altitude of 100 km (Dyer et al., 2007). Initiated in 2006, the propulsion system comprises of liquid nitrous oxide

and paraffin-based fuel, which delivers a 5 kg payload to its predetermined altitude. With a similar targeted apogee as the Peregrine rocket family, Purdue University aims to develop a series of hybrid sounding rockets capable of carrying microgravity experimental instruments (Tsohas et al., 2009). An intermediate low altitude rocket was launched in June 2009 powered by hypergolic propellants; 90% hydrogen peroxide oxidiser and low density polyethylene (LDPE) 4-port fuel grain. The two abovementioned university-based projects and other universities around the world are pursuing fundamental studies on hybrid combustion processes.

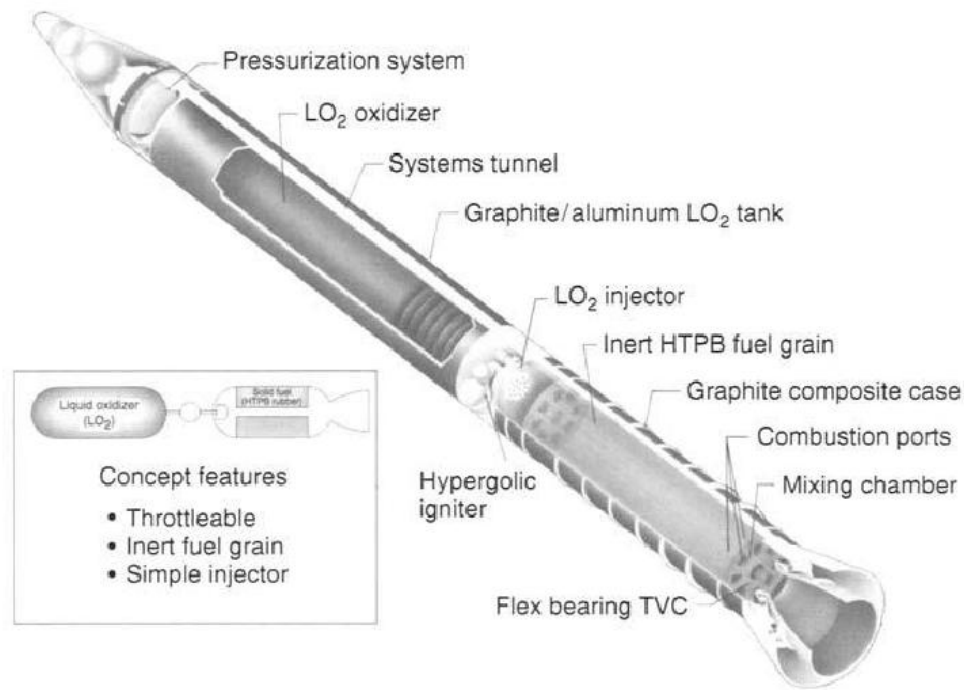


Figure 2.1 Conceptual design of a hybrid booster for NASA space shuttles (Sutton and Biblarz, 2001).

On 4 October 2004, the technological application of hybrid motors was extended to space commercial flights when the winning X Prize award SpaceShipOne vehicle flew to the edge of space, developed by Scaled Composites (Dornheim, 2004). The vehicle was propelled by the combustion of vaporised nitrous oxide with HTPB. Due to the low burning rate of the HTPB, a 4-cylindrical port grain configuration was used to improve combustion. Virgin Galactic (2009) is currently developing a reusable vehicle based on the fundamental hybrid propulsion system of Scaled Composite's SpaceShipOne. The sub-orbital vehicle was named SpaceShipTwo, after its predecessor. Another privately funded hybrid rocket programme is the Copenhagen Suborbitals organisation in Denmark that intends to launch a manned vehicle to space (Pedersen and Nyboe, 2011). Since the founding of this endeavour, hot-fire motor tests and intermediate flight tests have been conducted.

## 2.2 Fundamentals of Hybrid Propulsion

### 2.2.1 Hybrid Rocket Motor Functionality

A classical HRM separates the liquid or gaseous oxidiser from the solid-fuel grain in the storage compartments prior to the feed valve opening. Essentially, this configuration renders the solid-fuel grain inert, and reduces the risk of accidental ignition. A typical schematic of classical HRMs is given in Fig 2.2.

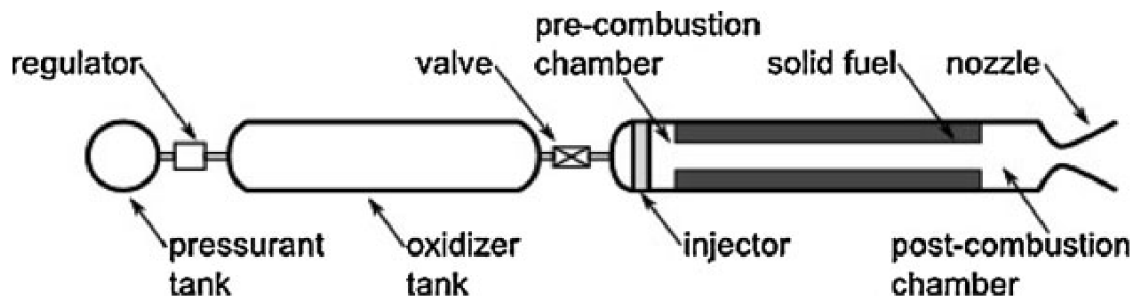


Figure 2.2 Classical hybrid rocket motor schematic (Greatrix, 2012).

Referring to Fig 2.2, three main compartments are depicted: 1) pressurant tank, 2) oxidiser tank, and 3) combustion chamber. The pressurant tank mounted to the upper dome of the oxidiser tank is one type of pressurisation system, which contains an insoluble and non-reactive gas. The gas, usually helium or nitrogen, maintains the required high oxidiser tank pressure throughout the burn by means of a pressure regulator. Other types of pressurisation system include a turbine driven pump or the use of a self-pressurising propellant. In the former configuration, the pump is incorporated in the feed system between the oxidiser tank and the combustion chamber. This high-technological equipment is primarily employed in large scale rockets to decrease the structural mass of oxidiser tanks which operate at low pressure. In the latter configuration, a self-pressurising oxidiser such as nitrous oxide upholds a higher working pressure than the combustion chamber. Increasing the working pressure can be achieved by filling the oxidiser tank with a supercharge gas such as helium or nitrogen. This pressurisation system is cost effective compared to the additional design and manufacture involved in the other two systems. The oxidiser flow is controlled by a valve in the feed system which also has the capability of throttling the mass flow rate to the combustion chamber. The combustion chamber integrates an injector, a fuel grain cartridge, and a nozzle into a single working environment. The injector is purposely designed to atomise the incoming oxidiser flow. In particular, an injector design is based on liquid rocket motors with the

commonly used: 1) axial showerhead, 2) impinging, and 3) swirl flow configurations. A pre-combustion chamber in the fore end of the motor allows for adequate vaporisation of the atomised oxidiser flow which facilitates the combustion mechanism. The length-to-diameter ratio of the vaporisation chamber is approximately 0.5 to account for sufficient residence time of the propellant (Humble et al., 1995). Likewise, a post-combustion chamber in the aft end of the motor provides additional volume for complete combustion of unburned gaseous propellant. To meet the propellant's residence time requirement, a length-to-diameter ratio of 0.5 to 1 is commonly adopted for the mixing chamber (Humble et al., 1995). Typically, appropriate dimensioning of the pre- and post-combustion chambers can improve HRM's poor volumetric fuel efficiency (volume of fuel / volume of chamber) (Greatrix, 2012). The combustion process is highly energetic with the flame temperature reaching up to 3000 K depending on the propellant combination, oxidiser-to-fuel ratio, and chamber pressure. Consequently, a thermal protective liner is used to insulate the chamber casing from this severe operational environment.

The hybrid rocket motor combustion process comprises both transient and steady-state operation phases. The transient phase coincides with significant and rapid change in chamber pressure with respect to time, mainly during the motor ignition and at the end of the burn. The steady-state phase corresponds to the prolonged high thrust level with moderate change in chamber pressure, potentially caused by a decrease in oxidiser mass flow rate and increase in grain port diameter. The ignition of a hybrid motor can be more problematic compared to liquid and solid motors due to its distinct two phase propellants. Generally, the combustion sequence of an HRM is as follows:

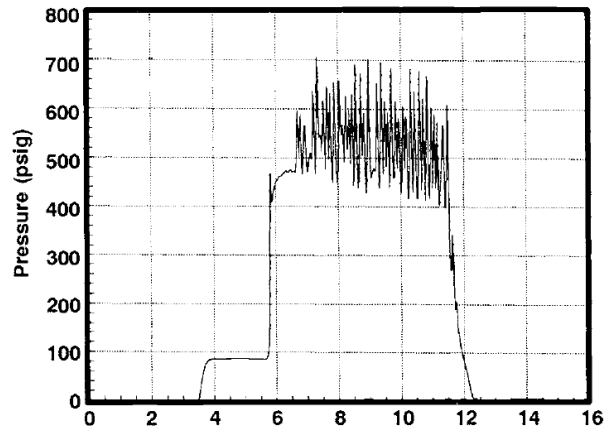
1. Prior to the flow of oxidiser into the combustion chamber, the igniters are fired which melt and evaporate the exposed surface of the solid-fuel grain.
2. At the valve opening command, the oxidiser is forced to flow into the combustion chamber due to the large pressure difference.
3. The injector atomises and vaporises the oxidiser. Concurrently, the oxidiser flow is chemically heated and/or decomposed by the overlapping hot exhaust gases of the ignition source.
4. Combustion is initiated and, thereafter, self-sustained by the mixing of decomposed oxidiser and sublimated solid-fuel grain.
5. This internal energy released from the exothermic chemical reaction of the propellants is converted into kinetic energy through the nozzle, thus generating the rocket thrust.

## 2.2.2 Combustion Instabilities

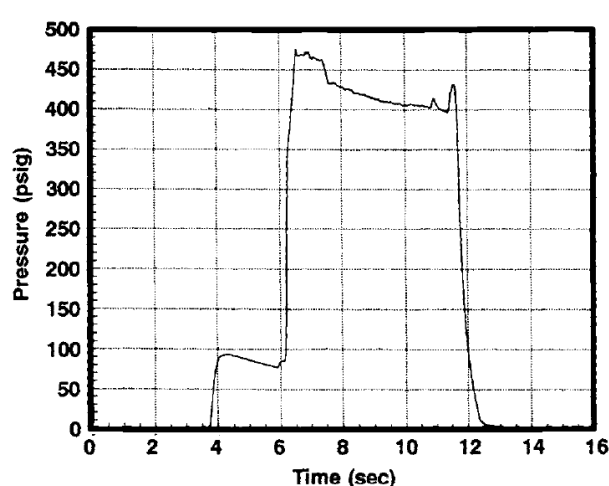
Most high energetic propellants can manifest undesirable oscillations due to the chemical energy that can be channelled through the system. It has been observed that HRMs experience combustion instabilities similar to liquid and solid motors. These can be diminished to approximately 2 to 3% of the average chamber pressure in a well-developed system (Sutton and Biblarz, 2001). Combustion instabilities are classified as low frequency (non-acoustic) and high frequency (acoustic).

Low frequency instabilities involve periodic pressure oscillations with non-acoustic behaviour, usually 10 to 50 Hz. These fluctuations result from the coupling of pressure between the oxidiser feed system and the combustion chamber. One solution to reduce low frequency oscillations is by stiffening the oxidiser feed system, that is, by increasing the injector pressure drop (smaller orifices), thus minimising back flow from occurring. According to Sutton and Biblarz (2001), an injector pressure drop of 15 to 25% of the chamber pressure is recommended for stable combustion in liquid motors. High frequency instabilities exhibit acoustic behaviour due to the interaction between the burned gaseous propellant pressure-wave forces and the chamber acoustical resonance properties. The acoustic frequency in hybrid motors appears to occur at longitudinal modes only. The typical higher frequency tangential and/or radial modes, which are experienced in both solid and liquid motors, have not been observed in hybrid motors (Sutton and Biblarz, 2001). These acoustic oscillations (longitudinal modes) in hybrid motors are due to the unstable flow field in the boundary layer throughout the grain port. One method to eradicate high frequency oscillations is to provide a strong axial oxidiser flow component. Furthermore, it was found by Boardman et al. (1995) that the hot gas recirculation zone in the fore end of the motor eases high frequency instabilities by preheating the oxidiser core flow which stabilises the boundary layer.

Figure 2.3 depicts the stable and unstable test data of a hybrid motor with the following specifications: 280 mm fuel grain diameter, gaseous oxygen (GOX) oxidiser, and HTPB fuel propellant combination. The first hot-fire test, Fig 2.3 (a), used a conical flow injector configuration whereas the second one, Fig. 2.3 (b), used an axial flow injector configuration. In the first test, it is noted that the combustion was highly unstable immediately after the ignition transient. The type of oscillation produced in the first hot-fire test is believed to be high frequency (longitudinal modes) in nature. This is due to the lack of a hot gas recirculation zone in the fore end of the motor as a conical flow-pattern injector was utilised. The second hot-fire test, Fig 2.3 (b), resulted in a stable combustion due to the use of the strong axial flow field injector. The injector flow field in the second hot-fire test provided sufficient oxidiser preheating from the hot gas recirculation zone to stabilize the combustion.



(a)



(b)

Figure 2.3 Difference between injector configurations on combustion stability: (a) Conical injector, and (b) Axial injector (Sutton and Biblarz, 2001).

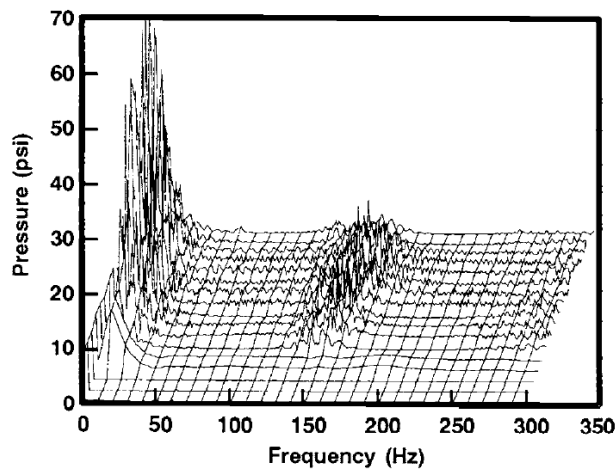


Figure 2.4 Frequency analysis of the unstable motor static test (Sutton and Biblarz, 2001).

## 2.3 Propellants

### 2.3.1 Typical Oxidisers and Fuels

The unique two-phase characteristics of a hybrid motor made it essential to undertake a comprehensive research of different propellant combinations. Due to the complexity involving the casting of moderate-to-large size solid oxidiser grains, reverse hybrid motor technology is less accessible than commonly used classical hybrid motors. A brief survey of typical oxidisers and fuels used in hybrid propulsion, based on the work of Humble et al. (1995) and Chiaverini and Kuo (2006), is given below.

The majority of hybrid fuels are polymers (rubber or plastic) because of their carbon-based content. Typical polymers include polybutadiene (PB), polyethylene (PE), and plexiglass (polymethyl-methacrylate or PMM). The polybutadiene monomer (PB with the formula  $C_4H_6$ ) can be further sub-classified as PB-acrylonitrile (PBAN), PB-acrylic acid (PBAA), hydroxyl-terminated polybutadiene (HTPB), and carbon-terminated PB (CTPB). In the past, the PMM fuel composition was highly studied because of its availability and cost effectiveness. Nowadays, HTPB is widely used in hybrid propulsion systems due also to its low cost, commercial availability, and inherent safety. Additional hydrocarbon-based fuels tested to date consist of paraffin waxes, metatoluene diamine/nylon, and, in the early history of hybrid technology, coal and wood. Additives can be uniformly mixed with PB polymers and paraffin waxes to enhance the fuel density and consequently reduce vehicle mass fraction. The list of additives include Al,  $AlH_3$ , Li,  $LiH$ ,  $Li_3AlH_6$ , B,  $B_{10}H_{14}$ ,  $LiBH_4$ , aromatic amines, and anthracene. Potential additives such as aluminium can effectively decrease the optimum oxidiser-to-fuel ratio of a propellant combination which reduces the required oxidiser mass. Cryogenic fuels include pentane, methane, carbon monoxide, oxygen, and hydrogen. Despite the high performance advantages, this class of fuels is relatively expensive and difficult to handle compared to traditional fuels.

Common liquid and gaseous hybrid oxidisers include oxygen (GOX or LOX), nitrous oxide ( $N_2O$ ), dinitrogen tetroxide ( $N_2O_4$ ), nitric acid ( $HNO_3$ ), hydrogen peroxide ( $H_2O_2$ ), FLOX ( $\frac{2}{3}F_2 + \frac{1}{3}O_2$ ), and hydroxyl amine nitrate (HAN). Basically, hybrid liquid oxidisers have also been tested in liquid rocket motors. Both oxygen and FLOX offer the highest motor characteristic velocities. Table 2.1, which has been reproduced from Chiaverini and Kuo (2006), shows a list of common hybrid propellant combinations. Sections 2.3.2 and 2.3.3 that follow, give a detailed description of Phoenix-1A selected propellants' properties (nitrous oxide and SASOL 0907 paraffin wax).

Table 2.1 Typical hybrid rocket propellant combinations,  $P_c = 34.5$  bar and  $P_a = 1.01325$  bar (Chiaverini and Kuo, 2006).

Fuel	Oxidiser	Optimum O/F	Sea level I <sub>sp</sub> [s]	c* [m/s]
HTPB	LOX	1.9	280	1820.3
PMM ( $C_5H_8O_2$ )	LOX	1.5	259	1660.9
HTPB	N <sub>2</sub> O	7.1	247	1604.5
HTPB	N <sub>2</sub> O <sub>4</sub>	3.5	258	1662.9
HTPB	RFNA	4.3	247	1590.7
HTPB	FLOX (OF <sub>2</sub> )	3.3	314	2042.5
Li/LiH/ HTPB	FLOX (OF <sub>2</sub> )	2.8	326	2118.4
PE	LOX	2.5	279	1791.3
PE	N <sub>2</sub> O	8.0	247	1599.6
Paraffin	LOX	2.5	281	1804.4
Paraffin	N <sub>2</sub> O	8.0	248	1605.7
Paraffin	N <sub>2</sub> O <sub>4</sub>	4.0	259	1666.9
HTPB/Al (40%)	LOX	1.1	274	1757.5
HTPB/Al (40%)	N <sub>2</sub> O	3.5	252	1636.8
HTPB/Al (40%)	N <sub>2</sub> O <sub>4</sub>	1.7	261	1679.1
HTPB/Al (60%)	FLOX (OF <sub>2</sub> )	2.5	312	2006.2
Cellulose ( $C_6H_{10}O_5$ )	GOX	1.0	247	1572.5
Carbon	Air	11.3	184	1224.4
Carbon	LOX	1.9	249	1598.7
Carbon	N <sub>2</sub> O	6.3	236	1521.6
<i>Cryogenic hybrids</i>				
Pentane (s)	LOX	2.7	279	1789.2
CH <sub>4</sub> (s)	LOX	3.0	291	1870.5
CH <sub>4</sub> (s)/Be (36%)	LOX	1.3	306	1917.8
NH <sub>3</sub> (s)/Be (26%)	LOX	0.47	307	1966.6
<i>Reverse hybrids</i>				
JP-4	AN	17.0	216	1417.6
JP-4	AP	9.1	235	1526.1
JP-4	NP	3.6	259	1669.1

### 2.3.2 Properties of Nitrous Oxide

Nitrous oxide is a binary molecular compound where two atoms of nitrogen are covalently bonded to a single oxygen atom, yielding the molecular formula N<sub>2</sub>O. The compound is used worldwide as an inhalation anaesthetic and analgesic agent in medical fields. Although nontoxic in nature, high consumptions of nitrous oxide may cause asphyxiation with general symptoms of loss of mobility and consciousness whereas low consumptions may lead to dizziness, headache, and nausea. The energetic oxygen component positions nitrous oxide substance as a suitable oxidiser propellant for rocketry applications. Moreover, nitrous oxide can be classified as a “green” propellant since its decomposition products are solely constituted of inert nitrogen and oxygen gases.

In hybrid propulsion systems, nitrous oxide offers beneficial propellant properties as it is relatively cheap, readily available, self-pressurising, storable at room temperature, and offers good motor performance. At room temperature, the chemical compound is subcritical, meaning that the gas and liquid phases coexist in equilibrium in a sealed compartment. Its critical temperature is 36.4°C, corresponding to a pressure of 72.4 bars (Perry and Green, 2007). The chemical properties of nitrous oxide are listed in Table 2.2, obtained from Karabeyoglu et al. (2008).

Table 2.2 Chemical properties of nitrous oxide (Karabeyoglu et al., 2008).

<b>Molecular Weight</b>	g/mol	44.013
<b>Melting Point</b>	°C	-90.86
<b>Boiling Point</b>	°C	-88.48
<b>Critical Temperature</b>	°C	36.4
<b>Critical Pressure</b>	bar	72.4
<b>Critical Density</b>	kg/m <sup>3</sup>	452
<b>Heat of Fusion</b>	J/kg	148654.2 (-90.86°C)
<b>Heat of Vaporisation</b>	J/kg	376248.3 (-88.48°C)
<b>Enthalpy of Formation</b>	J/mol	82087.5 (25°C)
<b>Stability</b>		stable
<b>Decomposition</b>		exothermic

This two-phase characteristic results in a self-pressurising propulsion system. As liquid nitrous oxide flows out of an initially filled tank, the head space volume above the liquid increases causing the vapour

pressure to drop due to expansion. To regain chemical equilibrium in the tank, liquid nitrous oxide at the gas-liquid interface is partly vaporised and the vapour pressure rises. Therefore, being a self-pressurising oxidiser, nitrous oxide propellant does not need the use of a turbine driven pump to increase its pressure above the chamber pressure. At standard conditions, its pressure and temperature are 56.6 bars and 25°C, respectively (Perry and Green, 2007). Clearly, the temperature affects the working pressure. Depending on the required tank pressure, the nitrous oxide propellant is usually cooled or warmed if the ambient temperature is too low or high. Precautions must be taken not to heat the tank above 36.4°C as nitrous oxide turns into supercritical fluid which results in a tank pressure higher than 72.4 bars. At working pressures higher than 72.4 bars, the designed tank wall-thickness, and hence its mass, increases significantly which in turn affects the rocket performance.

The decomposition reaction of nitrous oxide results in gaseous molecules of nitrogen and oxygen, plus heat liberated from the exothermic reaction, according to Equation 2.1. Upon decomposition, the free oxygen molecules maintain the combustion mechanism, while the nitrogen molecules facilitate the regression rate of the fuel grain and also act as a coolant for the rocket nozzle.



Under standard conditions, this exothermic reaction generates about 82 kJ of heat per mole of nitrous oxide compound (Zakirov, 2000). An external energy source, an igniter, is needed to initiate thermal decomposition, provided that the energy source surpasses the activation energy (250 kJ/mol) of nitrous oxide. Thermal decomposition temperature at this activation energy is above 520°C, whereas, the use of a catalyst can lower the decomposition temperature to 200°C. Figure 2.5 illustrates the effect of using a catalyst on the activation energy of nitrous oxide.

Accidental decomposition of the nitrous oxide during the oxidiser tank filling procedure, hot-fire motor tests, and flight missions may lead to catastrophic structural failures. Nitrous oxide is relatively safe for normal daily use in the industrial and medical fields but is a potential hazard in the field of propulsion where it is handled under extreme conditions. In July 2007, a composite run tank exploded at the Scaled Composites' Mojave test facility during a cold flow test, claiming the lives of three employees (Scaled Composites, 2008). The decomposition events of nitrous oxide are described in the work of Karabeyoglu et al. (2008). According to the research, unwanted decomposition can occur in the oxidiser tank, feed system, or even in the combustion chamber during the start-up phase. The oxidiser-rich environment of

the tank is potentially lethal as possible decomposition process may result in a pressure vessel explosion. This mode of failure occurs at the end of a burn when the liquid nitrous oxide has been completely consumed, especially in systems where the oxidiser tank and combustion chamber are closely coupled.

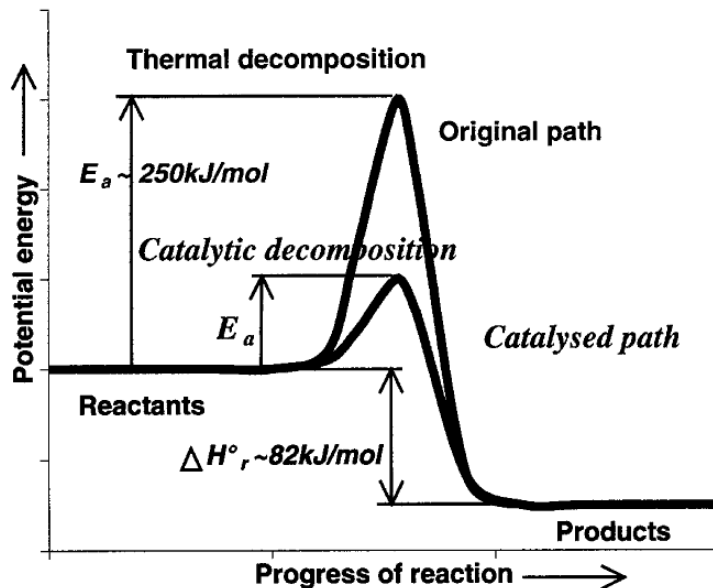


Figure 2.5 Decomposition process of nitrous oxide (Zakirov, 2000).

As the liquid nitrous oxide is depleted, the gaseous nitrous oxide can be decomposed when it comes in contact with the hot injector, provided that the temperature meets the required activation energy, thereby causing a deflagration wave to move upstream into the tank. A large amount of heat is released which results in over-pressurisation and structural failure of the oxidiser tank. Mitigation methods include the use of an inert supercharge gas (nitrogen or helium), and/or integrating a burst disk or pressure relief valve in the system. Nitrous oxide decomposition in the feed system is attributed to dead volumes in the lines, due to various fittings, which cause adiabatic compression heating of the oxidiser flow. In addition, during the motor start-up phase, possible accumulation of hot igniter products in the lines could dissociate the incoming nitrous oxide once the feed valve is opened. Mitigation methods for this type of decomposition hazard include minimising the system dead volumes, decreasing the oxidiser flow rate during the start-up transient by controlling the feed valve opening time, and directing the igniter away from the injector to prevent back flow of the hot combust gases through the orifices. At motor start-up phase, the timing sequence between the igniter charge and the feed valve commands must be closely investigated to eliminate “hard start” of the motor. “Hard start” is due to high concentrations of nitrous oxide in the combustion chamber prior to the igniter activation command. The system acts as an uncontrolled chemical explosion and results in over-pressurisation of the chamber, particularly the pre-

combustion chamber. A general guideline for hybrid rocket motors ignition sequence is given in Section 2.2.1 to eliminate “hard start” high transient pressure loading. Other external energy sources responsible for auto-ignition of nitrous oxide are electrostatic discharge, friction heating, and overheating of the fill pump station.

Some important handling procedures must be followed for safe operation of the system. In particular, the oxidiser tank and feed lines should be thoroughly cleaned from any catalytic sources that may reduce the activation energy threshold of the nitrous oxide. From the information gathered by Thicksten et al. (2008), the cleaning procedures of nitrous oxide systems are identical to liquid oxygen systems. As such, all Phoenix-1A critical components were cleaned using the following three-step process:

1. Pre-cleaning – removal of all dust with a brush or similar method.
2. Cleaning with a solvent – a trichloroethylene solvent is used to thoroughly clean the inner surfaces of all the components which are then rinsed with clear water. Precautions must be taken when handling trichloroethylene as it is classified as a carcinogenic substance. That is, protective gloves and respiratory masks must be worn during the cleaning procedure.
3. De-ionized water rinse – each component is rinsed and, if possible, submerged in de-ionized water a couple of times to ensure that the trichloroethylene solvent is completely removed. Thereafter, all components are left to dry in a clean environment.

After the cleaning procedure, the components are carefully inspected before the overall installation of the system. Any open-ended fittings and pipes are properly sealed with appropriate materials to prevent any contamination while the parts are being stored. In addition to the cleaning process, material compatibility checks for nitrous oxide systems must be rigorously performed before use. A list of the material compatibilities, obtained from Air Liquide (2002), is reproduced in Appendix B.

The vacuum specific impulse of nitrous oxide is compared to other well known oxidisers in Fig 2.6. Vacuum specific impulse is a measure of rocket efficiency for a particular propellant combination. It is defined as the thrust per unit weight of propellant, where the ambient pressure is assumed to be zero. In this case, the oxidisers are gaseous and liquid oxygen (GOX and LOX), hydrogen peroxide ( $H_2O_2$ ), dinitrogen tetroxide ( $N_2O_4$ ), and nitrous oxide ( $N_2O$ ), and the fuel is SASOL 0907 paraffin wax. The graph was produced by the Hybrid Rocket Performance Code (HRPC) an in-house modelling tool developed in this study as described in Chapters 3 and 4. For this particular example, inputs to the code include a chamber pressure of 40 bars and a nozzle expansion ratio of 5.99, together with the appropriate

properties of each propellant. Figure 2.6 illustrates the influence of oxidiser-to-fuel ratio and propellant combination on the vacuum specific impulse. Both gaseous- and liquid-oxygen oxidisers offer the highest motor performance at their respective optimum mixture ratios but decline considerably as the oxidiser-to-fuel ratio increases. Nitrous oxide has the lowest motor performance at its optimum oxidiser-to-fuel ratio of 8. However, within this mixture region it can be noted that the vacuum specific impulse of nitrous oxide is higher than gaseous and liquid oxygen, and dinitrogen tetroxide. One noticeable disadvantage of nitrous oxide is the high optimum oxidiser-to-fuel ratio compared to the other oxidisers. This elevated optimum oxidiser-to-fuel ratio requires a large quantity of nitrous oxide to be carried in the oxidiser tank, thus raising the tank mass.

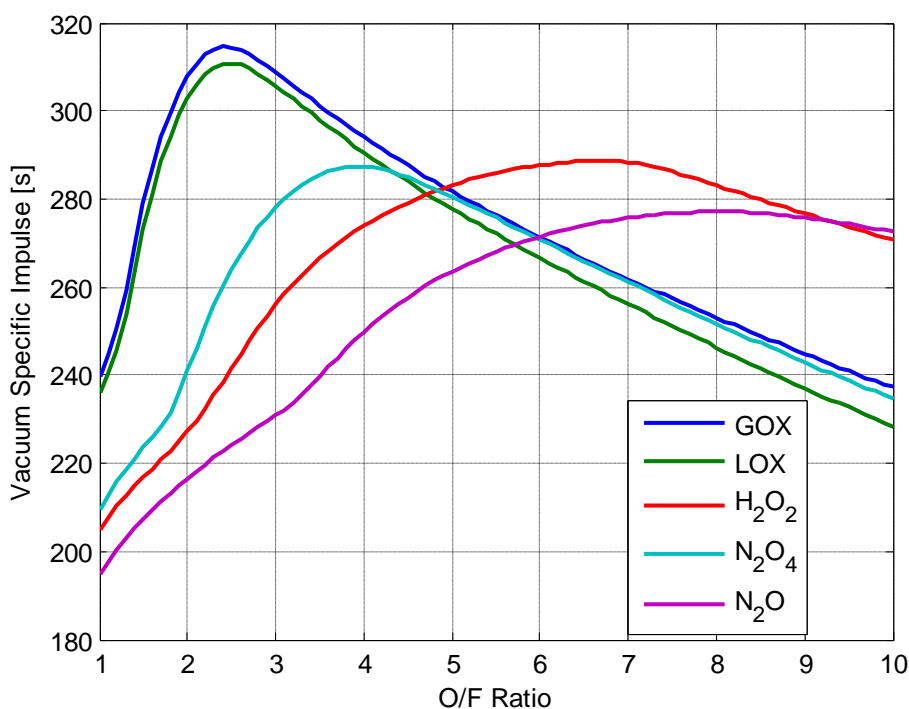


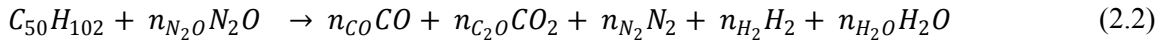
Figure 2.6 Vacuum specific impulse of various oxidisers with SASOL 0907 paraffin wax calculated at a chamber pressure of 40 bars and nozzle expansion ratio of 5.99.

### 2.3.3 Properties of SASOL 0907 Paraffin Wax

Paraffin waxes, also known as alkanes, are branch or straight-chain saturated organic compounds that consist exclusively of hydrogen and carbon atoms with the chemical formula  $C_nH_{2n+2}$ . This group of hydrocarbons is chemically bonded by means of single bonds. Paraffin wax is typically categorised into two groups: macrocrystalline and microcrystalline (Freund et al., 1982). Macrocrystalline paraffin waxes refer to mixtures which consist mainly of saturated hydrocarbons and smaller amounts of iso-alkanes and

cycloalkanes with carbon contents ranging from 18 to 40. In addition to the normal hydrocarbons, microcrystalline paraffin waxes constitute of large amounts of iso-alkanes and naphthenes with long alkyl side-chains. The typical carbon content in microcrystalline paraffin waxes ranges from 40 to 55. Paraffin hydrocarbons are non-toxic, nonhazardous, tasteless, odourless, white in colour, and are in a solid state at room temperature.

SASOL 0907 paraffin wax, chemical name pentacontane, is classified as a microcrystalline compound due to its molecular formula C<sub>50</sub>H<sub>102</sub>. Being a microcrystalline compound, SASOL 0907 paraffin wax has an average chain length of 50 carbon atoms (n-paraffin ~C34 = 36% and iso-paraffin ~C59 = 64%) with a congealing point of 84.5°C (Grosse, 2009). The exothermic reaction between nitrous oxide and SASOL 0907 paraffin wax yields mostly harmless gases such as hydrogen, nitrogen, and carbon dioxide. The reaction products depend significantly on the residence time of the hot gases in the post-combustion chamber. For incomplete combustion, carbon monoxide and hydrogen gases, among other minor species, are liberated from the dissociation of the ideal products (CO<sub>2</sub> + N<sub>2</sub> + H<sub>2</sub>O). The major combustion products for a non-ideal reaction are:



Recent research at Stanford University has shown that paraffin-based fuels burn three to four times faster than conventional rubber fuels (Karabeyoglu et al., 2004). Research by Karabeyoglu et al. (2004) shows that paraffin waxes form a liquid layer upon burning which is hydro-dynamically unstable leading to droplet entrainment into the gas stream. This mechanism is responsible for the enhancement in regression rate. As such, the high regression rate characteristic of paraffin waxes reduces the grain fabrication complexity of multi-ports to a single cylindrical port. Paraffin wax is reported to exhibit shrinkage of up to 25% of its original volume as it cools down (DeSain et al., 2009). Therefore, special techniques of fabrication must be employed to obtain uniform solidification. Additives can be added to pure paraffin waxes to modify their mechanical properties. A black dye is usually mixed with paraffin wax to minimise sloughing effects (Karabeyoglu et al., 2001). This phenomenon causes unburned fuel to be expelled out of the nozzle and consequently drops the chamber pressure. The black dye reduces the radiation heat of conducting through the solid-fuel grain which can potentially soften the grain structure. The physiochemical properties of C<sub>31</sub>H<sub>64</sub> and C<sub>50</sub>H<sub>102</sub> paraffin waxes are given in Table 2.3.

Table 2.3 Physical and chemical properties of C<sub>31</sub>H<sub>64</sub> and C<sub>50</sub>H<sub>102</sub> paraffin waxes.

		C <sub>31</sub> H <sub>64</sub>	C <sub>50</sub> H <sub>102</sub>
<b>Molecular Weight</b>	g/mol	436.8	703.4
<b>Enthalpy of Formation</b>	J/mol	-697200	-1438200
<b>Melting Temperature</b>	K	339.6	381
<b>Boiling Temperature</b>	K	727.4	544
<b>Vaporization Temperature</b>	K	-	558
<b>Density – Solid Phase</b>	kg/m <sup>3</sup>	930	900
<b>Density – Liquid Phase</b>	kg/m <sup>3</sup>	654.4	720
<b>Heat of Fusion</b>	J/kg	167200	221000
<b>Heat of Vaporization</b>	J/kg	163500	-
<b>Dynamic Viscosity – Liquid Phase</b>	Pa.s	0.00065	0.0047
<b>Thermal Conductivity – Liquid Phase</b>	W/(m.K)	0.12	0.246
<b>Specific Heat – Solid Phase</b>	J/(kg.K)	2030	2000
<b>Specific Heat – Liquid Phase</b>	J/(kg.K)	2920	3000
<b>Surface Tension – Liquid Phase</b>	N/m	0.0071	-

C<sub>31</sub>H<sub>64</sub> paraffin wax is widely used at Stanford University and associated material data was obtained from Karabeyoglu et al. (2002). The surface tension and other liquid properties are evaluated at the boiling temperature, and at the average temperature between the melting and vaporisation temperatures. The SASOL 0907 paraffin wax material properties other than the enthalpy of formation were provided by a representative from SASOL South Africa (Webber, personal communication, 2010). The enthalpy of formation was obtained from Grosse (2009) as hot-fire tests were performed on the same type of paraffin wax. The liquid phase density and dynamic viscosity are evaluated at 200°C whereas the liquid phase thermal conductivity is estimated at a temperature of 170°C.

The comparison in characteristic velocity between the two fuels is shown in Fig. 2.7 for a chamber pressure of 40 bars and a nozzle expansion ratio of 5.99, assuming 100% combustion efficiency. Both curves follow the same trend with an optimum oxidiser-to-fuel ratio occurring in the vicinity of 7. It is noted that C<sub>31</sub>H<sub>64</sub> yields better overall motor performance than C<sub>50</sub>H<sub>102</sub> paraffin wax.

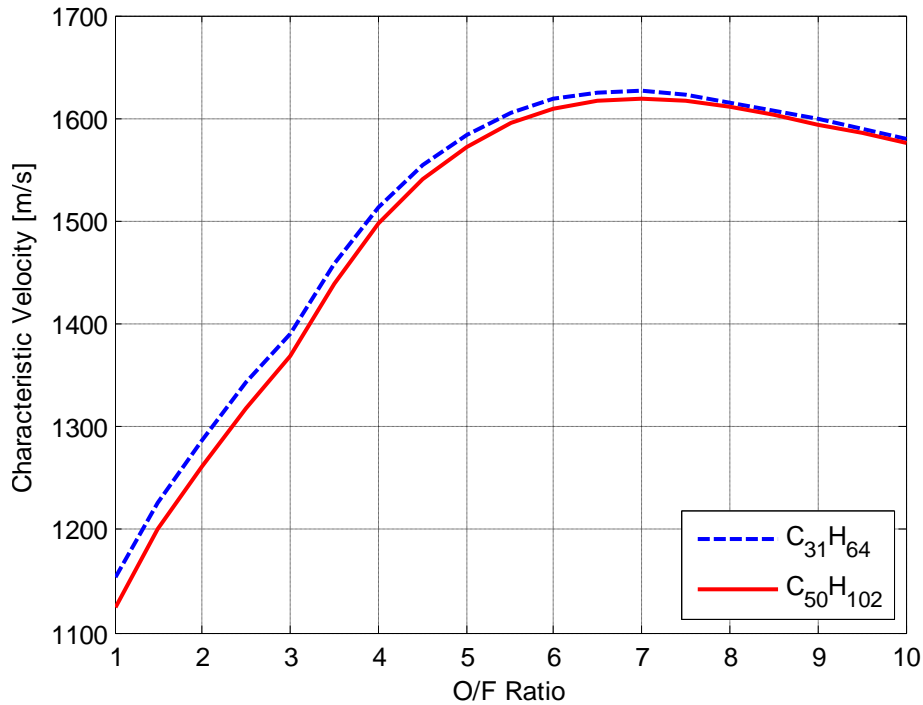


Figure 2.7 Characteristic velocity of typical paraffin waxes with nitrous oxide.

### 2.3.4 Fuel Grain Configurations

Development of the hybrid fuel grain relies on the propellant chemical and mechanical properties. From the early history of hybrid rocket motors, different fuel grain configurations have been produced and tested. Conventional circular solid grains vary in number of ports and port geometrical profiles. The most well-established grains include cylindrical, double-D, wagon wheel, and double row configurations (Fig. 2.8).

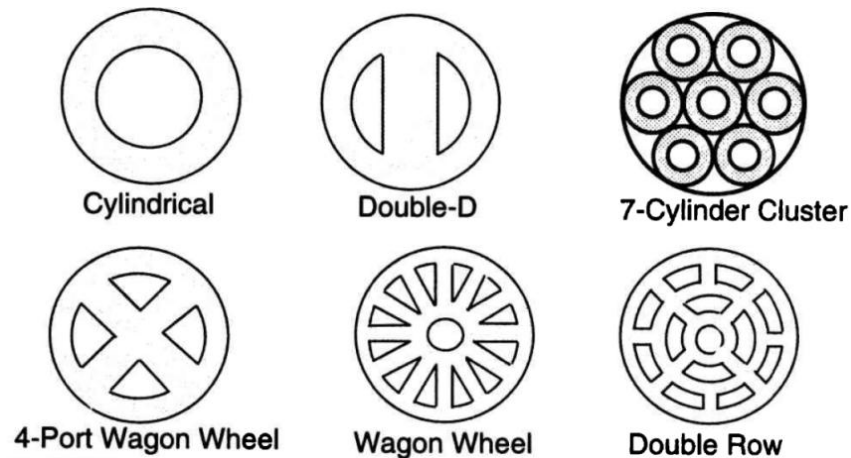


Figure 2.8 Typical hybrid fuel grain configurations (Humble et al., 1995).

Generally, the regression rate characteristic of individual propellants drives the solid grain conceptual design. For low fuel regression rates, such as HTPB, cylindrical multiple-port or wagon wheel grain configurations increase the burning surface thus decreasing its required length. The penalty of multiple cylindrical ports is the large residual web thickness or slivers at motor burnout. These unburned fuel slivers are volumetrically inefficient, which augments the vehicle dead mass. Among the range of cylindrical multi-port arrangements, the seven-cylinder cluster is the most effective, with its ports strategically positioned for minimal propellant volume loss. In addition, single- and four-port fuel grains are being developed for hybrid rocket motors. For example, the Purdue University hybrid rocket programme is based on a 4-port low density polyethylene (LDPE) fuel grain (Tsohas et al., 2009), and the Peregrine Sounding Rocket Programme is developing a large scale, high regression rate, motor based on a single-port paraffin wax fuel grain (Dyer et al., 2007). Multiple-port wagon wheel grain is usually designed with a cylindrical centre port to decrease its mass. The opening can either be blocked with a high temperature resistant material or burning can be allowed to occur through it. With the latter configuration, volumetric fuel efficiency is improved but asymmetrical burning is induced due to the difference in port geometry, affecting ballistic performance. After considering all these possible grain configurations, a cylindrical single-port was chosen for the Phoenix-1A's PV-1 motor due to the high regression rate characteristic of SASOL 0907 paraffin wax.

## CHAPTER 3

### Hybrid Rocket Motor Performance Modelling

#### 3.1 Description of the Hybrid Rocket Motor Physical and Chemical Models

The physicochemical combustion modelling of a hybrid rocket motor is highly dependent on the propellant combination and the type of pressurisation system incorporated in the design. Generally, classical hybrid propulsion systems can be segregated into three major control volumes as depicted in Fig. 3.1. In this study, these three control volumes were respectively modelled and coupled to provide the overall motor performance.

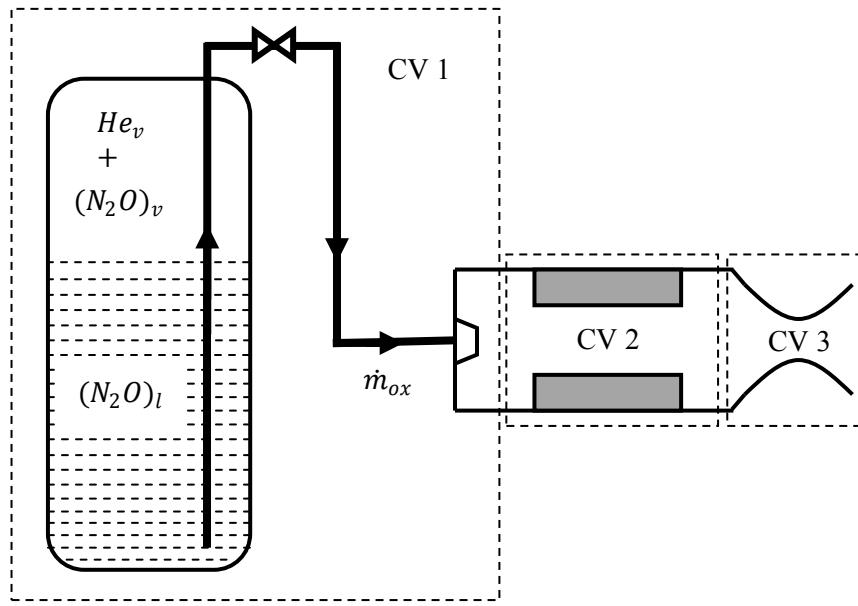


Figure 3.1 Hybrid propulsion system control volumes modelling (Geneviève et al., 2011).

Control volume 1 (CV1) represents the nitrous oxide self-pressurising delivery system which determines the oxidiser mass flow rate through the injector. The emptying of the oxidiser tank is considered a blowdown process due to the self-pressurising feature of nitrous oxide, supercharged with inert helium gas. At present, other oxidiser tank pressurisation methods are not being considered. The pyrolysis mechanism of solid fuel grain is analysed in control volume 2 (CV2). In particular, two regression rate methods for paraffin-based fuel will be described. The NASA-CEA equilibrium chemistry code (Gordon et al., 1994) is employed to compute the change in thermodynamic properties of the gaseous product

throughout the duration of the burn. The motor performance output is obtained through fundamental propulsion equations in control volume 3 (CV3).

### 3.2 Oxidiser Tank Pressurisation and Blowdown Process

Nitrous oxide, which is volatile at room temperature, generates useful high tank pressure that forces fluid flow to the combustion chamber. A conventional self-pressurising delivery system employs a non-condensable gas to supercharge the oxidiser tank pressure. This insoluble non-reactive gas resides above the liquid oxidiser and is discharged with the gaseous oxidiser after depletion of the liquid oxidiser. For the present research, the working fluids are two-phase liquid-vapour nitrous oxide and single-phase helium vapour mixture as illustrated in control volume 1 (Fig. 3.1). Gaseous helium assists the blowdown process by supercharging nitrous oxide above its ambient vapour pressure.

In control volume 1, the properties of the self-pressurising propellant vary as the oxidiser tank is discharged over time. Modelling this change in the fluid thermodynamic property is critical for determining the oxidiser mass flow rate through the feed line. The thermodynamic state variation of nitrous oxide is dependent on the oxidiser tank environmental temperature and on the liquid flowing out of CV1. During the blowdown process, there is a loss of internal energy due to the draining of the liquid nitrous oxide. As the tank empties some of the liquid oxidiser evaporates to equilibrate the system resulting in a decrease in thermal energy. The loss in thermal energy of the system, defined in Equation 3.15 as the change in oxidiser temperature, reduces the tank pressure accordingly. This causes a noticeable decay in motor thrust which correlates to the decrease in vapour pressure of nitrous oxide, that is, tank pressure. By evaluating the propellant temperature and mass in the tank, the change in the system's pressure can be simulated. The mathematical model which follows is based on the work of Fernandez (2009) who described and compared two numerical models for simulating a nitrous oxide tank blowdown process, namely ideal and non-ideal methods. The ideal method is adopted in this dissertation with a few differences in solution structure of the unknown parameters. In addition, the discharging of gaseous nitrous oxide is modelled.

Consider the blowdown process of an oxidiser tank partially filled with liquid nitrous oxide as shown in Fig. 3.2. The tank ullage contains a mixture of nitrous oxide and helium vapour which expels the liquid nitrous oxide out of control volume 1 due to the differential pressure between the tank and combustion chamber. Following the laws of mass and energy conservation, with general assumptions to simplify the

model, the pressure history of the system can be solved for the initial known parameters of nitrous oxide mass and tank temperature. The assumptions implemented in the system are:

1. The propellant remains in thermodynamic equilibrium throughout the blowdown process.
2. The system obeys the ideal gas law.
3. The oxidiser tank wall is assumed to be adiabatic and in thermal equilibrium with the propellant.
4. The liquid phase consists of pure nitrous oxide whereas the gas phase is a mixture of nitrous oxide vapour and helium gas.
5. The amount of helium in the tank ullage remains constant.
6. Evaporation at the liquid-vapour interface is not influenced by boiling phenomena.
7. Potential and kinetic energy of the propellant is neglected.
8. The gravitational head in the tank is negligible for both static and flight tests.

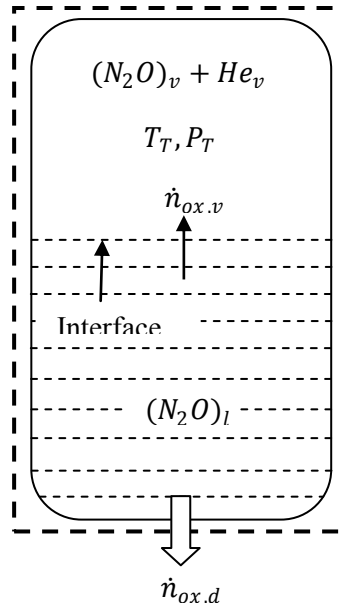


Figure 3.2 Control volume 1 blowdown process (Fernandez, 2009).

### 3.2.1 Liquid Nitrous Oxide Blowdown Modelling

Referring to Fig. 3.2, a set of differential equations derived from the conservation of mass and energy are numerically solved to determine the unknown parameters such as the tank pressure, temperature, and the number of moles of the liquid and vapour nitrous oxide inside the tank. The system must be coupled with the chamber pressure feedback, obtained from the gas dynamics modelling in the combustion chamber, to fully simulate the blowdown process.

By the conservation of mass, the change in number of moles of the whole system is given by Equation 3.1:

$$\frac{d}{dt}(n_g + n_{ox,l}) = -\dot{n}_{ox,d} \quad (3.1)$$

where  $n_{ox,l}$  is the number of moles of the liquid nitrous oxide and  $n_g$  represents the summation of the number of moles of nitrous oxide vapour  $n_{ox,v}$  and helium gas  $n_{sp,v}$ . As it is assumed that gaseous helium remains constant throughout the burn, because it remains primarily in the ullage volume,  $\frac{d}{dt}(n_{sp,v}) = 0$ , Equation 3.1 can be further simplified to:

$$\frac{d}{dt}(n_{ox,v} + n_{ox,l}) = -\dot{n}_{ox,d} \quad (3.2)$$

where  $\dot{n}_{ox,d}$  is the number of moles of the discharge flow rate out of the oxidiser tank. The conventional steady-state equation for the mass flow rate through an orifice, Equation 3.3, is transformed into molar form, Equation 3.4:

$$\dot{m}_{ox,d} = C_d N_{inj} A_{inj} \sqrt{2\rho_{ox,l}(P_T - P_{losses} - P_c)} \quad (3.3)$$

$$\dot{n}_{ox,d} = C_d N_{inj} A_{inj} \sqrt{\frac{2(P_T - P_{losses} - P_c)}{(MW)_{ox} \bar{V}_{ox,l}}} \quad (3.4)$$

where  $C_d$  is the dimensionless discharge coefficient,  $A_{inj}$  is the cross-sectional area of the orifice,  $N_{inj}$  is the number of orifices,  $\rho_{ox}$  is the oxidiser density,  $P_T$  is the tank pressure,  $P_{losses}$  is the pressure drop in the feed system and through the injector,  $P_c$  is the chamber pressure,  $(MW)_{ox}$  is the molecular weight of nitrous oxide, and  $\bar{V}_{ox,l}$  is the molar volume of liquid nitrous oxide. By equating Equation 3.4 to 3.2, the rate of change of propellant mass inside the tank is determined as:

$$\frac{dn_{ox,v}}{dt} + \frac{dn_{ox,l}}{dt} = -C_d N_{inj} A_{inj} \sqrt{\frac{2(P_T - P_{losses} - P_c)}{(MW)_{ox} \bar{V}_{ox,l}}} \quad (3.5)$$

The internal volume of the oxidiser tank is defined as the sum of the liquid phase nitrous oxide volume  $V_l$  and the gas phase (nitrous oxide vapour + gaseous helium) volume  $V_g$  Equation 3.6. As previously mentioned, the gas is assumed to obey the perfect gas law given by Equation 3.7.

$$V_T = V_g + n_{ox,l} \bar{V}_{ox,l} \quad (3.6)$$

$$P_T V_g = n_g R_u T_T \quad (3.7)$$

Raoult's law is used to describe the thermodynamic equilibrium state of the system. This states that the partial pressure of nitrous oxide is equal to the tank pressure times the number of moles of the nitrous oxide in the gas phase mixture. For Raoult's law to hold, the liquid nitrous oxide is assumed to evaporate and saturate the gas mixture instantaneously throughout the blowdown process. Using Raoult's law, the tank pressure is related to the saturated vapour pressure of nitrous oxide  $P_{ox}^*$ , which is a function of the tank temperature, and the mole fraction of the gas mixture:

$$P_T = \frac{P_{ox}^*|_{T_T}}{\left[ \frac{n_{ox,v}}{n_{ox,v} + n_{sp,v}} \right]} \quad (3.8)$$

substituting Equation 3.8 into 3.7:

$$P_{ox}^* V_g = n_{ox,v} R_u T_T \quad (3.9)$$

Equation 3.9 relates the saturated vapour pressure of nitrous oxide to the number of moles of nitrous oxide vapour, volume occupied by the gas mixture, and the tank temperature. Now, substituting Equation 3.9 into 3.6, and differentiating with respect to time:

$$\begin{aligned} -\bar{V}_{ox,l} P_{ox}^* \frac{dn_{ox,l}}{dt} + & \left[ [V_T - n_{ox,l} \bar{V}_{ox,l}] \frac{dP_{ox}^*}{dT} - n_{ox,l} P_{ox}^* \frac{d\bar{V}_{ox,l}}{dT} \right] \frac{dT_T}{dt} \\ & = R_u \left[ n_{ox,v} \frac{dT_T}{dt} + T_T \frac{dn_{ox,v}}{dt} \right] \end{aligned} \quad (3.10)$$

According to the first principle of thermodynamics for an open system, an energy balance is taken for the entire CV1 with the following simplifications: neglecting heat exchange to the environment,  $\dot{Q} = 0$ , and

no moving boundary work being done on the system,  $\dot{W} = 0$ . The tank wall and the propellant are assumed to be in thermal equilibrium. With these assumptions, the fundamental equation can be simplified to Equation 3.12:

$$\frac{dU}{dt} = \dot{Q} + \dot{W} + \dot{m}H \quad (3.11)$$

$$\frac{d}{dt}(m_T u_T + n_{ox,l} \bar{U}_{ox,l} + n_g \bar{U}_g) = -\dot{n}_{ox,d} \bar{H}_{ox,l} \quad (3.12)$$

where  $m_T$  and  $u_T$  correspond to the mass of the tank and specific internal energy of the tank, respectively. In addition,  $\bar{U}$  is the internal energy of the liquid and gas phases, and  $\bar{H}_{ox,l}$  stands for the molar enthalpy of liquid phase nitrous oxide. The negative sign represents the total energy loss of the system through the draining process of the tank. Expanding Equation 3.12:

$$\begin{aligned} m_T \frac{du_T}{dt} + n_{ox,l} \frac{d\bar{U}_{ox,l}}{dt} + n_{ox,v} \frac{d\bar{U}_{ox,v}}{dt} + n_{sp,v} \frac{d\bar{U}_{sp,v}}{dt} \\ = \frac{dn_{ox,v}}{dt} [\bar{H}_{ox,l} - \bar{U}_{ox,v}] + \frac{dn_{ox,l}}{dt} [\bar{H}_{ox,l} - \bar{U}_{ox,l}] \end{aligned} \quad (3.13)$$

The heat of vaporisation of nitrous oxide is defined as the difference between its vapour and liquid phase enthalpies,  $\Delta\bar{H}_{ox,v} = \bar{H}_{ox,v} - \bar{H}_{ox,l}$ . The enthalpy of vapour nitrous oxide is described as,  $\bar{H}_{ox,v} = \bar{U}_{ox,v} + P_T \bar{V}_{ox,v}$ . These two equations, in addition to the ideal gas law;  $P_T \bar{V}_{ox,v} = R_u T_T$ , are substituted into the right hand side of Equation 3.13:

$$\begin{aligned} m_T \frac{du_T}{dt} + n_{ox,l} \frac{d\bar{U}_{ox,l}}{dt} + n_{ox,v} \frac{d\bar{U}_{ox,v}}{dt} + n_{sp,v} \frac{d\bar{U}_{sp,v}}{dt} \\ = \frac{dn_{ox,v}}{dt} [R_u T_T - \Delta\bar{H}_{ox,v}] + \frac{dn_{ox,l}}{dt} [P_T \bar{V}_{ox,l}] \end{aligned} \quad (3.14)$$

where  $P_T$  and  $T_T$  are the tank pressure and temperature, respectively. For an ideal gas, in this case nitrous oxide vapour, the specific heat at constant volume and pressure are defined as:  $c_V = \left(\frac{dU}{dT}\right)_V = \left(\frac{dQ}{dT}\right)_V$  and  $c_P = \left(\frac{dH}{dT}\right)_P = \left(\frac{dQ}{dT}\right)_P$ , respectively. Therefore, the rate of change of molar internal energy of nitrous oxide vapour is given by:  $\frac{d\bar{U}_{ox,v}}{dt} = \bar{C}_{V_{ox,v}} \frac{dT_T}{dt}$ , and for gaseous helium:  $\frac{d\bar{U}_{sp,v}}{dt} = \bar{C}_{V_{sp,v}} \frac{dT_T}{dt}$ . The rate of change of

specific internal energy of the oxidiser tank, which is a solid, is approximated by:  $\frac{du_T}{dt} \approx \frac{dH_T}{dt} = c_{P_T} \frac{dT_T}{dt}$ . Assuming that liquid nitrous oxide behaves as an incompressible fluid, its rate of change of molar internal energy with respect to time is approximated:  $\frac{d\bar{U}_{ox,l}}{dt} = \bar{C}_{V_{ox,l}} \frac{dT_T}{dt} \approx \bar{C}_{P_{ox,l}} \frac{dT_T}{dt}$ . Substituting these equations back into Equation 3.14:

$$\begin{aligned} & [m_T c_{P_T} + n_{ox,l} \bar{C}_{P_{ox,l}} + n_{ox,v} \bar{C}_{V_{ox,v}} + n_{sp,v} \bar{C}_{V_{sp,v}}] \frac{dT_T}{dt} \\ &= \frac{dn_{ox,v}}{dt} [R_u T_T - \Delta \bar{H}_{ox,v}] + \frac{dn_{ox,l}}{dt} [P_T \bar{V}_{ox,l}] \end{aligned} \quad (3.15)$$

The Equations 3.5, 3.10, and 3.15 respectively describe the mass conservation, Raoult's Law, and energy conservation of the self-pressurising delivery system and are solved simultaneously for the three unknown time derivatives: number of moles of the liquid nitrous oxide,  $\frac{dn_{ox,l}}{dt}$ , number of moles of the vapour nitrous oxide,  $\frac{dn_{ox,v}}{dt}$ , and the tank temperature,  $\frac{dT_T}{dt}$ . A fourth order Runge Kutta numerical approach is employed in Hybrid Rocket Performance Code (HRPC) to integrate the three unknowns at each time step. Thereafter, the oxidiser tank pressure solution for the next time step is determined through Equation 3.16 below.

$$P_T = \frac{(n_{ox,v} + n_{sp,v}) R_u T_T}{V_T - n_{ox,l} \bar{V}_{ox,l}} \quad (3.16)$$

### 3.2.2 Gaseous Nitrous Oxide Blowdown Modelling

The above unknown equations are only valid for the draining of liquid nitrous oxide. A new set of differential equations must be derived for the special case where liquid nitrous oxide is completely consumed. In that instance, gaseous nitrous oxide flows out of the tank with a considerable drop in mass flow rate thus affecting the fuel regression rate in the combustion chamber. Consequently, the chamber pressure and motor thrust decrease significantly during this shift in fluid phase. Modelling the discharge of gaseous nitrous oxide is not considered critical for overall motor performance simulation due to the duration of this phase compared to the liquid flow. Nevertheless, this short burn time phase produces a somewhat beneficial thrust performance in the flight mission, particularly when liquid burn-out occurs at high altitude.

The original assumptions are still valid for the nitrous oxide and helium gaseous mixture. Additionally, it is assumed that fluid flowing out of the oxidiser tank consists of pure gaseous nitrous oxide. That is, the helium supercharge gas resides above the gaseous nitrous oxide because of its lower density. Following the same procedure as Section 3.2.1, two equations are derived:

$$\frac{dn_{ox,v}}{dt} = -C_d N_{inj} A_{inj} \sqrt{\frac{2(P_T - P_{losses} - P_C)}{(MW)_{ox} \bar{V}_{ox,v}}} \quad (3.17)$$

$$[m_T c_{P_T} + n_{ox,v} \bar{C}_{V_{ox,v}} + n_{sp,v} \bar{C}_{V_{sp,v}}] \frac{dT_T}{dt} = \frac{dn_{ox,v}}{dt} [R_u T_T] \quad (3.18)$$

These are solved for the two unknown time derivatives: number of moles of the vapour nitrous oxide,  $\frac{dn_{ox,v}}{dt}$ , and the tank temperature,  $\frac{dT_T}{dt}$ . It is noted that all the properties of the liquid phase nitrous oxide are cancelled out, which greatly simplifies the differential equations. Again, a fourth order Runge Kutta numerical approach is used to integrate the two unknowns at each time step, follow by the oxidiser tank pressure calculation:

$$P_T = \frac{(n_{ox,v} + n_{sp,v}) R_u T_T}{V_T} \quad (3.19)$$

### 3.2.3 Initial Conditions and Thermodynamic Properties

A series of input variables is required to determine the initial conditions inside the oxidiser tank and provide the starting-point for the numerical solution of the ordinary differential equations. Important inputs to the system are: the initial nitrous oxide and helium loaded masses, the initial tank temperature which is equal to the ambient or environment temperature of the system, and the oxidiser tank mass and internal volume. The total number of nitrous oxide moles is the sum of its liquid and vapour number of moles, that is;  $n_{ox,t} = n_{ox,l} + n_{ox,v}$ . The initial liquid-vapour mole compositions of nitrous oxide are determined by the combination of Raoult's law, ideal gas law, and the vapour pressure of the nitrous oxide as a function of the initial tank temperature input variable:

$$n_{ox,l} = \frac{n_{ox,t} R_u T_T - P_{ox}^* V_T}{R_u T_T - P_{ox}^* \bar{V}_{ox,l}} \quad (3.20)$$

$$n_{ox,v} = \frac{P_{ox}^*(V_T - n_{ox,t}\bar{V}_{ox,l})}{R_u T_T - P_{ox}^*\bar{V}_{ox,l}} \quad (3.21)$$

To provide closure of the system, the change in thermodynamic properties of the liquid-vapour phase nitrous oxide, gaseous helium, and oxidiser tank material need to be specified, in particular, the change in specific/molar heat capacities at constant pressure (nitrous oxide, helium, and oxidiser tank material), the heat of vaporisation and molar specific volume of the liquid nitrous oxide, and the vapour pressure of the nitrous oxide. Perry and Green (2007) provide useful formulae for the thermodynamic properties of various fluids and materials as functions of temperature. The necessary formulae applied in this work were extracted from the handbook and are reproduced in Appendix C for convenience.

In short, the ideal mathematical model assumes no intermolecular interactions in the gas phase mixture consisting of nitrous oxide and helium. The model is described by Raoult's law which states that the oxidiser tank pressure is proportional to the vapour pressure and mole fraction of each substance, namely nitrous oxide vapour and gaseous helium, occupying the system. Furthermore, Raoult's law assumes that the liquid-vapour phase quality distribution of nitrous oxide is independent of the amount of gaseous helium in the tank. This applies only to low-pressure systems where the intermolecular forces are weak. Even if the nitrous oxide blowdown process may exceed the limits for which this theory is valid, the ideal model can be used to predict the oxidiser tank pressure history within acceptable accuracy.

### 3.3 Solid Fuel Regression Rate Modelling

The combustion mechanism of a hybrid rocket motor essentially relies on the propellant regression rate characteristic. The regression rate of a solid fuel, also referred to as the burning rate or pyrolysis process, determines the degree of oxidiser-to-fuel mixture composition throughout the local grain port. Each propellant combination has an optimum oxidiser-to-fuel ratio called the stoichiometric ratio. As such, variation in the mixture composition greatly affects the performance of a hybrid rocket motor, which requires critical regression rate analysis.

To date, numerous regression rate theories have been developed for a range of propellant combinations but a universal law does not exist. However, one common characteristic of the theories is the strong dependency of solid-fuel burning rate on oxidiser flow rate. The two most recognised theories will now be described, namely the classical diffusion limited theory by Marxman et al. (1964), and the non-classical liquefying entrainment mass-transfer theory by Karabeyoglu et al. (2002).

### 3.3.1 Classical Regression Rate Theory

The early work of Marxman et al. (1964) on solid-fuel regression rate set the fundamental baseline for other derived theories. In this approach, the self-sustained combustion process in hybrid rocket motors is due to a diffusion flame zone or combustion zone where the propellants are continually reacting within a boundary layer (Fig. 3.3). The flame zone is supplied with vaporised fuel due to heat convection and with oxidiser from the main stream, by diffusion and turbulence. The theory shows that the established flame zone is formed at a distance from the fuel slab in the turbulent boundary layer. It is postulated that the rate at which a solid-fuel burns, is dependent on the oxidiser mass flux and heat transfer to the grain. Referring to Sutton and Biblarz (2001), deriving the classical diffusion limited theory, an energy balance is analysed at the fuel grain inner wall to obtain the local instantaneous regression rate of the propellant:

$$\dot{r}_{cl} = 0.036 \frac{G_t^{0.8}}{\rho_f} \left( \frac{\mu}{x} \right)^{0.2} \beta^{0.23} \quad (3.22)$$

where  $G_t$  is the total mass flux (sum of the oxidiser mass flux and the eroded fuel mass flux),  $x$  is the axial coordinate,  $\rho_f$  is the solid fuel density,  $\mu$  is the combustion gas viscosity, and  $\beta$  ( $5 < \beta < 100$ ) is the non-dimensional fuel mass flux known as the blowing coefficient, which is inversely proportional to the heat of vaporisation, evaluated at the fuel surface. A detailed derivation of Equation 3.22 is given by Sutton and Biblarz (2001).

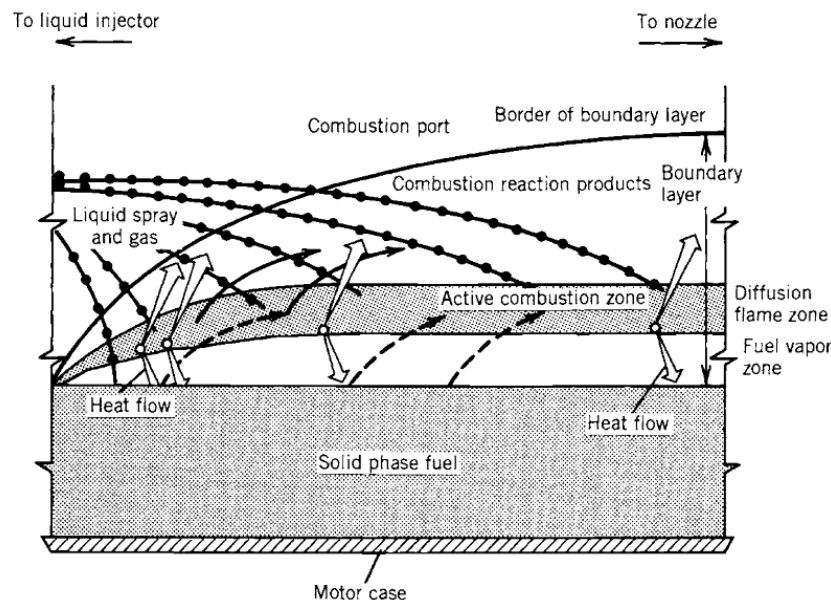


Figure 3.3 Classical diffusion limited theory of hybrid rocket propellants (Sutton and Biblarz, 2001).

Based on this study, the burning rate of a solid fuel is more dependent on the total mass flux  $G_t$  through the port than the axial coordinate  $x$  and blowing coefficient  $\beta$ . The weak dependency of axial coordinate and blowing coefficient on regression rate is illustrated in the above formula. In addition, the regression rate is invariant with chamber pressure. This is supported by typical behaviour of the solid fuel burning rate with respect to the flow of oxidiser; Fig. 3.4. The pyrolysis mechanism can be classified into three distinct regions. Hybrid rocket motors usually operate in the diffusion region where the classical diffusion limited theory is valid. In the diffusion region, the regression rate depends on the total mass flux. However, two operational regimes may be affected by the variation in chamber pressure: at significantly high oxidiser mass flux where combustion is governed by chemical kinetics, and at significantly low oxidiser mass flux where heat transfer by radiation is more pronounced than convection. Additionally, the fuel chemical composition determines the combustion regime. This is particularly true for metallised hybrid propellants.

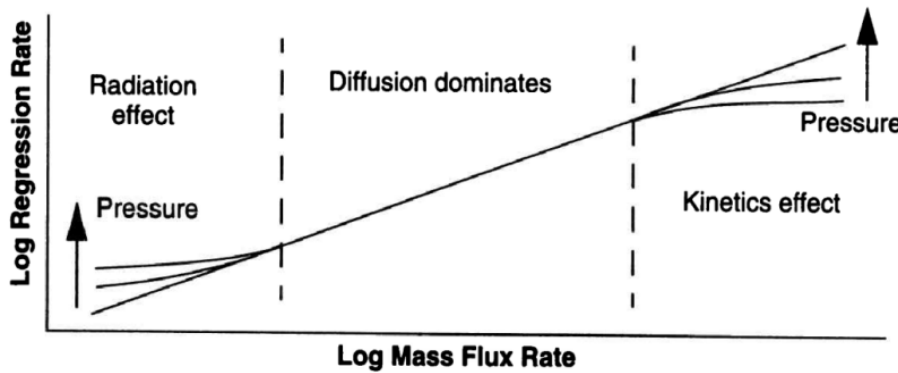


Figure 3.4 Effects of pressure on regression rate (Humble et al., 1995).

The diffusion limited theory can be simplified into a semi-empirical expression for general motor design and analysis with reasonable accuracy. The blowing coefficient  $\beta$ , combustion gas viscosity  $\mu$ , and fuel density  $\rho_f$ , are compacted into one factor,  $a$ . The reduced power law expression is given in terms of the total mass flux and axial coordinate in the port:

$$\dot{r} = a G_t^n x^m \quad (3.23)$$

where  $a, n$  and  $m$  are the ballistic coefficients, and  $x$  is the distance down the port. The three ballistic coefficients are determined by experiments for a specific propellant combination. In the literature, the axial position exponent  $m$  tends to be much less than 1, as shown in the original regression rate diffusion theory formula, so the space variation can be ignored and  $m = 0$ . This low dependency of fuel regression

rate on the axial length is due to the fact that both the boundary layer thickness and total mass flux increase along the port. The increase in boundary layer thickness is responsible for the decrease in heat transfer to the grain wall causing a decrease in regression rate whereas the total mass flux is increased as more gaseous fuel is added to the main stream causing an increase in regression rate. These two opposing effects result in weak dependence on the axial port length. In addition, the total mass flux,  $G_t = G_{ox} + G_f$ , is replaced by the oxidiser mass flux  $G_{ox}$  as the fuel mass flux is relatively much smaller than the oxidiser flowing down the port. Thus, the widely used semi-empirical regression rate expression is given as:

$$\dot{r} = aG_{ox}^n \quad (3.24)$$

where  $a$  and  $n$  are experimentally obtained for individual oxidiser/fuel combinations, range of oxidiser mass flow rate, injector configuration, and scale of the fuel grain. Typical ballistic coefficients for a variety of propellant combinations are given in Table 3.1.

Table 3.1 Typical values of ballistic coefficients  $a$  and  $n$ , for  $[\dot{r}] = \text{m/s}$  and  $[G_{ox}] = \text{kg}/(\text{m}^2\text{s})$ .

Fuel	Oxidiser	$a$	$n$	Reference
HTPB	GOX	$0.025 \times 10^{-3}$	0.65	Karabeyoglu et al. (2002)
HTPB	GOX	$0.0304 \times 10^{-3}$	0.681	Sutton and Biblarz (2001)
HTPB	GOX	$0.087 \times 10^{-3}$	0.53	George et al. (2001)
HTPB	GOX	$0.077 \times 10^{-3}$	0.53	George et al. (2001)
HTPB	N <sub>2</sub> O	$0.094 \times 10^{-3}$	0.325	Lohner et al. (2006)
Paraffin wax	GOX	$0.091 \times 10^{-3}$	0.69	Karabeyoglu et al. (2002)
Paraffin wax	LOX	$0.117 \times 10^{-3}$	0.62	Karabeyoglu et al. (2003)
Paraffin wax	H <sub>2</sub> O <sub>2</sub>	$0.0344 \times 10^{-3}$	0.959	Brown and Lydon (2005)
Paraffin wax	N <sub>2</sub> O	$0.132 \times 10^{-3}$	0.555	Grosse (2009)
Paraffin wax	N <sub>2</sub> O	$0.155 \times 10^{-3}$	0.5	McCormick et al. (2005)
HDPE	N <sub>2</sub> O	$0.0462 \times 10^{-3}$	0.352	Lohner et al. (2006)
PMMA	N <sub>2</sub> O	$0.0466 \times 10^{-3}$	0.377	Lohner et al. (2006)

This experimental data can only be used for similar hybrid rocket motor designs. To illustrate this point, various ballistic coefficients for different motor configuration are reported for HTPB/GOX propellant combinations as shown in Table 3.1. The paraffin wax/nitrous oxide ballistic coefficients from Grosse (2009) and McCormick et al. (2005) were used for all the analyses relating to Phoenix-1A motor design

due the similarity in motor configuration. The differences in motor performance regarding these parameters are relatively small as they are nearly identical.

By definition, the oxidiser mass flux rate is determined by the flow of oxidiser over the cross-sectional area of the grain port. Therefore, the oxidiser mass flux rate per port  $G_{ox,p}$  is defined as:

$$G_{ox,p} = \frac{\dot{m}_{ox,t}}{N_p A_p} \quad (3.25)$$

$$G_{ox,t} = N_p G_{ox,p} \quad (3.26)$$

where  $\dot{m}_{ox,p} = \frac{\dot{m}_{ox,t}}{N_p}$  is the total oxidiser mass flow rate into the combustion chamber,  $N_p$  represents the number of grain ports,  $A_p$  is the grain port cross-sectional area, and  $G_{ox,t}$  is the total oxidiser mass flux. The fuel mass flow rate is a function of the oxidiser flow and the rate at which the solid fuel regresses. For a small change in time, the total fuel mass generated  $\dot{m}_{f,t}$  is calculated using:

$$\dot{m}_{f,p} = \rho_f A_b \dot{r} \quad (3.27)$$

$$A_b = P_{per} L_g \quad (3.28)$$

$$\dot{m}_{f,t} = N_p \dot{m}_{f,p} \quad (3.29)$$

where  $\dot{m}_{f,p}$  is the fuel mass flow rate per port,  $\dot{m}_{f,t}$  is the total fuel mass flow rate in the combustion chamber,  $A_b$  is the instantaneous burnt area,  $P_{per}$  is the perimeter of the burnt surface, and  $L_g$  is the fuel grain length. For a cylindrical port,  $P_{per} = 2\pi R_p$  where  $R_p$  corresponds to the radius, the fuel mass flow rate per port is given as:

$$\dot{m}_{f,p} = 2a \dot{m}_{ox}^n \pi^{1-n} R_p^{1-2n} L_g \rho_f \quad (3.30)$$

The expression for a circular port suggests that the fuel mass flow rate is independent of the port radius when  $n=0.5$ . That is, for a constant oxidiser mass flow, the oxidiser-to-fuel ratio remains constant throughout the burn. Effectively, this applies to paraffin wax/nitrous oxide hybrid motors as the ballistic coefficient  $n$  is in the vicinity of this critical value. The inherent characteristic of paraffin wax/nitrous

oxide facilitates to maintain an optimum oxidiser-to-fuel ratio, hence maximising motor performance for a constant oxidiser mass flow rate. However, fuel mass flow increases and decreases when  $n < 0.5$  and  $n > 0.5$ , respectively. For the upper and lower limit cases, the shift in oxidiser-to-fuel ratio affects the stoichiometric reaction which results in an increase or decrease in motor thrust. Another aspect to consider when designing a hybrid rocket motor is the solid-propellant's stoichiometric length. The fuel grain stoichiometric length is defined as the position where the local oxidiser/fuel mixture reaches its optimum value. That is, fuel grains are designed according to their theoretical stoichiometric lengths.

### 3.3.2 Non-Classical Regression Rate Theory

The non-classical regression rate theory by Karabeyoglu et al. (2002) extends the classical theory to solid fuels that liquefy as heat is transferred to the inner surface. Typical examples of such fuel are cryogenic alkanes, paraffin waxes, and polyethylene waxes. These solid fuels have shown significant higher regression rates than conventional polymeric fuels. Karabeyoglu et al. (2002) postulate that these fuels form an unstable liquefied layer over the burning surface which is entrained in the form of droplets into the high velocity gas stream as illustrated in Fig. 3.5. The theory suggests that the liquid instability increases as surface tension and viscosity of the melt layer decrease. To summarise, the high regression rate of these fuels is attributed to the combination of the entrainment mass transfer into the gas stream and the conventional fuel vaporisation process of the classical theory.

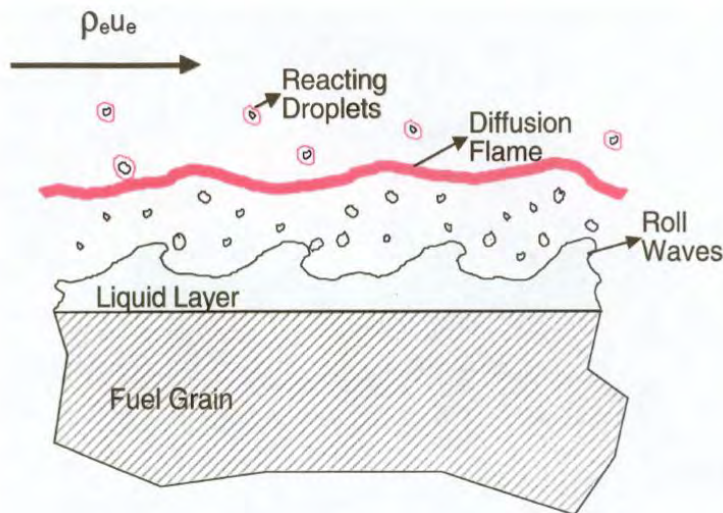


Figure 3.5 Entrainment mass transfer mechanism (Karabeyoglu et al., 2001).

A brief description of the theory is now given with a focus on the primary formulae for the solution of the non-classical regression rate. Based on Karabeyoglu et al.'s work, the non-classical regression rate theory is derived from the classical combustion theory with the addition of the entrainment mass transfer from the melt layer. To account for the mass transfer mechanism involving the entrainment of unstable liquid droplets into the main stream, the classical regression rate, Equation 3.22, is altered by the following assumptions:

1. The energy required to vaporise the fuel for the gasification mechanism is reduced because of the mass entrainment of the liquid layer.
2. The blowing coefficient  $\beta$  is solely due to the gasification mechanism, that is, the vaporised fuel from the burning surface. The evaporation of the liquid droplets is assumed to occur above the diffusive flame zone due to the high gas velocity.
3. Heat transfer from the flame zone to the liquid layer interface is enhanced due to the formation of waves on the surface.

The non-classical regression rate of hybrid propellants can be stated as the sum of the evaporation regression rate  $\dot{r}_v$  due to the gasification mechanism and the entrainment regression rate  $\dot{r}_{ent}$  due to the mass transfer of the liquid droplets:

$$\dot{r}_t = \dot{r}_v + \dot{r}_{ent} \quad (3.31)$$

Taking an energy balance at the liquid-gas interface, the correlation between the regression rate parameters, combustion gas viscosity  $\mu$ , blowing coefficient  $\beta$ , radiative heat transfer  $\dot{Q}_r$ , convective heat transfer  $\dot{Q}_c$ , fuel density  $\rho_f$ , and total mass flux  $G_t$  is obtained:

$$\dot{r}_v + \left[ R_{he} + R_{hv} \left( \frac{\dot{r}_v}{\dot{r}_t} \right) \right] \dot{r}_{ent} = F_r \frac{0.03\mu^{0.2}}{\rho_f} \left( 1 + \frac{\dot{Q}_r}{\dot{Q}_c} \right) \beta \frac{C_H}{C_{HO}} G_t^{0.8} \frac{1}{x^{0.2}} \quad (3.32)$$

where  $R_{he}$  is the nondimensional energy parameter for entrainment,  $R_{hv}$  is the nondimensional energy parameter for vaporisation,  $F_r$  is the roughness parameter which accounts for the increase in heat transfer, and  $C_H/C_{HO}$  is the blocking factor which is a function of the blowing coefficient. These parameters are defined as:

$$R_{hv} = \frac{C_l \Delta T_1}{h_e + L_v} \quad (3.33)$$

$$R_{he} = \frac{h_m}{h_e + L_v} \quad (3.34)$$

$$F_r = 1 + \frac{14.1 \rho_g^{0.4}}{G_t^{0.8} (T_g/T_v)^{0.2}} \quad (3.35)$$

$$\frac{C_H}{C_{HO}} \cong \frac{2}{2 + 1.25 B_g^{0.75}} \quad (3.36)$$

where  $C_l$  is the liquid specific heat,  $\Delta T_1 = T_v - T_m$  is the difference between vaporisation and melting temperature,  $h_e$  is the total heat of entrainment,  $L_v$  is the latent heat of vaporization,  $h_m$  is the total heat of melting,  $\rho_g$  is the gas density,  $T_g$  is the average gas phase temperature, and  $T_v$  is the vaporization temperature. The entrainment regression rate is related to the total mass flux through the grain port and total regression rate:

$$\dot{r}_{ent} = a_{ent} \left( \frac{G_t^{2\alpha}}{\dot{r}_t^\gamma} \right) \quad (3.37)$$

where the coefficient  $a_{ent}$  is dependent on the propellant combination and average gas density in the combustion chamber. Comparing the classical and non-classical regression rate formulae, Equations 3.22 and 3.32, it can be noted that the latter was derived from the classical theory as it is proportional to:

$$\dot{r}_t \propto \left( \frac{G_t^{0.8}}{\rho_f} \left[ \frac{\mu}{x} \right]^{0.2} \beta \right) \quad (3.38)$$

Equations 3.33 to 3.37 can be substituted into Equation 3.22 to obtain a nonlinear equation that can be solved for a specified oxidiser and fuel combination, with reasonable assumptions to obtain the total regression rate as a function of space. This equation models the variation in regression rate through the grain port.

## 3.4 Gas Dynamics Modelling

### 3.4.1 Rocket Fundamental Formulae

Rocket propulsion is achieved by obeying Newton's third law of motion that states "for every action there is an equal and opposite reaction". Basic thermodynamic and gas dynamic relations describe the fundamental formulae of rocket propulsion. In order to compare the performance of rocket motors, fundamental formulae such as theoretical thrust, specific impulse, and characteristic velocity must be stated. Better performance results from increasing these parameters, hence optimising design motor parameters such as nozzle configuration. The following governing equations are employed to predict the theoretical performance of any propulsion system that expands gaseous mixture at high velocity through a nozzle to generate the propulsive thrust (Sutton and Biblarz, 2001).

The characteristic velocity  $c^*$  of a rocket motor depends on propellant characteristics and combustion chamber design; it is not dependent on nozzle characteristics. Specifically, it is a function of the exothermic reaction temperature and the gas properties of the propellants. As it is readily determined by measurable parameters such as chamber pressure, nozzle throat area, and mass flow rate, it is used as a measure of rocket motor performance:

$$c^* = \frac{V_{exh}}{\eta_{eff} C_F} = \frac{P_c A_t}{\eta_{eff} \dot{m}_{noz}} = \frac{\eta_{eff} \sqrt{R_c T_c}}{\left[ k_c \left( \frac{2}{k_c + 1} \right)^{\frac{(k_c + 1)}{(k_c - 1)}} \right]^{1/2}} \quad (3.39)$$

where  $V_{exh}$  is the exhaust velocity,  $C_F$  is the thrust coefficient,  $A_t$  is the nozzle throat area,  $R_c$  is the combustion gas constant,  $T_c$  is the combustion temperature,  $k_c$  is the specific heat ratio of combustion,  $\dot{m}_{noz}$  is the nozzle gas mass flow rate, and  $\eta_{eff}$  is the combustion efficiency. The combustion efficiency  $\eta_{eff}$  is the degree of energy extraction from the reaction process of the propellants. In a well designed rocket motor, the typical range of combustion efficiency is 92% to 99%. It is defined as the experimental characteristic velocity  $c_{exp}^*$  over the theoretical value  $c_{the}^*$ :

$$\eta_{eff} = \frac{c_{exp}^*}{c_{the}^*} \quad (3.40)$$

The thrust coefficient  $C_F$  is a non-dimensional parameter that is defined as the propulsive force divided by the chamber pressure  $P_c$  and the nozzle throat area  $A_t$ :

$$C_F = \lambda \sqrt{\left(\frac{2k_c^2}{k_c - 1}\right) \left(\frac{2}{k_c + 1}\right)^{\left(\frac{k_c+1}{k_c-1}\right)} \left(1 - \left[\frac{P_e}{P_c}\right]^{\left(\frac{k_c-1}{k_c}\right)}\right) + \left(\frac{P_e - P_a}{P_c}\right) \left(\frac{A_e}{A_t}\right)} \quad (3.41)$$

where  $\lambda$  is the nozzle exit angle correction factor,  $P_e$  is the nozzle exit plane pressure,  $P_a$  is the atmospheric pressure, and  $A_e$  is the nozzle exit area. Thrust coefficient is a function of nozzle characteristics and the specific heat ratio of combustion; it is not dependent on combustion temperature. The first term on the right hand side of the equation is called the momentum-thrust and the second term in the equation is called the pressure-thrust. The optimum coefficient of thrust occurs when the pressure-thrust term is zero, that is, when  $P_e = P_a$ . At vacuum condition;  $P_a = 0$ , atmospheric pressure is eliminated in Equation 3.41. The thrust coefficient can be determined experimentally by proper measurements of the thrust, chamber pressure, and nozzle throat area:

$$C_F = \frac{F}{P_c A_t} \quad (3.42)$$

where  $F$  is the measured thrust. Typical values of thrust coefficient range from 0.8 to 1.9. The exhaust velocity  $V_{exh}$  is defined as the average velocity at which the reacted gaseous products are ejected through the nozzle:

$$V_{exh} = \eta_{eff} c^* C_F \quad (3.43)$$

To reach the supersonic flow condition in the diverging section of the nozzle, the flow must be choked at the throat. The nozzle mass flow rate determined from the standard choked flow equation is a function of chamber pressure, nozzle throat area, and thermodynamic gas properties (implicit in the characteristic velocity) which define sonic conditions at the throat:

$$\dot{m}_{noz} = \frac{P_c A_t}{\eta_{eff} c^*} \quad (3.44)$$

Rocket thrust is defined as the summation of the momentum thrust caused by the ejected hot gases and the pressure thrust caused by the resultant pressure difference at the nozzle exit plane. For a steadily operating rocket propulsion system, and accounting for the imbalance of atmospheric pressure  $P_a$  and exit pressure  $P_e$ , the total thrust ( $F = \dot{m}_{noz} V_{exh}$ ) is given by:

$$F = \dot{m}_{noz} \eta_{eff} c^* \left[ \lambda \sqrt{\left( \frac{2k_c^2}{k_c - 1} \right) \left( \frac{2}{k_c + 1} \right)^{\left( \frac{k_c+1}{k_c-1} \right)} \left( 1 - \left[ \frac{P_e}{P_c} \right]^{\left( \frac{k_c-1}{k_c} \right)} \right)} + \left( \frac{P_e - P_a}{P_c} \right) \left( \frac{A_e}{A_t} \right) \right] \quad (3.45)$$

The optimum thrust for a particular nozzle operating at its design conditions,  $P_e = P_a$ :

$$F_{opt} = \dot{m}_{noz} \eta_{eff} c^* \left[ \lambda \sqrt{\left( \frac{2k_c^2}{k_c - 1} \right) \left( \frac{2}{k_c + 1} \right)^{\left( \frac{k_c+1}{k_c-1} \right)} \left( 1 - \left[ \frac{P_e}{P_c} \right]^{\left( \frac{k_c-1}{k_c} \right)} \right)} \right] \quad (3.46)$$

In the absence of atmospheric pressure (vacuum)  $P_a = 0$ :

$$F_{vac} = \dot{m}_{noz} \eta_{eff} c^* \left[ \lambda \sqrt{\left( \frac{2k_c^2}{k_c - 1} \right) \left( \frac{2}{k_c + 1} \right)^{\left( \frac{k_c+1}{k_c-1} \right)} \left( 1 - \left[ \frac{P_e}{P_c} \right]^{\left( \frac{k_c-1}{k_c} \right)} \right)} + \left( \frac{P_e}{P_c} \right) \left( \frac{A_e}{A_t} \right) \right] \quad (3.47)$$

The total impulse  $I_t$  of a rocket motor is given in Equation 3.48. It is defined as the thrust integrated over the total burn time  $t_b$  of the propulsion system. The specific impulse  $I_{sp}$  is defined as the total impulse per unit weight flow of propellant, and is a comparative performance parameter of rocket motors. Vacuum specific impulse  $I_{vac}$  is obtained from vacuum thrust as shown in Equation 3.50.

$$I_t = F t_b \quad (3.48)$$

$$I_{sp} = \frac{F}{\dot{m}_{noz} g} \quad (3.49)$$

$$I_{vac} = \frac{F_{vac}}{\dot{m}_{noz} g} \quad (3.50)$$

### 3.4.2 Zero-Dimensional Combustion Chamber Gas Model

The full transient modelling of the hybrid combustion mechanism involves complex coupling of dynamic subsystem models such as the filling/emptying gas dynamics of the combustion chamber, the vaporisation lags of the oxidiser, the solid-fuel thermal lags, and the progression of the turbulent boundary layer during the start-up phase. The combustion chamber is therefore divided into a series of control volumes where the principles of conservation of mass and energy are applied at each node. These control volumes are linked through the conservation of momentum equation to produce a continual gas dynamics solution.

In this study, only the filling/emptying gas dynamics of the combustion chamber are modelled. In particular, a zero-dimensional model was employed to capture the transient behaviour of the fluid flow. The model is based on a single control volume, CV2, where no variation in chamber pressure is assumed to occur through the combustion chamber. The conservation of mass and energy are applied to CV2 to obtain the change in chamber pressure, oxidiser-to-fuel ratio, and combustion gas properties (Fig. 3.6). The following assumptions are implemented to simplify the mathematical model:

1. The combustion gas product behaves as a perfect gas.
2. The propellant mass stored in CV2 is non-uniform due to the change in chamber volume and gaseous mass flow out of the nozzle.
3. Uniform regression rate is assumed across the fuel grain.
4. There is no heat transfer through the chamber wall.
5. The spatial change in thermodynamic gas properties is not modelled.

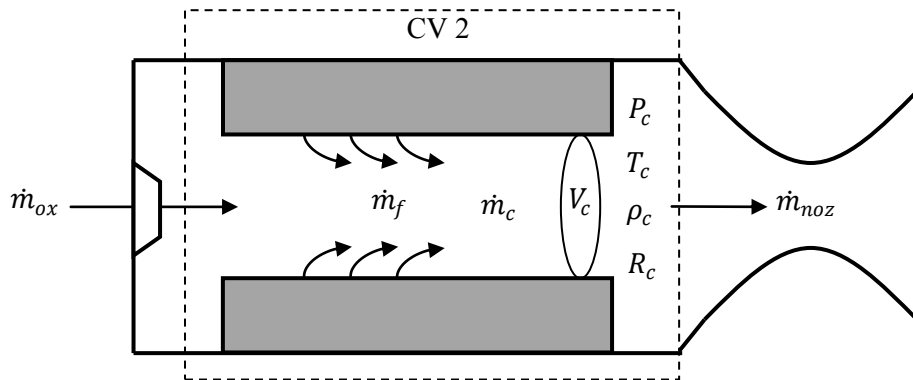


Figure 3.6 Combustion chamber model (Geneviève et al., 2011).

Considering CV2, by differentiating the conventional enthalpy expression of a homogeneous system, the change in combustion chamber enthalpy is defined as:

$$\frac{dH_c}{dt} = \frac{dU_c}{dt} + V_c \frac{dP_c}{dt} + P_c \frac{dV_c}{dt} \quad (3.51)$$

where  $H_c$  is the combustion chamber enthalpy,  $U_c$  is the combustion chamber internal energy, and  $V_c$  is the chamber volume which equals the summation of the port volume  $V_p$ , pre-combustion chamber volume  $V_{pre}$ , and post-combustion chamber volume  $V_{post}$ . Applying the first principle of thermodynamic states for an open system:

$$\frac{dU_c}{dt} = \frac{dQ_c}{dt} + \frac{dW_c}{dt} + h \frac{dm_c}{dt} \quad (3.52)$$

where  $\dot{Q}_c = 0$ : neglecting heat exchange through the environment,  $\dot{W}_c = -P_c \frac{dV_c}{dt}$ : work done by pressure forces,  $h = c_p T$  is the specific enthalpy, and  $\dot{m}_c$  is the gaseous mass storage in the combustion chamber. Using the conservation of mass to determine the change of gaseous mass in CV2, the mass stored in the chamber is defined as:

$$\frac{dm_c}{dt} = \dot{m}_{ox} + \dot{m}_f - \dot{m}_{noz} \quad (3.53)$$

Simplifying Equation 3.52:

$$\frac{dU_c}{dt} = -P_c \frac{dV_c}{dt} + (\dot{m}_{ox} + \dot{m}_f)(c_p T)_c - \dot{m}_{noz}(c_p T)_t \quad (3.54)$$

where  $(c_p T)_c$  and  $(c_p T)_t$  are the specific enthalpies of the combustion chamber and at nozzle throat plane, respectively. Using the ideal gas law, and differentiating with respect to time, the change in combustion chamber enthalpy  $\frac{dH_c}{dt}$  is given as:

$$H_c = \frac{k_c}{k_c - 1} P_c V_c \quad (3.55)$$

$$\frac{dH_c}{dt} = \frac{1}{k_c - 1} \left[ k_c \left( P_c \frac{dV_c}{dt} + V_c \frac{dP_c}{dt} \right) + P_c V_c \frac{dk_c}{dt} \right] - \left[ \frac{k_c P_c V_c}{(k_c - 1)^2} \right] \frac{dk_c}{dt} \quad (3.56)$$

Substituting Equations 3.54 and 3.56 into 3.51, the time derivative of the chamber pressure is determined as:

$$\frac{dP_c}{dt} = \frac{k_c - 1}{V_c} \left[ (\dot{m}_{ox} + \dot{m}_f)(c_p T)_c - \dot{m}_{noz} (c_p T)_t \right] - \left[ \frac{k_c P_c}{V_c} \right] \frac{dV_c}{dt} + \left[ \frac{P_c}{V_c - 1} \right] \frac{dk_c}{dt} \quad (3.57)$$

Assuming that  $(c_p T)_t \approx (c_p T)_c$ , Equation 3.57 can be further simplified:

$$\frac{dP_c}{dt} = \frac{k_c - 1}{V_c} \left[ (\dot{m}_{ox} + \dot{m}_f - \dot{m}_{noz})(c_p T)_c \right] - \left[ \frac{k_c P_c}{V_c} \right] \frac{dV_c}{dt} + \left[ \frac{P_c}{V_c - 1} \right] \frac{dk_c}{dt} \quad (3.58)$$

where a one-sided differencing technique is used to solve for the change in specific heat ratio of the combustion chamber:  $\frac{dk_c}{dt} = \frac{k_c(i) - k_c(i-1)}{\Delta t}$ . The instantaneous change in chamber volume is calculated by multiplying the fuel burnt area with the regression rate:

$$\frac{dV_c}{dt} = A_b \dot{r} \quad (3.59)$$

For a cylindrical port,  $A_b = 2\pi R_p L_g$ :

$$\frac{dV_c}{dt} = 2\pi R_p L_g \dot{r} \quad (3.60)$$

The increase in port radius is described as:

$$\frac{dR_p}{dt} = \dot{r} \quad (3.61)$$

The combustion characteristic of the rocket motor depends on the mixture composition of the oxidiser and fuel propellants. The oxidiser-to-fuel ratio of a chemical reaction in the combustion chamber is defined as the storage of oxidiser mass  $M_{oc}$  divided by the storage of fuel mass  $M_{fc}$ :

$$OF = \frac{M_{oc} + \frac{dM_{oc}}{dt} \Delta t}{M_{fc} + \frac{dM_{fc}}{dt} \Delta t} \quad (3.62)$$

The changes in oxidiser and fuel mass storages are determined by the difference in the fluid flow into and out of the system, CV2:

$$\frac{dM_{oc}}{dt} = \dot{m}_{ox,in} - \dot{m}_{ox,out} = \dot{m}_{ox,in} - \frac{\dot{m}_{noz}}{1 + \left(\frac{1}{OF}\right)} \quad (3.63)$$

$$\frac{dM_{fc}}{dt} = \dot{m}_{f,in} - \dot{m}_{f,out} = \dot{m}_{f,in} - \frac{\dot{m}_{noz}}{1 + OF} \quad (3.64)$$

Equations 3.58, 3.61, 3.63 and 3.64 are integrated for their respective state variables of chamber pressure, port radius, oxidiser mass storage, and fuel mass storage. HRPC employs a fourth order Runge Kutta time marching scheme to solve for the state vectors. The solution provides the transient behaviour of the hybrid combustion process, in particular the response of the fuel regression rate and chamber pressure with respect to any change in oxidiser mass flow rate, for example, hybrid rocket motors employing self-pressurising blowdown delivery systems and oxidiser feed valve throttling.

The term  $(\dot{m}_{ox} + \dot{m}_f - \dot{m}_{noz})$  in the chamber pressure derivative equation determines the filling or emptying of the combustion chamber. If the chamber pressure derivative is negative, the flow rate out of the system surpasses the flow rate into the system and the combustion mechanism experiences a drop in pressure. This occurs at the shut down phase or by closing the oxidiser feed valve throttling if possible. If the chamber pressure derivative is positive, the inflow of oxidiser plus gaseous fuel is greater than the outflow of the combusted gaseous product through the nozzle, and the combustion mechanism experiences a boost in pressure. This particularly occurs during the start-up phase of the motor or by throttling up the oxidiser feed valve during the flight. Steady state is reached when the chamber pressure derivative is approximately zero:  $\frac{dP_c}{dt} \approx 0$ , at which condition the inflow and outflow are balanced. The designed chamber pressure and thrust generated for the propulsion system are attained at the steady state condition. The combustion gas properties such as the flame temperature  $T_c$ , specific heat ratio  $k_c$ , and specific heat capacity at constant pressure, are obtained from NASA's Chemical Equilibrium with Applications (CEA) programme (Gordon and McBride, 1994), for the chamber pressure and oxidiser-to-fuel ratio at each time step.

### 3.4.3 One-Dimensional Nozzle Gas Flow Model

Control volume 3 models the fluid flow effects through the nozzle with idealised assumptions. The real flow is reduced to a one-dimensional flow theory, which provides the adequate solution of the rocket fundamental equations. The combustion chamber gas properties obtained from the zero-dimensional model provide the nozzle inlet boundary conditions, as illustrated in Fig. 3.7. The idealised nozzle gas flow assumptions are described below.

1. The gaseous mixture is homogeneous.
2. The fluid obeys the perfect gas law.
3. No heat loss occurs across the nozzle walls, therefore assuming adiabatic flow expansion.
4. All exhaust gases leaving the rocket have an axially directed velocity (one-dimensional flow).
5. The thermodynamic gas properties are all uniform across any section normal to the nozzle axis.
6. Stoichiometric combustion is reached in the chamber and the gas composition does not change in the nozzle (constant specific heat ratio and molecular weight - frozen flow).
7. There is no pressure drop across the chamber, ( $P_{inj} = P_c$ ).
8. The chamber pressure and temperature are equal to the stagnation pressure and temperature, respectively.
9. The inlet nozzle gas velocity is assumed to be zero.
10. The boundary layer effects caused by fluid viscosity are ignored.
11. Shock waves in the nozzle diverging section are modelled as normal standing waves. Lambda shocks caused by boundary layer effects are ignored.

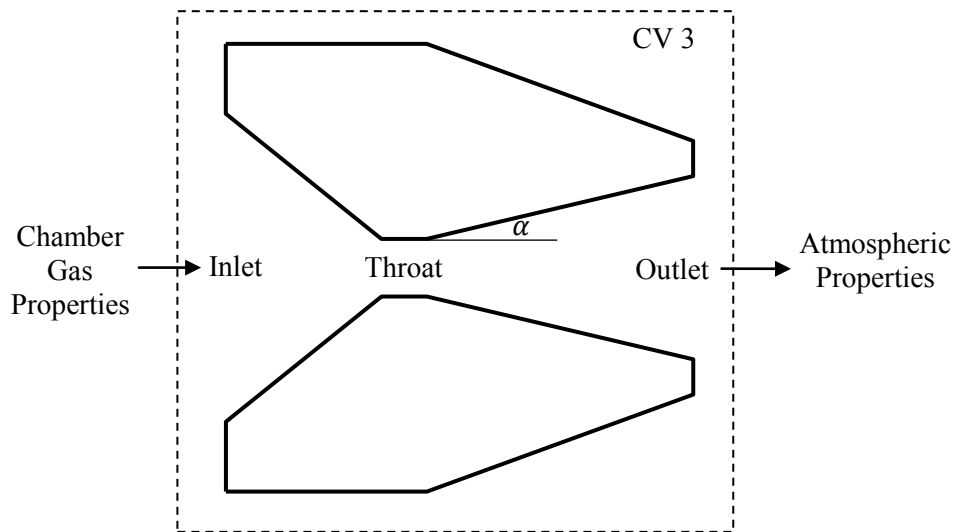


Figure 3.7 1D nozzle gas flow model (Geneviève et al., 2011).

The nozzle operating pressure ratio and the ratio of the atmospheric pressure to the chamber pressure determine the gas flow properties and conditions. Particularly, three critical pressure ratios subdivide all flow conditions that rocket nozzles can experience during hot-fire and flight tests. Figure 3.8 illustrates the change in fluid pressure in a converging-diverging nozzle, and the three critical pressure ratios. For pressure ratios above the first critical (line *abg*), the nozzle acts as a venturi where the flow is unchoked and entirely subsonic. Pressure ratios coinciding with the first critical line *abg* creates choked flow conditions at the throat (Mach number of 1) but the flow is still subsonic throughout the converging nozzle.

As the chamber pressure increases, for example during the start-up phase of the motor, the pressure ratio decreases below the first critical point. From this point, all flow conditions below the first critical are choked.

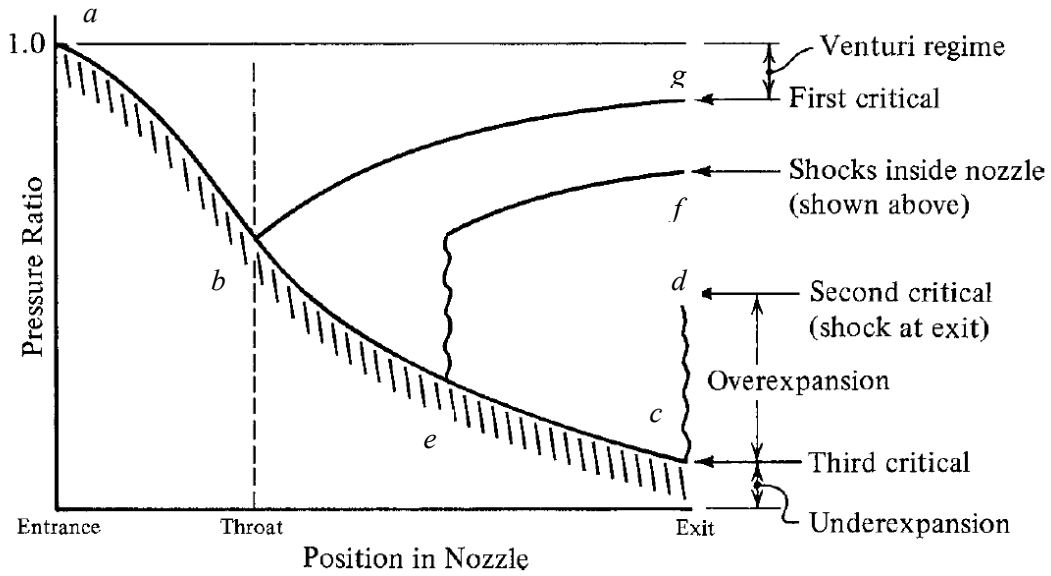


Figure 3.8 Nozzle operating modes (Zucker and Biblarz, 2002).

If the pressure ratio is between the first and second critical points, a normal shock wave is incurred downstream of the throat. The flow is supersonic from the throat to the normal shock wave and thereafter subsonic. The nozzle acts as a diffuser with the exit pressure equivalent to the atmospheric pressure. The location of the shock wave depends on the pressure ratio. As the chamber pressure is further increased, or during flight missions where the atmospheric pressure drops, the shock moves toward the nozzle exit plane. The second critical point, line *abcd*, is defined as the pressure ratio where a shock wave is located at the nozzle exit plane. Below line *abcd*, flow regimes are supersonic.

The optimum nozzle operating condition is represented by the third critical point, line *abc*. At this pressure ratio, the flow is fully isentropic and the exit pressure is equivalent to the atmospheric pressure. From Equation 3.46, optimum rocket thrust occurs when the exit pressure is equal to the atmospheric pressure at the design specifications of the nozzle. Flow regimes between the second and third critical and below the third critical points are categorised as over-expanded and under-expanded flows, respectively. Over-expansion flow (exit pressure lower than atmospheric pressure) creates compression waves outside the nozzle. Under-expansion flow (exit pressure greater than atmospheric pressure) creates expansion waves outside the nozzle.

In general, hybrid rocket motors can experience a wide change in operating pressure ratios due to the start-up and shut-down transient phases and decrease in atmospheric and oxidiser feed pressures. In addition, throttling the feed value causes the motor to operate at off design conditions. These jumps in pressure ratio affect motor performance as the nozzle exit gas parameters are dependent on the flow regime. Modelling each regime is therefore crucial to predict the unsteady performance behaviour of a rocket motor. For a specified nozzle expansion ratio and inlet boundary conditions, the critical pressure ratios must be determined to classify the working flow regime. The equations below can be obtained from Zucker and Biblarz (2002) with the appropriate explanations.

The first and third critical points are obtained from the relation of the Mach number and the pressure at the nozzle exit plane. As previously mentioned, the flow throughout the nozzle is assumed to be isentropic, and choked. Using the conventional expression relating to the nozzle expansion ratio and Mach numbers at the throat and exit planes:

$$\frac{A_e}{A_t} = \frac{M_t}{M_e} \left[ \frac{1 + ([k_c - 1]/2)M_e^2}{1 + ([k_c - 1]/2)M_t^2} \right]^{\frac{k_c+1}{2(k_c-1)}} e^{\Delta s/R} \quad (3.65)$$

where  $M_t$  is the Mach number at nozzle throat,  $M_e$  is the Mach number at nozzle exit,  $A_e$  is the nozzle exit area, and  $\Delta s$  is the entropy change. Simplifying Equation 3.65 for isentropic flow,  $\Delta s = 0$ , and choked condition,  $M_t = 1$ :

$$\frac{A_e}{A_t} = \frac{1}{M_e} \left[ \frac{1 + ([k_c - 1]/2)M_e^2}{1 + ([k_c - 1]/2)} \right]^{\frac{k_c+1}{2(k_c-1)}} \quad (3.66)$$

The quadratic expression produces two values of exit Mach numbers,  $M_e > 1$  and  $M_e < 1$ , for a given nozzle expansion ratio. The subsonic condition represents the first critical point whereas the supersonic condition represents the third critical point. For isentropic flow, the stagnation pressures are equivalent throughout the nozzle,  $P_{o,c} = P_{t,e}$ . That is, stagnation pressure at the nozzle inlet is equal to stagnation pressure at the nozzle outlet. Therefore, the exit pressure  $P_e$  is related to the exit Mach number by:

$$P_e = \frac{P_{o,c}}{\left[1 + \left(\frac{k_c - 1}{2}\right) M_e^2\right]^{\frac{k_c}{k_c - 1}}} \quad (3.67)$$

Equation 3.68 is computed for both Mach numbers. Hence the first and third critical pressure ratios, setting the exit pressure as the atmospheric pressure, are defined as:

$$P_{1st} = \frac{P_e}{P_{o,c}} = \frac{P_a}{P_{o,c}} \quad (3.68)$$

$$P_{3rd} = \frac{P_e}{P_{o,c}} = \frac{P_a}{P_{o,c}} \quad (3.69)$$

where  $P_{1st}$  and  $P_{3rd}$  are the first and third critical pressure ratios, respectively. For the second critical point, the flow is isentropic up to the normal shock located at the nozzle exit plane. The Mach number after the shock wave at the exit plane is determined by:

$$M_2 = \left[ \frac{M_1^2 + (2/[k_c - 1])}{([2k_c]/[k_c - 1])M_1^2 - 1} \right]^{1/2} \quad (3.70)$$

where  $M_2$  is the Mach number after the shock, and  $M_1$  represents the Mach number before the shock which is equal to the exit Mach number of the third critical point. The pressure ratio  $P_2/P_1$  through the shock is calculated as:

$$\frac{P_2}{P_1} = \frac{1 + (k_c M_1^2)}{1 + (k_c M_2^2)} \quad (3.71)$$

Therefore, the second critical point is computed as follows:

$$P_{2nd} = \frac{P_a}{P_{o,c}} = \frac{P_2}{P_1} \frac{P_1}{P_{o,1}} \frac{P_{o,1}}{P_{o,c}} \quad (3.72)$$

$$P_{2nd} = \frac{P_a}{P_{o,c}} = \frac{P_2}{P_1} P_{3rd} \quad (3.73)$$

Knowing the critical pressure ratios of a nozzle design, the flow characteristics can be determined by comparing the operating pressure ratio to the critical points. The nozzle gas dynamic properties at the inlet, throat, and exit plane provide the solution to the fundamental rocket equations. The gas properties depend on the operating region of the flow. In the following sections, all flow characteristics (subsonic, normal shock wave, and supersonic) through a nozzle will be described, and a methodological solution of each regime is given, in particular, to determine the motor thrust.

### 3.4.3.1 Subsonic Flow Modelling

Nozzle subsonic gas flow occurs when the operating pressure ratio is greater or equal to the first critical pressure ratio. The following conditions apply for both regions:

1. The flow is subsonic in nozzle converging-diverging section.
2. The nozzle is operating off design conditions.
3. For operating pressure ratio greater than first critical point, the nozzle is unchoked ( $M_t < 1$ ). Nozzle acts as a venturi.
4. For operating pressure ratio equal to first critical point, the nozzle is unchoked ( $M_t = 1$ ). Sonic flow occurs at the throat.
5. The nozzle gas exit pressure is equal to atmospheric pressure ( $P_e = P_a$ ).
6. The flow is isentropic.

Assuming all the nozzle inlet boundary conditions and atmospheric pressure are known, the exit Mach number  $M_e$  is computed from:

$$M_e = \left[ \frac{\left( P_{o,e}/P_e \right)^{(k_c-1)/k_c} - 1}{([k_c - 1]/2)} \right]^{1/2} \quad (3.74)$$

where the stagnation exit pressure is equal to the stagnation chamber pressure,  $P_{o,e} = P_{o,c}$ , due to isentropic flow. In addition, the static and stagnation chamber pressures are equivalent:  $P_{o,c} = P_c$ , as the nozzle gas inlet velocity is assumed to be negligible:  $v_{in} = 0$ . The exit temperature  $T_e$  is given by:

$$T_e = \frac{T_{o,e}}{[1 + ([k_c - 1]/2)M_e^2]} \quad (3.75)$$

where  $T_{o,e} = T_{o,c} = T_c$ , the stagnation temperatures at nozzle exit and chamber, and the static chamber temperature are equivalent due to perfect gas assumption and negligible nozzle gas inlet velocity. The nozzle gas exit velocity is calculated by multiplying the Mach number by the velocity of sound:

$$v_e = M_e a_e = M_e \sqrt{k_e R_e T_e} \quad (3.76)$$

where  $k_e$  is the specific heat ratio at exit,  $k_c$  is the chamber specific heat ratio,  $R_e$  is the gas constant at exit, and  $R_c$  is the chamber gas constant. Assuming the flow composition remains unchanged:  $k_e = k_c$ , and  $R_e = R_c$ . The throat Mach number is 1 for pressure ratio equivalent to the first critical point. However, an iterative process is used to compute the throat Mach number for pressure ratios greater than the first critical point. With the known parameters of nozzle expansion ratio  $\frac{A_e}{A_t}$  and the exit Mach number  $M_e$ , the throat Mach number is computed from:

$$\frac{A_e}{A_t} = \frac{M_t}{M_e} \left[ \frac{1 + ([k_c - 1]/2)M_e^2}{1 + ([k_c - 1]/2)M_t^2} \right]^{\frac{k_c+1}{2(k_c-1)}} \quad (3.77)$$

The conventional choked flow Equation 3.44 is used to calculate the mass flow rate through the nozzle for the pressure ratio equivalent to the first critical point whereas the mass flow rate for the other condition, ( $M_t < 1$ ), is given by Equation 3.78.

$$\dot{m}_{noz} = \frac{P_c A_t}{\eta_{eff} c^*} \quad (3.44)$$

$$\dot{m}_{noz} = \frac{\rho_e A_e v_e}{\eta_{eff}} \quad (3.78)$$

where  $\rho_e = (P_e/R_e T_e)$  from the ideal gas assumption. The thrust can be determined by using Equation 3.45, or additionally by:

$$F = \lambda \eta_{eff} \dot{m}_{noz} v_e + (P_e - P_a) A_e \quad (3.79)$$

### 3.4.3.2 Supersonic Flow Modelling

Supersonic flow throughout the nozzle occurs when the operating pressure ratio is lower than the second critical pressure ratio. The following conditions apply for the region:

1. The flow is subsonic in nozzle converging section.
2. The flow is supersonic in nozzle diverging section.
3. Nozzle is choked ( $M_t = 1$ ).
4. For operating pressure ratios between the second and third critical points, the flow is over-expanded ( $P_e < P_a$ ).
5. For operating pressure ratio equal to the third critical point, the flow is perfectly expanded ( $P_e = P_a$ ).
6. For operating pressure ratio greater than third critical point, the flow is under-expanded ( $P_e > P_a$ ).
7. The flow is entirely isentropic.

For supersonic flow, ( $M_t = 1$ ), the exit Mach number  $M_e$  is computed through an iterative process using the already mentioned Equation 3.66:

$$\frac{A_e}{A_t} = \frac{1}{M_e} \left[ \frac{1 + ([k_c - 1]/2) M_e^2}{1 + ([k_c - 1]/2)} \right]^{\frac{k_c + 1}{2(k_c - 1)}} \quad (3.66)$$

The nozzle exit pressure  $P_e$  is determined as follows, where  $P_{o,e} = P_{o,c} = P_c$ :

$$P_e = \frac{P_{o,e}}{[1 + ([k_c - 1]/2) M_e^2]^{\frac{k_c}{(k_c - 1)}}} \quad (3.80)$$

Following the same procedure as Section 3.4.3.1, the nozzle exit temperature and velocity can be calculated using Equations 3.75 and 3.76. The choked mass flow rate is determined by Equation 3.44.

These parameters are used as inputs at each time step to simulate the thrust curve, Equation 3.79. If the exit pressure is greater than atmospheric pressure, for higher chamber pressure, the pressure-thrust term adds onto the overall thrust. Therefore, under-expanded flow is more efficient than over-expanded flow.

$$F = \lambda \eta_{eff} \dot{m}_{noz} v_e + (P_e - P_a) A_e \quad (3.79)$$

### 3.4.3.3 Normal Shock Wave Flow Modelling

A normal shock wave occurs when the operating pressure ratio is lower than the first critical pressure point but greater than the second critical point. The following conditions apply for the region:

1. The flow is subsonic in nozzle converging section.
2. The flow is supersonic in nozzle diverging section up to the normal shock wave. Thereafter, flow is subsonic.
3. The nozzle is operating at off design conditions.
4. The nozzle is choked ( $M_t = 1$ ).
5. The nozzle gas exit pressure is equal to atmospheric pressure after shock wave ( $P_e = P_a$ ).
6. The flow is isentropic upstream and downstream of the shock wave.
7. All losses occur across the shock.
8. The location and strength of the shock wave are determined by the operating pressure ratio.

By multiplying Equations 3.66 and 3.80, the subsonic exit Mach number  $M_e$  is determined through an iterative process:

$$\frac{A_e P_e}{A_t P_c} = \frac{1}{M_e} \left[ \frac{1 + ([k_c - 1]/2) M_e^2}{1 + ([k_c - 1]/2)} \right]^{\frac{k_c + 1}{2(k_c - 1)}} \times \frac{1}{[1 + ([k_c - 1]/2) M_e^2]^{k_c/(k_c - 1)}} \quad (3.81)$$

Defining the stagnation pressures before and after the normal shock wave, since all the loss is assumed to occur across the shock:

$$P_{o,1} = P_{o,c} \quad (3.82)$$

$$P_{o,2} = P_{o,e} \quad (3.83)$$

where  $P_{o,1}$  is the stagnation pressure before the shock wave, and  $P_{o,2}$  represents the stagnation pressure after the shock wave. The pressure ratio across the shock wave is given by:

$$\frac{P_{o,2}}{P_{o,1}} = \frac{P_{o,e}}{P_{o,c}} \quad (3.84)$$

The stagnation exit pressure is determined using equation 3.80. The following equation is employed to calculate the Mach number just before the shock  $M_1$ :

$$\frac{P_{o,2}}{P_{o,1}} = \left[ \frac{([k_c + 1]/2)M_1^2}{1 + ([k_c - 1]/2)M_1^2} \right]^{k_c/(k_c-1)} \times \left[ \left( \frac{2k_c}{k_c + 1} \right) M_1^2 - \left( \frac{k_c - 1}{k_c + 1} \right) \right]^{1/(1-k_c)} \quad (3.85)$$

The shock wave is located at an area expansion ratio of:

$$\frac{A_1}{A_t} = \frac{1}{M_1} \left[ \frac{1 + ([k_c - 1]/2)M_1^2}{1 + ([k_c - 1]/2)} \right]^{\frac{k_c+1}{2(k_c-1)}} \quad (3.86)$$

Following a step-wise approach, the gas temperatures and pressures before and after the shock are calculated:

$$T_1 = \frac{T_c}{[1 + ([k_c - 1]/2)M_1^2]} \quad (3.87)$$

$$P_1 = \frac{P_c}{[1 + ([k_c - 1]/2)M_1^2]^{k_c/(k_c-1)}} \quad (3.88)$$

$$T_2 = T_1 \left[ \frac{1 + ([k_c - 1]/2)M_1^2}{1 + ([k_c - 1]/2)M_2^2} \right] \quad (3.89)$$

$$P_2 = P_1 \left[ \frac{1 + k_c M_1^2}{1 + k_c M_2^2} \right] \quad (3.90)$$

Using the temperature and pressure after the shock wave, the stagnation conditions after the shock are determined, followed by the exit gas temperature. The flow is isentropic after the shock, that is,  $P_{o,2} = P_{o,e}$  and  $T_{o,2} = T_{o,e}$ .

$$P_{o,2} = P_2 [1 + ([k_c - 1]/2)M_2^2]^{k_c/(k_c-1)} \quad (3.91)$$

$$T_{o,2} = T_2 [1 + ([k_c - 1]/2)M_2^2] \quad (3.92)$$

$$T_e = \frac{T_{o,2}}{[1 + ([k_c - 1]/2)M_e^2]} \quad (3.93)$$

At this point, the exit gas velocity can be computed from Equation 3.68 and the choked mass flow rate from Equation 3.44. Knowing all the necessary gas properties at the nozzle exit, the thrust is determined using Equation 3.79.

## CHAPTER 4

### Hybrid Rocket Performance Code

#### 4.1 Scope and Specifications

A hybrid rocket performance model is essential to the overall design and analysis of a motor for a specific flight mission. The utility of such model is to accurately size the propulsion system for a targeted thrust as well as to predict its theoretical performance. In the design process of the Phoenix-1A hybrid rocket, a model was developed to analyse the combustion process of the paraffin wax and nitrous oxide propellant combination which can be extended to other oxidiser/fuel combinations. The computational tools integrate the derived equations of Chapter 3 into two distinct codes, namely a preliminary motor design code (HRPC Motor Design) and a predictive motor performance code (HRPC) which were both programmed in MATLAB.

The first code, referred to as HPRC Motor Design, determines among other parameters the optimum nozzle expansion ratio, nozzle critical pressure ratios, dimensions of the fuel grain and oxidiser mass flow rate for a specified thrust, the chamber and atmospheric pressures, and the oxidiser-to-fuel ratio. In addition, it plots the converging-diverging contour for a bell-shaped or conical-shaped nozzle which can be imported into CAD software. These critical outputs are used as inputs in the predictive motor performance code, HRPC, to compute the theoretical motor performance and to analyse the physical change of the solid-fuel grain. The two codes extract necessary thermodynamic properties from the NASA-CEA equilibrium chemistry code (Gordon and McBride, 1994) throughout the simulation.

#### 4.2 NASA-CEA

NASA-CEA is a computer programme that determines the thermodynamic and transport properties together with the chemical equilibrium compositions of a reaction mechanism. In addition, the main programme consists of internal sub-models for theoretical rocket performance, Chapman-Jouguet detonations, shock-tube parameters for incident and reflected shocks, and combustion properties. It contains a transport and thermodynamic database of over 2000 solid, liquid, and gaseous chemical species. The NASA-CEA equilibrium chemistry code was developed by Bonnie J. McBride and Sanford Gordon in FORTRAN, and is continually updated with new species.

The NASA-CEA combustion and theoretical rocket performance sub-models are extensively utilised in both HRPC applications. The theoretical rocket performance sub-model offers the capability of modelling either frozen or equilibrium flow composition through the rocket nozzle. For the case of frozen flow, the product composition is assumed to remain constant during flow expansion, whereas, for the case of equilibrium flow, the change in product composition during flow expansion is modelled. Moreover, the non-uniformity of gas product specific heat ratio through the nozzle is correctly modelled as NASA-CEA computes the change in specific heat capacity at constant pressure which is a function of temperature.

The inputs which both codes feed into NASA-CEA are oxidiser/fuel properties, combustion or rocket problem, equilibrium or frozen flow composition, oxidiser-to-fuel ratio, chamber pressure, and nozzle expansion ratio or inverse pressure ratio. The interaction between the two programmes is achieved by creating an input file with the problem fully stated, running NASA-CEA, and reading calculated data from the output plot file. Depending on the problem, lookup tables of the output parameters are created. Post-processing of the NASA-CEA output data is crucial before HRPC solves for the rocket motor performance. Firstly, the ideal gas exit velocity of NASA-CEA  $v_{e,CEA}$  must be corrected for the divergence nozzle exit angle as described in Equations 4.1, 4.2 and 4.5. Additionally, the user's input combustion efficiency in HRPC corrects NASA-CEA's characteristic velocity  $c_{CEA}^*$  in Equation 4.3.

$$\lambda = \frac{1}{2}(1 + \cos \alpha_c) \quad (4.1)$$

$$v_{e,HRPC} = \lambda v_{e,CEA} \quad (4.2)$$

$$c_{HRPC}^* = \eta_{eff} c_{CEA}^* \quad (4.3)$$

Since the NASA-CEA programme assumes that the nozzle gas flow is perfectly expanded (third critical point condition), the difference in exit and atmospheric pressure must be implemented by adding the pressure-thrust term. In particular, the pressure-thrust term is added to NASA-CEA's thrust coefficient  $C_{F,CEA}$ , specific impulse  $I_{sp,CEA}$ , and vacuum specific impulse  $I_{vac,HRPC}$  as illustrated in Equations 4.4 to 4.8. These NASA-CEA corrected parameters are used to accurately compute for the rocket motor performance in HRPC.

$$C_{F,CEA} = \sqrt{\left(\frac{2k_c^2}{k_c - 1}\right)\left(\frac{2}{k_c + 1}\right)^{\left(\frac{k_c + 1}{k_c - 1}\right)}\left(1 - \left[\frac{P_e}{P_c}\right]^{\left(\frac{k_c - 1}{k_c}\right)}\right)} \quad (4.4)$$

$$C_{F,HRPC} = \lambda C_{F,CEA} + \left( \frac{P_e - P_a}{P_c} \right) \left( \frac{A_e}{A_t} \right) \quad (4.5)$$

$$I_{sp,CEA} = \frac{v_{e,CEA}}{g} \quad (4.6)$$

$$I_{sp,HRPC} = \frac{\eta_{eff} \left[ \lambda v_{e,CEA} + \left( \frac{P_e - P_a}{P_c} \right) \varepsilon_r c_{CEA}^* \right]}{g} \quad (4.7)$$

$$I_{vac,HRPC} = \frac{\eta_{eff} \left[ \lambda v_{e,CEA} + \left( \frac{P_e}{P_c} \right) \varepsilon_r c_{CEA}^* \right]}{g} \quad (4.8)$$

### 4.3 HRPC Motor Design

The HRPC Motor Design application is a MATLAB code employed to predetermine the required inputs for the predictive performance HRPC model. It permits useful analysis and the development of a hybrid rocket motor configuration. The code is divided into three sub-models: 1) Fuel Grain and Nozzle Designs, 2) Motor Performance Analysis, and 3) Nozzle Contour Design as displayed in Fig. 4.1. For a typical run, the user selects the model type together with the propellant properties if required. The following sections detail pre- and post-processing of the individual model.

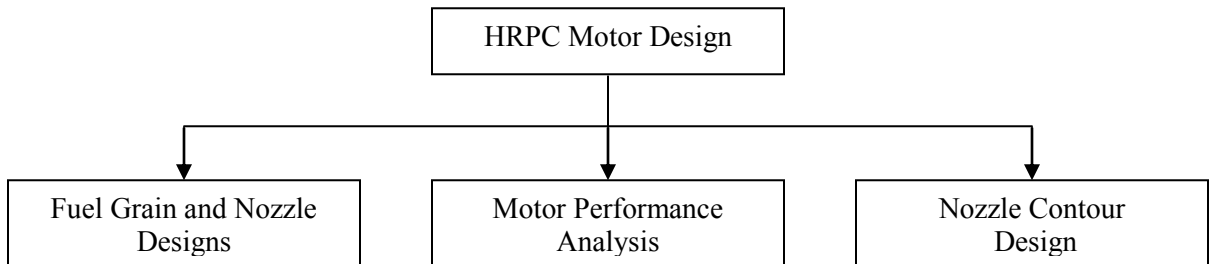


Figure 4.1 Flowchart of HRPC Motor Design.

#### 4.3.1 Fuel Grain and Nozzle Designs

The propulsion system requirements of a hybrid rocket depend on the flight mission. Its development is based on specified flight mission motor performance such as thrust. In this model, preliminary hybrid rocket motor designs can be achieved for the targeted thrust, chamber pressure, and oxidiser-to-fuel ratio.

In particular, this model determines the dimensions of the fuel grain and nozzle for the system requirements. The motor design can be optimised through a manual iterative process of the code. Generally, the targeted thrust and chamber pressure are known for a mission. The optimum oxidiser-to-fuel ratio of the selected propellant combination is used to maximise the efficiency of the motor. The compulsory inputs of the model to design a hybrid propulsion system are depicted in Table 4.1.

Table 4.1 Input and output parameters for fuel grain and nozzle designs model.

Inputs		Outputs	
Thrust	$F$	First Critical Pressure Ratio	$P_{1st}$
Oxidiser-to-Fuel Ratio	$OF$	Second Critical Pressure Ratio	$P_{2nd}$
Chamber Pressure	$P_c$	Third Critical Pressure Ratio	$P_{3rd}$
Atmospheric Pressure	$P_a$	Characteristic Velocity	$c^*$
Combustion Efficiency	$\eta_{eff}$	Thrust Coefficient	$C_F$
Fuel Density	$\rho_f$	Expansion Ratio	$\varepsilon_r$
Ballistic Coefficient	$a$	Nozzle Throat Area	$A_t$
Ballistic Coefficient	$n$	Nozzle Exit Area	$A_e$
Burn Time	$t_b$	Nozzle Throat Diameter	$D_t$
Additional Web Thickness	$w_a$	Nozzle Exit Diameter	$D_e$
Number of Ports	$N_p$	Total Oxidiser Mass Flow Rate	$\dot{m}_{ox,t}$
Initial Port Diameter	$D_{p,i}$	Oxidiser Mass Flow Rate per Port	$\dot{m}_{ox,p}$
		Total Fuel Mass Flow Rate	$\dot{m}_{f,t}$
		Fuel Mass Flow Rate per Port	$\dot{m}_{f,p}$
		Nozzle Mass Flow Rate	$\dot{m}_{noz}$
		Fuel Grain Length	$L_g$
		Fuel Grain Diameter	$D_g$
		Initial Fuel Grain Volume	$V_{f,i}$
		Final Fuel Grain Volume	$V_{f,f}$
		Initial Fuel Grain Mass	$M_{f,i}$
		Final Fuel Grain Mass	$M_{f,f}$
		Burnt Web Thickness	$w_b$
		Total Web Thickness	$w_t$
		Final Port Diameter	$D_{p,f}$

These inputs are partly fed to NASA-CEA to determine the thermodynamic data of the fluid flow for a given nozzle expansion ratio, which is determined by the entered pressure for both the chamber and atmospheric conditions. The atmospheric pressure is based on the altitude where the flow is fully expanded, that is, at the third critical nozzle pressure ratio. Figure 4.2 illustrates the logic flow of the model.

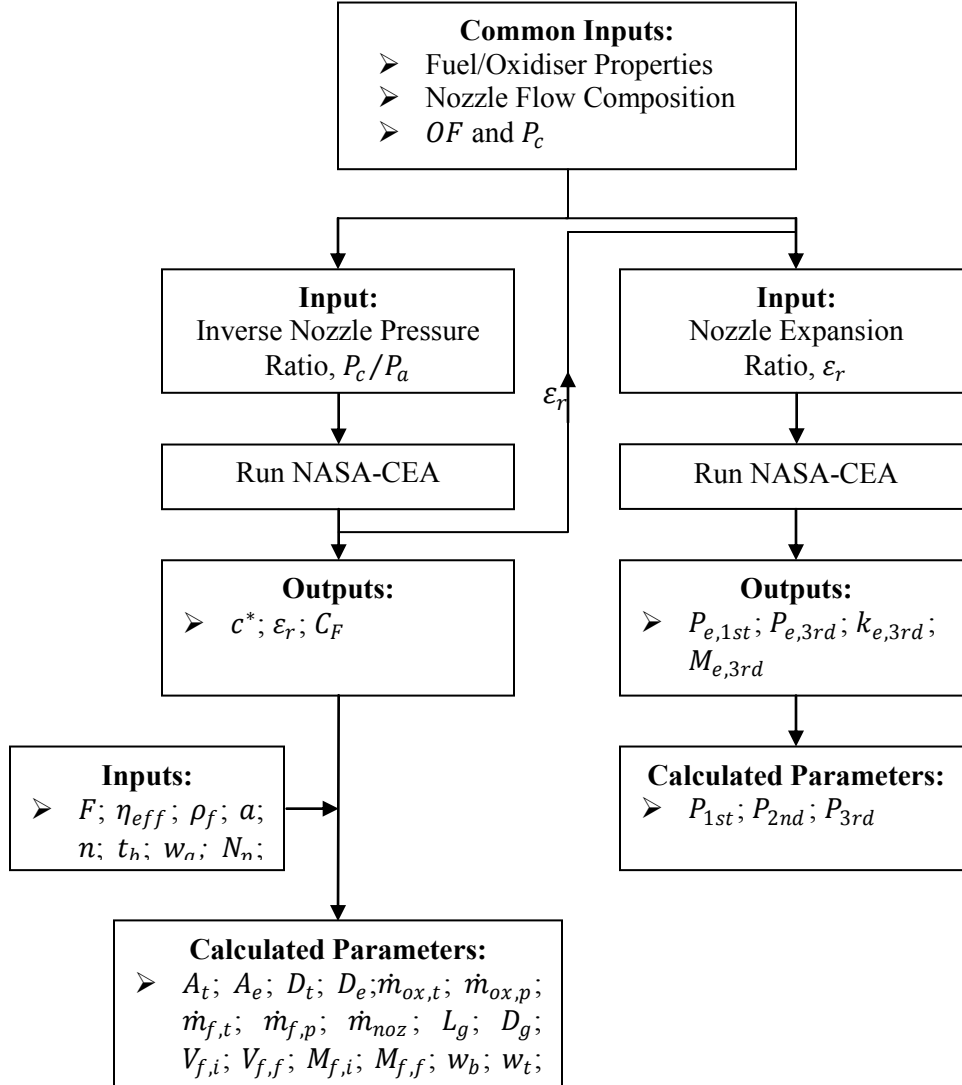


Figure 4.2 Flowchart of fuel grain and nozzle designs model.

The output characteristic velocity  $c^*$  and thrust coefficient  $C_F$  parameters are used to calculate the fuel grain and nozzle dimensions through a series of computations using the equations below as well as equations derived in Chapter 3. For the targeted thrust  $F$  and chamber pressure  $P_c$ , the nozzle throat area is given by Equation 4.9 using the optimum thrust coefficient  $C_F$  from NASA-CEA. Equation 4.10 calculates the total fuel mass flow rate  $\dot{m}_{f,t}$  due to the optimum oxidiser-to-fuel ratio and the total mass

flow rate  $\dot{m}_t$  flowing out of the nozzle. Assuming steady-state conditions, this quantity is determined from the choked flow Equation 3.44, that is,  $\dot{m}_t = \dot{m}_{noz}$ .

$$A_t = \frac{F}{C_F P_c} \quad (4.9)$$

$$\dot{m}_{f,t} = \frac{\dot{m}_t}{OF + 1} \quad (4.10)$$

The oxidiser-to-fuel ratio relates the total oxidiser and fuel mass flow rates by,  $OF = \dot{m}_{o,t}/\dot{m}_{f,t}$ . The length of the fuel grain is given as:

$$L_g = \frac{\dot{m}_{f,t}}{2\pi N_p R_p \rho_f \dot{r}} \quad (4.11)$$

where fuel regression rate is obtained from Equation 3.24. By definition, the grain length and diameter affect the motor thrust and burn time respectively. Using the input burn time variable, the total web thickness  $w_t$  of the grain can be determined by Equation 4.12, assuming constant oxidiser mass flow rate and regression rate. In this model, the total web thickness  $w_t$  is the summation of the allowable additional thickness  $w_a$  and the theoretical burnt thickness  $w_b$  associated with the chosen burn time.

$$w_t = w_a + w_b \quad (4.12)$$

The allowable additional thickness  $w_a$  is small, or can be defined as zero by the user, compared to the calculated theoretical burnt thickness  $w_b$ . This additional web thickness can be used for uncertainty in regression rate ballistic coefficients, particularly for high regression rate fuels. Moreover, it provides adequate end of burn sliver material that retains the structural geometry of the grain, therefore minimising catastrophic nozzle blockage. HRPC fuel grain geometries are shown in Appendix D. At present, the code is limited to cylindrical grain with a maximum number of 10 ports. The dimensional formulae for each grain are tabulated in Table D.1. The blue and red lines in Fig. D.1 respectively represent the initial and final port diameters. The fuel grain outer diameter is displayed as a black line. The optimum nozzle expansion ratio obtained from the initial NASA-CEA run is fed into a second run of the chemistry code to acquire the parameters needed to determine the nozzle's first, second, and third critical pressure ratios using the equations defined in Section 3.4.3.

### 4.3.2 Motor Performance Analysis

The motor performance analysis model provides the means to graphically visualise the propulsion system characteristics for a set of user defined inputs. It is particularly practical for comparing different propellant combinations and determining the optimum oxidiser-to-fuel mixture ratio. This assists the designer in selecting a suitable oxidiser/fuel combination for the system requirements. The inputs and outputs of the model are shown in Table 4.2 below. Note that the output constitutes various graphs with oxidiser-to-fuel ratios and chamber pressures being the independent variables.

Table 4.2 Input and output parameters for motor performance analysis model.

Inputs		Outputs	
Atmospheric Pressure	$P_a$	Nozzle Exit Pressure	$P_e$
Expansion Ratio	$\varepsilon_r$	Combustion Temperature	$T_c$
Combustion Efficiency	$\eta_{eff}$	Expansion Ratio	$\varepsilon_r$
Bell-shaped Nozzle Correction Factor	$\lambda_b$	Nozzle Exit Velocity	$v_e$
Conical Nozzle Div. Cone Half-Angle	$\alpha_c$	Characteristic Velocity	$c^*$
Range of Oxidiser-to-Fuel Ratio	$OF$	Thrust Coefficient	$C_F$
Range of Chamber Pressure	$P_c$	Vacuum Thrust Coefficient	$C_{F,vac}$
Nozzle Flow Composition		Specific Impulse	$I_{sp}$
		Vacuum Specific Impulse	$I_{vac}$

Generally, NASA-CEA theoretical rocket performance can be run by either specifying an inverse nozzle pressure ratio or nozzle expansion ratio with common inputs such as propellant properties, nozzle flow composition, oxidiser-to-fuel ratios, and chamber pressure. In the former, the atmospheric pressure is used as the input which computes the optimum nozzle expansion ratios for the range of oxidiser-to-fuel ratios and chamber pressure. That is, the nozzle exit and atmospheric pressures are identical. For the case where the nozzle expansion ratio is used as the input, the nozzle exit pressures are assumed to represent the atmospheric pressure. Both scenarios model the optimum thrust coefficients and specific impulses of the motor configuration being investigated. In this model, the entered combustion efficiency affects the NASA-CEA characteristic velocity, specific impulse, and vacuum specific impulse but not the combustion temperature value. The output parameters from NASA-CEA are corrected through the set of equations described in Section 3.2 to account for flow losses. Figure 4.3 illustrates the two types of NASA-CEA runs for the same common inputs. The code runs NASA-CEA for the specified range of

oxidiser-to-fuel ratios and chamber pressure, and creates a series of tables for the output parameters mentioned in Table 4.2.

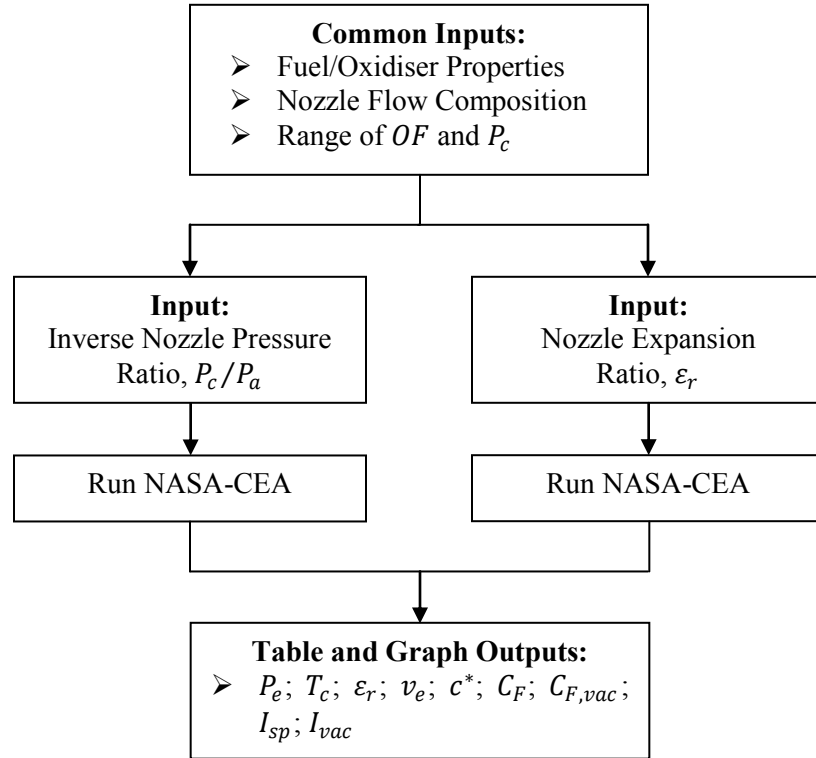
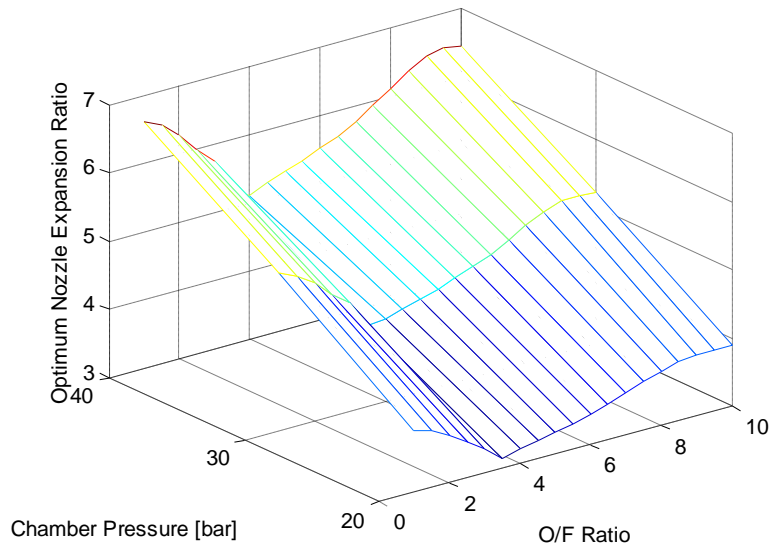
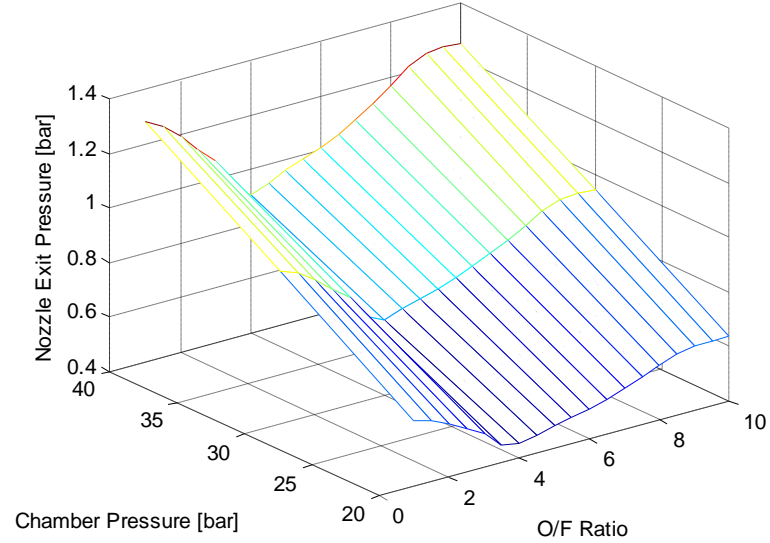


Figure 4.3 Flowchart of the motor performance analysis model.

To verify the post-processing of the extracted data from NASA-CEA, two typical runs of the model are shown in Appendix E.1. In the first run, a constant atmospheric pressure was used with the other common inputs as illustrated in Table E.1. As a means of cross-checking the models, one of the nozzle expansion ratios from the first model's output file was inputted in the second model. Both methods result in the same motor characteristics for an oxidiser-to-fuel ratio of 6 and chamber pressure of 40 bars, as depicted in Table E.2. Selected output graphs for the two runs are shown in Figures E.1. In addition, two output graphs from Appendix E.1 are reproduced in Fig. 4.4. Figure 4.4 (a) illustrates the variation of the optimum nozzle expansion ratio for the specified constant atmospheric pressure run whereas Fig. 4.4 (b) shows the variation of nozzle exit pressure for the specified constant expansion ratio.



(a)



(b)

Figure 4.4 Example of the output graphs of the code: (a) Constant atmospheric pressure, and (b) Constant expansion ratio.

### 4.3.3 Nozzle Contour Design

HRPC Motor Design application offers the capability to develop two nozzle configurations: bell- or conical-shaped nozzles. The code shapes the internal converging-diverging nozzle contour, and determines the critical parameters for a given design. These critical output parameters together with the

input design variables are saved in a spreadsheet file for each analysis. That is, the output file contains the coordinates required to form the nozzle's inner geometry. This nozzle analysis is independent of the NASA-CEA programme. The converging nozzle contour from the combustion chamber's aft end and the nozzle throat is considered to be identical for both configurations as it is not critical to motor performance. A bell-shaped nozzle differs from a conical-shaped one in the diverging section of the nozzle. It decreases the losses as the flow is gradually turned and trended to an ideal axial direction at the nozzle exit where the divergence angle is smaller compared to conical-shaped nozzles. Therefore, for a given nozzle contraction  $C_r$  and expansion  $\varepsilon_r$  ratios, the code produces the same nozzle converging length  $L_{ni}$  but can differ in nozzle diverging length  $L_{ne}$ . Figure 4.5 and Table 4.3 represent the critical variables considered in the analysis.

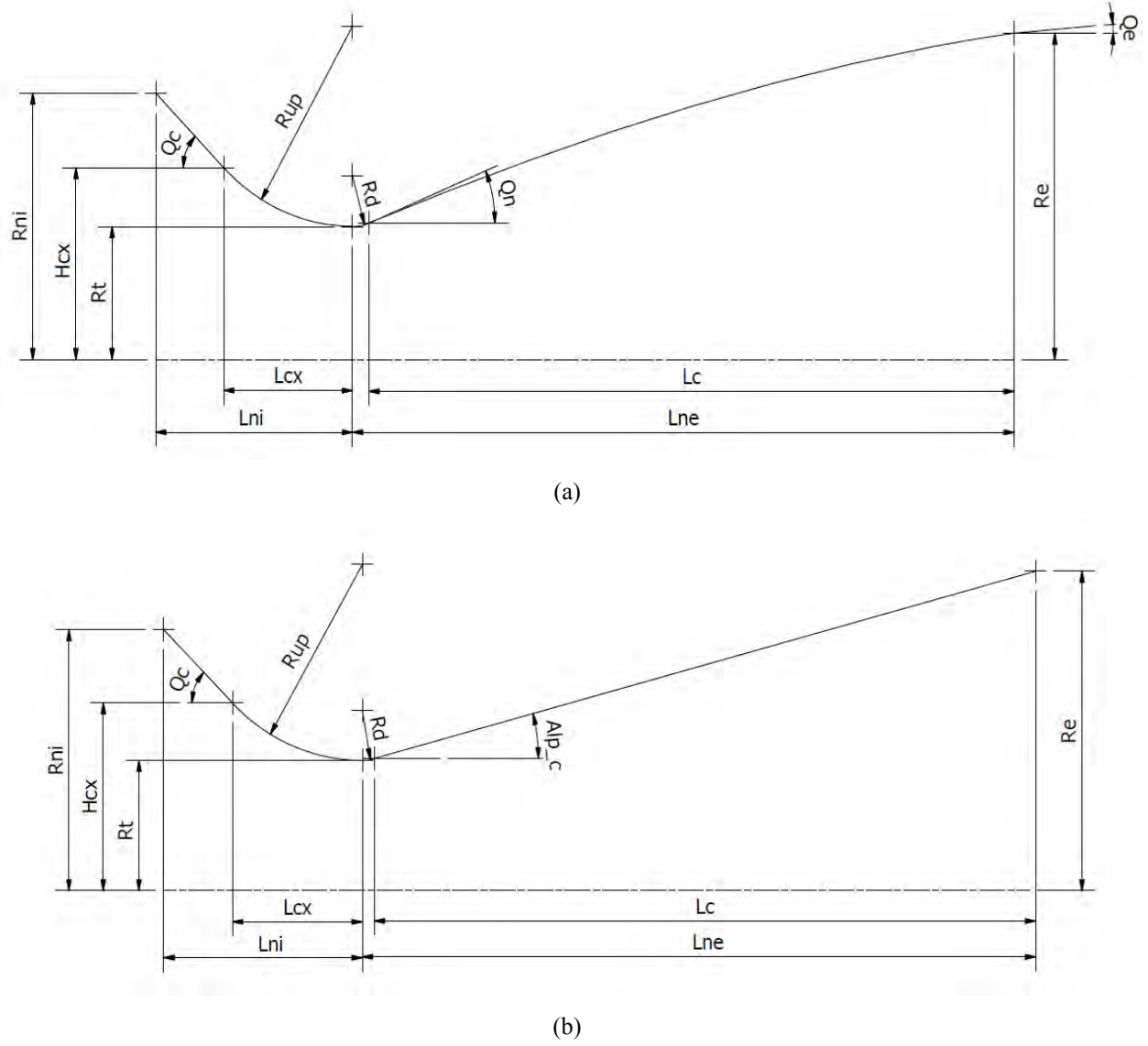


Figure 4.5 Nozzle configuration: (a) Bell-shaped, and (b) Conical-shaped.

Unlike the expansion ratio, the nozzle contraction ratio  $C_r$  is defined as the cross-sectional area of the combustion chamber divided by the nozzle throat cross-sectional area. In the absence of an aft end mixing chamber in hybrid rocket motors, the contraction ratio augments as the fuel-grain port diameter increases with burn time. Nozzle upstream arc radius ratio  $R_{up}/R_t$  and downstream arc radius ratio  $R_d/R_t$  are defined as upstream radius over throat radius and downstream radius over throat radius respectively. The nozzle upstream arc radius ratio is usually approximated as 1.5 and the nozzle downstream arc radius ratio as 0.382 (Humble et al., 1995). These two arcs determine the nozzle shape from the contraction angle  $\theta_c$  point to the diverging inflection point.

Table 4.3 Input and output parameters for nozzle contour design model.

Inputs		Outputs	
Nozzle Throat Diameter	$D_t$	Chamber Radius	$R_{ni}$
Expansion Ratio	$\varepsilon_r$	Nozzle Throat Radius	$R_t$
Contraction Ratio	$C_r$	Nozzle Exit Radius	$R_e$
Nozzle Upstream Arc Radius Ratio	$R_{up}/R_t$	Nozzle Upstream Arc Radius	$R_{up}$
Nozzle Downstream Arc Radius Ratio	$R_d/R_t$	Nozzle Downstream Arc Radius	$R_d$
Nozzle Contraction Angle	$\theta_c$	Nozzle Inlet to Throat Plane Length	$L_{ni}$
Bell-shaped Nozzle Parabola Inlet Angle	$\theta_n$	Cont. Angle Point to Throat Plane Length	$L_{cx}$
Bell-shaped Nozzle Parabola Exit Angle	$\theta_e$	Cont. Angle Point to Throat Plane Radius	$H_{cx}$
Bell-shaped Nozzle Fractional Length	$L_f$	Nozzle Throat to Exit Plane Total Length	$L_{ne}$
Conical Nozzle Div. Cone Half-Angle	$\alpha_c$	Bell-shaped Parabolic Length	$L_c$
		Conical-shaped Nozzle Cone Length	$L_c$
		Conical-shaped Nozzle Correction Factor	$\lambda_c$
		Nozzle X-Y Coordinates	
		Nozzle Graphical Geometry Output	

The contraction angle point defines the position where the chamber aft end cross-sectional area meets the beginning of the upstream arc radius. The contraction angle  $\theta_c$  has a range of  $1^\circ$  to  $90^\circ$ , and is a function of the nozzle contraction ratio  $C_r$ . As such, there is a maximum contraction angle value which corresponds to the given contraction ratio. If the entered contraction angle exceeds its limited value for the corresponding contraction ratio, HPRC Motor Design determines the maximum value and overrides the user contraction angle input. An error message informs the user about the change in contraction angle.

Conical-shaped nozzles are widely used in the rocket industry due to their ease of manufacture. The diverging section consists of a cone which can be represented by two coordinate points at a defined angle  $\alpha_c$ . This cone half-angle  $\alpha_c$  determines the nozzle correction factor through Equation 4.1. The nozzle length which forms the throat plane to the exit plane for a conical nozzle is defined as:

$$(L_{ne})_{conical} = \frac{R_t[\sqrt{\varepsilon_r} - 1] + R_d[(1/\cos \alpha_c) - 1]}{\tan \alpha_c} \quad (4.13)$$

A bell-shaped nozzle is more efficient than a conical-shaped one as flow losses are minimised. The degree to which the flow tends to the axial direction depends on the diverging parabola inlet  $Q_n$  and the exit angles  $Q_e$ . The length of a bell-shaped diverging section is defined as the fraction  $L_f$  of a conical nozzle for a given half-cone  $\alpha_c$ :

$$(L_{ne})_{bell} = L_f \left[ \frac{R_t[\sqrt{\varepsilon_r} - 1] + R_d[(1/\cos \alpha_c) - 1]}{\tan \alpha_c} \right] \quad (4.14)$$

Typically, an equivalent 15° half-angle is used for the design of a bell-shaped nozzle. The method of characteristic developed by Rao (1958) determines the exact geometry of the diverging section. However, a parabolic approximation can be employed to determine the geometry with reasonable accuracy. The latter method is used in the HRPC Motor Design to model the entire diverging bell-contour. Humble et al. (1995) and Sutton and Biblarz (2001) give the relationship between the nozzle expansion ratio  $\varepsilon_r$ , parabola inlet  $Q_n$  and exit angles  $Q_e$ , and fractional length  $L_f$ . These input parameters must be obtained from the textbooks mentioned above to correctly shape the diverging contour for a particular nozzle design.

Appendix E.2 shows an example of the spreadsheet files generated for the design of a nozzle, bell- and conical-shaped, with the same inputs being used. As can be noted, the converging coordinates for both nozzle shapes coincide. These points can be imported into CAD software to revolve a three-dimensional drawing of the nozzle's inner converging-diverging contour. In addition, the graphical MATLAB outputs for each run are depicted for a contraction angle of 90°. Note that the blue lines represent the nozzle contour whereas the red lines illustrate the combustion chamber.

## 4.4 HRPC

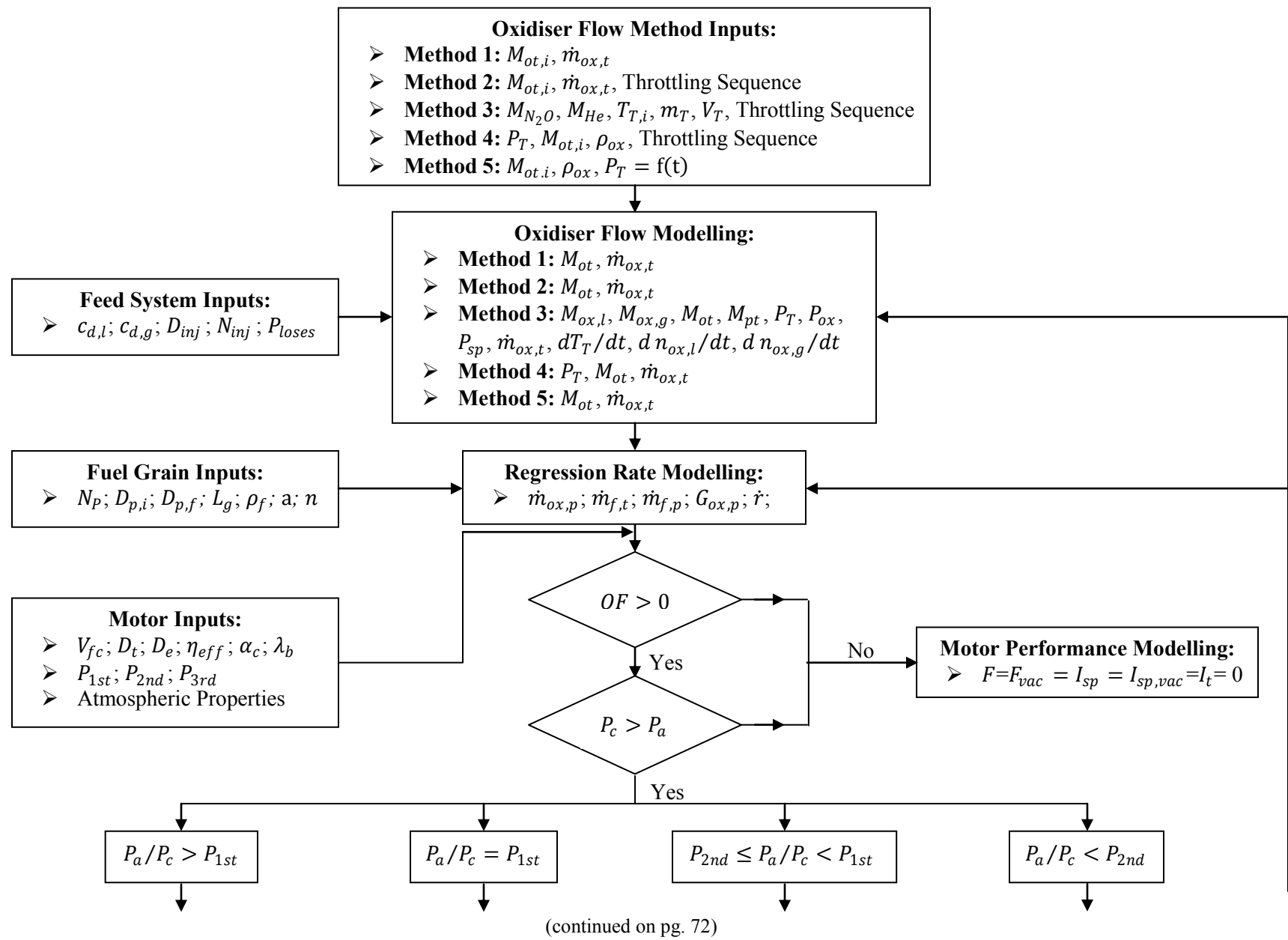
### 4.4.1 Data Processing and Numerical Solution

In the development of a hybrid rocket motor, a mathematical model of the physical and chemical processes is vital for motor performance prediction. Such a tool is used to optimise the motor characteristics and, in addition, facilitates the development procedure with regard to the time consumed in testing different motor dimensions. HRPC application is a numerical model that couples and solves the individual described sub-systems of a hybrid rocket motor to predict the performance variation with burn time. The pre-determined propulsion parameters from the output files of the HRPC Motor Design application are fed into HRPC as required inputs. The code computes the instantaneous motor performance for a given time step until it reaches the maximum burn time, provided that other comparative variables are below their critical values.

As the NASA-CEA programme is integrated into the core of HRPC, lookup tables of the important parameters are created for a specific propellant combination, nozzle expansion ratio, and nozzle flow composition. Supplementary inputs are the oxidiser-to-fuel ratio and chamber pressure ranges. These ranges must be well spanned over the expected operating conditions of the simulation. HRPC has the capability to define a fuel propellant of two compositions which is entered as a percentage. The fuels' percentages are passed to NASA-CEA together with their names and the grain inert temperature. If NASA-CEA's thermodynamic database does not contain the fuel being investigated, the user must define its molecule formula and enthalpy in HRPC which will pass on the data to NASA-CEA. The oxidiser properties, that is, the molecular formula and inert temperature must also be defined in HRPC. Additionally, NASA-CEA's 'only' and 'omit' subroutines are implemented in HRPC.

Subsequent to the creation of the lookup tables, the main code can be run for the same motor configurations. The flowchart of HRPC is depicted in Fig. 4.6. Referring to Fig. 4.6, a series of input parameters for the individual sub-systems is required. This includes the oxidiser flow method, fuel grain dimensions, and motor specifications. HRPC has the capability to model five types of oxidiser flow methods. The oxidiser flow methods, defined by the user, are:

1. Method 1 – a constant oxidiser mass flow rate is used throughout the burn.
2. Method 2 – constant oxidiser mass flow rate with throttling sequence is employed.
3. Method 3 – nitrous oxide self-pressurising delivery model.



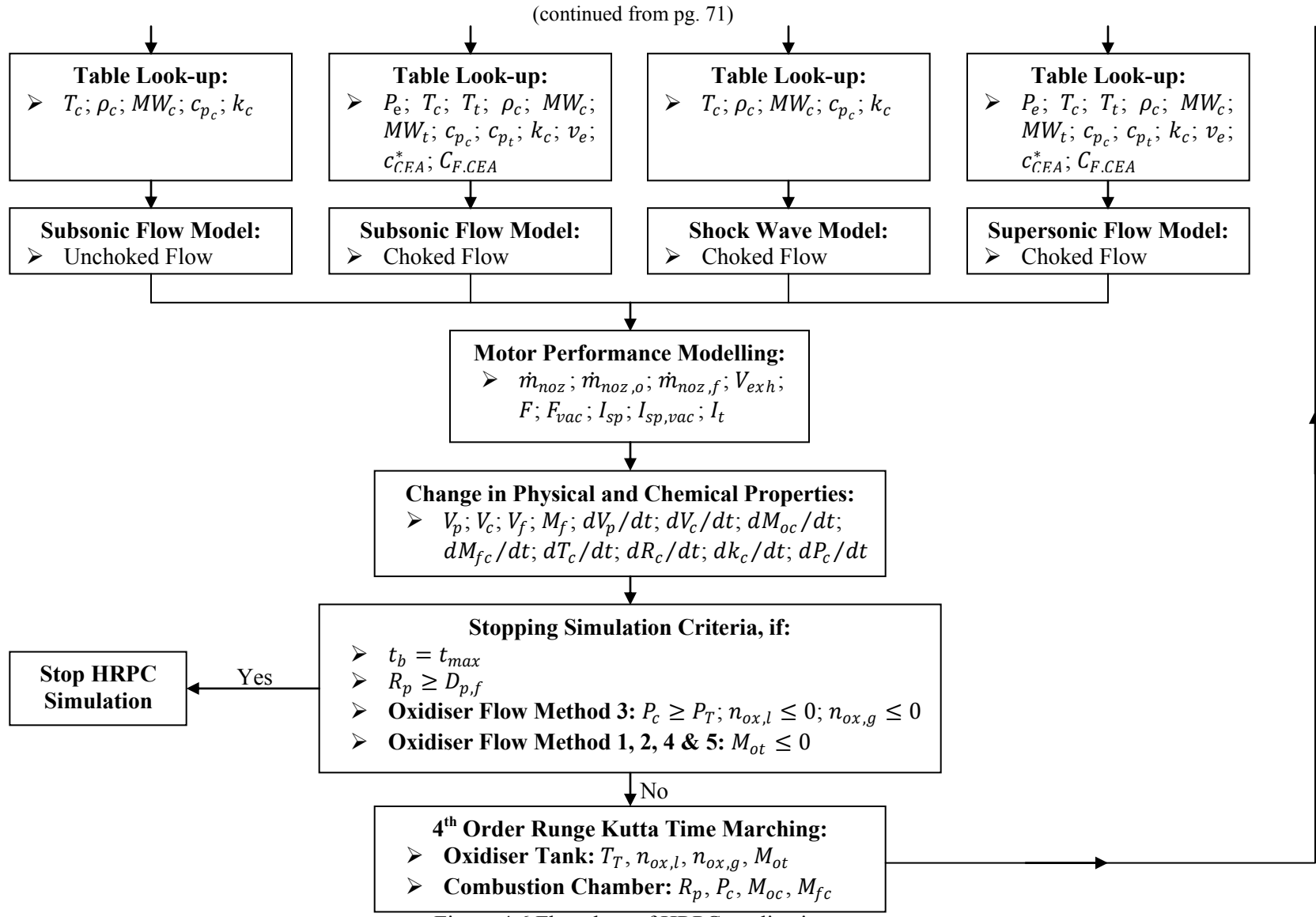


Figure 4.6 Flowchart of HRPC application.

4. Method 4 – a constant oxidiser tank pressure is used throughout the burn.
5. Method 5 – a polynomial curve fit is employed for the oxidiser tank pressure (function of time).

Throttling sequences can be defined for methods 2, 3, and 4 by the user. Typically, method 1 duplicates the operation of a turbine driven pump where the oxidiser flow is relatively uniform. Method 3 uses the oxidiser tank pressurisation and blowdown process described in Chapter 3 and is only applicable for the nitrous oxide propellant. Method 4 considers the utilisation of a high pressure gaseous oxidiser such as oxygen propellant. Method 5 is particularly useful for comparing hybrid rocket performance models and/or if the blowdown process of other propellants is known. The oxidiser mass flow rate for methods 3 to 5 is determined by a conventional discharge formula: Equation 3.3. With the selected oxidiser flow method, oxidiser parameters, feed system inputs and pressure difference, the oxidiser mass flow rate is calculated at each time step. Note that the discharge coefficients for liquid and gaseous phases of the same propellant are not identical.

Fuel regression rate is computed using Equation 3.24 with the appropriate ballistic coefficients for the motor configuration. The expected final port diameter obtained from the HRPC Motor Design is employed as an input to determine the fuel grain diameter as per HRPC fuel grain standard geometrics, (Appendix D). In addition, it provides a stopping criterion if the instantaneous port diameter surpasses the value. The fuel grain length, number of ports, and initial port diameter are also supplied for computation of the fuel mass flow rate.

The combustion products will only flow out of the nozzle if the chamber pressure exceeds the atmospheric pressure. Furthermore, the motor experiences useful thrust when the oxidiser-to-fuel ratio is greater than zero and the chamber pressure greater than the atmospheric pressure. The nozzle's critical pressure ratios obtained from the HRPC Motor Design are assumed to remain constant for the variation in gaseous flow. HRPC compares the operating nozzle pressure ratio with its critical points and thus determines the type of flow through the nozzle. The code only considers a constant atmospheric pressure. Before solving for the nozzle flow model, the required parameters are extracted and interpolated from the original lookup tables for the instantaneous mixture ratio and chamber pressure. The characteristic velocity and momentum-thrust term are modified by the input combustion efficiency and nozzle correction factor, respectively. Depending on the flow characteristics (subsonic, shock wave, or supersonic), the code models the rocket performance as described in Chapter 3. The changes in physical and chemical properties provide solutions for the chamber pressure derivative, Equation 3.58, and in the

case of the blowdown process of nitrous oxide, the time derivatives of the number of moles of liquid nitrous oxide  $\frac{dn_{ox,l}}{dt}$ , the number of moles of vapour nitrous oxide  $\frac{dn_{ox,v}}{dt}$ , and the tank temperature  $\frac{dT_T}{dt}$ .

The current application either employs a 4<sup>th</sup> order Runge Kutta or explicit Euler numerical method to integrate the ordinary differential equations. As expected, a 4<sup>th</sup> order Runge Kutta scheme offers better accuracy with a larger time-step relative to the explicit Euler method. Depending on the oxidiser flow method, a smaller time-step, lower than 0.002 s, is usually required to stabilise the initial spike in chamber pressure. It was observed that the solutions become saturated for time-steps shorter than 0.001 s. Figure 4.7 shows the difference in chamber pressure solutions between 4<sup>th</sup> order Runge Kutta and explicit Euler methods for a time-step of 0.004 s. For this test-run example, explicit Euler is initially unstable but converges rapidly towards the 4<sup>th</sup> order Runge Kutta method. All design simulations for the Phoenix-1A hybrid rocket motor are based on the 4<sup>th</sup> order Runge Kutta numerical solution. The simulation is terminated if at least one of its stopping criteria is met, as displayed in Fig. 4.6. The computed dependent variables are fed back to different sub-models for the next time-step solution. HRPC creates an output spreadsheet file which contains the instantaneous parameters and average rocket motor performances. Moreover, the code produces a series of graphs and a two-dimensional representation of the burnt fuel grain.

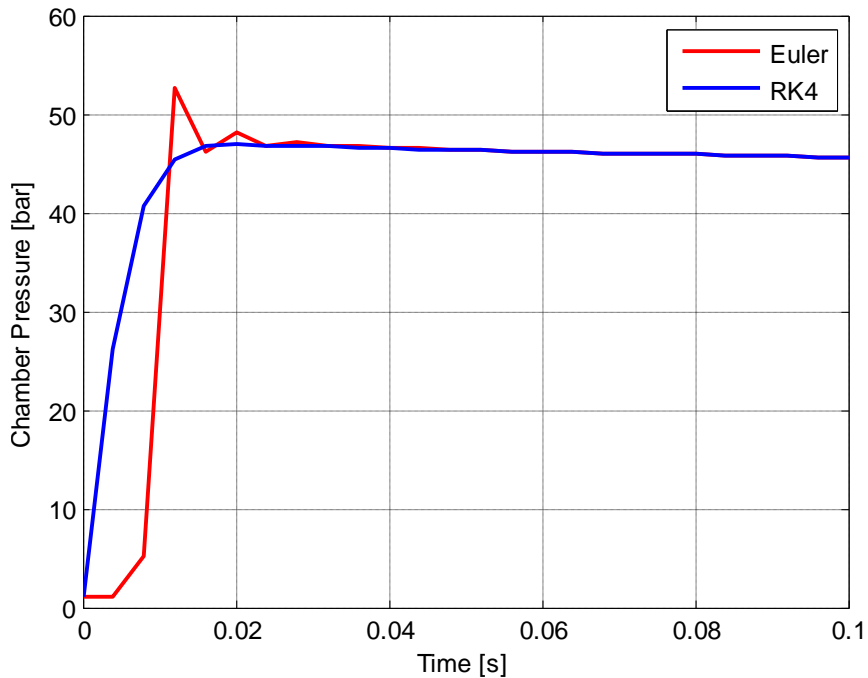


Figure 4.7 Difference between explicit Euler and 4<sup>th</sup> order Runge Kutta methods in the calculation of chamber pressure.

#### 4.4.2 Code Validation

To verify its reliability, HRPC must be compared to other similar hybrid rocket motor performance models. This procedure is critical as the Phoenix-1A rocket development depends significantly on the motor characteristics predicted by HRPC. Ideally, a comparison should be performed against a generic software tool that can model a variety of propellant combinations with a self-pressurising oxidiser delivery system. To the author's knowledge, such a software tool has not been commercialised to date. Therefore, reported hot-fire motor test data and performance modelling data are used for comparison purposes.

HRPC application has the capability to model different propellant combinations due to its interaction with NASA-CEA's thermodynamic library. However, to validate the predicted Phoenix-1A's motor performance, the code should be compared with reported data from the literature that falls within the range of Phoenix-1A's motor scale and utilises identical propellant combinations. The main issue with reported hot-fire motor test or performance modelling data is the lack of information on the propulsion system specifications, particularly the grain dimensions and nozzle geometry. Consequently, appropriate assumptions were made for the comparison procedure. Following extensive research, the second phase of the Stanford Sounding Rocket Programme (Karabeyoglu et al., 2003), showed promising motor specifications that can be used to validate HRPC.

The aim of the second phase of the Stanford Sounding Rocket Programme was to develop a sounding rocket for a targeted altitude of approximately 26.8 km which is powered by nitrous oxide and an aluminised paraffin wax propellant combination. The weight composition of the resultant fuel is 40% aluminium and 60% paraffin wax  $C_{31}H_{64}$ . The scale of the propulsion system falls within the range used in the Phoenix-1A rocket. In particular, the motor was designed to produce a peak thrust of 5000 N at an initial chamber pressure of 31 bars. Other mentioned parameters are an initial oxidiser mass flow rate of 1.9 kg/s, an initial mass flux of 500 kg/(m<sup>2</sup>s), an average oxidiser-to-fuel ratio of 4, a fuel mass of 6.8 kg, a nozzle expansion ratio of 4.5, an initial tank pressure of 56 bars, an oxidiser tank volume of 0.035 m<sup>3</sup>, and an oxidiser tank mass of 14.6 kg. An intuitive guess was required for the grain length based on the provided cross-sectional view of the combustion chamber. The initial grain port was calculated from the given initial oxidiser mass flow rate and mass flux, and the grain diameter was computed by the fuel mass and the approximated grain length. In addition, the nozzle geometry was determined in HRPC Motor Design for the initial thrust, chamber pressure, oxidiser-to-fuel ratio, and nozzle expansion ratio. Table 4.4 shows the reported parameters together with calculated values.

Table 4.4 Stanford Sounding Rocket Programme phase 2 propulsion system specifications.

Parameters as described in Karabeyoglu et al. (2003)		
<b>Initial Oxidiser Flow Rate</b>	<b>kg/s</b>	1.9
<b>Initial Mass Flux</b>	<b>kg/(m<sup>2</sup>s)</b>	500
<b>Initial Thrust</b>	<b>N</b>	5000
<b>Initial Chamber Pressure</b>	<b>bar</b>	31
<b>Average Oxidiser-to-Fuel Ratio</b>		4
<b>Nozzle Expansion Ratio</b>		4.5
<b>Fuel Mass</b>	<b>kg</b>	6.8
<b>Loaded Nitrous Oxide Mass</b>	<b>kg</b>	25
<b>Initial Tank Pressure</b>	<b>bar</b>	56
<b>Tank Volume</b>	<b>kg/m<sup>3</sup></b>	0.035
<b>Tank Mass</b>	<b>kg</b>	14.6
Calculated Parameters		
<b>Grain Length</b>	<b>m</b>	0.385
<b>Initial Port Diameter</b>	<b>m</b>	0.069
<b>Grain Diameter</b>	<b>m</b>	0.151
<b>Nozzle Throat Diameter</b>	<b>m</b>	0.0375
<b>Nozzle Exit Diameter</b>	<b>m</b>	0.0795

The oxidiser tank specifications provided sufficient information for the modelling of the nitrous oxide self-pressuring delivery system. This models the realistic decay in chamber pressure and thrust. Some important assumptions were made for the modelling of the Stanford Sounding Rocket Programme phase 2 motor:

1. The regression rate ballistic coefficient  $\alpha$  for pure paraffin wax/nitrous oxide combination was increased by 10% to account for the higher regression rate of the aluminised paraffin wax fuel (McCormick et al., 2005). It has been reported that the regression rate of a pure paraffin wax/nitrous oxide combination can be increased by 25% using aluminised paraffin wax fuel. This resulted in a ballistic coefficient:  $\alpha = 0.1705 \times 10^{-3}$ .
2. A fixed atmospheric pressure is assumed at sea-level.
3. Combustion efficiency of 95%.
4. Bell-shaped nozzle with 0.985 correction factor.

5. The feed system was designed according to the initial chamber pressure of 31 bars. That is, a discharged coefficient of 0.8, an orifice diameter of 0.002 m, the number of orifices 15, and a pressure drop of 8 bars in the feed line.

With the already mentioned motor specifications and assumptions, the Stanford Sounding Rocket Programme phase 2 motor was modelled in HRPC, and the results compared with their predicted motor performance. The primary focus was on the difference between the predicted motor thrust of the two models, shown in Fig. 4.8.

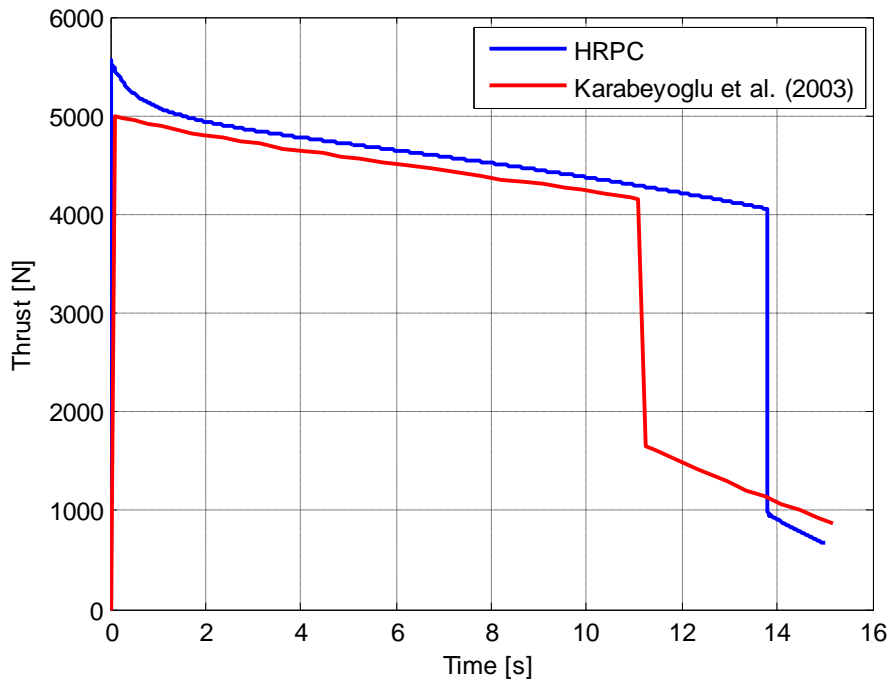


Figure 4.8 Motor performance validation of HRPC.

It can be seen that the HRPC predicted thrust profile follows the same trend as the reported thrust prediction. The main discrepancy exists at the predicted consumption of liquid nitrous oxide, which was reported to occur at approximately 11.2 s. However, HRPC predicts that the depletion occurs at approximately 13.8 s. This difference may be due to the uncertainty in the loaded nitrous oxide mass and/or a higher oxidiser mass flow rate obtained in Stanford's model due to the difference in tank and chamber pressures. The overall difference between the two models is mainly attributed to the initial assumptions made to run HRPC. In particular, the regression rate ballistic coefficient for aluminised paraffin wax/nitrous oxide was approximated as it was not reported in Karabeyoglu et al. (2003). Moreover, HRPC assumed a fixed atmospheric pressure whereas Stanford's predictive code models the

flight dynamics of the rocket, and consequently models the change in atmospheric pressure. The main source of error is probably the determination process of the fuel grain dimensions and nozzle geometry. In general, good agreement was obtained between the models.

#### 4.4.3 Implementation into the UKZN HYROPS Software

The HRPC application has been integrated with the UKZN Hybrid Rocket Performance Simulator (HYROPS) software as an alternative high-fidelity propulsion model. HYROPS is an integrated hybrid rocket trajectory simulation tool intended to predict the sub-orbital flight performance of a generic multi-stage hybrid sounding rocket (Chowdhury, 2012). The HYROPS software tool provides full coupling between the hybrid motor performance model which is described in this dissertation and the flight dynamics model developed in a parallel work by Chowdhury (2012). The HRPC's MATLAB programming platform was transferred to Microsoft Visual C++ programming language for its beneficial computing capabilities (Fig. 4.9).

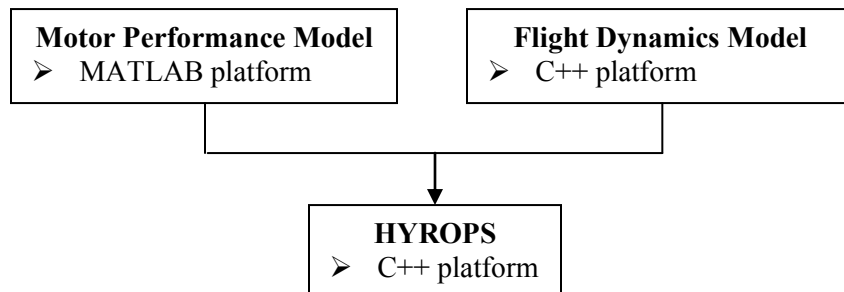


Figure 4.9 Coupling of motor performance and flight dynamics models to form HYROPS software.

The HYROPS software tool numerically solves the core six-degree-of-freedom rocket flight dynamics equations, given initial conditions, a vehicle inertia model, a vehicle propulsion system model, a vehicle aerodynamic model, a model for the Earth's gravitation and atmosphere, and a model of the vehicle's recovery system. The gravitational and geodetic models include effects for the rotation and shape of the earth whilst the altitude-dependent atmospheric model is also used to simulate density changes and winds. All the functionality offered by the software developed through this work is available in parallel in the HYROPS framework. The motor performance outputs such as the momentum-thrust history, nozzle exit pressure history, oxidiser and fuel consumption histories, and fuel volumes and dimensions are used in a fully coupled manner in simulation time to model the high fidelity operation of a hybrid rocket motor on a sounding rocket. When the hybrid propulsion model is activated, at each time step of the numerical

solution process, the HYROPS tool executes a corresponding time step in the hybrid motor performance code and uses the outputs in a dynamic manner.

The self-pressurising delivery system model from HRPC application is used to compute the residual oxidiser mass and volume at each time step which in turn determines the length of the column of oxidiser in the tank. This change in oxidiser characteristics is coupled to the vehicle structural model of HYROPS to simulate the variation in the vehicle mass distribution and centre of gravity. Similarly, the motor fuel masses and dimensions are coupled to the HYROPS vehicle structural model while the thrust vector is determined by the nozzle exit pressure and momentum-thrust outputs. The coupled simulation is capable of capturing subtle dynamics such as the effects of a nonlinear fuel-grain regression rate on the vehicle inertia and added thrust due to the nonlinear variation of nozzle exit pressure and the drop in ambient atmospheric pressure as the vehicle ascends. The HYROPS software tool is also capable of interfacing with the NASA-CEA package in a similar fashion to that described in this dissertation.

The motor performance and flight dynamics models are integrated using a graphical user interface through which the user may input details of the vehicle structure, geometry, and power-plant. These inputs are used to generate high fidelity mathematical models for the vehicle inertia, aerodynamics, and propulsion system. The output of the HYROPS software tool is the flight trajectory, a time history of the position, and the velocity and acceleration of the sounding rocket. Numerous other variables of interest such as the maximum altitude and range, the aerodynamic conditions of flight, and the structural responses and loads are also calculated. Note that the HRPC inputs are also available through the HYROPS graphical user interface (Fig. 4.10). Using this feature, the HRPC application can also be executed for a motor configuration without the flight performance modelling.

Referring to the work of Chowdhury (2012), the HYROPS tool also performs a multivariate stochastic analysis of flight performance using the Monte Carlo method. Using this technique, the effects of input uncertainties in the vehicle design on the flight performance are easily quantified. The HYROPS tool also offers an optimisation feature capable of tuning all the subsystems in a given vehicle design for better flight performance. The software relies on genetic algorithms to perform the optimisation function. Outputs from the software tool are available in animated 3D visualisations as well as a variety of graphical and tabular formats for ease of analysis, interpretation, and application to the rocket design. A 3D trajectory visualisation of a designed sounding rocket is shown in Fig. 4.11 with its overall trajectory parameters and instantaneous flight conditions.

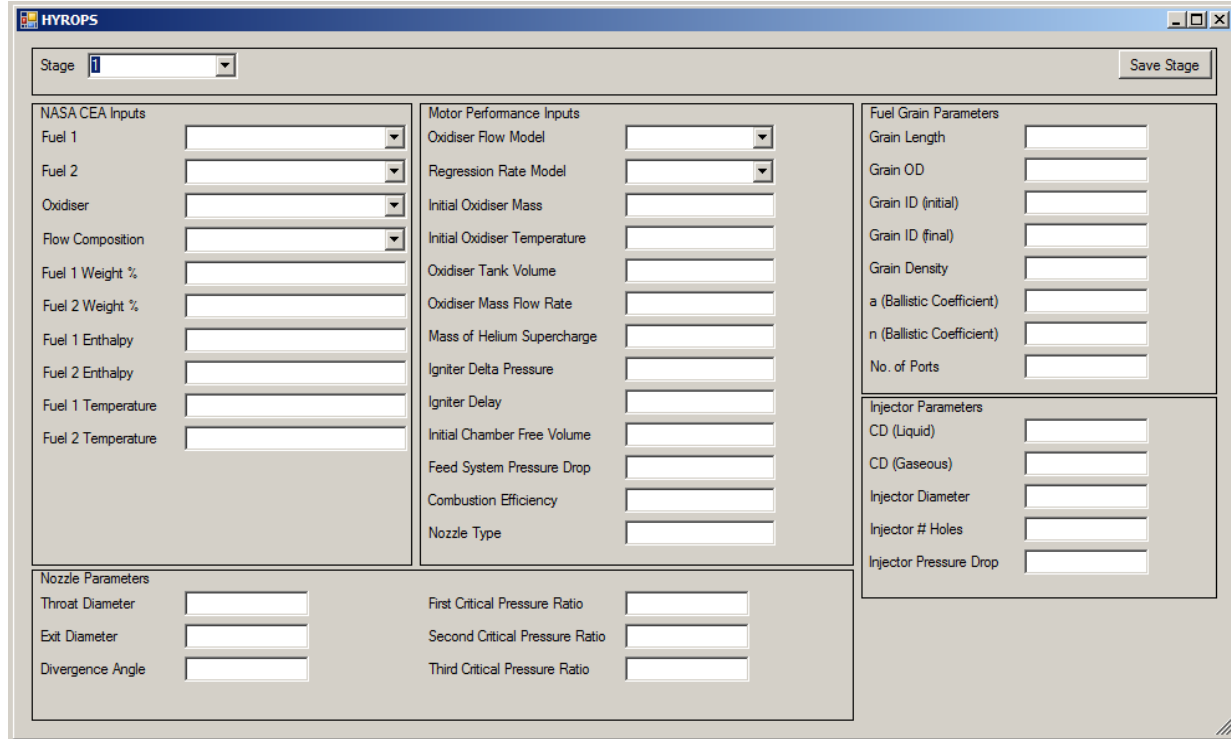


Figure 4.10 Screenshot of the HYROPS's user interface where the HRPC parameters are inputted.

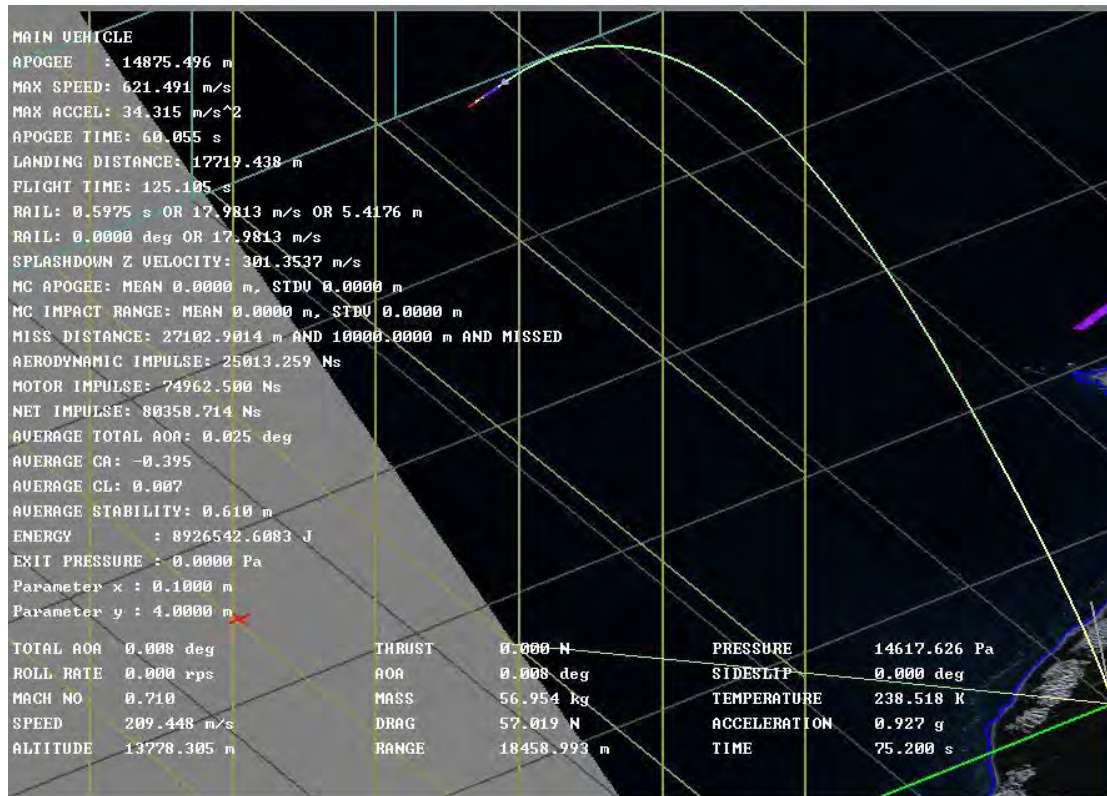


Figure 4.11 Screenshot of the HYROPS three dimensional trajectory visualisation window (Chowdhury, 2012).

## CHAPTER 5

### PV-1 Flight Motor Design and Manufacture

#### 5.1 Specifications and Design Goals

The flight mission requirement of the Phoenix-1A hybrid sounding rocket is to reach an apogee of 10 km with the capability to safely house and carry a 1 kg payload. The propulsion power needed to propel the 10 km apogee rocket was analysed in a parallel project through the HYROPS software tool developed by Chowdhury (2012). The total impulse obtained from the flight performance mathematical model drove the development of the Phoenix-1A hybrid rocket motor, which is designated as PV-1 motor.

In the following section, the design and manufacture of the PV-1 hybrid rocket motor will be discussed, excluding the structural development of the oxidiser tank which was designed by Chowdhury (2012). This chapter includes the optimisation process of the PV-1 hybrid motor for the aimed 10 km apogee, and provides a detailed description of its final design specifications.

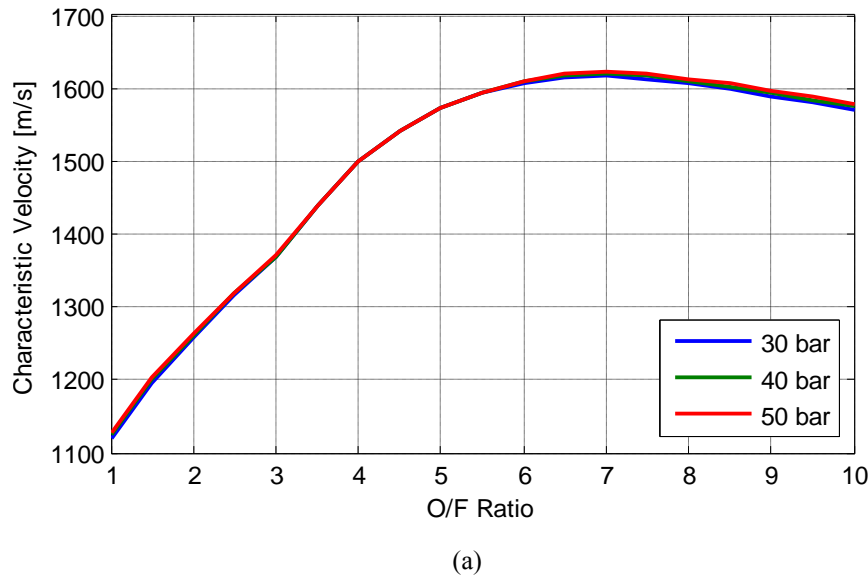
#### 5.2 Phoenix-1A Propulsion System Design

##### 5.2.1 Nitrous Oxide/Paraffin Wax Performance Analysis

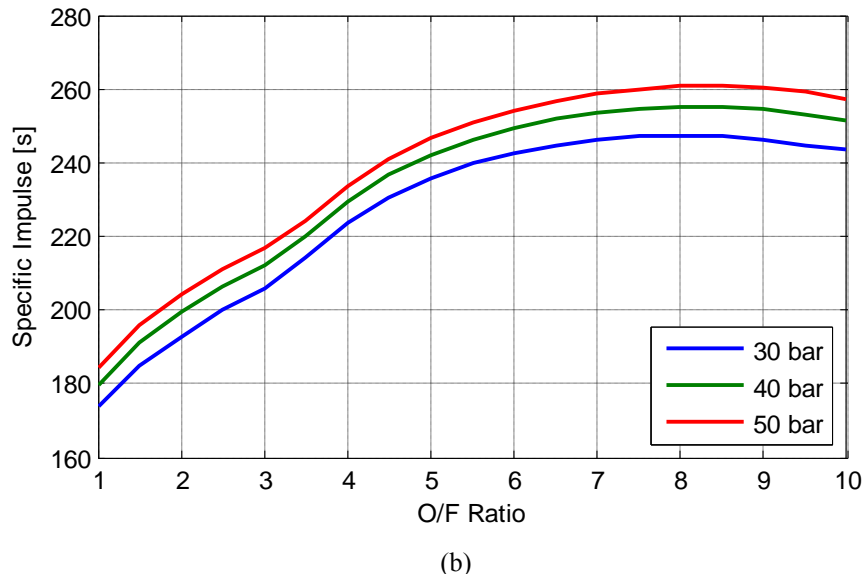
A full performance analysis of the hybrid rocket's propellant combination, nitrous oxide, and paraffin wax is required prior to the development of its propulsion system. This investigation characterises the optimum mixture ratio for the targeted chamber pressure. The HRPC Motor Design application facilitates the investigation by generating a series of motor performance output graphs and tables for a range of oxidiser-to-fuel ratios and chamber pressures.

Figures 5.1 (a) to (c), produced by the HRPC Motor Design application, referring to Sections 4.2 and 4.3, display the characteristic velocity, optimum nozzle expansion ratio, and specific impulse for a range of mixture ratio and chamber pressures of 30 to 50 bars. These curves represent the motor characteristics for an atmospheric pressure of 0.8987 bar, 100% combustion efficiency, and a bell-shaped nozzle configuration without flow losses. It can be noted that the optimum mixture ratio is in the vicinity of 7

with regard to characteristic velocity whereas it is close to 8 for the specific impulse. By definition, the characteristic velocity, which is a measure of combustion efficiency, is dependent on chamber pressure and oxidiser-to-fuel ratio (equilibrium composition of the combustion gases), whereas, independent on nozzle expansion ratio. Figure 5.1 (a) shows that the gain in combustion temperature by increasing the chamber pressure is relatively insignificant. However, a noticeable increase in specific impulse, which is the comparative performance parameter of rocket motors, is experienced with higher chamber pressures as shown in Fig. 5.1 (b).



(a)



(b)

Figure 5.1 Nitrous Oxide/Paraffin wax performance analyses for PV-1 hybrid rocket motor: (a) Characteristic velocity, (b) Specific impulse, and (c) Optimum nozzle expansion ratio.

Figure 5.1 (c) illustrates the optimum nozzle expansion ratios for the range of oxidiser-to-fuel ratio operating at an atmospheric pressure of 0.8987 bar, that is, at an altitude of 1000 m. Note the sensitivity of optimum nozzle expansion ratio occurring at low oxidiser-to-fuel ratios due to the present of condensed species in the combustion reaction. The overall analysis suggests that there is a significant improvement in specific impulse as chamber pressure increases as well as an undesirable gain in nozzle mass due to the increase in expansion ratio.

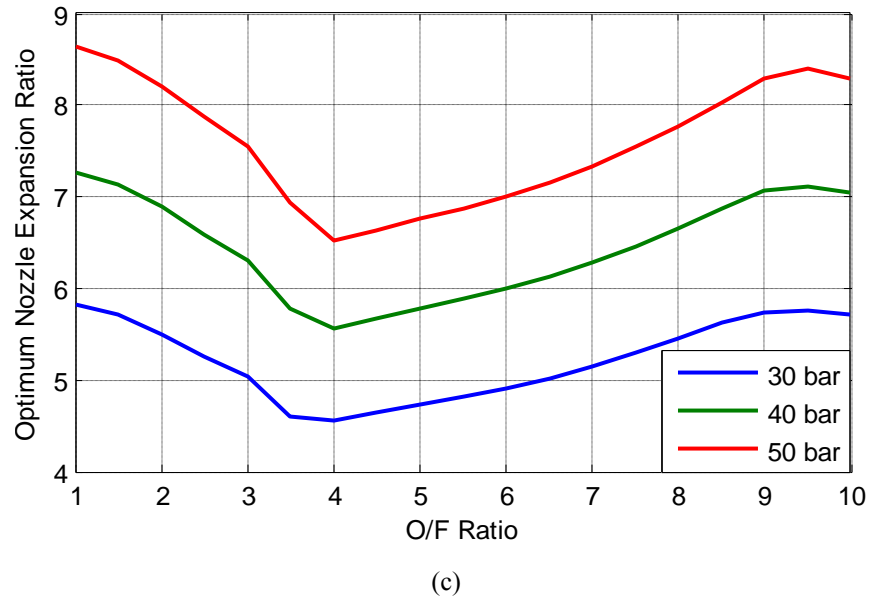


Figure 5.1 Nitrous Oxide/Paraffin wax performance analyses for PV-1 hybrid rocket motor: (a) Characteristic velocity, (b) Specific impulse, and (c) Optimum nozzle expansion ratio.

The PV-1 motor targeted chamber pressure is limited by the oxidiser tank pressure. An assumed average tank pressure of 56 bars during the self-pressurising blowdown process was used as the benchmark to determine the ideal operating chamber pressure. As mentioned previously, for stable combustion, the injector pressure drop needs to be at least 15-25% of the chamber pressure. Assuming a pressure drop of 20% through the injector and a pressure drop of 5 bars in the feed system, the expected operating chamber pressure is 39.8 bars for an averaged value of 56 bars tank pressure. Supercharging the oxidiser tank will boost the chamber pressure but this will increase the designed wall-thicknesses of the tank and combustion chamber casing, consequently, resulting in a weight penalty of the sounding rocket. In addition, higher chamber pressures are more likely to produce unstable combustion throughout the burn. On the other hand, lowering the chamber pressure below 30 bars decreases the motor performance considerably. Therefore, a chamber pressure and oxidiser-to-fuel ratio of 40 bars and 7 were targeted for the PV-1 flight motor.

## 5.2.2 PV-1 Motor Design

Ideally, direct optimisation of a hybrid rocket motor is accomplished through the coupling of the vehicle flight dynamics and motor performances such as the capabilities incorporated in the current HYROPS version. In the preliminary versions, HYROPS and HRPC were uncoupled, and any optimisation of the rocket was achieved through data exchange. Hence, the design and optimisation of the PV-1 motor was performed through an iterative manual process between HRPC and the preliminary version of HYROPS. In particular, this process was achieved by linking the PV-1 motor data outputs from HRPC to HYROPS, which in turns predict the Phoenix-1A hybrid sounding rocket's apogee.

For the preliminary design of the Phoenix-1A rocket, HYROPS determined a required motor total impulse of 75000 Ns for an approximate vehicle mass including the PV-1 motor. Targeting a 20 s burn time, the required thrust for the total impulse and burn time was computed as 3750 N. The targeted apogee of the Phoenix-1A hybrid rocket for such conditions is 10 km. From these conditions, HRPC Motor Design was employed to calculate the fuel grain and nozzle dimensions for a set of critical inputs. In addition, the HRPC application generated the motor performance histories which were supplied to HYROPS. The optimisation procedure of the PV-1 motor is depicted in Fig. 5.2.

Firstly, the fuel grain and nozzle designs were performed in the HRPC Motor Design application for a series of altitudes, fixed chamber pressure of 40 bar, and varying oxidiser-to-fuel ratios from 6 to 8. Commonly, a rocket nozzle is designed for an optimum expansion ratio occurring at the mid-burn of the motor. From the flight performance prediction, the Phoenix-1A motor burnout occurs at an altitude of 6000 m depending on the launch angle. Hence, the nozzle was designed to operate between sea-level and 3000 m. Due to the self-pressurising blowdown system, the motor thrust will decay with the tank pressure during the burn, resulting in an average motor thrust lower than the targeted 3750 N. Consequently, the PV-1 motor was designed for a peak thrust of 4250 N, which theoretically decreases to approximately 3000 N after the 20 s. Table F.1 in Appendix F shows the different fuel grain and nozzle designs (Design 1 to 4) for an incremental altitude. The inputs and selected outputs of each run are provided in Table F.1. Note the significant changes in optimum expansion ratio and fuel grain length and mass. The grain length decreases as the oxidiser-to-fuel ratio increases to 8, becoming a more oxygen-rich environment. However, the web thickness or grain diameter is solely dependent on burn time and does not affect the motor thrust.

Secondly, the outputs from each HRPC Motor Design run are fed to the HRPC application to compute the instantaneous performances of the PV-1 motor. The injector was designed for the respective oxidiser mass flow rate corresponding to its Motor Design run together with the tank volume for a 20 s burn time. The predicted momentum-thrust, nozzle exit pressure, and changes in the propellants' masses of each model were passed on to HYROPS which determined the apogee. Design 2, with an average mixture ratio of 6 and an optimum nozzle expansion ratio of 5.99 at 1000 m altitude, produced the highest apogee for the Phoenix-1A hybrid rocket.

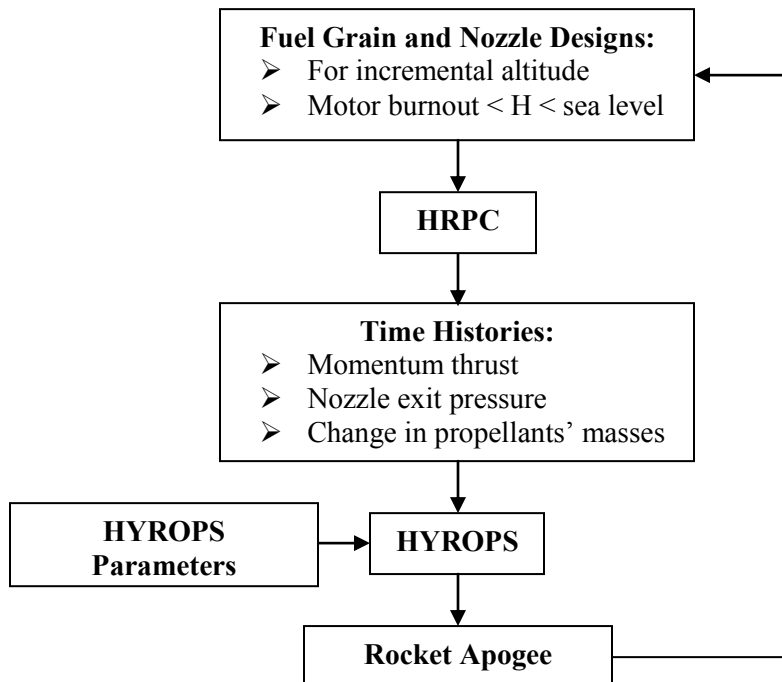


Figure 5.2 PV-1 motor manual performance optimisation.

The Design 2 motor specifications were run in the HRPC application at two fixed atmospheric pressures, namely sea-level ( $P_a = 1.01325$  bar) and 3000 m ( $P_a = 0.7009$  bar), to investigate the gain in performance due to the difference in pressures. Figure 5.3 illustrates the improvement in motor thrust due to the increase in pressure-thrust term. Note that the graph stops at the liquid nitrous oxide burnout. The averaged performance parameters, taken over the liquid or gaseous nitrous oxide burnout for the two simulations, are shown in Table F.2. It can be noted that the gaseous nitrous oxide mass flow rate increases the total impulse of the PV-1 motor by 3.5% and 4.3% for cases of sea-level and 3000 m simulations, respectively. The complete thrust curve for the Design 2 motor operating at 3000 m is displayed in Fig. 5.4. In addition, other instantaneous motor performance parameters are reproduced in Figures F.1, Appendix F.

Referring to Fig. 5.4, the initial peak in thrust is due to the high oxidiser mass flow rate as a result of the significant pressure difference between the oxidiser tank and combustion chambers. As expected, the motor thrust decreases during the blowdown process. The liquid burnout occurs at 19.814 s, where a significant drop in motor thrust is noticeable. The total motor impulse for this typical simulation is 75648.3 Ns, including the gaseous oxidiser mass flow rate phase. Table 5.1 shows the PV-1 motor (Design 2) specifications aiming to power the Phoenix-1A hybrid sounding rocket.

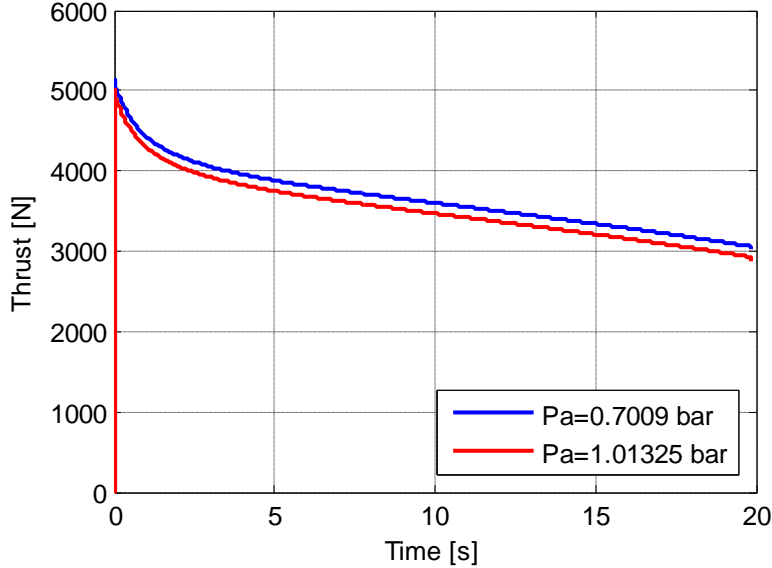


Figure 5.3 Thrust curves of PV-1 motor selected design 2 operating at sea-level ( $P_a = 1.01325 \text{ bar}$ ) and 3000 m ( $P_a = 0.7009 \text{ bar}$ ).

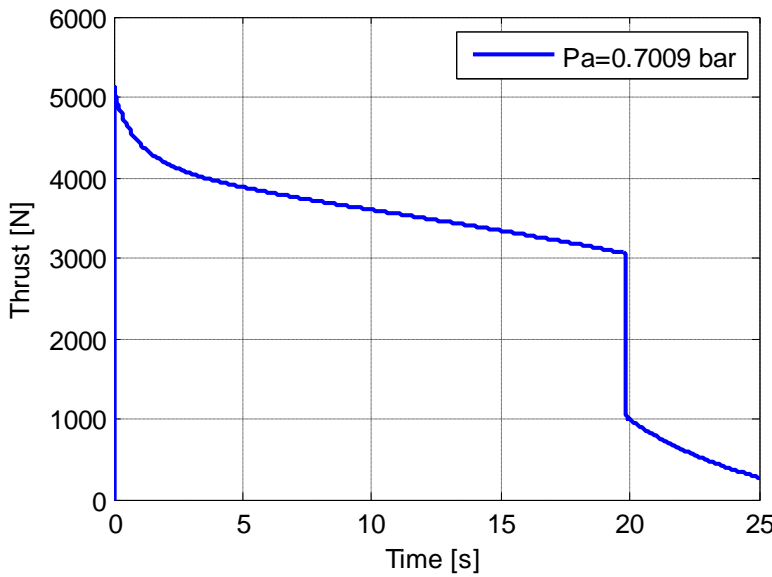


Figure 5.4 Complete thrust curve of PV-1 motor design 2 operating at 3000 m ( $P_a = 0.7009 \text{ bar}$ ).

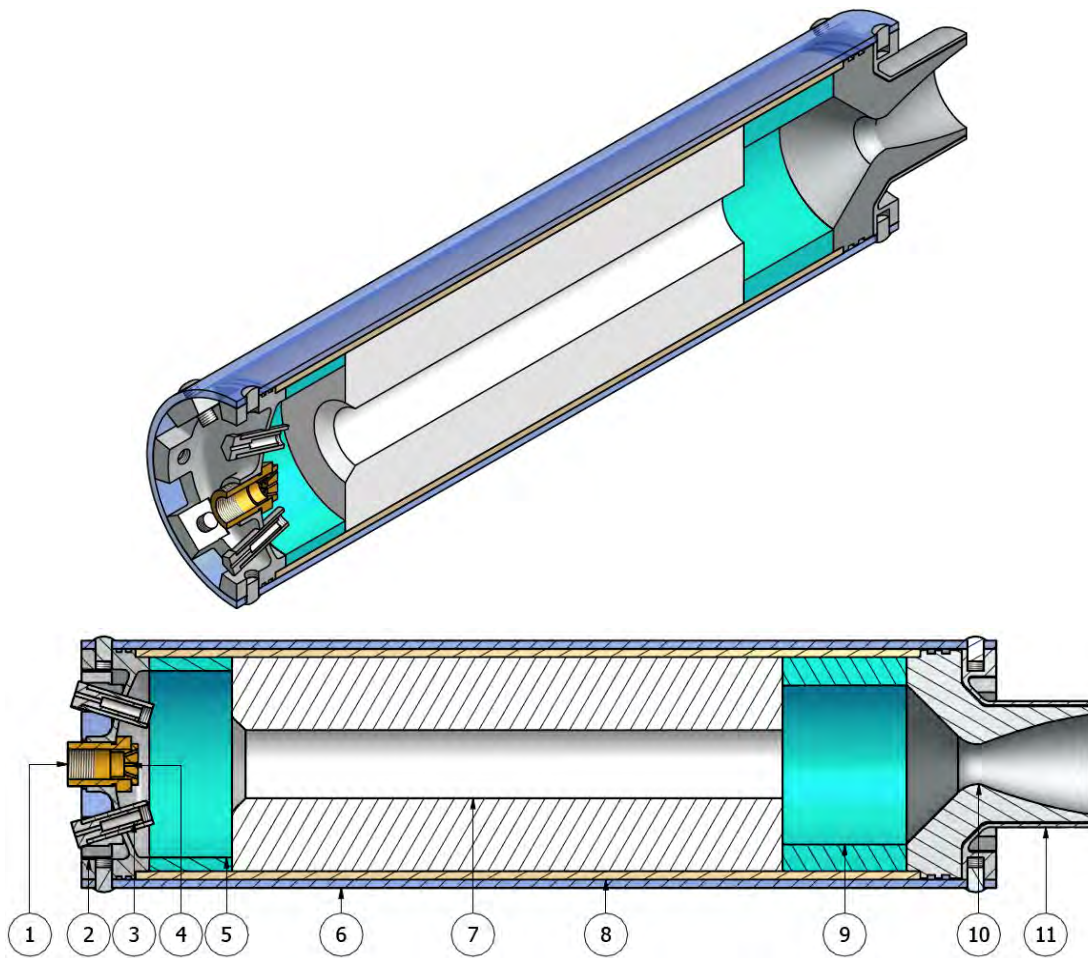
Table 5.1 Phoenix-1A PV-1 propulsion system final design.

Phoenix-1A Propulsion System Final Design				
<b>PV-1 Motor</b>	<b>Fuel Grain</b>	<b>Propellant</b>		SASOL 0907 Paraffin Wax
		<b>Composition</b>		97% Wax, 3% Charcoal
		<b>Grain Configuration</b>		Cylindrical
		<b>Number of Ports</b>		1
		<b>Initial Port Diameter</b>	<b>m</b>	0.05
		<b>Grain Diameter</b>	<b>m</b>	0.156
		<b>Grain Length</b>	<b>m</b>	0.4
		<b>Oxidiser-to-Fuel Ratio</b>		6
		<b>Material</b>		Graphite
		<b>Shape</b>		Bell-Shaped
<b>Nozzle</b>		<b>Expansion Ratio</b>		5.99
		<b>Throat Diameter</b>	<b>m</b>	0.0298
		<b>Exit Diameter</b>	<b>m</b>	0.0731
<b>Oxidiser Tank</b>	<b>Oxidiser</b>			Nitrous Oxide
	<b>Supercharge Gas</b>			Helium
	<b>Loaded Oxidiser Mass</b>		<b>kg</b>	30
	<b>Loaded Supercharge Gas Mass</b>		<b>kg</b>	0.006
	<b>Tank Volume</b>		<b>m<sup>3</sup></b>	0.043
	<b>Ullage</b>		<b>%</b>	10
	<b>Initial Tank Pressure</b>		<b>bar</b>	65

### 5.3 PV-1 Motor Structural Design and Manufacture

The development of the PV-1 hybrid motor was mainly driven by the fuel grain overall dimensions. In particular, the circumference of the chamber casing was constrained by the outer diameter of the solid fuel. The grain diameter, as depicted in Table 5.1, incorporated an additional thickness of paraffin wax to the theoretical burnt web thickness due to the uncertainty in the fuel regression rate. Moreover, this additional web thickness provides for useful combustion during the gaseous oxidiser mass flow tail-off phase.

Cross-sectional views of the PV-1 motor are shown in Fig. 5.5 with its fundamental components identified. The motor essentially consists of a 6082-T6 aluminium combustion chamber casing, a grade 431 stainless steel torispherical injector bulkhead and nozzle retainer, a fine grain ATJ graphite nozzle, and a fuel grain cartridge, as the core of the propulsion system. The fuel grain is enclosed within a protective thermal liner which is manufactured from a combination of cotton/glass/phenolic composite materials, and is situated between two polyethylene pre- and post-combustion chamber inserts at its extremities. The injector bulkhead and nozzle retainer consists of circumferentially-bolted joints which secure the internal components to the chamber casing. The overall design provides for relatively quick and easy assembly and disassembly. In addition, each component is independently replaceable if damaged beyond repair. Dual O-rings are fitted into the machined grooves in the injector bulkhead and nozzle for sealing purposes. Detailed drawings of the PV-1 motor are attached in the Appendix G.



1) Injector Manifold, 2) Injector Bulkhead, 3) Igniter, 4) Injector, 5) Pre-Combustion Chamber, 6) Chamber Casing,  
7) Fuel Grain, 8) Thermal Liner, 9) Post-Combustion Chamber, 10) Nozzle, 11) Nozzle Retainer

Figure 5.5 Sectional views of PV-1 motor

A finite element analysis and a computational fluid dynamics analysis were performed to evaluate and design the critical components for worst case loading conditions. Commercial MSc SimXpert and StarCCM+ tools were used for FEA and CFD, respectively. The following sections describe the detailed analyses carried out on the combustion chamber casing, injector bulkhead, and nozzle and its retainer. The boundary conditions and equivalent stress distributions with the safety factors are discussed.

### 5.3.1 Combustion Chamber Casing

The combustion chamber casing was developed from lightweight structural 6082-T6 aluminium due to its local availability and beneficial mechanical properties subsequent to heat treatment. Three types of material were considered: duplex stainless steel, aluminium, and titanium alloys. Among these materials, aluminium 6082-T6 was chosen as it offers better thrust-to-weight ratio than duplex stainless steel and is significantly cheaper than titanium alloys. One disadvantage of the alloy is its general reduction in strength near the vicinity of welded joints, that is, in the heat affected zone. For this reason, welding components to the casing was avoided. The mechanical properties of 6082-T6 aluminium are reported in Table 5.2 below. Note that the material's tensile and compressive strengths are assumed to be equivalent to the yield strength which is a conservative approach with regard to the casing design.

Table 5.2 Mechanical properties of 6082-T6 aluminium (MatWeb, 2012).

<b>Yield Strength</b>	$\sigma_{y,Al}$	<b>MPa</b>	260
<b>Shear Strength</b>	$\sigma_{s,Al}$	<b>MPa</b>	210
<b>Tensile Strength</b>	$\sigma_{t,Al}$	<b>MPa</b>	260
<b>Compressive Strength</b>	$\sigma_{c,Al}$	<b>MPa</b>	260
<b>Young's Modulus</b>	$E_{Al}$	<b>GPa</b>	70
<b>Poisson's Ratio</b>	$\nu_{Al}$		0.35
<b>Density</b>	$\rho_{Al}$	<b>kg/m<sup>3</sup></b>	2700
<b>Melting Point</b>		<b>K</b>	828
<b>Coefficient of Thermal Expansion</b>	$\alpha_{Al}$	<b>10<sup>-6</sup>/K</b>	24
<b>Thermal Conductivity</b>	$\kappa_{Al}$	<b>W/(m.K)</b>	180

The chamber casing was designed and analysed as a cylindrical pressure vessel to determine its wall thickness for the PV-1 motor operating conditions with an adequate safety margin. A theoretical approach

was used to calculate the wall thickness and its corresponding stress distributions, followed by a finite element analysis of the same wall thickness. The results from the two methods are compared.

For a cylindrical pressure vessel subjected to an internal pressure loading, the three normal stresses (hoop, axial and radial) are determined using the following equations:

$$\sigma_h = \frac{r_i^2 P}{(r_o^2 - r_i^2)} \left( 1 + \frac{r_o^2}{r^2} \right) \quad (5.1)$$

$$\sigma_a = \frac{r_i^2 P}{(r_o^2 - r_i^2)} \quad (5.2)$$

$$\sigma_r = \frac{r_i^2 P}{(r_o^2 - r_i^2)} \left( 1 - \frac{r_o^2}{r^2} \right) \quad (5.3)$$

$$r_o = r_i + t \quad (5.4)$$

$$t = \left[ \frac{r_i^2 (1 + (\sigma_y / P_d))}{(\sigma_y / P_d) - 1} \right]^{1/2} - r_i \quad (5.5)$$

where  $\sigma_h$  is the hoop stress,  $\sigma_a$  is the axial stress,  $\sigma_r$  is the radial stress,  $P$  is the internal pressure,  $r_i$  is the inner radius,  $r_o$  is the outer radius,  $r$  is the radial variable,  $t$  is the wall-thickness, and  $\sigma_y$  is the yield strength of the material. From the theory and Equations 5.1 and 5.3, hoop and radial stresses vary through the wall thickness, whereas axial stress remains constant. Appendix H.1 shows the calculation of the wall-thickness for a design pressure of;  $P_d = S_f P_c = 12$  MPa, and inner radius of;  $r_i = 0.084$  m. A wall-thickness of 4 mm was calculated for the design operating conditions. Due to the circumferential bolt joints around the casing, the wall-thickness was increased to 6 mm to eliminate the risk of failure modes (tensile, compressive, and double shear) at the joints.

The maximum and minimum normal stresses for the 6 mm wall-thickness were calculated for a chamber pressure of 40 bars, and the results are shown in Table H.1, Appendix H. In addition, a finite element analysis was performed on a quarter geometry of the chamber casing with identical operating conditions. The results for the hoop, radial, and axial stresses at the inner and outer casing radius are depicted and

compared with the theoretical ones. Good agreement between FEA and the fundamental formulae are noted. Furthermore, graphs of the variation in hoop and radial stresses through the wall-thickness are given in Fig. H.1. The von Mises stress distributions in the chamber casing are displayed in Fig. 5.6. The results suggest that the internal wall experiences a maximum stress of 54.45 MPa for an operating chamber pressure of 40 bars, which produces a significant safety factor of 4.8 over the yield strength of 6082-T6 aluminium. However, from Table H.2, the safety factor decreases to 1.7 at the bolt joints for the same chamber pressure. In the rocket industry, a safety factor more than 1.5 is deemed acceptable for the targeted working conditions.

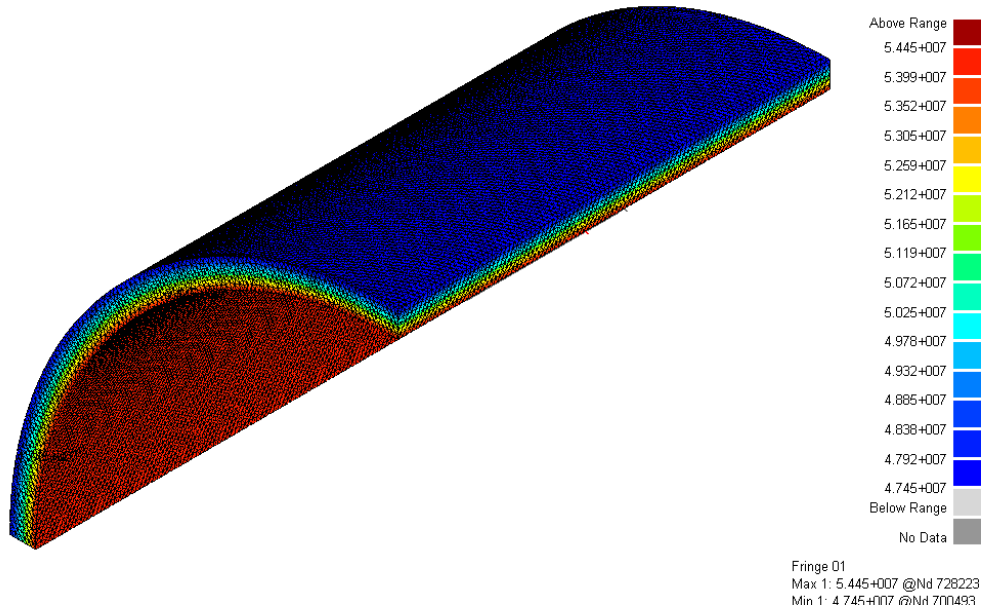


Figure 5.6 FEA von Mises stress distributions in combustion chamber casing.

Due to the local unavailability of standard sizes 6082-T6 aluminium tubing, a 200 mm solid billet was machined down to the required wall-thickness and length. The correct outer diameter was firstly machined, followed by internal machining. The boring, shown in Fig. 5.7 (a), was performed through both ends due to the length of the casing. Finally, the circumferential holes were marked and drilled. In addition to the injector bulkhead and nozzle retainer, the combustion chamber casing accommodates the fin arrangement which were designed by Chowdhury (2012). Figure 5.7 (b) shows the Phoenix-1A's manufactured fins attached to the chamber casing. The manufactured injector bulkhead, with all the holes plugged and a stainless steel cap for the nozzle side were used to enclose the ends of the chamber casing for a pressure test. A hydrostatic pressure test was performed at 1.5 times the working pressure for 10 mins, hence confirming the design and structural integrity of the chamber casing. Figure 5.8 shows the motor in the hydrostatic test configuration.

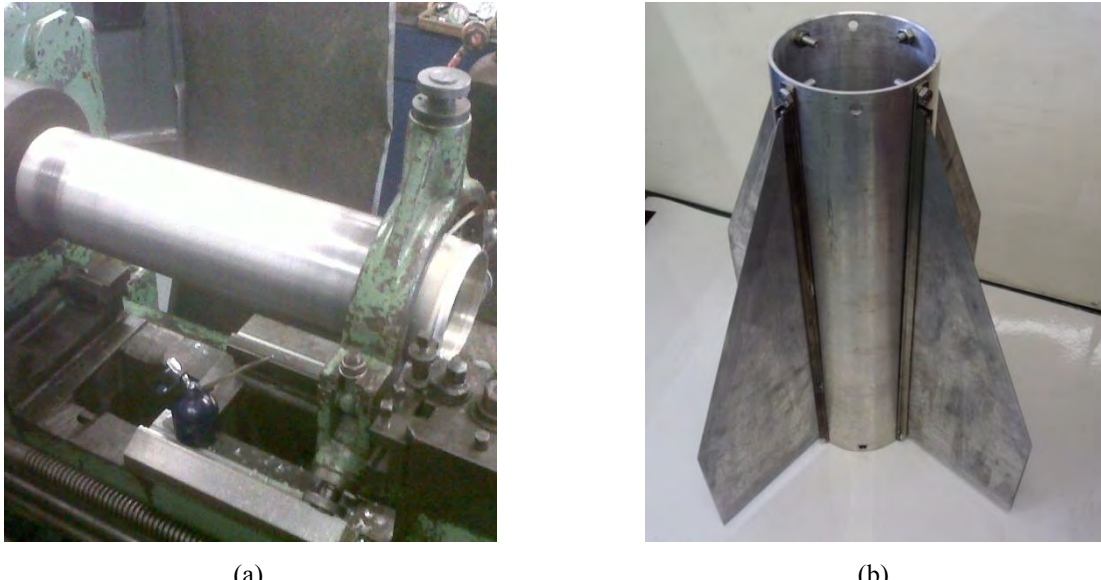


Figure 5.7 Combustion chamber casing.



Figure 5.8 PV-1 motor in hydrostatic test configuration.

### 5.3.2 Injector Bulkhead

The injector bulkhead was designed from grade 431 stainless steel due to its higher yield strength and overall mechanical properties over 6082-T6 aluminium. Its mechanical properties are produced in Table 5.3. The material's tensile and compressive strengths are assumed to be equivalent to the yield strength; however the shear strength is approximated as 60% of the yield strength value.

Like the chamber casing, the injector bulkhead was considered a typical pressure vessel head in the development process. It was designed as a torispherical head which accommodates the injector manifold, igniters, and pressure transducer. The torispherical shape aids to reduce the stresses, particular in the outer

Table 5.3 Mechanical properties of 431 stainless steel (Kotecki and Armao, 2003).

<b>Yield Strength</b>	$\sigma_{y,st}$	<b>MPa</b>	655
<b>Shear Strength</b>	$\sigma_{s,st}$	<b>MPa</b>	300
<b>Tensile Strength</b>	$\sigma_{t,st}$	<b>MPa</b>	655
<b>Compressive Strength</b>	$\sigma_{c,st}$	<b>MPa</b>	655
<b>Young's Modulus</b>	$E_{st}$	<b>GPa</b>	200
<b>Poisson's Ratio</b>	$\nu_{st}$		0.3
<b>Density</b>	$\rho_{st}$	<b>kg/m<sup>3</sup></b>	7750
<b>Thermal Conductivity</b>	$\kappa_{st}$	<b>W/(m.K)</b>	20.2

region of the bulkhead. Figure 5.9 illustrates the main graphic guideline in designing a torispherical pressure vessel head. From the work presented by Megyesy (2001), the thickness of the bulkhead is computed using the following equation:

$$t = \frac{PLM}{2SE + P(M - 0.2)} \quad (5.6)$$

where  $P$  is the design pressure,  $L$  is the inside radius of the dish,  $M$  is a factor which depends on  $L/r$ ,  $S$  is the yield strength of material,  $E$  is the joint efficiency, and  $r$  is the knuckle radius. The joint efficiency defines the loss in mechanical properties of the material due to welding. A thickness of 4 mm was determined with a safety factor of 3 over the operating chamber pressure of 40 bars.

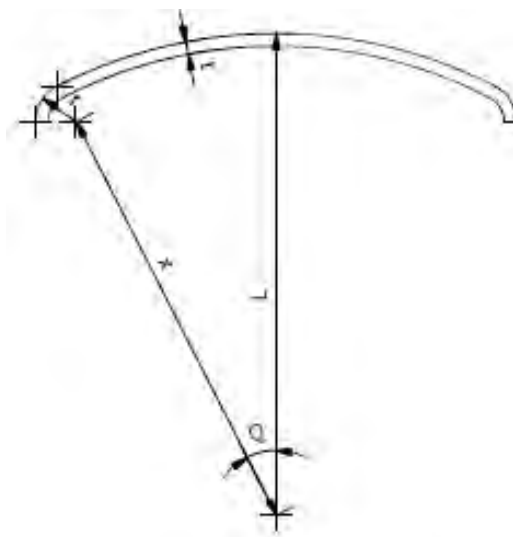


Figure 5.9 Torispherical head design guideline.

A finite element analysis was conducted on the injector bulkhead with the bolts' connections fully constrained. The post-processing of the von Mises stress distribution in the bulkhead is shown in Fig 5.10. The results show an adequate safety factor of 3.5 over the yield strength for the applied internal pressure loading of 40 bars. It is noted that stress concentrations occur around the knuckle radius. The injector bulkhead, shown in Fig. 5.11, was CNC machined from a 180 mm solid billet. The outer geometry was shaped to reduce its mass. Following the CNC machining, the igniter and pressure transducer housings were welded at their allocated positions.

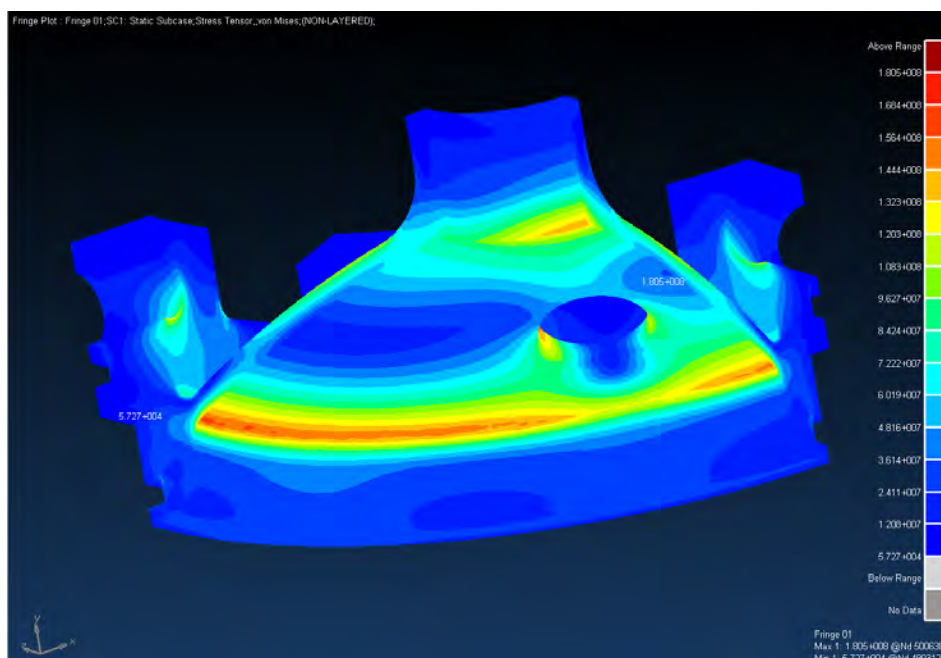


Figure 5.10 FEA von Mises stress distributions in injector bulkhead.



Figure 5.11 PV-1 motor injector bulkhead.

### 5.3.3 Nozzle

A nozzle area ratio of 5.99 with an optimum flow expansion at 1000 m altitude was determined to maximize the Phoenix-1A's apogee. The nozzle convergent-divergent contour was designed using the HPRC Motor Design application. The output spreadsheet of the modelling is attached in Appendix H.2. In particular, a bell-shaped nozzle was adopted for the PV-1 motor to improve flow performance. The geometry coordinates from the spreadsheet were imported into CAD to complete the external shape of the nozzle. The nozzle was essentially shaped to minimise its weight without compromising its structural strength. ATJ graphite was selected as the complete nozzle material due to its common use in hybrid rocket motors, and because of its low cost. However, ATJ graphite mechanical properties, shown in Table 5.4, are relatively lower than other common materials used in rocket nozzle design. The shear strength noted in Table 5.4 is approximated as 60% of the tensile strength value.

Table 5.4 Mechanical properties of ATJ graphite.

<b>Density</b>	$\rho_{ATJ}$	<b>kg/m<sup>3</sup></b>	1760
<b>Yield Strength</b>	$\sigma_{y,ATJ}$	<b>MPa</b>	-
<b>Shear Strength</b>	$\sigma_{s,ATJ}$	<b>MPa</b>	16.299
<b>Tensile Strength</b>	$\sigma_{t,ATJ}$	<b>MPa</b>	27.165
<b>Compressive Strength</b>	$\sigma_{c,ATJ}$	<b>MPa</b>	66.4
<b>Flexural Strength</b>	$\sigma_{f,ATJ}$	<b>MPa</b>	31.03
<b>Young's Modulus</b>	$E_{ATJ}$	<b>GPa</b>	9.7
<b>Coefficient of Thermal Expansion</b>	$\alpha_{ATJ}$	<b>10<sup>-6</sup>/°C</b>	2.2
<b>Thermal Conductivity</b>	$\kappa_{ATJ}$	<b>W/(m.°C)</b>	125

The pressure and thermal loading on the bell-shaped nozzle and equivalent stress distribution was investigated by conducting a fluid structure interaction (FSI) analysis. A computational fluid dynamic package, StarCCM+, was used for the analysis as it can simulate the coupling and interaction between solid and fluid bodies. NASA-CEA was run to obtain the inlet boundary condition assuming complete combustion of the propellants. The simulation was performed for the optimum flow expansion of the nozzle, that is, at its third critical point. The inputs of NASA-CEA were a mixture ratio of 6, the optimal nozzle expansion ratio, the propellants' properties, and a frozen flow condition. The computed combustion temperature together with the chamber pressure was applied at the inlet boundary. The atmospheric properties at a 1000 m altitude were applied at the outlet boundary. The working fluid is

modelled as air with properties altered to simulate the exhaust gas mixture. A fluid-solid interface boundary was defined at the nozzle internal wall. The nozzle was constrained in the axial direction on its rearward facing surface which is in contact with the nozzle retainer. Figure 5.12 shows the equivalent stress distributions in the bell-shaped nozzle due to both thermal and pressure loading conditions. The figure indicates that the highest stresses (which appear to exceed the material's strength) occur in a very localised circumferential region at the outer surface of the nozzle. Refining the mesh density showed that the stress region became even more localised. This stress concentration may have been induced by the simplified fully-rigid constraint which could have led to excessive radial restriction of the nozzle. In addition, it was noted that the temperature distribution through the nozzle's wall remained within acceptable limits during the relatively short firing period. Although the results appear to indicate that the nozzle would be over-stressed, the laboratory-scale motor, described in Chapter 6, showed very similar FSI results with no subsequent failure during the hot-fire tests. The machined PV-1 graphite nozzle is shown in Fig. 5.13.

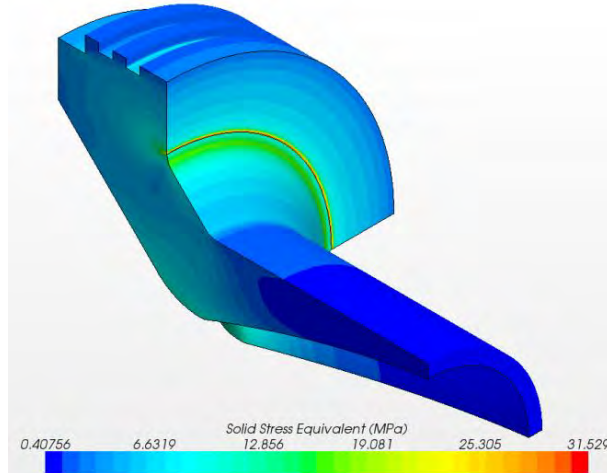


Figure 5.12 Equivalent stress distributions in bell-shaped nozzle.



Figure 5.13 PV-1 graphite nozzle.

### 5.3.4 Nozzle Retainer

The purpose of a retainer is to encase and protect the brittle nozzle material. In addition, it transfers the force generated by the nozzle to the chamber casing which is connected to the vehicle structure. Due to the high forces involved in this interaction, the nozzle retainer was developed from the same high strength stainless steel material as the injector bulkhead. Table 5.3 shows its physical and mechanical properties. The inner geometry of the material duplicates the outer nozzle contour to provide a seamless match. However, a clearance was implemented between the nozzle and retainer as illustrated in Fig. 5.14. This clearance allows for free thermal expansion that the nozzle experiences in its divergent contour, hence reducing the stress concentration at the fillets.

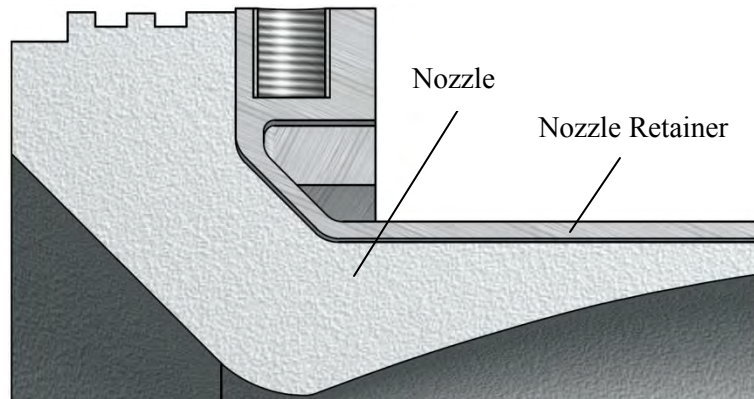


Figure 5.14 Clearance between nozzle and its retainer.

A liner static stress analysis was carried out on a quarter geometry of the nozzle retainer to verify its structural integrity. The circumferential holes were constrained in all directions and a mesh size of 2 mm was used. The isotropic material was analysed under the worst case loading condition, that is, in the event of nozzle throat blockage by a lump of the fuel grain. For this worst case scenario, a uniform force was applied to the vertical and diagonal surfaces of the nozzle retainer. The force was calculated for a 40 bar chamber pressure and the projected area of both surfaces. Figure 5.15 shows the localised maximum stress concentrations (von Mises) in the nozzle retainer. The design has a safety factor of 2.1 over the yield strength for a 40 bar chamber pressure, and considering a maximum von Mises stress of 313.5 MPa. Like the injector bulkhead, the nozzle retainer was CNC machined from the same solid billet. The maximum material was removed according to the design to minimise its structural mass. Figure 5.16 shows the final product of the nozzle retainer.

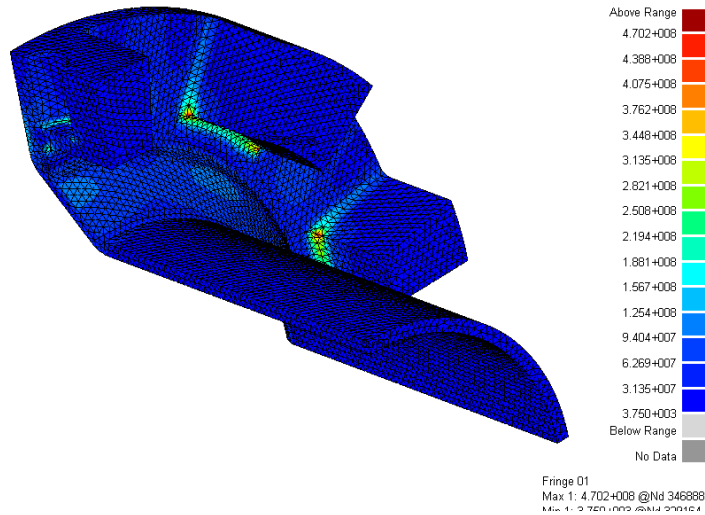


Figure 5.15 FEA von Mises stress distributions in nozzle retainer.



Figure 5.16 PV-1 nozzle retainer.

### 5.3.5 Feed System and Injector

Chemical rockets involving liquid propellants need specially designed injectors to ensure proper atomisation and mixing of the propellants for efficient and stable combustion. In the case of liquid chemical rockets, the purpose of the injector is to simultaneously deliver, atomise, and mix the oxidiser and fuel, both in liquid phase, in the combustion chamber. In classical hybrid chemical rockets, the oxidiser is atomised as it passes through the injector and mixing is effectively achieved as the solid fuel

evaporates. To an extent, research on liquid motors' injector designs exceeds hybrid motors and is well documented. However, the same principle is used to develop hybrid motor injector configurations.

The typical configurations of injectors employed in hybrid motor systems are: 1) axial/straight showerhead, 2) impinging, 3) and swirl flow patterns. The axial/straight showerhead delivers the oxidiser flow in an axial direction with no change in the flow pattern angle. It is the simplest design and easily manufactured. Conversely, it does not provide an effective regression rate for a considerably large fuel grain port. The burning rate tends to be higher at the aft end of the grain. In the impinging injector configuration, the flow pattern is orientated towards the inner grain surface, depending on the angles of the orifices, aiming to provide a uniform oxidiser flow through the port. Swirl injectors are the most efficient with regard to uniform oxidiser flow distribution through the port and increase in regression rate, as the residence time of the oxidiser increases enabling efficient combustion.

Two injector configurations were considered and designed for the PV-1 motor: 1) an axial/straight showerhead, and 2) an impinging flow pattern. Both configurations consist of 17 orifices with 2 mm diameter; the design methodology is discussed below. For the impinging injector, the outer orifices were orientated at an angle of 20° in addition to the 5 axial orifices. The angular orifices impinge the oxidiser flow on the inside of the cylindrical fuel grain port. The number of orifices was determined from the conventional discharge equation of an incompressible fluid for an average oxidiser mass flow rate of 1.5 kg/s, an average oxidiser density of 822.82 kg/m<sup>3</sup>, system pressure drop of 20%, orifice diameter of 2 mm, and a discharged coefficient of 0.8:

$$N_{inj} = \frac{\dot{m}_{ox}}{C_d A_{inj} \sqrt{2\rho_{ox} \Delta P}} \quad (5.7)$$

where  $C_d$  is the dimensionless discharge coefficient,  $A_{inj}$  is the cross-sectional area of the orifice,  $N_{inj}$  is the number of orifices,  $\rho_{ox}$  is the oxidiser density,  $\dot{m}_{ox}$  is the oxidiser mass flow rate, and  $\Delta P$  is the system pressure drop. The sectional views of PV-1 motor's injector configurations are shown in Fig. 5.17.



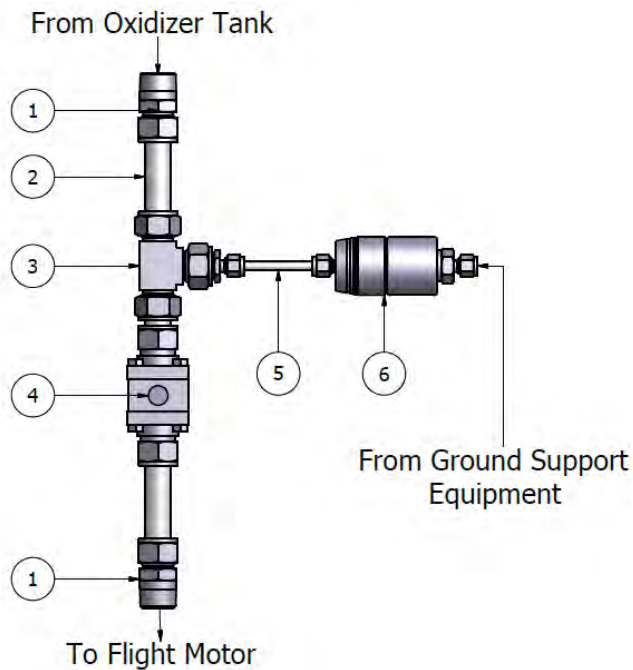
Figure 5.17 Sectional views of PV-1 motor injectors: (a) Axial/straight showerhead, and (b) Impinging.

The injector and its manifold are machined from grade 316 stainless steel material. The injector manifold is screwed into the bulkhead and is connected to the feed system. The two injector configurations are displayed in Fig. 5.18.



Figure 5.18 PV-1 motor injectors: (a) Axial/straight showerhead, and (b) Impinging.

The dual purpose Phoenix-1A feed system, shown in Figure 5.19, offers the capability to fill the oxidiser tank and deliver oxidiser flow to the combustion chamber using the same system. This eliminates the need for a second system connected to the tank for the filling procedure.



- 1) Oxidiser Tank and Injector Manifold Fittings, 2) 1/2 in Primary Line, 3) Tee Union Fitting, 4) 1/2 in Ball Valve,
- 5) 1/4 in Filling Line, 6) Bidirectional Flow Quick Connect Valve

Figure 5.19 Feed system schematic (Pitot de la Beaujardiere et al., 2011).

During filling, a bidirectional quick connect valve directs the nitrous oxide and helium supercharge gas from the ground support equipment to the oxidiser tank as the 1/2 inch ball valve is closed. In case of emergency during hot-fire tests and prior to launch missions, the bidirectional quick connect valve is used to vent the oxidiser tank. The main delivery line consists of 1/2 inch straight tubing and a ball valve to minimise losses in the pipe. An estimated total pressure drop of 6.5 bars was calculated in the feed system for the targeted oxidiser mass flow rate of the PV-1 motor. A servo-motor actuates the opening and closing of the 1/2 inch ball valve which is controlled by an onboard programmable micro-controller. The overall system is fully automated and controlled by a LabVIEW application. The feed system was assembled from Swagelok parts. Figure 5.20 shows the inter-stage section where the feed system is lodged between the oxidiser tank and combustion chamber.

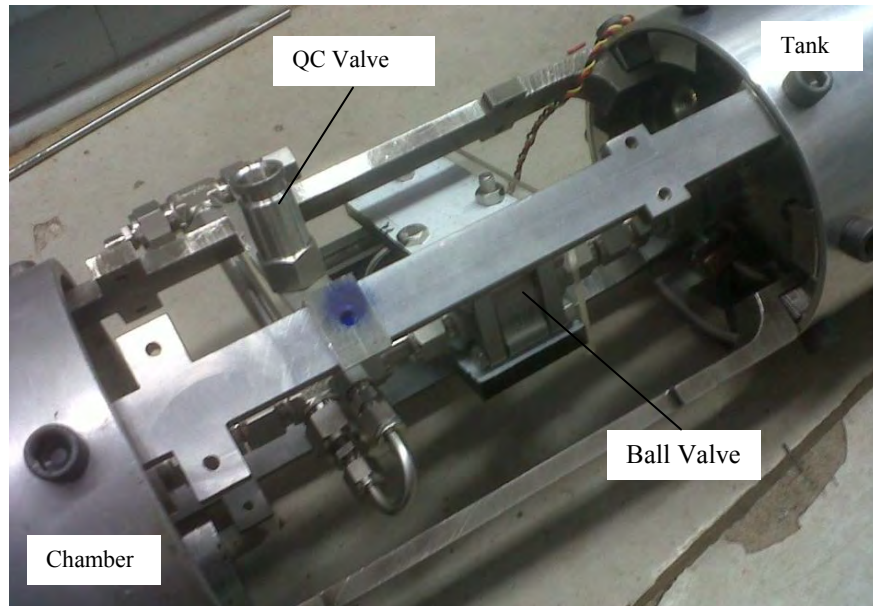


Figure 5.20 Feed system assembly.

## 5.4 Fuel Grain Cartridge Development

### 5.4.1 Fuel Grain

The fuel grain cartridge consists of the paraffin wax fuel core and the pre- and post-combustion inserts which are surrounded by a protective thermal liner, reducing the heat transfer to the casing's wall. As previously mentioned, the thermal liner is fabricated from layers of glass/cotton phenolic composite, targeting an overall 6 mm wall-thickness to produce a transition fit within the chamber casing. The pre-

and post-combustion inserts are machined out of a 160 mm solid rod of polyethylene to a length and thickness of 60 mm by 10 mm and 90 mm by 15 mm, respectively.

Fabricating a uniform solidified grain is critical as it experiences severe pressure and temperature loading conditions during combustion. Any cracks can potentially result in an undesired grain structural failure. Due to its physicochemical properties, liquefied paraffin wax tends to form internal voids, and shrinks as it solidifies. These two casting flaws can lead to catastrophic failure of the motor. The shrinkage was reported to be in the region of 15 to 25% (DeSain et al., 2009). Spin casting is the typical fabrication method widely used to cast paraffin wax grains. In this technique, molten wax sealed in a cylindrical container is spun about the desired port axis. The molten fluid is forced outwards by the centrifugal force, and is solidified as the system cools down. A novel casting method developed during the Phoenix Hybrid Sounding Programme by Smyth et al. (2010) was employed to manufacture the PV-1 motor's fuel grain. The casting technique utilises a circular mould consisting of a central mandrel and a spring-loaded piston mechanism which applies uniform pressure onto the molten paraffin wax during solidification. The system is completely sealed to prevent leakage of molten paraffin wax around the mandrel and piston. As the mould consists of a removable lower end, the solid grain is easily pushed out from the top end. This casting technique, if well applied, minimises void-formation as air is removed from the mould prior to compression of the wax against the walls of the mould by the piston.

The PV-1 motor utilises a black pigmented grain to minimise sloughing effects as discussed in Chapter 2. This prevents the high combustion temperature from radiating through the exposed inner surface layer. Two types of black pigments were investigated: charcoal and carbon black. Charcoal was selected for the fuel grain development due to its consistency in producing a uniform black-pigmented grain. The final design of the PV-1 motor's fuel grain comprises four equal size segments of SASOL 0907 paraffin wax mixed with charcoal additive; each segment contains a weight composition of 97% paraffin wax and 3% charcoal.

The fabrication process of a 100 mm paraffin wax grain segment, equivalent to a mass of 1.6 kg, is outlined below. The end goal was to produce four grain segments which were bonded together with the pre- and post-combustion chamber inserts. Figures 5.21 (a) to (g) illustrates the major steps of the procedure.

1. 2.25 kg of paraffin wax pellets were poured in a container, followed by 0.0675 kg of ground and filtered fine grain charcoal. The mixture was stirred thoroughly and placed into an oven set at

130°C, which is above the melting point of SASOL-0907 paraffin wax as shown in Table 2.3. For this quantity, it usually takes 6-7 hours to completely liquefy the wax. Figures 5.21 (a) and (b) show the phase transition for pure paraffin wax, that is, without additives (Smyth et al., 2010).

2. The mixture was stirred thoroughly every 2 hours to provide a uniform fluid composition.
3. While the paraffin wax/charcoal mixture was melting, the mould components were placed into a second oven set at approximately 110°C but not higher than 130°C.
4. After 3 hours, the components of the mould were taken out of the oven, and thoroughly cleaned of any residual wax from the previous casting process. The mandrel, base plate, and casing were assembled, and O-rings placed into the grooves of the piston. All the components were put back into the same oven until the wax was liquefied.
5. Once the paraffin wax was melted, the mixture was poured into the mould and stirred before the piston was pressed into position until liquefied paraffin wax emerged from the two opened bleed holes on the piston. Two cap screws were used to close the bleed holes. The spring-loaded mechanism was placed into position so that the spring constantly compressed against the piston as depicted in Fig. 5.21 (c). A thermal insulation material was wrapped around the mould assembly, shown in Fig. 5.21 (d), to provide a gradual cooling process. The mould was left to cool for 12-18 hours.
6. After the cooling period, the mould was disassembled and the solid grain segment carefully pressed out of the casing. The segment, shown in Fig. 5.21 (e), was machined down to the desired length on a lathe for accuracy. Figure 5.21 (f) displays the final product of one grain segment.
7. The process was repeated to produce three other segments with identical dimensions. The four segments were bonded and compressed together with the pre- and post-combustion chamber inserts. The total length of the grain is shown in Fig. 5.21 (g).



(a)



(b)

Figure 5.21 Fuel grain manufacture.



(c)



(d)



(e)



(f)



(g)

Figure 5.21 Fuel grain manufacture.

A typical shrinkage level during solidification can be noticed in Fig. 5.22 (a). This shows the effectiveness of the spring-loaded mechanism in keeping the molten mixture under compression. One advantage of the casting method is that the shrinkage percentage of the paraffin wax can be easily quantified. Figure 5.22 (b) shows an example of void formation at the top of a grain sample. This resulted from wrongly positioning the spring mechanism.



Figure 5.22 Inherent characteristics of paraffin wax: (a) Shrinkage level, and (b) Void formation.

#### 5.4.2 Thermal Liner

The duty of a thermal insulation liner is to protect a chamber casing wall from an excessively high combustion temperature. An ablative composite material is the most suitable candidate as it pyrolyzes layer-by-layer when heat is applied to its surface, absorbing the thermal energy. Due to the web thickness of the grain, the thermal liner does not experience direct contact with the flame except at the end of the burn.

The PV-1 motor thermal liner is fabricated from layers of glass fibre and cotton composite. The inner layers of glass fibre add mechanical strength to the grain, and the outer layers of cotton material complete the required thermal liner wall thickness. The materials are bonded by phenolic resin due to its ablative properties and good thermal resistance. A catalyst ratio of 8% is added to resin for the curing process. Following the method developed by Smyth et al (2010), the glass/cotton/phenolic composite material is laid directly onto the fuel grain. A fabricated lay-up frame, shown in Fig. 5.23 (a), accommodates the fuel grain and a PVC pipe. The PVC pipe is used as a delivery spool for the glass and cotton materials. Tensioning of the materials is achieved by turning the grain and PVC pipe in opposite directions. The thermal liner of PV-1 motor was manufactured as follows:

1. 10 layers of glass fibre and 15 layers of cotton material were cut into pieces of 1000 mm by 600 mm.
2. The cotton layers were rolled into the PVC, followed by the glass fibre as shown in Fig. 5.23 (a).
3. A cup of phenolic resin mixture was prepared with the already mentioned specification. A typical cup provides a working time of 20 minutes before hardening.
4. The resin was applied onto the fuel grain prior to the first glass fibre lay-up.
5. The layers of glass fibre were applied with the resin mixture onto the grain, followed by the cotton layers, illustrated in Fig. 5.23 (b). New phenolic resin mixtures were prepared throughout the lay-up process.
6. Figure 5.23 (c) shows the initial colour of the thermal liner after the lay-up was done.
7. The product was left to cure unheated for 24 hours, displayed in Fig. 5.23 (d). Thereafter, it was placed in an oven for 18 hours set at a temperature of 30°C. This minimises grain deformation.
8. After the curing process, the thermal liner was trimmed at the ends and machined down to the required diameter, shown in Fig. 5.23 (e).
9. The support inserts at the ends were removed.
10. Figure 5.23 (f) shows the final product of the manufactured fuel grain cartridge.

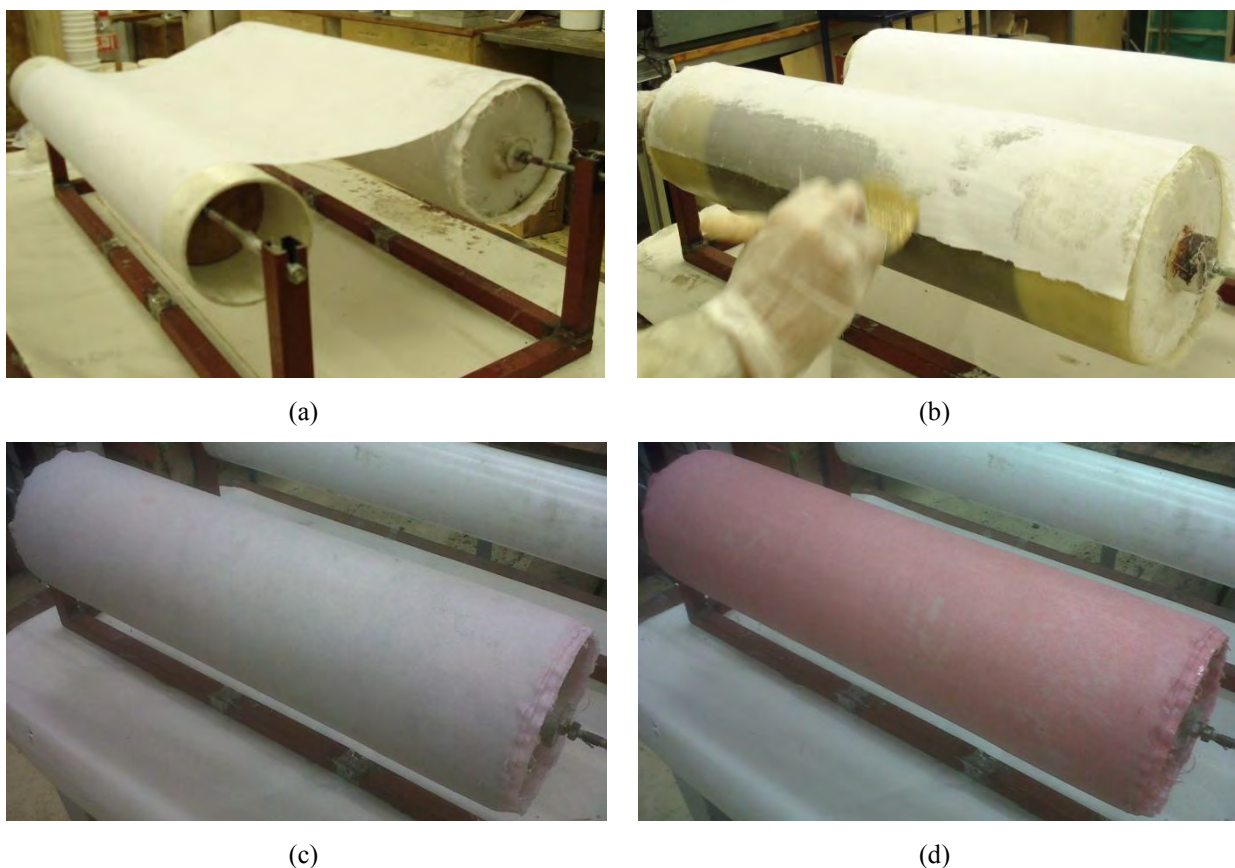
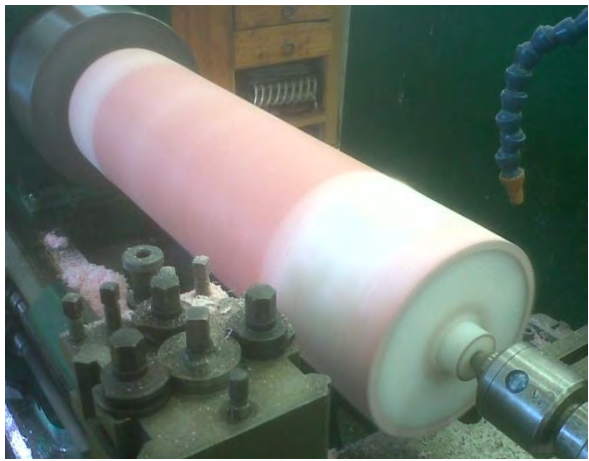


Figure 5.23 Development of the complete fuel grain cartridge.



(e)



(f)

Figure 5.23 Development of the complete fuel grain cartridge.

## CHAPTER 6

### PL-1 and PV-1 Static Motor Tests

#### 6.1 PL-1 Laboratory-Scale Motor

Prior to the development of the PV-1 flight motor, a laboratory scale motor was designed, manufactured, and tested to study the combustion characteristics and motor performance of a paraffin wax/nitrous oxide propellant combination. This feasibility study formed the foundation of the Phoenix Hybrid Sounding Rocket Programme. The phase involved the development of a scaled down version of the PV-1 flight motor, called the PL-1 lab-scale motor, together with a test facility. These tasks were performed by undergraduate project teams (Smyth et al., 2010 and Reddy et al., 2010) under the co-supervision of the author. The assembled test rig, shown in Fig. 6.1, incorporates the lab-scale motor, load cell, oxidiser delivery system and control sub-systems on a movable test stand.

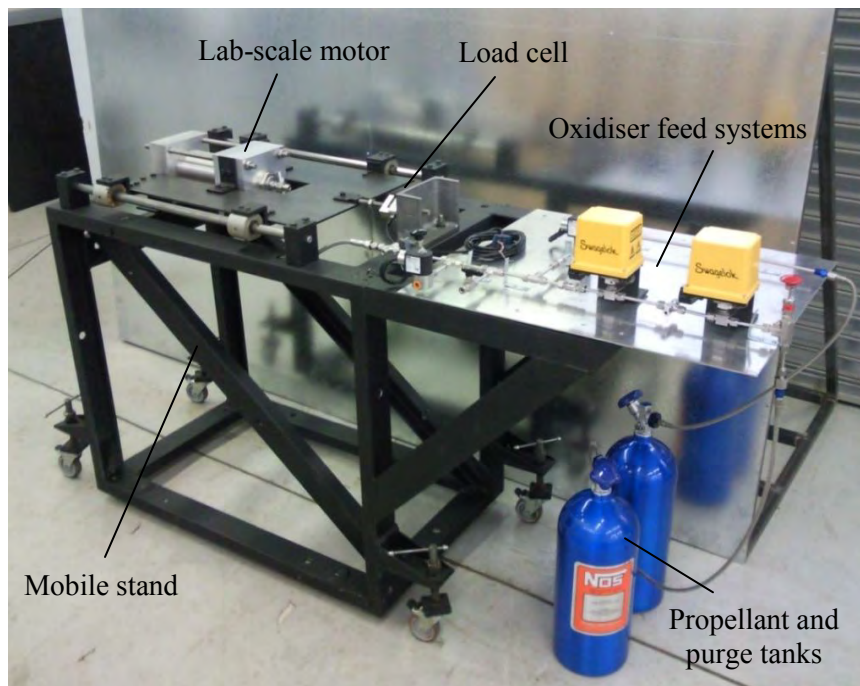


Figure 6.1 UKZN hybrid rocket motor test cell (Geneviève et al., 2011).

The PL-1 lab-scale motor was primarily manufactured from 6061-T6 aluminium and 316L grade stainless steel. The motor consists of an expandable fuel grain cartridge, graphite nozzle, interchangeable injector

configurations, and two aluminium blocks held together by means of four high strength steel rods. For safety considerations, the chamber casing wall-thickness was designed with a safety factor of 10. In addition, the motor was designed to fail at the four rods to mitigate the risk of a catastrophic failure of the chamber casing. In the former event, a purposely fabricated blast shield is placed at the rear end of the test rig to absorb the kinetic energy of the nozzle block.

The oxidiser feed system delivers the preloaded nitrous oxide propellant to the combustion chamber through a 1/4 inch pipe. A series of pressure transducers, thermocouples, actuated ball valves, and solenoid valves were installed in the system to measure and control the delivery of the nitrous oxide and the nitrogen purge gas. For safety considerations, check and relief valves were introduced in the system. The system is operated and controlled remotely through a National Instruments CompactRIO DAQ box with a pre-programmed LabVIEW application. This application fires the igniter and actuates the valves for a set of predefined parameters. However, the LabVIEW application has full control in case of emergency shutdown scenarios. A scale measures the rate of change of the tank mass which is captured by the data acquisition for post-analysis of the oxidiser mass flow rate.

Unlike the PV-1 flight motor, the PL-1 lab-scale motor utilises pure SASOL 0907 paraffin wax. The PL-1 motor has a theoretical average thrust five times lower than its flight scale version. The difference in fuel grain cartridge scale is shown in Fig. 6.2. The design specifications of the PL-1 motor are provided in Table 6.1.



Figure 6.2 PL-1 (top) and PV-1 (bottom) fuel grain cartridges.

Table 6.1 PL-1 lab-scale motor specifications.

<b>Oxidiser</b>	<b>Propellant</b> <b>Supercharge Gas</b> <b>Mass Flow Rate</b>	<b>kg/s</b>	Nitrous Oxide Helium 0.3
<b>Fuel</b>	<b>Propellant</b> <b>Composition</b> <b>Grain Configuration</b> <b>Number of Ports</b> <b>Initial Port Diameter</b> <b>Grain Diameter</b> <b>Grain Length</b>		SASOL 0907 Paraffin Wax 100% Wax Cylindrical 1 m 0.032 m 0.064 m 0.16
<b>Nozzle</b>	<b>Material</b> <b>Shape</b> <b>Expansion Ratio</b> <b>Throat Diameter</b> <b>Exit Diameter</b>		Graphite Conical-Shaped 5.56 m 0.0131 m 0.0309
<b>Theoretical Performance</b>	<b>Thrust</b> <b>Chamber Pressure</b> <b>Burn Time</b>	<b>N</b> <b>bar</b> <b>s</b>	800 40 7

## 6.2 Phoenix-1A Mobile Rocket Launch Platform

A Mobile Rocket Launch Platform (MRLP) was designed and manufactured by undergraduate project teams to launch the Phoenix-1A hybrid rocket as well as to perform hot-fire tests of the PV-1 flight motor (Giovanni et al., 2011 and Gopal et al., 2011). The MRLP consists of all the required electrical and mechanical Ground Support Equipment (GSE), including a launch gantry for static and flight tests of Phoenix-1A. For mobility purposes, a custom-built trailer forms the base structure of the MRLP.

In the hot-fire test configuration, the assembled propulsion system (oxidiser tank and PV-1 motor) is secured onto the gantry by means of three steel brackets fitted around the oxidiser tank and motor. These brackets allow translation movement to measure the motor thrust by a load cell placed between the oxidiser tank and a back support bracket, shown in Fig 6.3. Stabilising arms are fitted at each corner to

raise the MRLP off the ground and provide structural stability during motor static tests. The platform was developed to withstand the PV-1 motor predicted thrust with an additional safety factor of 4. In the launch configuration, the triangular truss launch gantry is raised into position using an electrical winch attached at its base, and locked into position by a linearly translating support arm situated underneath the tower. The MRLP has a 60° to 90° launch angle range and a 7 m long rail attached to the gantry.



Figure 6.3 Mobile Rocket Launch Platform (MRLP) and a mock-up of Phoenix-1A hybrid rocket.

The ground support equipment (GSE) consists of a generator, an air compressor, the nitrous oxide and helium supply tanks, and the propellant filling system (PFS). These components and systems provide the means to control the filling procedure of the oxidiser tank. The air compressor and generator are used to operate a series of mechanical hardware placed on the MRLP. The PFS, shown in Fig. 6.4, consists of pressure transducers, thermocouples, a pressure relief valve, a positive displacement pump, a pressure regulator, solenoid valves and electrically actuated ball valves. The PFS is mostly assembled from Swagelok stainless steel pipes, valves, and fittings which are compatible with nitrous oxide propellant. The assembled system passed a high pressure test using helium gas.

For safety concerns, ground and flight tests are remotely controlled from a reasonable distance through a National Instruments CompactRIO DAQ box, situated in the control box above the PFS, with a pre-programmed LabVIEW application running on a laptop computer. All the instruments are connected to

the CompactRIO DAQ box. Nitrous oxide is delivered to the oxidiser tank by the positive displacement pump driven by the air compressor, followed by the helium gas, until the tank reaches the targeted pressure. In the case of an emergency shutdown, the LabVIEW programme has the capability to vent the oxidiser tank through the bi-directional quick connect valve safely into the atmosphere. As previously mentioned, the bi-directional quick connect valve is attached to the rocket's feed system, and is disengaged by the air driven pneumatic linear actuator activated prior to launch.

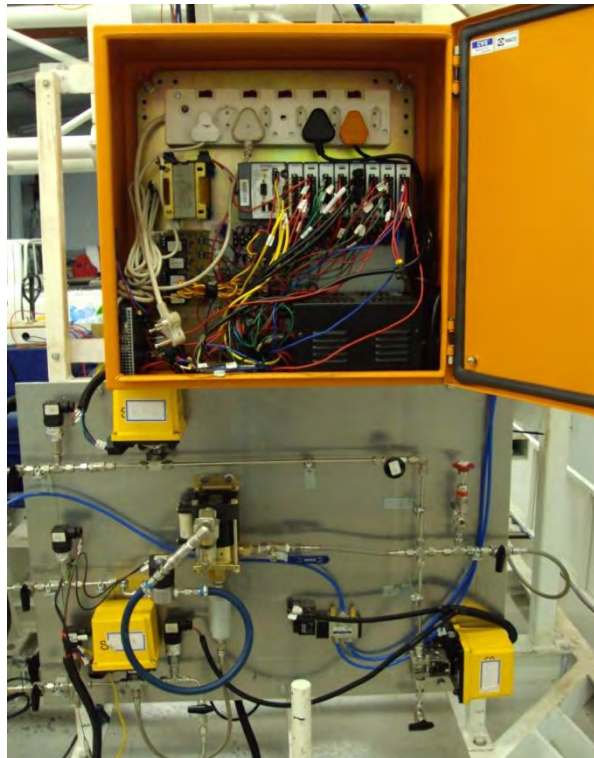


Figure 6.4 Propellant Feed System (PFS) and control box (Geneviève et al., 2012).

### 6.3 PL-1 Motor Tests and Post-Analyses

Two hot-fire tests of the laboratory-scale PL-1 motor were accomplished with all experimental data fully captured by the LabVIEW data acquisition and control system. Prior to each hot-fire test, a series of standard cold-flow tests were conducted to verify the control system, ignition firing sequence, and to characterise the oxidiser flow rate and pressure drop in the feed line. A pyrotechnic black powder mixture, discussed in the next section, provided sufficient thermal energy to ignite both hot-fire tests. The experiments, shown in Fig. 6.5 and Fig. 6.6, were performed at a secure location on the University's premises with the test-rig bolted to a concrete foundation.



Figure 6.5 PL-1 motor hot-fire test 1.

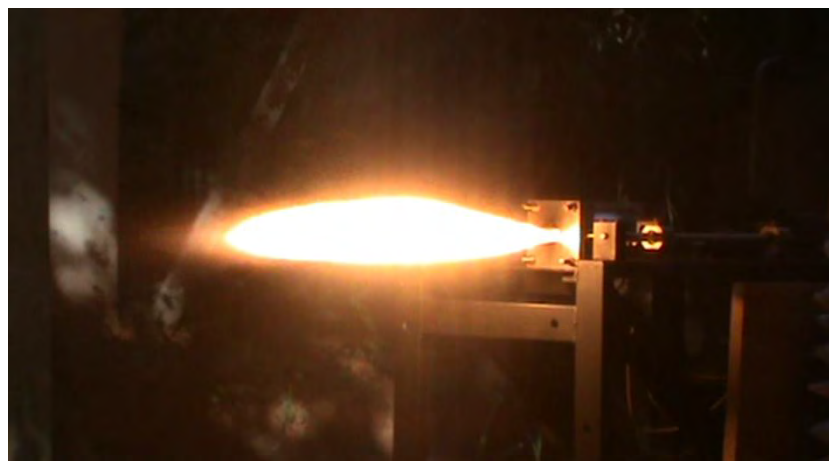
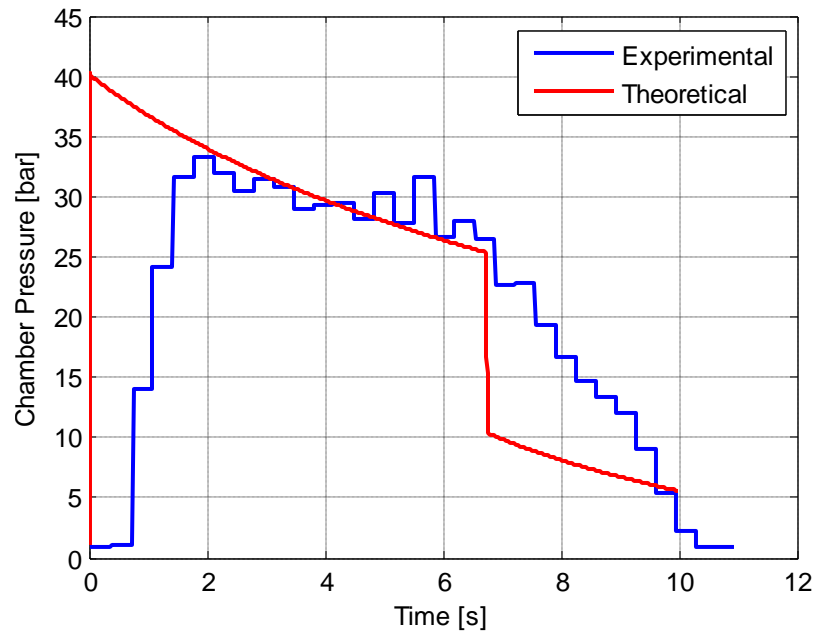
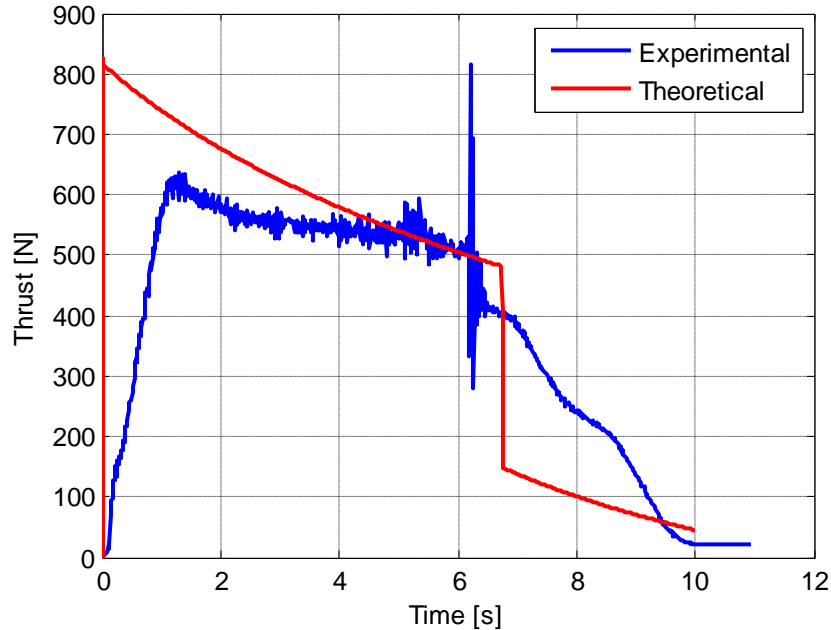


Figure 6.6 PL-1 motor hot-fire test 2.

The PL-1 motor was designed for a chamber pressure and thrust of 40 bars and 800 N, respectively. However, a maximum chamber pressure of only 33.3 bars was achieved in hot-fire test 1 (Fig. 6.7 (a)). This was due to the excessive pressure drop in the feed system, particularly the oxidiser tank outlet orifice and the 1/4 inch line and fittings. As a result, the motor was running below its full thrust capacity, illustrated in Fig. 6.7 (b). Referring to the experimental thrust profile, Fig. 6.7 (b), the motor reached a thrust of 631 N momentarily after igniter burnout, and steady-state combustion was sustained for approximately 6.5 s until the fuel grain was depleted. Following the depletion of the fuel grain at 6.5 s, combustion was maintained, with a significant drop in thrust, between the residual liquid and gaseous nitrous oxide and the pre- and post- combustion chamber polyethylene inserts until the feed valve was closed. The measured peak thrust at approximately 6.3 s is attributed to a build-up in chamber pressure due to sloughing effects. These fuel grain fragments caused a nozzle throat blockage resulting in over-pressurisation of the chamber and, consequently increased the thrust as they were forced out of the nozzle.



(a)



(b)

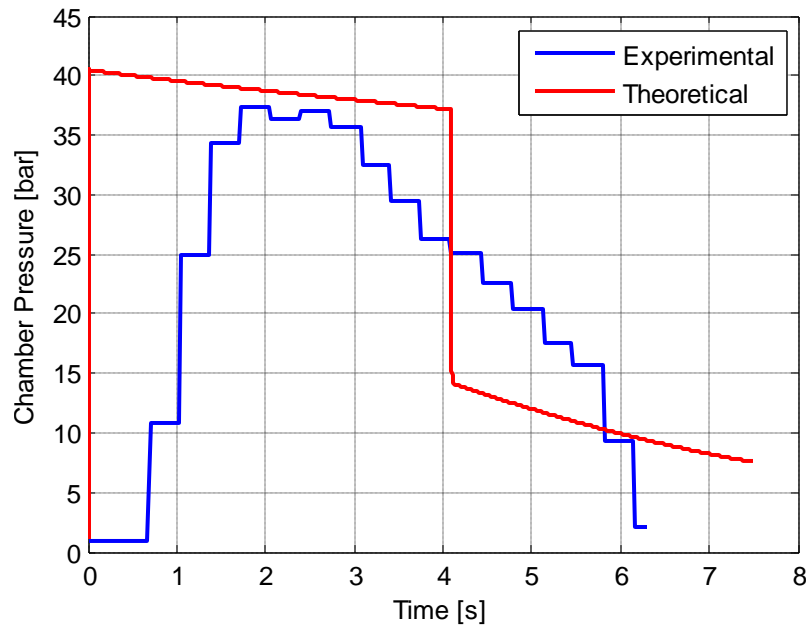
Figure 6.7 Hot-fire test 1 experimental time history and theoretical output from HRPC: (a) Chamber pressure, and (b) Thrust.

Due to the slow actuation of the oxidiser ball valve, the experimental pressure and thrust curves, Fig. 6.7, were shifted by 1.5 s where a noticeably increase in thrust was recorded. Typically, the opening and

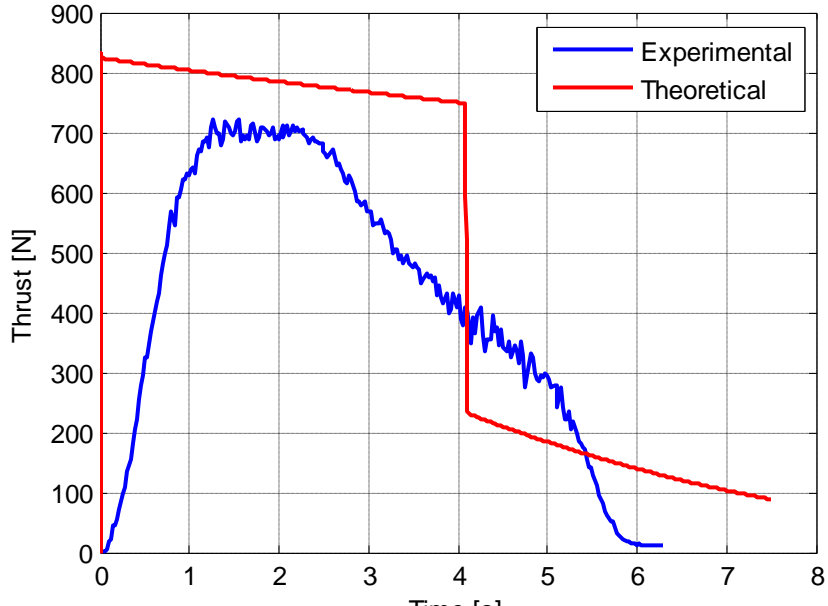
closing operational time of the oxidiser ball valve is 2.5 s. As a result, the start-up transient phase is longer, due to the low oxidiser mass flow rate. The initial difference between the experimental and theoretical thrust curves is primarily due to the discrepancies in oxidiser flow rate and chamber pressure. HRPC assumes no lag in oxidiser ball valve actuation. That is, the transient phase of the flow in the feed system is not being modelled. Consequently, the oxidiser flow rate is higher due to the pressure difference between the tank and chamber/atmospheric. Moreover, HRPC does not model the vaporisation lags of the oxidiser and the spreading of the combustion boundary layer. For these reasons, the theoretical curves initially peak above the experimental data. The sudden decrease in theoretical chamber pressure and thrust curves, which occurs at 6.74 s, corresponds to the consumption of the liquid nitrous oxide.

During the data logging, a problem was experienced with the sampling rate of the chamber pressure. There was a delay between reading and recording the chamber pressure. This was noted during the start-up transient phase (below 0.75 s) where the thrust increased significantly without any corresponding increase in chamber pressure. Consequently, the measured chamber pressure affected the post-analysis of the hot-fire test. The data reduction for determining the ballistic regression rate coefficients was unfeasible due to the complete consumption of the fuel grain and the slow oxidiser ball valve operation. However, the PL-1 motor experimental specific impulse, characteristic velocity, and thrust coefficient were estimated using the ballistic coefficients,  $a = 0.155 \times 10^{-3}$  and  $n = 0.5$ , and an average oxidiser mass flow rate at the steady-state combustion, between 3 and 4 s. The experimental motor performances were: 1) specific impulse of 192.88 s, 2) characteristic velocity of 1437.13 m/s, and 3) thrust coefficient of 1.317. The theoretical motor performances obtained from HRPC were: 1) specific impulse of 233.88 s, 2) characteristic velocity of 1601.62 m/s, and 3) thrust coefficient of 1.433. Therefore, for the mentioned steady-state period, the combustion efficiency was estimated as 89.7% using Equation 3.40.

Following the full consumption of the fuel grain in test 1, hot-fire test 2 was intended to be run for a shorter time to be able to determine the ballistic regression rate coefficients. For test 2, the feed system was replaced with a 3/8 inch line and fittings to minimise the pressure drop. Additionally, the loaded nitrous oxide mass was lower than in test 1. The test sequence was as follows: 1) open the ball at  $t = 0$  s, 2) igniter firing at 0.5 s, and 3) close the ball valve at 4.75 s. Figures 6.8 (a) and (b) reproduced the experimental and theoretical chamber pressures and thrust curves for the hot-fire test 2.



(a)



(b)

Figure 6.8 Hot-fire test 2 experimental time history and theoretical output from HRPC: (a) Chamber pressure, and (b) Thrust.

Like the hot-fire test 1, the experimental graphs were shifted by 0.96 s to alleviate the slow response of the ball valve. Referring to Figures 6.8 (a) and (b), the ball valve was fully opened at 1.54 s and started closing at 3.78 s. At steady-state operation, between 1.4 and 2.4 s, the average chamber pressure and

thrust were 36 bars and 700 N, respectively. This average chamber pressure is still below the design condition of 40 bars. Consequently, a lower thrust was produced. From the graphs, it can be noted that the chamber pressure and thrust decayed rapidly after approximately 2.4 s. It is believed that this corresponds to the consumption of liquid nitrous oxide before the valve closing operation at 3.78 s. HRPC underestimated the oxidiser flow rate as the theoretical consumption of liquid nitrous oxide occurred at 4.1 s. This is likely due to the uniform injector discharge coefficient implemented in the code and/or due to the over estimation of the pressure drop in the feed system.

As mentioned, hot-fire test 2 was intended to characterise the regression rate property of the fuel grain. However, due to the slow actuation of the ball valve, which was fully closed at 7.25 s, the fuel grain was almost completely consumed and data reduction could not be performed. Figure 6.9 shows the post-burning of the fuel grain cartridge.



Figure 6.9 Post analysis of test 2 fuel grain cartridge.

Using the same process as the post-analysis of hot-fire test 1, the specific impulse, characteristic velocity, and thrust coefficient of test 2 were estimated at the steady-state operation, between 1.4 and 2.4 s. The experimental motor performances were: 1) a specific impulse of 228.2 s, 2) a characteristic velocity of 1553.83 m/s, and 3) a thrust coefficient of 1.419. The theoretical motor performances obtained from HRPC were: 1) a specific impulse of 224.34 s, 2) a characteristic velocity of 1527.48 m/s, and 3) a thrust coefficient of 1.419. Therefore, for the mentioned steady-state period, the combustion efficiency was estimated as 92.2% using Equation 3.32. The improvement in motor performance correlated with the increase in average chamber pressure. Therefore, the PL-1 motor in test 2 was operating closer to its design conditions.

## 6.4 PV-1 Motor Tests and Post-Analyses

### 6.4.1 Igniter and Cold Flow Tests

Combustion is initiated through a complex chemical reaction between the dissociation of liquid nitrous oxide and the sublimation of solid paraffin wax. Due to the unknown energy required for this reaction to occur, different types of igniters were developed and tested throughout the Phoenix programme. With the successful ignition of the two lab-scale motor static tests, it was decided to utilise the same pyrotechnic ignition technique for the PV-1 motor.

To date, three types of pyrotechnic igniters have been developed and investigated with the collaboration of a pyrotechnician. Igniters A and B consist of a pyrotechnic mixture with black powder and titanium powder as the main constituents. Igniter A, used for the PL-1 lab-scale motor initiation, burns rapidly with a spark-based appearance as depicted in Fig 6.10 (a). Typically, a 1 g of pyrotechnic mixture A is consumed within 1 s. To increase the burning phase, charcoal additives were mixed with the main constituents to produce Igniter B. The burn time of pyrotechnic mixture B, shown in Fig. 6.10 (b), is effectively increased up to 3 s for the same amount of powder. However, the range of the sparks is reduced. The third type of ignition system, Igniter C, was developed from a commercial hand-held sparkler firework. A set of sparkler fireworks was modified to be fitted into the igniter housings. Depending on the amount, Igniter C burns much longer than the other pyrotechnic igniters. Moreover, it burns with a flame which facilitates the fuel-grain melting process. The flame produced by Igniter C can be visualised in Fig. 6.10 (c). All three types of pyrotechnic igniters are initiated by a Nichrome bridge wire connected to a power supply through the LabVIEW application. Upon triggering, the Nichrome bridge wire is heated to a high temperature that combusts the pyrotechnic composition. The PV-1 motor incorporates two igniters into the injector bulkhead for redundancy which are directed towards the solid fuel grain. These igniters were tested through the LabVIEW application to verify its functionality.

In the preparation phase of the PV-1 motor hot-fire test, a valuable cold flow test was performed to check the propellant feed system functionality, the LabVIEW programme control and data acquisition, and the ignition and oxidiser flow timing sequences. The MRLP was set in the hot-fire test configuration with the oxidiser tank secured to the gantry. To visualise the injector flow pattern, shown in Fig 6.11, the test was conducted without a complete assembled motor. That is, the injector bulkhead was the only motor component integrated into the base of the oxidiser tank. The axial showerhead injector was used for the experiment.

A mass of 5 kg of nitrous oxide was loaded into the oxidiser tank together with helium gas supercharge to raise the tank pressure up to its normal operating condition. The test was run for the total theoretical burn time of the PV-1 motor. Due to the lower loaded nitrous oxide mass, the blowdown phase of the nitrous oxide was completed within 7 s. The data was fully captured and the overall system performed correctly.



(a)



(b)



(c)

Figure 6.10 Igniter system development: (a) Igniter A, (b) Igniter B, and (c) Igniter C.

#### 6.4.2 Hot-Fire Tests

To date, three hot-fire tests of the PV-1 motor have been attempted following the cold flow experiment, with no successful propellant ignition. All of the tests were conducted on the purposely built MRLP set up in the hot-fire test configuration. The propulsion system, oxidiser tank, and PV-1 motor were secured

onto the gantry, inclined at a  $60^{\circ}$  angle. The configuration of the hot-fire tests are discussed in the following paragraphs and depicted in Table 6.2.

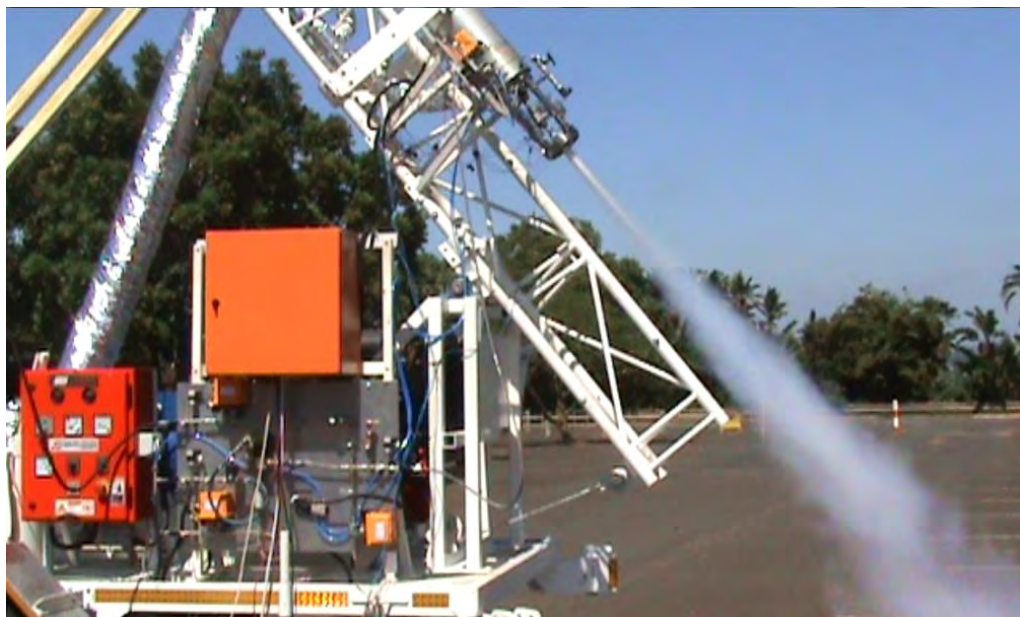


Figure 6.11 PV-1 motor cold flow test (Geneviève et al., 2012).

The hot-fire test 1 motor consisted of the axial showerhead injector and pyrotechnic mixture A. Two problems were encountered during the experiment. First, the feed system ball valve on the rocket was not fully closed, and consequently caused nitrous oxide to leak through the combustion chamber during the filling phase. The ball valve, controlled by the servo-motor, was correctly repositioned and the filling process was continued without any leaks. Second, a nitrous oxide mass of approximately 20 kg was loaded into the flight tank. Once the firing command was given, the igniters fired at the correct time sequence, however the feed system ball valve failed to open due to an incorrect setting of the manual override system. The failure was partly attributed to human error.

The hot-fire test 2 motor was set up as in test 1 with the axial showerhead injector and Igniter A located on the injector bulkhead. Likewise, the flight tank was loaded with approximately 20 kg of nitrous oxide followed by the helium supercharge. No leaks were encountered during the filling phase. Following the firing command, the feed system ball valve actuated correctly but the pyrotechnic mixture A failed to ignite the propellants. The failure was attributed to igniter quenching due to the strong flow of nitrous oxide.

Following the two failed attempts, the PV-1 motor was reconfigured by changing the injector and ignition system. The hot-fire test 3 motor utilised an impinging flow pattern injector and pyrotechnic mixture B. In addition, it was deemed that the nitrous oxide flow had to be decreased to eliminate the risk of igniter quenching. The servo-motor was pre-programmed to initially decrease the flow rate to 25% and hold the position for 1s. A loaded nitrous oxide mass of 25 kg was measured. The motor failed to ignite with these changes incorporated in the motor. Figure 6.12 shows the motor test 3 attempt where nitrous oxide is expelled out of the motor without igniting.

Table 6.2 PV-1 motor hot-fire test outcomes.

<b>Hot-Fire Test</b>	<b>Injector Configuration</b>	<b>Igniter Type</b>	<b>Servo-Motor Valve Initial Throttling</b>	<b>Notes</b>
1	Axial showerhead	A	No	Valve failed to open
2	Axial showerhead	A	No	Ignition failure
3	Impinging	B	25% throttling for 1s	Ignition failure



Figure 6.12 PV-1 motor static test 3 ignition failure.

A post-analysis of the motor test 3 fuel grain and pre-combustion chamber end showed that the paraffin wax was ineffectively melted. Figure 6.13 confirms that the igniter partly melted the top surface of the grain. Following these failures, extensive research was undertaken on the ignition sequences of hybrid

rocket motors and other feasible and reliable ignition systems. It was found that ignition failures are more common in hybrid motors than liquid and solid propulsion systems. One possible reason is due to the fact that the inert propellants are in two different phases prior to combustion. The ignition sequence of hybrid rocket motors differs from liquid and solid motors as the process depends on the timing between the pre-heating mechanism of the solid fuel and the introduction of the oxidiser into the combustion chamber. That is, the ignition source must respectively vapourise the solid fuel and decompose the liquid/gaseous oxidiser for successful motor start-up phase. Moreover, it was suggested that firing the igniters should always precede the flow of oxidiser into the combustion chamber (SPG, 2012 and Moretto, 2011). This prevents the accumulation of oxidiser in the chamber which could lead to catastrophic motor failure.



Figure 6.13 Fuel grain post analysis of static motor test 3, pre-combustion chamber end.

Consequently, Igniter C was developed to produce a substantial energetic flame capable of melting the paraffin wax. Extensive tests are currently being performed on the fuel grain samples to investigate the burn characteristics. The LabVIEW application has been re-programmed to initially fire the igniters prior to the actuation of the ball valve in order to minimize the risk of extinguishing the igniters. Future hot-fire tests will follow the HRM combustion sequence described in Chapter 2.

## CHAPTER 7

### Conclusion

The core objective of this research was to design, manufacture, and test a hybrid rocket motor with a thrust capability to propel its vehicle to a targeted apogee of 10 km. The motor is intended to power the first sounding rocket emanating from the UKZN Phoenix Hybrid Sounding Programme. Initiated in 2010, the programme's goal is to produce a series of low-to-medium altitude hybrid sounding rockets to cater for the needs of the African scientific community. The first milestone involves the development of Phoenix-1A, capable of delivering a 1 kg payload to an altitude of 10 km. This study described the developmental process of Phoenix-1A's hybrid rocket motor (PV-1), including a predictive performance model used to optimise the motor combustion characteristics. The vehicle's airframe and internal component designs are described in a parallel project.

An extensive survey of hybrid rocket propulsion was performed to determine potential propellants for the Phoenix-1A rocket propulsion system, and to characterise critical components of a typical motor. Through this process, a propellant combination of liquid nitrous oxide as the oxidiser and solid paraffin wax as the fuel was selected due to their inherent advantages described in Chapter 2. Nitrous oxide's self-pressurising behaviour in an enclosed storage compartment eliminates the incorporation of a complex turbine driven pump in the feed system, or installing an additional pressurant system. Due to the high regression rate characteristic of paraffin wax, a single port design was chosen which in turn facilitated the casting method. Medical-grade nitrous oxide was obtained from the local market and SASOL donated a substantial amount of 0907 grade paraffin wax.

The combustion process of nitrous oxide and paraffin wax was investigated to create a useful mathematical model for the design purposes of the motor. The modelling of a hybrid rocket motor can be carried out using three control volumes: 1) the oxidiser delivery system, 2) the fuel regression rate, and 3) the gas dynamic flow through the rocket nozzle. In control volume 1, nitrous oxide is delivered to the combustion chamber under its own pressure with the aid of helium gas which increases the oxidiser tank pressure. The model is based on existing work but includes additional features such as the gaseous nitrous oxide blowdown process. This self-pressurising nitrous oxide delivery system provides a more realistic description of the decay of the motor thrust than using a constant oxidiser mass flow rate. In control volume 2, which represents the combustion chamber, a semi-empirical regression rate equation was used

to define the burning rate of paraffin wax with ballistic coefficients found in the literature. These ballistic coefficients will be compared to experimental data, once available. Control volume 3 dealt with the gaseous flow of combustion products through the nozzle to produce thrust.

Following the derivation of the governing equations of these control volumes, a computational model was developed based on the described theory. The model, programmed in MATLAB, consists of two codes: 1) a preliminary motor design code (HRPC Motor Design), and 2) a predictive motor performance code (HRPC). The HRPC Motor Design application is typically useful for sizing a hybrid motor, including the fuel grain and nozzle dimensions. The HRPC application models actual instantaneous performance of the motor by solving the unknown equations of the three control volumes. In particular, a 4<sup>th</sup> order Runge Kutta numerical method was employed in HRPC to integrate the ordinary differential equations. The two codes extracted essential thermodynamic properties from the NASA-CEA equilibrium chemistry code throughout the simulation. The HRPC application was compared with experimental data obtained during hot-fire testing of the laboratory-scale PL-1 motor which utilises a nitrous oxide/paraffin wax propellant combination. Good agreement between the code and the performance curve data was obtained.

The PV-1 motor was designed through an iterative process using HRPC and HYROPS (Hybrid Rocket Performance Simulator). The HYROPS software is an integrated hybrid rocket trajectory simulation tool, developed in a parallel project and intended to predict the sub-orbital flight performance of a generic multi-stage hybrid sounding rocket. The critical dimensions of the PV-1 motor were obtained from the HRPC Motor Design at incremental altitudes. That is, the fuel grain and nozzle were designed for a set of atmospheric pressures. The range investigated was from sea-level to an altitude of 3000 m. For each design, the motor parameters were transferred to HRPC for the computation of the flow characteristics. Following the analyses in HRPC, the momentum thrust, nozzle gas exit pressure, and change in the propellants' masses were entered into HYROPS, for each design, to assess the maximum apogee of the Phoenix-1A hybrid rocket. The results show that an optimum nozzle expansion ratio at 1000 m maximises the apogee. However, despite this approach, the targeted total impulse of the motor could not be achieved within the required 20 s of the liquid nitrous oxide blowdown phase due to the rapid decay in tank pressure, and consequently chamber pressure and thrust. The maximum apogee relies on the additional thrust produced by the gaseous nitrous oxide blowdown phase. This improves the total impulse by approximately 4%, thus increasing the rocket's apogee.

The development of the PV-1 motor was focused around the outer diameter of the fuel grain as it defines burn time and, therefore, the total impulse. Finite element analyses were conducted on the combustion

chamber casing, injector bulkhead, and nozzle retainer under worst case loading conditions. All the components showed a safety factor of more than 1.5. In addition, thermal and pressure loading distributions on the motor's nozzle and its subsequent responses were estimated by conducting fluid-structure interaction analyses. The combustion chamber, manufactured from 6082-T6 aluminium alloy, was hydrostatically pressure tested to 1.5 of its working pressure. The combustion chamber maintained the pressure for 10 mins, validating its structural integrity. The injector bulkhead and nozzle retainer were manufactured from high strength 431 grade stainless steel due to the thermal loading expected at the pre- and post-combustion chamber ends. The PV-1 motor solid grain was manufactured using a novel casting technique developed during the project, as described in Chapter 5. Unlike the laboratory-scale motor, the PV-1 motor fuel grain composition is made up of 97% paraffin wax and 3% charcoal. The size of the charcoal particles determines the mass distribution in the molten paraffin wax mixture. Large particle size tends to sink and settle at the bottom of the mixture, resulting into a non-uniform grain composition. This can be visualised by the fading colour of the black grain. As a result, the charcoal additive must be ground, crushed, and filtered several times to obtain a suitably fine particle size which can then be added to the molten paraffin wax.

Subsequent to a cold flow test, three hot-fire tests of the PV-1 motor were attempted with no successful ignition. The failures were attributed mainly to the ignition system. The nitrous oxide flow quenched the pyrotechnic charge in the last two hot-fire tests. As a result, a new ignition system has been developed, and is currently being thoroughly tested. This new ignition system is composed of commercial firework material which is modified to fit into the injector bulkhead. In addition, it is believed that the ignition system must first melt the paraffin wax prior to the introduction of nitrous oxide into the combustion chamber. This requires re-programming of the LabVIEW data acquisition and control system. During the hot-fire test attempts, the filling system failed to load the oxidiser tank with the full 30 kg nitrous oxide as required and a new filling system design is presently under consideration.

Future work on the preliminary motor design and predictive motor performance codes is required for a more generic hybrid rocket motor modelling. Towards the end of the project, different grain configurations such as the double-D, multiple-port wagon wheel, and star-type were implemented into the HRPC applications but remain unvalidated. In addition, the graphical visualisations of the grain configurations must be incorporated into the codes. Future research also consists of using the method of characteristics to design the diverging section of bell-shaped nozzle instead of the parabolic approximation used in HRPC Motor Design application. To ensure complete combustion, the aft end mixing chamber must be appropriately dimensioned according to the combustion residence time of the

propellants. As such, implementation of various residence time equations for the corresponding propellant combinations will be highly beneficial for a complete hybrid rocket motor model. The present zero-dimensional combustion chamber gas model can be extended to a one-dimensional model to capture the realistic variation in gas properties and chamber pressure through the fuel-grain port. In addition, the one-dimensional combustion chamber gas model with the non-classical liquefying entrainment mass-transfer theory will capture the space-time variation in solid-fuel regression rate of paraffin wax. As HRPC applications can be expanded for other oxidiser/fuel combinations, a wide-range of regression rate equations will need to be implemented, in particular, for solid fuels which are pressure dependent. The HRPC tool can potentially integrate a numerical model for the study of combustion instabilities. In particular, the low frequency instabilities, discussed in Chapter 2, can be modelled by coupling the feed system, including the injector, to the combustion chamber dynamics which models the solid fuel thermal lag and oxidiser vaporisation mechanisms. Finally, the HRPC application requires a built-in optimisation function to maximise motor performance.

Thus far, the design and manufacture of the PV-1 motor has been completed. The HRPC application is fully operational and was used in the design of the PV-1 motor. Following the three failed hot-fire attempts, a more energetic ignition system is being tested and will be used for the next hot-fire test. Once the PV-1 motor is successfully tested, the vehicle's airframe and internal components will be integrated to the propulsion system. Phoenix-1A is planned to be launched over the sea from the Denel Overberg Test Range (OTR), South Africa.

## REFERENCES

Air Liquide, *Gas Encyclopaedia*, Elsevier Science B. V., Amsterdam, Netherlands, 2002.

Altman, D., "Hybrid Rocket Development History", 27<sup>th</sup> *AIAA/ASME/SAE/ASEE Joint Propulsion Conference & Exhibit*, Sacramento, CA, United States of America, 24-26 June 1991.

Boardman, T. A., Brinton, D. H., Carpenter, R. L., and Zoladz, T. F., "An Experimental Investigation of Pressure Oscillations and their Suppression in Subscale Hybrid Rocket Motors," 31<sup>st</sup> *AIAA/ASME/SAE/ASEE Joint Propulsion Conference & Exhibit*, San Diego, CA, United States of America, 10-12 July 1995.

Brooks, M. J., Pitot de la Beaujardiere, J. P., Chowdhury, S. M., Genevieve, B. and Roberts, L., "Introduction to the UKZN Hybrid Sounding Rocket Program", Proceedings of the 46<sup>th</sup> *AIAA/ASME/SAE/ASEE Joint Propulsion Conference & Exhibit*, Nashville, TN, United States of America, 25-28 July 2010.

Brown, T. R. and Lydon, M. C., "Testing of Paraffin-Based Hybrid Rocket Fuel Using Hydrogen Peroxide Oxidizer", *AIAA Region 5 Student Conference*, Wichita, USA, 2005.

Chiaverini, M. J., and Kuo, K. K., *Fundamentals of Hybrid Rocket Combustion and Propulsion*, AIAA, Progress in Astronautics and Aeronautics, Vol. 218, 2006.

Chowdhury, S., "Design and Performance Simulation of a Hybrid Sounding Rocket", Masters Dissertation, School of Agriculture, Science and Engineering, University of KwaZulu-Natal, Durban, South Africa, Submitted, December 2012.

Covault, C., "Curiosity's Mission to Mars", *AIAA Aerospace America Journal*, Vol. 49, No. 1, Jan. 2012, pp. 28-34.

DeSain, J. D., Brady B. B., Metzler, K. M., Curtiss, T. J., and Albright, T. V., "Tensile Tests of Paraffin Wax for Hybrid Rocket Fuel Grains", 45<sup>th</sup> *AIAA/ASME/SAE/ASEE Joint Propulsion Conference & Exhibit*, Denver, Colorado, United States of America, 2-5 August 2009.

Dornheim, M. A., "SpaceShipOne Won", *Aviation Week and Space Technology*, Vol. 161, No. 14, 10 Oct 2004, pp. 34-36.

Dyer, J., Doran, E., Dunn, Z., and Lohner, K., "Design and Development of a 100 km Nitrous Oxide/Paraffin Hybrid Rocket Vehicle", *43<sup>rd</sup> AIAA/ASME/SAE/ASEE Joint Propulsion Conference & Exhibit*, Cincinnati, OH, United States of America, 8-11 July 2007.

Fernandez M. M., "Propellant Tank Pressurization Modelling for a Hybrid Rocket", Masters Dissertation, Department of Mechanical Engineering, Kate Gleason College of Engineering, Rochester Institute of Technology, Rochester, New York, 2009.

Freund, M., Csikos, R., Keszthelyi, S., and Mozes, G. Y., *Paraffin Products: Properties, Technologies, Applications*, Elsevier Scientific Publishing Company, Amsterdam, 1982.

Genevieve, B., Brooks, M. J., Pitot de la Beaujardiere, J. F. and Roberts, L. W., "Performance Modeling of a Paraffin Wax / Nitrous Oxide Hybrid Rocket Motor", *Proceedings of the 49<sup>th</sup> AIAA Aerospace Sciences Meeting*, Orlando, Florida, United States of America, 4-7 January 2011.

Genevieve, B., Chowdhury, S. M., Brooks, M. J., Pitot de la Beaujardiere, J. P., Veale, K. And Roberts, L. W., "The Phoenix Sounding Rocket Program: A Progress Report 2012", Proceedings of the 48<sup>th</sup> Annual AIAA/ASME/SAE/ASEE Joint Propulsion Conference and Exhibit and 10th Annual International Energy Conversion Engineering Conference, Atlanta, GA, United States of America, 29 July – 1 August 2012.

George, P., Krishnan, S., M. Varkey, P., Ravindran, M., and Ramachandran, L., "Fuel Regression Rate in Hydroxyl-Terminated-Polybutadiene/Gaseous-Oxygen Hybrid Rocket Motors", *Journal of Propulsion and Power*, vol. 17, no. 1, pp. 35–42, 2001.

Gopal, T., Govinder, N., and Reddy, K. R., "Phoenix-1A Flight Motor Test Stand", Mechanical Engineering Undergraduate Dissertation, Department of Mechanical Engineering, University of KwaZulu-Natal, Durban, South Africa, 2011.

Gordon, C. O., *Aerothermodynamics of Gas Turbine and Rocket Propulsion*, 3rd Edition, American Institute of Aeronautics and Astronautics, Reston, Virginia, 1997.

Gordon, S., and McBride, B. J., "Computer Program for Calculation of Complex Chemical Equilibrium Compositions and Applications", NASA RP-1311, 1994.

Greatrix, D. R., *Powered Flight: The Engineering of Aerospace Propulsion*, Springer, London, 2012.

Green, L., "Introductory Considerations on Hybrid Rocket Combustion", *AIAA Heterogeneous Combustion Conference*, Palm Beach, Florida, United States of America, 11-13 December 1963.

Grosse, M., "Effect of a Diaphragm on Performance and Fuel Regression of a Laboratory Scale Hybrid Rocket Motor Using Nitrous Oxide and Paraffin", *45<sup>th</sup> AIAA/ASME/SAE/ASEE Joint Propulsion Conference & Exhibit*, Denver, Colorado, United States of America, 2-5 August 2009.

Humble, R. W., Henry, G. N., and Larson, W. J., *Space Propulsion Analysis and Design*, McGraw-Hill, United States of America, 1995.

Karabeyoglu, M. A., Cantwell, B. J., and Altman, D., "Development and Testing of Paraffin-based Hybrid Rocket Fuels", *Proceedings of the 37th AIAA/ASME/SAE/ASEE Joint Propulsion Conference & Exhibit*, July 8-11, 2001, Salt Lake City, Utah.

Karabeyoglu, M. A., Altman, D., Cantwell, B. J., "Combustion of Liquefying Hybrid Propellants: Part 1, General Theory", *Journal of Propulsion and Power*, Vol. 18, No. 3, May-June 2002.

Karabeyoglu, M. A., Zilliac, G., Cantwell, B. J., De Zilwa, S., and Castelluci, P., "Scale-Up Tests of High Regression Rate Liquefying Hybrid Rocket Fuels", *41<sup>st</sup> AIAA/ASME/SAE/ASEE Joint Propulsion Conference & Exhibit*, Reno, Nevada, United States of America, 6-9 July 2003.

Karabeyoglu, A., Dyer, J., Stevens, J., and Cantwell, B., "Modelling of N<sub>2</sub>O Decomposition Events", *44<sup>th</sup> AIAA/ASME/SAE/ASEE Joint Propulsion Conference & Exhibit*, Hartford, CT, United States of America, 21-23 July 2008.

Kotecki, D., and Armao, F., "Stainless Steels Properties – How to Weld Them –Where to Use Them", *The Lincoln Electric Company*, 2003.

Lohner, K., Dyer, J., Doran, E., Dunn, Z., and Zilliac, G., "Fuel Regression Rate Characterization Using a Laboratory Scale Nitrous Oxide Hybrid Propulsion System", *42<sup>nd</sup> AIAA/ASME/SAE/ASEE Joint Propulsion Conference & Exhibit*, Sacramento, California, United States of America, 9-12 July 2006.

Maharaj, S., Pather, K., and Zoli, G., "Mobile Rocket Launch Platform", Mechanical Engineering Undergraduate Dissertation, Department of Mechanical Engineering, University of KwaZulu-Natal, Durban, South Africa, 2011.

Marxman, G. A., Wooldridge, C. E., and Muzzy, R. J., "Fundamentals of Hybrid Boundary Layer Combustion", *Progress in Aeronautics and Astronautics*, Vol. 15, 1964, pp. 485-522.

MatWeb, Aluminum 6082-T6, Online, <http://www.matweb.com/search/datasheetText.aspx?bassnum=MA6082T6>, Accessed 20 October 2012.

McCormick, A., Hultgren, E., Lichtman, M., Smith, J., Sneed, R., and Azimi, S., "Design, Optimization, and Launch of a 3" Diameter N2O/Aluminized Paraffin Rocket", *41<sup>st</sup> AIAA/ASME/SAE/ASEE Joint Propulsion Conference & Exhibit*, Tucson, Arizona, United States of America, 10-13 July 2005.

Megyesy, E. F., *Pressure Vessel Handbook*, 12th ed., Pressure Vessel Publishing, Inc., Tulsa, Oklahoma, 2001.

Moretto, F., "Performance Characterization of Propulsion Systems for Spacecraft Applications", PhD Thesis, Science Technologies and Measures for Space, University of Padova, Padua, Italy, 2011.

Pedersen, T., and Nyboe, F., "Heat-1X / Tycho Brahe: Flight Trajectory Analysis," *Copenhagen Suborbitals*, Online, [http://www.copenhagensuborbitals.com/resources\\_downloads.php](http://www.copenhagensuborbitals.com/resources_downloads.php), Accessed 15 October 2012.

Perry, R. H., and Green, D. W., *Perry's Chemical Engineers' Handbook*, 8th Edition, McGraw-Hill, United States, 2007.

Hill, P., Peterson, C., *Mechanics and Thermodynamics of Propulsion*, 2nd Edition, Addison Wesley Longman, United States of America, 1992.

Pitot de la Beaujardiere, J. P., Brooks, M. J., Chowdhury, S. M., Genevieve, B. and Roberts, L. W., "The Phoenix Hybrid Sounding Rocket Program: A Progress Report", *Proceedings of the 47th AIAA/ASME/SAE/ASEE Joint Propulsion Conference & Exhibit*, 2011, San Diego, CA.

Rao, G. V. R., "Exhaust Nozzle Contour for Optimum Thrust", *Jet Propulsion*, Vol. 28, June 1958, pp. 377-382.

Reddy, J., Mahomed, B. G., and Mabaso, S., "Hybrid Rocket Test Stand", Mechanical Engineering Undergraduate Dissertation, School of Agriculture, Science and Engineering, University of KwaZulu-Natal, Durban, South Africa, 2010.

Scaled Composites, LLC, Online, [http://www.scaled.com/images/uploads/news/airelease\\_8\\_1\\_08.pdf](http://www.scaled.com/images/uploads/news/airelease_8_1_08.pdf), Accessed 20 October 2012.

Smyth, J., Booyens, D., and Moodley, S., "Hybrid Rocket Motor Design", Mechanical Engineering Undergraduate Dissertation, School of Agriculture, Science and Engineering, University of KwaZulu-Natal, Durban, South Africa, October 2010.

SPG, "Nitrous Oxide Safety", Online, <http://www.spg-corp.com/nitrous-oxide-safety.html>, Accessed 8 December 2012.

Sutton, G. P. and Biblarz, O., *Rocket Propulsion Elements*, 7th Edition, John Wiley & Sons, New York, 2001.

Thicksten, Z., Macklin, F., and Campbell, J., "Handling Considerations of Nitrous Oxide in Hybrid Motor Testing", *44th AIAA/ASME/SAE/ASEE Joint Propulsion Conference & Exhibit*, Hartford, CT, United States of America, 21-23 July 2008.

Tsohas, J., Appel, B., Rettenmaier, A., Walker, M., and Heister, S. D., "Development and Launch of the Purdue Hybrid Rocket Technology Demonstrator", *45th AIAA/ASME/SAE/ASEE Joint Propulsion Conference & Exhibit*, Colorado, Denver, United States of America, 2-5 August 2009.

Virgin Galactic, Online, [http://www.virgingalactic.com/assets/downloads/Virgin\\_Galactic\\_Brochure.pdf](http://www.virgingalactic.com/assets/downloads/Virgin_Galactic_Brochure.pdf), Accessed 12 October 2012.

Webber, G., *Personal communication*, SASOL Limited, South Africa, 2010.

Zakirov, V., “Catalytic Decomposition of Nitrous Oxide for Spacecraft Propulsion Applications”, Surrey Satellite Technology Limited, Centre for Satellite Engineering Research, University of Surrey, Guildford, Surrey, UK, 2000.

Zucker, R. D. and Biblarz, O., *Fundamentals of Gas Dynamics*, 2<sup>nd</sup> Edition, John Wiley & Sons, New Jersey, 2002.

## **APPENDIX A**

### **Phoenix-1A Hybrid Sounding Rocket**

## **Appendix A.1**

### **Specifications and Goals**

The primary goal of the Phoenix-1A vehicle is to demonstrate the feasibility of locally developed hybrid rockets with low-to-medium altitude range capability. Being the first member of the Phoenix family, the Phoenix-1A targeted apogee was set to a low altitude of 10 km. The rocket, powered by a hybrid propulsion system, aims to deliver a 1 kg payload to the set mission's altitude.

In conjunction with the developmental phase of the propulsion system, described in this dissertation, the Phoenix-1A's internal components and vehicle airframe, including the oxidiser tank, have been designed in a parallel project (Chowdhury, 2012). Currently, the vehicle's structure is under manufacture, and awaits the post-analysis of a successful PV-1 motor hot-fire test. In the following section, a brief overview of Phoenix-1A's vehicle and internal components is given.

### **Overview of Phoenix-1A Hybrid Sounding Rocket**

A cross-sectional view of the Phoenix-1A vehicle airframe assembled to the propulsion system is shown in Fig A.1. The PV-1 hybrid motor drove the overall design of the rocket. The vehicle's aerodynamic and structural configurations have been optimised through an iterative process with the predicted motor performance using HYROPS for transonic flight. The rocket utilises a dual parachute recovery system controlled by two dependent flight computers for land or sea recovery. Using a dual parachute recovery system, the rocket is expected to splash down at a nominal velocity of 5 m/s. For safety considerations, Phoenix-1A is incorporated with onboard flight termination and telemetry systems.

Referring to Fig. A.1, the vehicle's airframe consists of an ogive nose cone with aluminium tip, drogue and main parachute bays, a flight computer bay, four stabilising fins, a boat-tail, and a tapered inter-stage section for encasing the feed system. These components are fitted to the oxidiser tank and the PV-1 motor. The pressure vessel-based oxidiser tank was manufactured from 6082-T6 aluminium alloy. The welded tank consists of two torispherical heads and a cylindrical shell. The oxidiser tank is bolted to the motor by four high strength stainless steel struts which were specially machined. The rocket's four trapezoidal fins, machined from 6082-T6 aluminium alloy, are located in the stainless steel rail structures secured to the combustion chamber. The fin arrangement is canted at an angle of 0.5° to the motor axis. A

carbon-phenolic composite boat-tail is attached to the nozzle side for base drag minimisation. All airframe components, excluding the boat-tail, are fabricated from a carbon fibre epoxy composite with a wall thickness of 2 mm.



*1) Boat-tail, 2) PV-1 Flight Motor, 3) Oxidiser Feed System, 4) Oxidiser Tank, 5) Drogue Parachute Bay, 6) Flight Computer Bay, 7) Main Parachute Bay, 8) Nose-Payload Compartment, 9) Aluminium Nose Tip*

Figure A.1 Sectional view of Phoenix-1A hybrid sounding rocket (Pitot de la Beaujardiere et al., 2011).

The flight computer bay houses the Phoenix-1A's recovery system electronics and carbon dioxide deployment charges. Due to the targeted altitude, a carbon dioxide-based deployment system is more appropriate than pyrotechnic charges. Two carbon dioxide charges triggered by lithium-polymer batteries are placed on either side of the flight computer bay to respectively deploy the drogue and main chutes. Internal aluminium 6082-T6 bulkheads separate the parachute and flight computer compartments. Kevlar shock cords are employed to attach the parachutes to the internal bulkheads and oxidiser tank. The total length of the rocket, from the nose tip to the boat-tail, is 4.55 m and the fully fuelled mass is 95 kg.

## **APPENDIX B**

### **Air Liquide: Nitrous Oxide Material Compatibility**

## Appendix B.1

### Nitrous Oxide Materials' Compatibility

Air Liquide has assembled data on the compatibility of gases with materials to assist you in evaluating which products to use for a gas system. Although the information has been compiled from what Air Liquide believes are reliable sources (International Standards: Compatibility of cylinder and valve materials with gas content; Part 1: ISO 11114-1 (Jul 1998), Part 2: ISO 11114-2 (Mar 2001)), it must be used with extreme caution. No raw data such as this can cover all conditions of concentration, temperature, humidity, impurities and aeration. It is therefore recommended that this table is used to choose possible materials and then more extensive investigation and testing is carried out under the specific conditions of use. The collected data mainly concern high pressure applications at ambient temperature and the safety aspect of material compatibility rather than the quality aspect.

Table B.1 Nitrous oxide material compatibility.

Material	Compatibility
<b>Metals</b>	
<b>General Behavior:</b> Equipment must be thoroughly degreased before use. Risk of violent reaction particularly with the valves.	
Aluminium	Satisfactory
Brass	Satisfactory but corrosive in presence of moisture.
Copper	Satisfactory but corrosive in presence of moisture.
Ferritic Steels (e.g. Carbon steels)	Satisfactory but corrosive in presence of moisture.
Stainless Steel	Satisfactory
<b>Plastics</b>	
Polytetrafluoroethylene (PTFE)	Satisfactory
Polychlorotrifluoroethylene (PCTFE)	Satisfactory
Vinylidene polyfluoride (PVDF) (KYNAR™)	Acceptable <b>but possible ignition</b> under certain conditions.
Polyamide (PA) (NYLON™)	Acceptable <b>but possible ignition</b> under certain conditions.

Table B.1 Nitrous oxide material compatibility.

<b>Plastics</b>	
Polypropylene (PP)	Acceptable <b>but possible ignition</b> under certain conditions.
<b>Elastomers</b>	
Butyl (isobutene - isoprene) rubber (IIR)	Not recommended, possible ignition and significant swelling.
Nitrile rubber (NBR)	Not recommended, possible ignition and significant swelling.
Chloroprene (CR)	Not recommended, possible ignition and significant swelling.
Chlorofluorocarbons (FKM) (VITON™)	Not recommended, significant swelling.
Silicon (Q)	Satisfactory
Ethylene - Propylene (EPDM)	Not recommended, possible ignition and significant swelling.
<b>Lubricants</b>	
Hydrocarbon based lubricant	Not recommended, possible ignition.
Fluorocarbon based lubricant	Satisfactory

## **APPENDIX C**

### **Oxidiser Tank Blowdown Process: Thermodynamic Properties**

## Appendix C.1

### Thermodynamic Properties of Nitrous Oxide, Helium, and Aluminium Oxidiser Tank

The following thermodynamic property equations were obtained from Perry and Green (2007) handbook. Thermodynamic constants for each material can be found in the handbook, that is, constants  $C_1$  to  $C_5$ . As Phoenix-1A vehicle utilises an aluminium oxidiser tank, the equation property of this material was extracted and implemented in HRPC. Therefore, other oxidiser tank material properties must be inputted in HRPC before running the numerical simulation.

Specific heat capacity at constant pressure of aluminium oxidiser tank:

$$c_{P_T} = (C_1 + C_2 T_T) C_3 \quad (\text{C.1})$$

Molar heat capacity at constant volume of liquid nitrous oxide is approximated as its molar heat capacity at constant pressure:

$$\bar{C}_{V_{ox,l}} \approx \bar{C}_{P_{ox,l}} = C_1 + C_2 T_T + C_3 T_T^2 + C_4 T_T^3 + C_5 T_T^4 \quad (\text{C.2})$$

Specific heat capacity at constant pressure of vapour nitrous oxide:

$$\bar{C}_{P_{ox,v}} = C_1 + C_2 \left[ \frac{\frac{C_3}{T_T}}{\sinh\left(\frac{C_3}{T_T}\right)} \right]^2 + C_4 \left[ \frac{\left(\frac{C_5}{T_T}\right)}{\cosh\left(\frac{C_5}{T_T}\right)} \right]^2 \quad (\text{C.3})$$

Specific heat capacity at constant pressure of gaseous helium:

$$\bar{C}_{P_{sp,v}} = C_1 + C_2 T_T + C_3 T_T^2 + C_4 T_T^3 + C_5 T_T^4 \quad (\text{C.4})$$

For an ideal gas, specific heat capacities are related to the universal gas constant:

$$\bar{C}_V = \bar{C}_P - R_u \quad (\text{C.5})$$

Reduced Temperature:

$$T_r = \frac{T_T}{T_c} \quad (\text{C.6})$$

Heat of vaporization of liquid nitrous oxide:

$$\Delta\bar{H}_{ox,v} = C_1 [1 - T_r]^{C_2 + C_3 T_r + C_4 T_r^2 + C_5 T_r^3} \quad (\text{C.7})$$

Molar specific volume of liquid nitrous oxide:

$$\bar{V}_{ox,l} = \frac{C_2 \left( 1 + \left( 1 - \frac{T_T}{C_3} \right)^{C_4} \right)}{C_1} \quad (\text{C.8})$$

Saturated vapour pressure of nitrous oxide:

$$P_{ox}^* = e^{\left( C_1 + \frac{C_2}{T_T} + C_3 \ln T_T + C_4 T_T^{C_5} \right)} \quad (\text{C.9})$$

## **APPENDIX D**

### **HRPC Fuel Grain Standard Geometries**

## Appendix D.1

### HRPC Fuel Grains Graphical Output

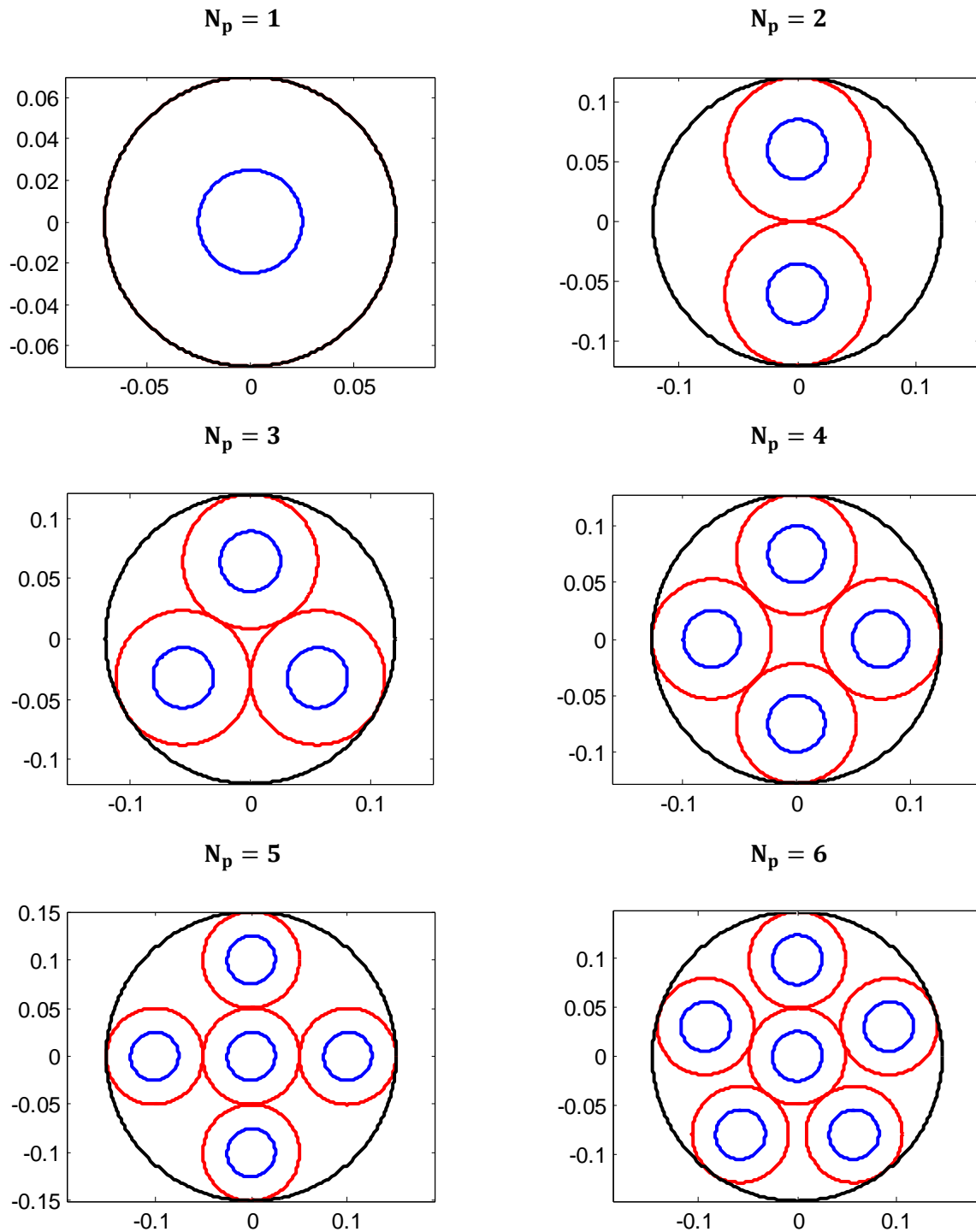


Figure D.1 HRPC fuel grains graphical output.

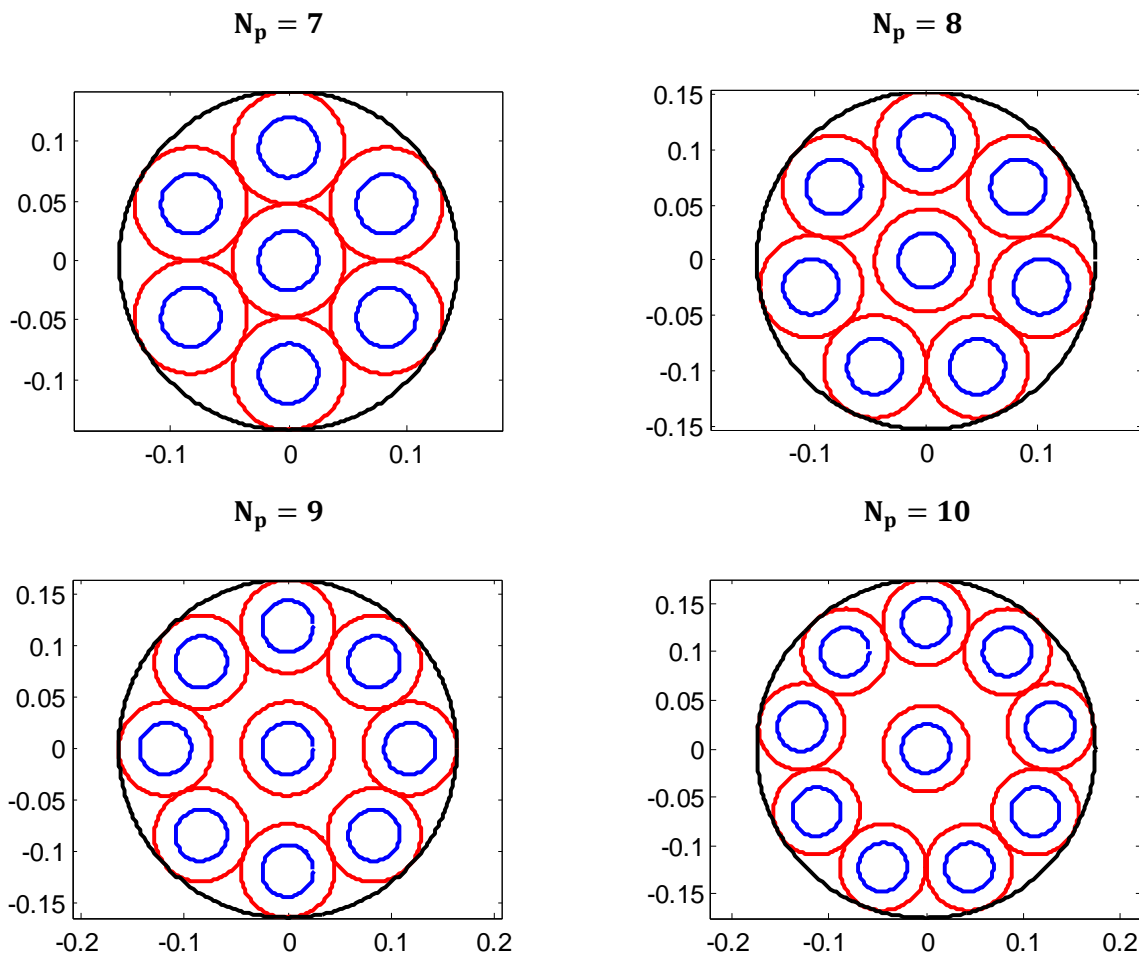


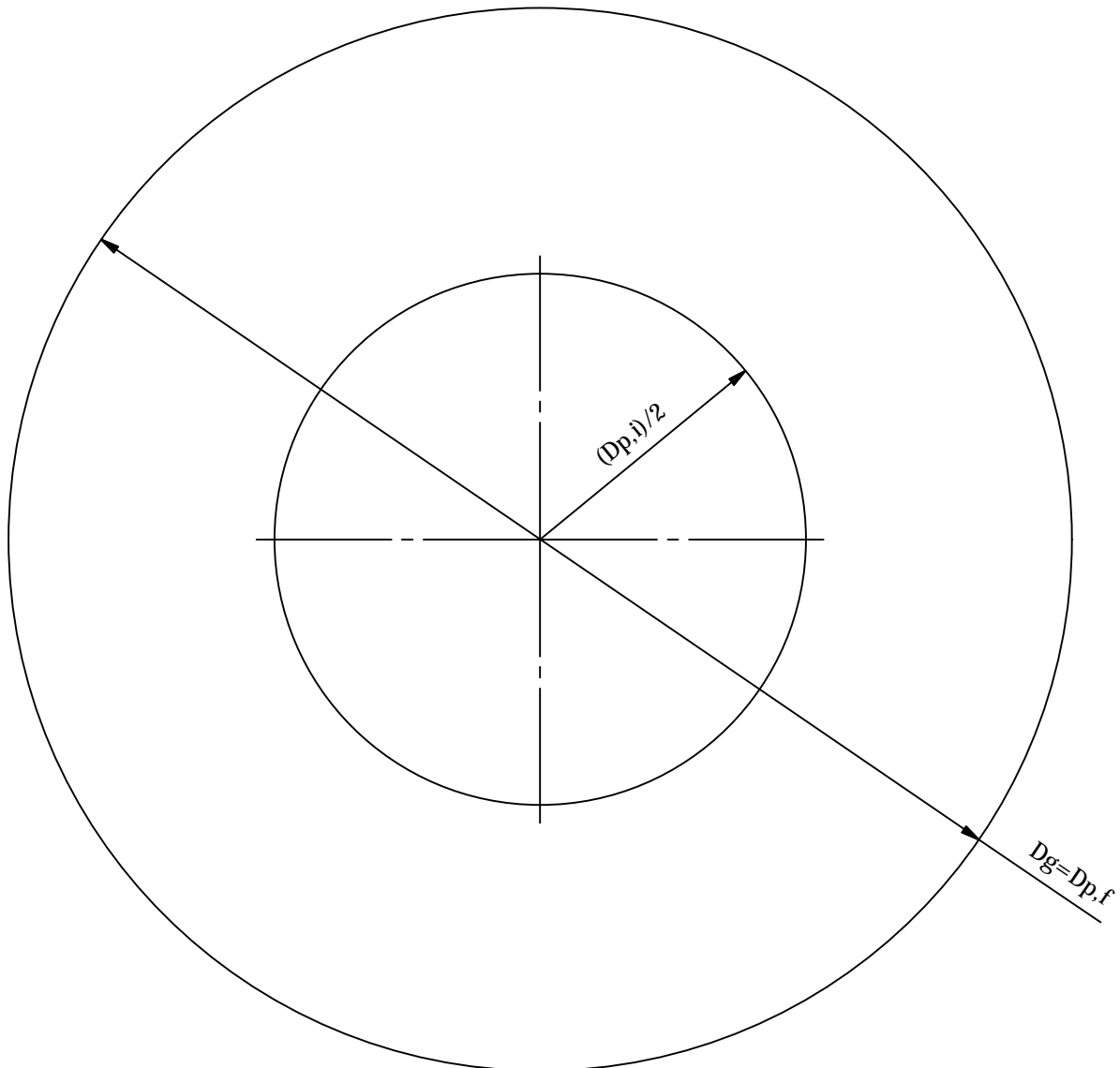
Figure D.1 HRPC fuel grains graphical output.

## Appendix D.2

### HRPC Fuel Grains' Dimensions

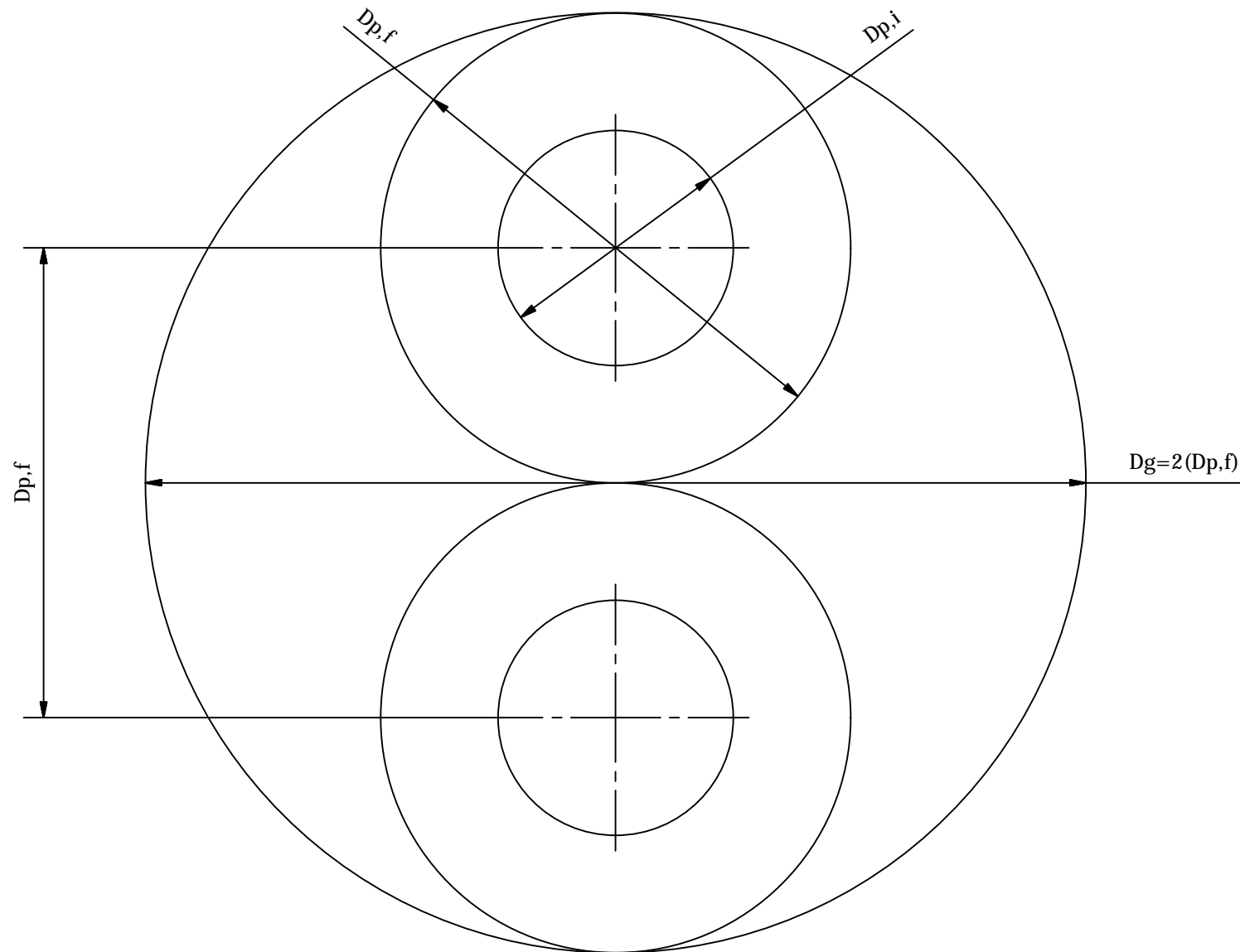
Table D.1 Fuel grain diameter and port angle formulae.

Number of Ports	Grain Diameter [m]	$\theta$ [°C]
1	$D_g = D_{p,f}$	N/A
2	$D_g = 2D_{p,f}$	$360/N_p = 180$
3	$D_g = [(2/\sqrt{3}) + 1]D_{p,f}$	$360/N_p = 120$
4	$D_g = [\sqrt{2} + 1]D_{p,f}$	$360/N_p = 90$
5, 6, and 7	$D_g = 3D_{p,f}$	$360/(N_p - 1)$
8, 9, and 10	$sp = \left[ \frac{1 - 2 \sin(\theta/2)}{2 \sin(\theta/2)} \right] D_{p,f}$ $D_g = 3D_{p,f} + 2sp$	$360/(N_p - 1)$



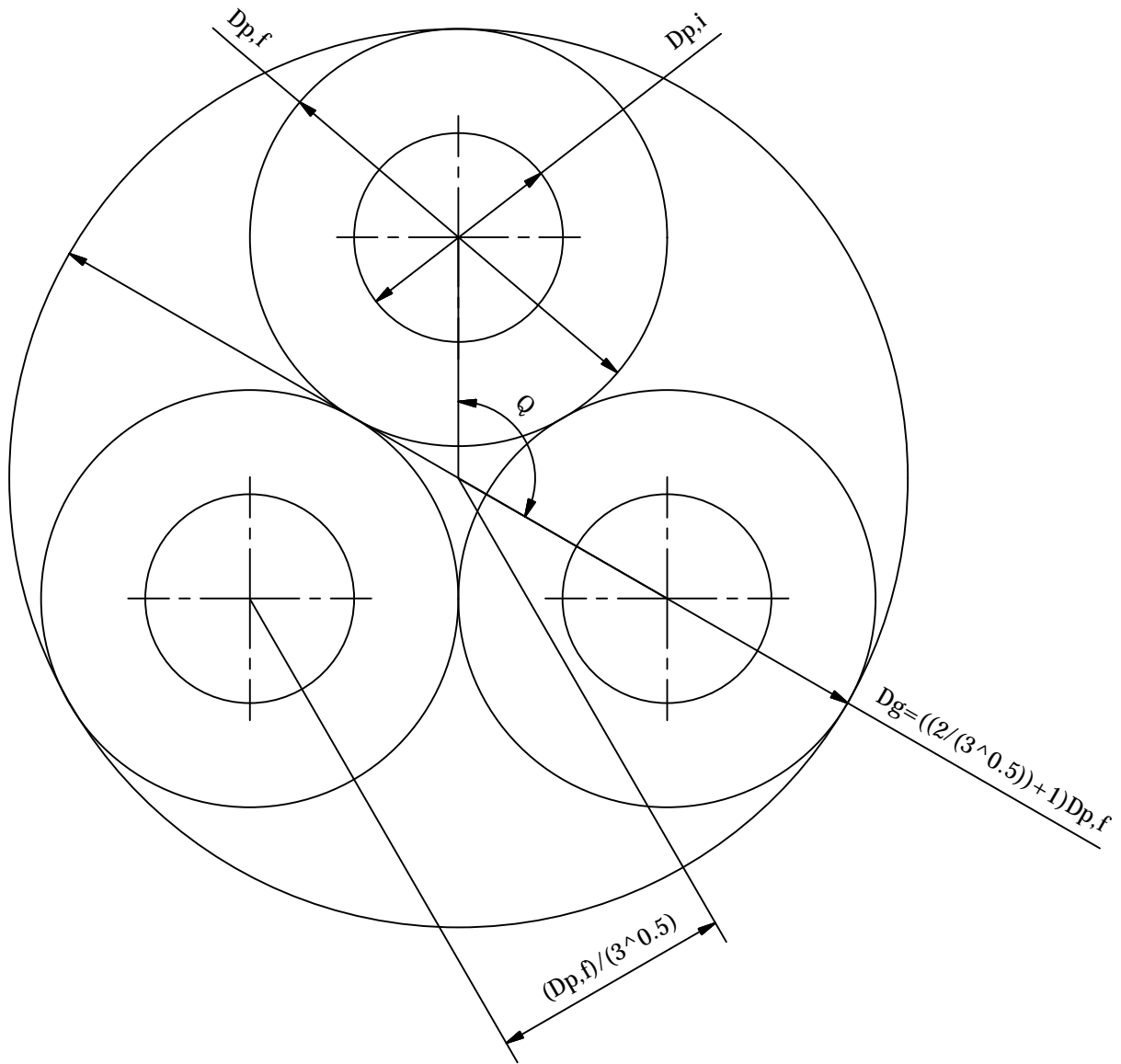
School of Mechanical  
Engineering

PROJECT SUPERVISOR	DATE	CHECKED	SCALE	PROJECT	NO.
W'SHOP TECHNICIAN			STUDENT NAME Bernard Genevieve	HRPC Cylindrical Grain	1
TECHNICAL OFFICER			E-MAIL 206504262@stu.ukzn.ac.za		
TEL NO.					TITLE Np=1



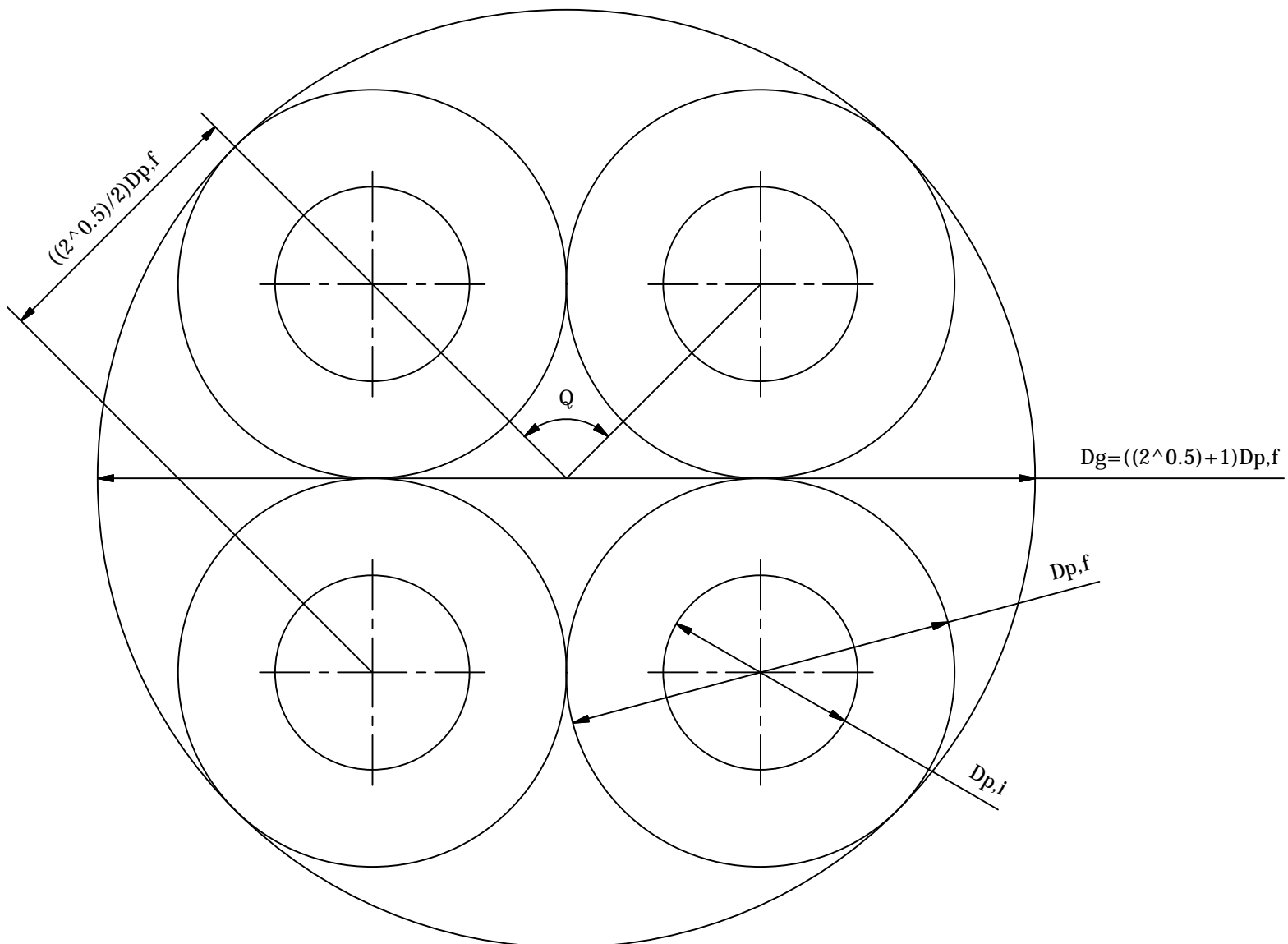
School of Mechanical  
Engineering

PROJECT SUPERVISOR		DATE	CHECKED	SCALE	PROJECT	NO.
W'SHOP TECHNICIAN				STUDENT NAME Bernard Genevieve E-MAIL 206504262@stu.ukzn.ac.za	HRPC Cylindrical Grain	2
TECHNICAL OFFICER				TEL NO.	TITLE	
					Np=2	



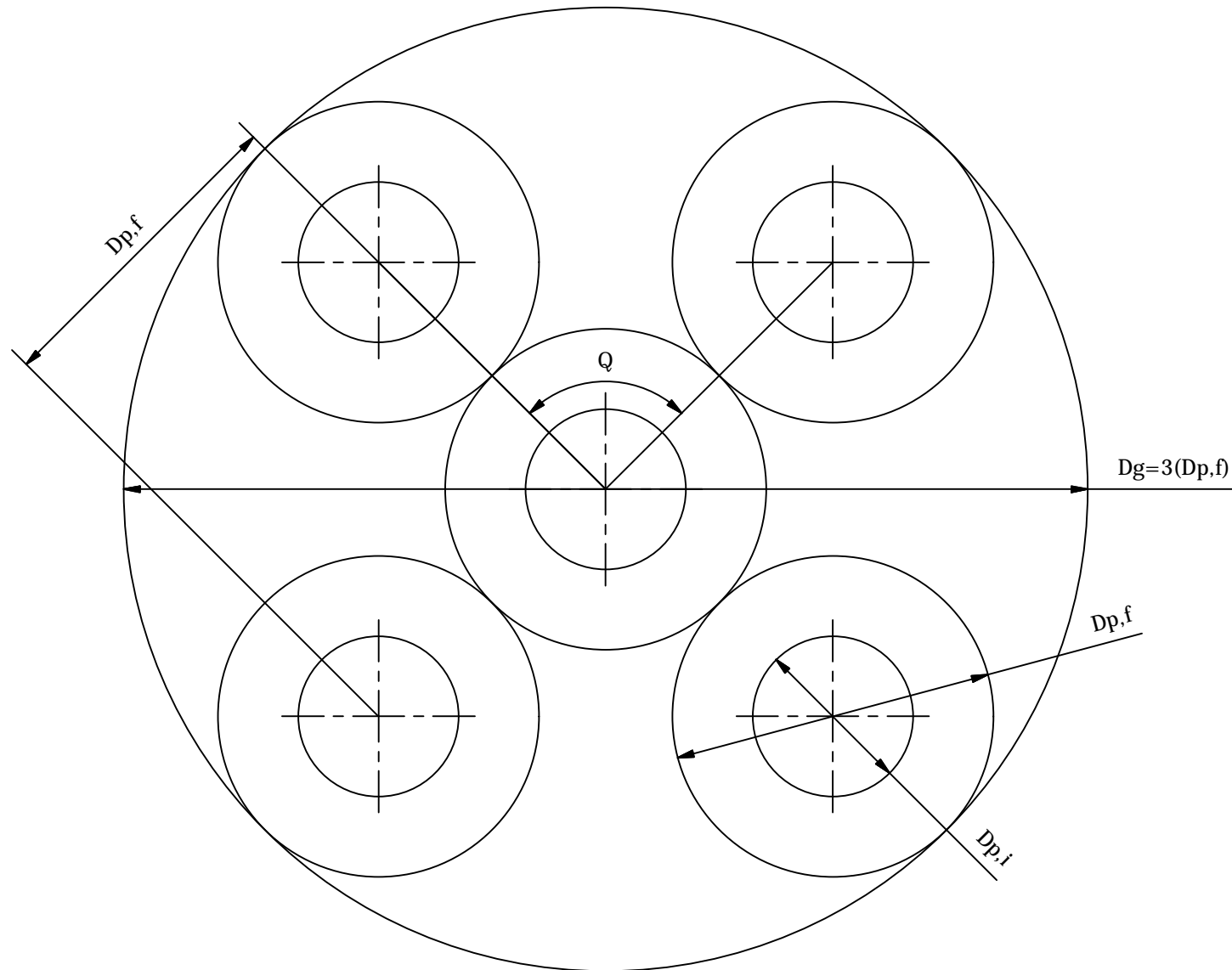
School of Mechanical  
Engineering

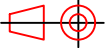
	DATE	CHECKED	SCALE	PROJECT	NO.
PROJECT SUPERVISOR			STUDENT NAME	Bernard Genevieve	3
W'SHOP TECHNICIAN			E-MAIL	206504262@stu.ukzn.ac.za	
TECHNICAL OFFICER			TEL NO.		
				TITLE	Np=3

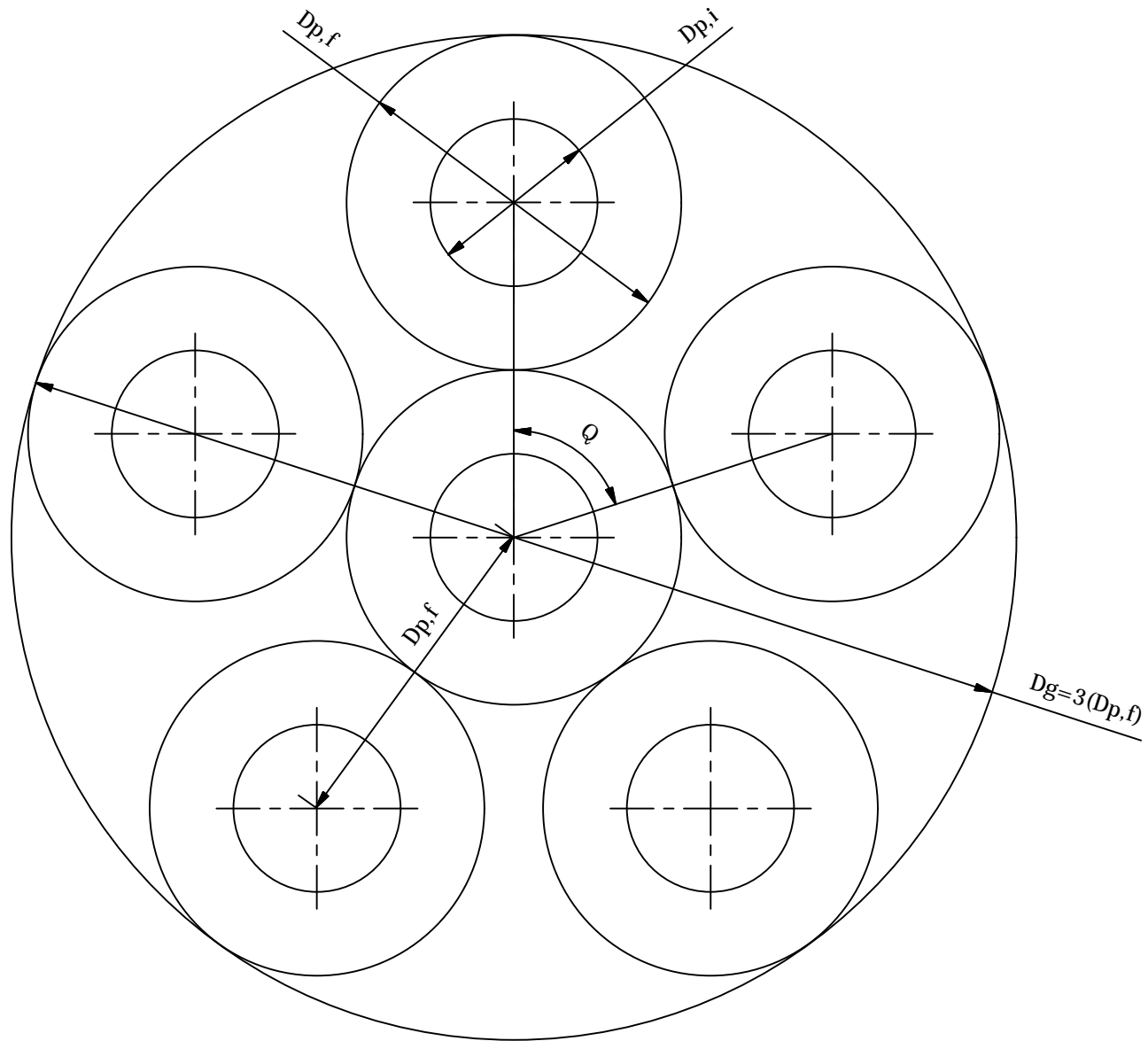


School of Mechanical  
Engineering

PROJECT SUPERVISOR	DATE	CHECKED	SCALE	PROJECT	NO.
			STUDENT NAME Bernard Genevieve	HRPC Cylindrical Grain	4
W'SHOP TECHNICIAN			E-MAIL 206504262@stu.ukzn.ac.za		
TECHNICAL OFFICER			TEL NO.	TITLE Np=4	

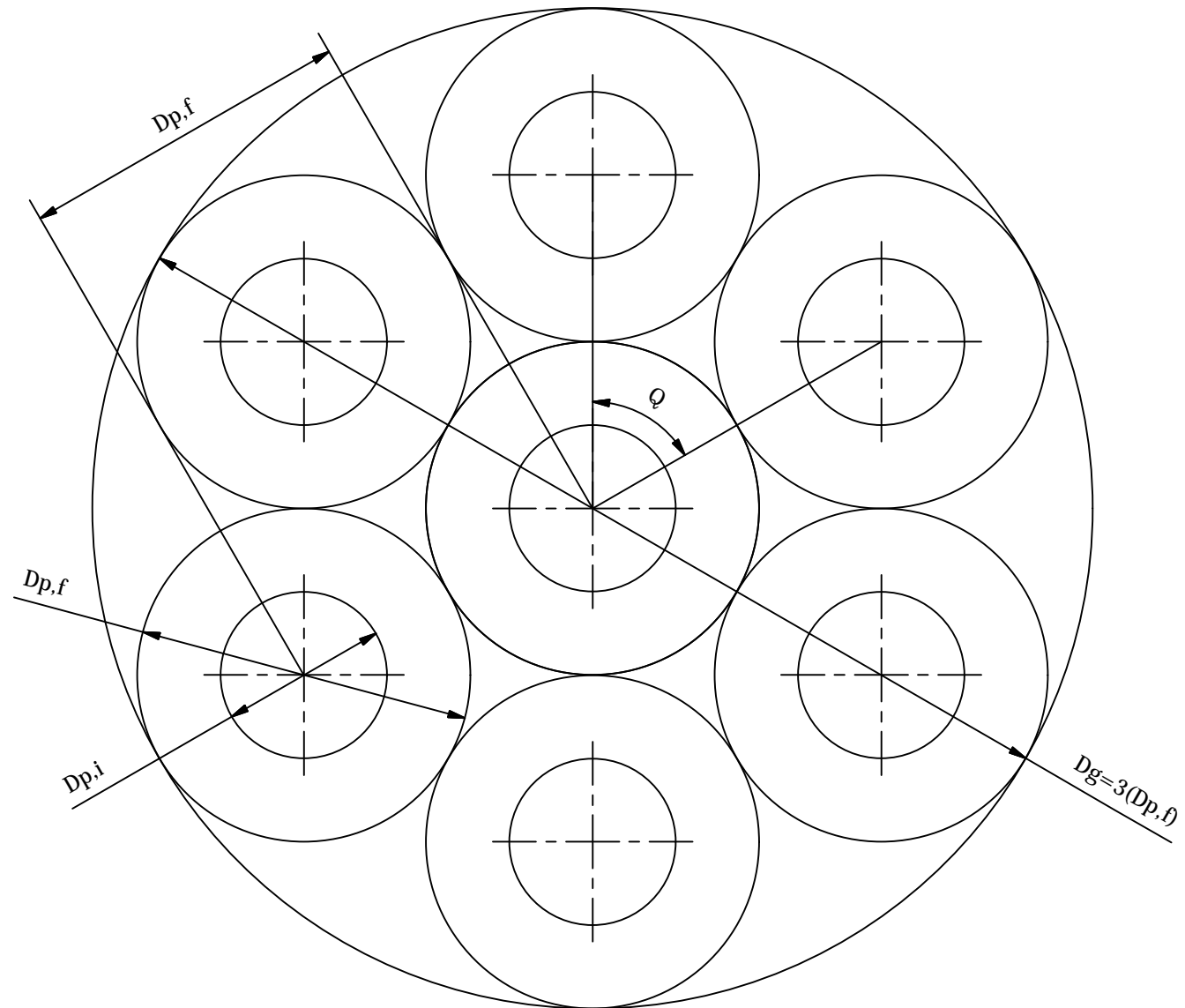


 <b>School of Mechanical Engineering</b>		DATE	CHECKED	SCALE		PROJECT	HRPC Cylindrical Grain	NO.
	PROJECT SUPERVISOR			STUDENT NAME	Bernard Genevieve			5
	W'SHOP TECHNICIAN			E-MAIL	206504262@stu.ukzn.ac.za			
	TECHNICAL OFFICER			TEL NO.		TITLE	Np=5	
								



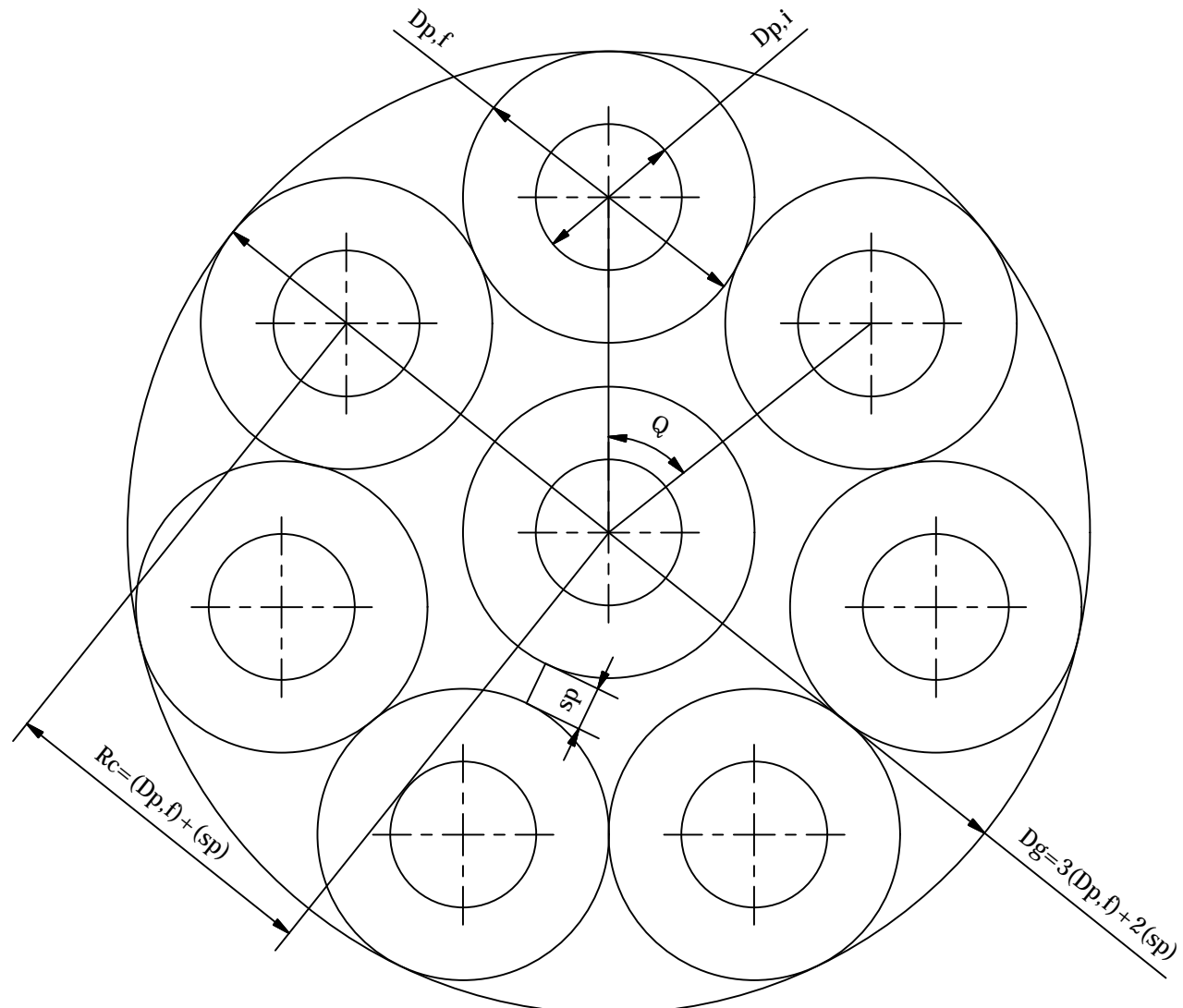
School of Mechanical  
Engineering

PROJECT SUPERVISOR	DATE	CHECKED	SCALE	PROJECT	NO.
			STUDENT NAME Bernard Genevieve	HRPC Cylindrical Grain	6
WSHOP TECHNICIAN			E-MAIL 206504262@stu.ukzn.ac.za		
TECHNICAL OFFICER			TEL NO.	TITLE Np=6	



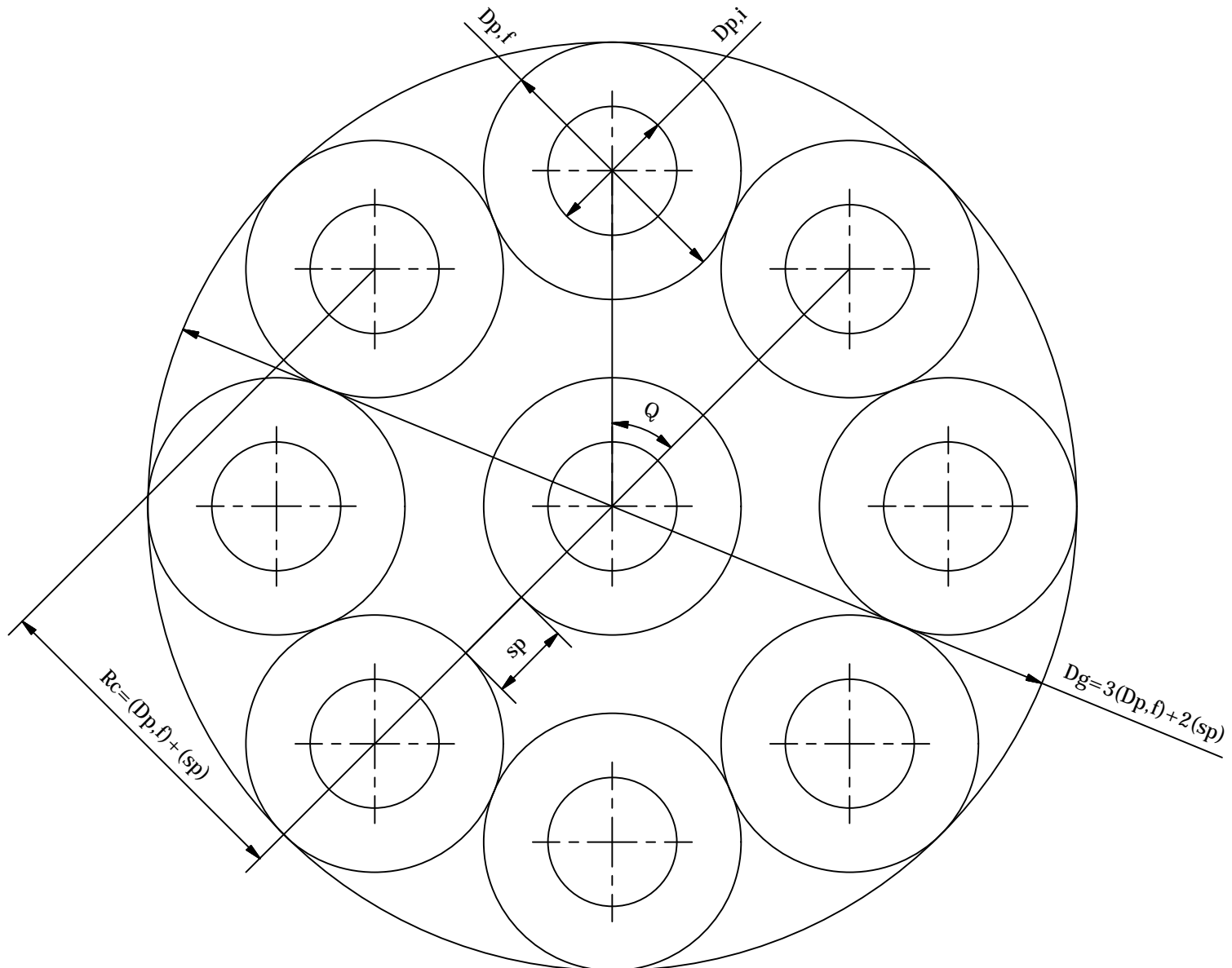
School of Mechanical  
Engineering

PROJECT SUPERVISOR	DATE	CHECKED	SCALE	PROJECT	NO.
			STUDENT NAME Bernard Genevieve	HRPC Cylindrical Grain	7
W'SHOP TECHNICIAN			E-MAIL 206504262@stu.ukzn.ac.za		
TECHNICAL OFFICER			TEL NO.	TITLE Np=7	



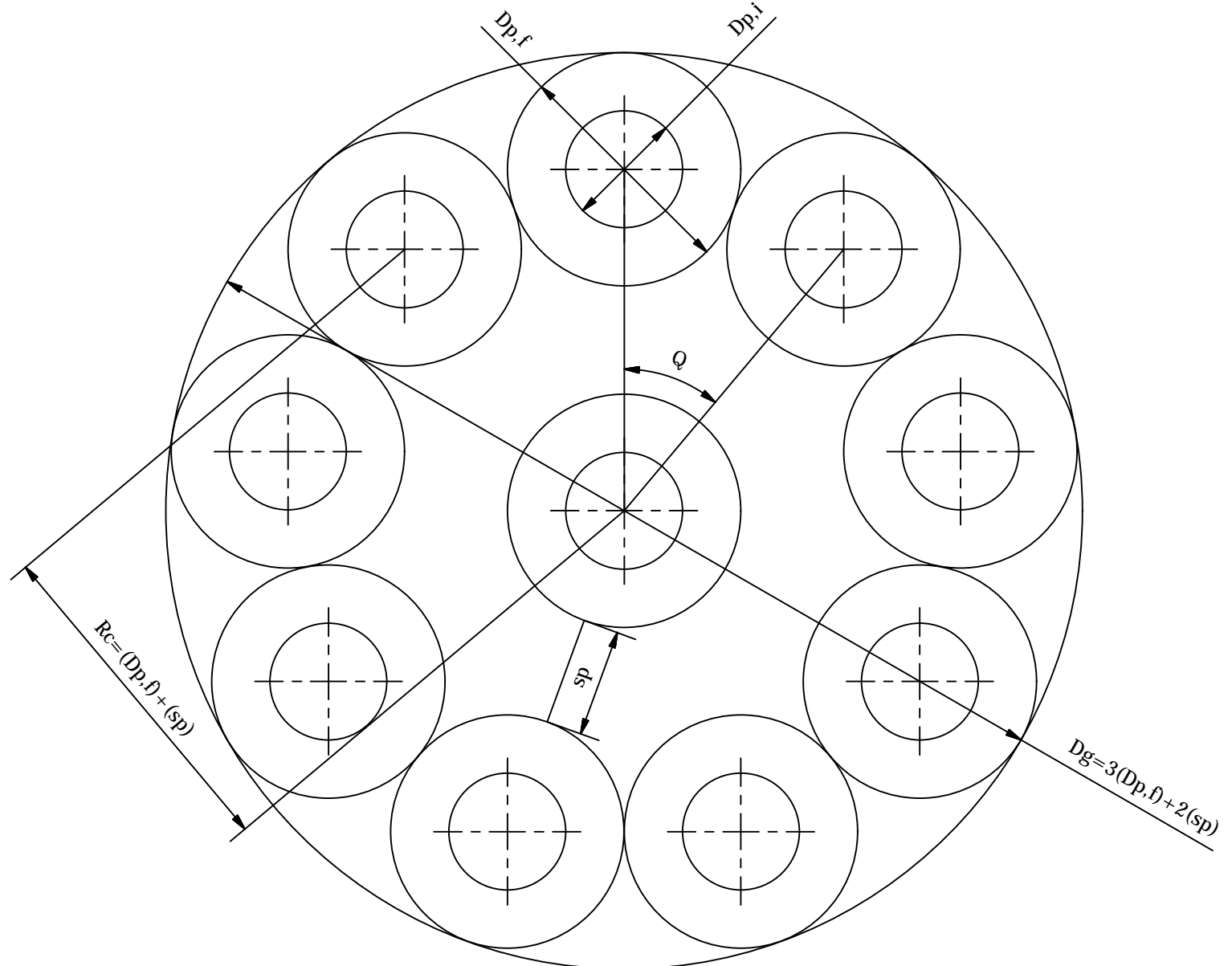
School of Mechanical  
Engineering

PROJECT SUPERVISOR	DATE	CHECKED	SCALE	PROJECT	NO.
			STUDENT NAME Bernard Genevieve	HRPC Cylindrical Grain	8
W'SHOP TECHNICIAN			E-MAIL 206504262@stu.ukzn.ac.za		
TECHNICAL OFFICER			TEL NO.	TITLE Np=8	



School of Mechanical  
Engineering

	DATE	CHECKED	SCALE	PROJECT	NO.
PROJECT SUPERVISOR			STUDENT NAME	Bernard Genevieve	9
W'SHOP TECHNICIAN			E-MAIL	206504262@stu.ukzn.ac.za	
TECHNICAL OFFICER			TEL NO.		
155				TITLE	Np=9



School of Mechanical  
Engineering

PROJECT  
HRPC Cylindrical Grain  
NO.  
10  
TITLE  
Np=10



## **APPENDIX E**

### **HRPC Motor Design Application**

## Appendix E.1

### Motor Performance Analysis Model

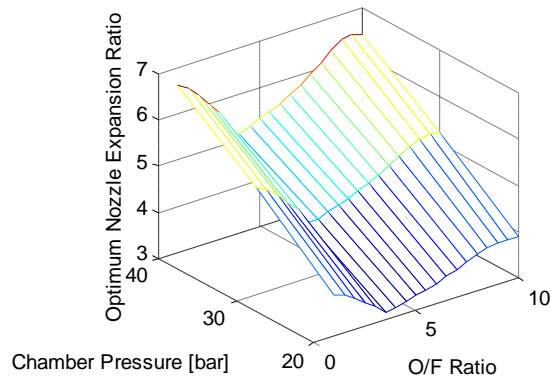
Table E.1 Input parameters for the two typical runs.

<b>Fuel</b>	SASOL 0907 Paraffin-wax
<b>Oxidiser</b>	Nitrous Oxide
<b>Nozzle Flow Composition</b>	Equilibrium Flow
<b>Combustion Efficiency [%]</b>	100
<b>Nozzle Shape</b>	Bell-shaped
<b>Nozzle Correction Factor</b>	1
<b>Oxidiser-to-fuel Ratio Range</b>	$1 \leq OF \leq 10$
<b>Chamber Pressure Range [bar]</b>	$20 \leq P_c \leq 40$
<b>Constant Atmospheric Pressure [bar]</b>	1.01325
<b>Constant Nozzle Expansion Ratio</b>	5.51

Table E.2 Selected output parameters for both test runs.

	<b>Constant Atmospheric Pressure</b>	<b>Constant Expansion Ratio</b>
<b>Nozzle Exit Pressure [bar]</b>	1.01325	1.01325
<b>Combustion Temperature [K]</b>	3211.2	3211.2
<b>Nozzle Expansion Ratio</b>	5.5129	5.5129
<b>Nozzle Exit Velocity [m/s]</b>	2420.3	2420.3
<b>Characteristic Velocity [m/s]</b>	1609.6	1609.6
<b>Thrust Coefficient</b>	1.5037	1.5037
<b>Vacuum Thrust Coefficient</b>	1.6433	1.6433
<b>Specific Impulse [s]</b>	246.7	246.7
<b>Vacuum Specific Impulse [s]</b>	269.6	269.6

**Constant Atmospheric Pressure**



**Constant Expansion Ratio**

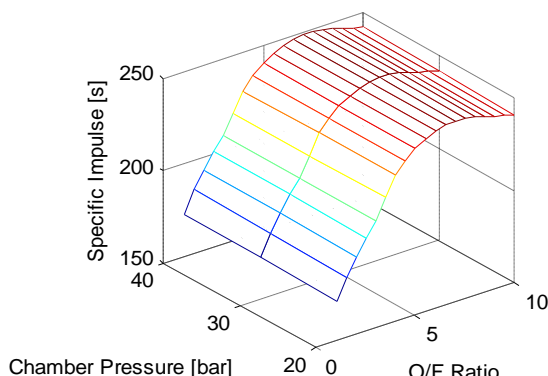
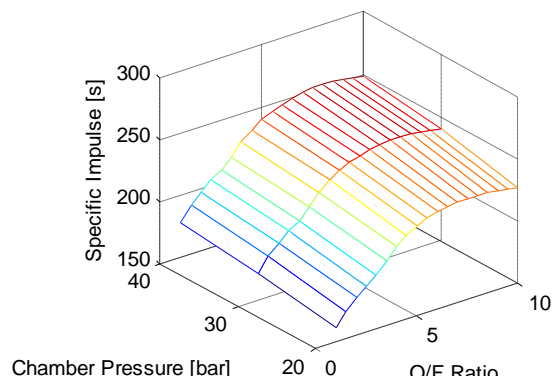
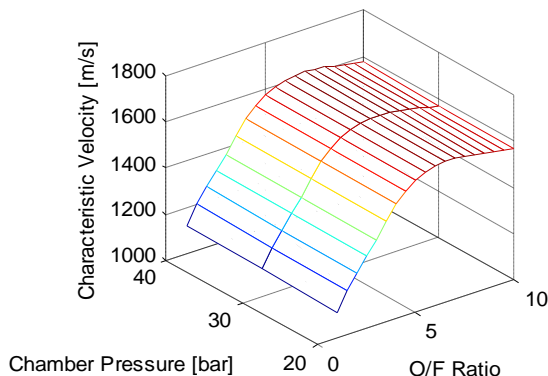
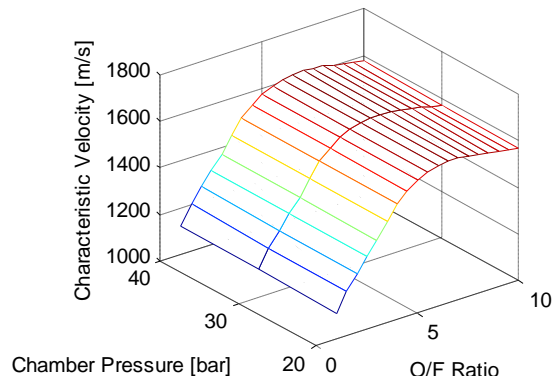
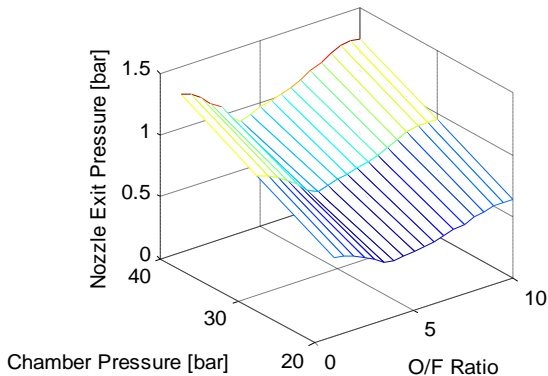


Figure E.1 Selected output graphs for both test runs.

## Appendix E.2

### Bell-Shaped Nozzle Test Run: Output Excel File

\*\*\*\*\*

#### Nozzle Design Contour

\*\*\*\*\*

#### \*\*\*\* INPUTS \*\*\*\*

Nozzle throat diameter	Dt	0.029833 m
Nozzle expansion ratio	ExpRat	5.99
Nozzle contraction ratio	ConRat	8
Nozzle contraction angle	Qc	90 deg
Ratio of upstream to throat radius	Rup/Rt	1.5
Ratio of downstream to throat radius	Rd/Rt	0.382
Nozzle Type	Bell-Shaped Nozzle	
Nozzle parabola inlet angle	Qn	20.75 deg
Nozzle parabola exit angle	Qe	7.5 deg
Nozzle fractional length	Lf	1
Nozzle half cone angle	Alp_c	15 deg

#### \*\*\*\* OUTPUTS \*\*\*\*

Chamber radius	Rni	0.04219 m
Nozzle throat radius	Rt	0.014916 m
Nozzle exit radius	Re	0.036507 m
Nozzle upstream radius	Rup	0.022375 m
Nozzle downstream radius	Rd	0.005698 m
Nozzle length from inlet to throat plane	Lni	0.022375 m
Length from contraction angle position to throat plane	Lcx	0.022375 m
Radius of contraction angle position to throat plane	Hcx	0.037291 m
Nozzle total length from throat to exit plane	Lne	0.081328 m
Nozzle parabolic bell length	Lc	0.07931 m

#### \*\*\*\* Divergent Contour Co-ordinate \*\*\*\*

X co-ordinate [m]

Y co-ordinate [m]

0.002018786	0.0152861
0.012018786	0.018956237
0.022018786	0.022378875
0.032018786	0.025536983
0.042018786	0.028411483
0.052018786	0.030980886
0.062018786	0.033220847
0.072018786	0.035103597
0.081328297	0.036507338

## Conical-Shaped Nozzle Test Run: Output Excel File

\*\*\*\*\*  
Nozzle Design Contour  
\*\*\*\*\*

### \*\*\*\* INPUTS \*\*\*\*

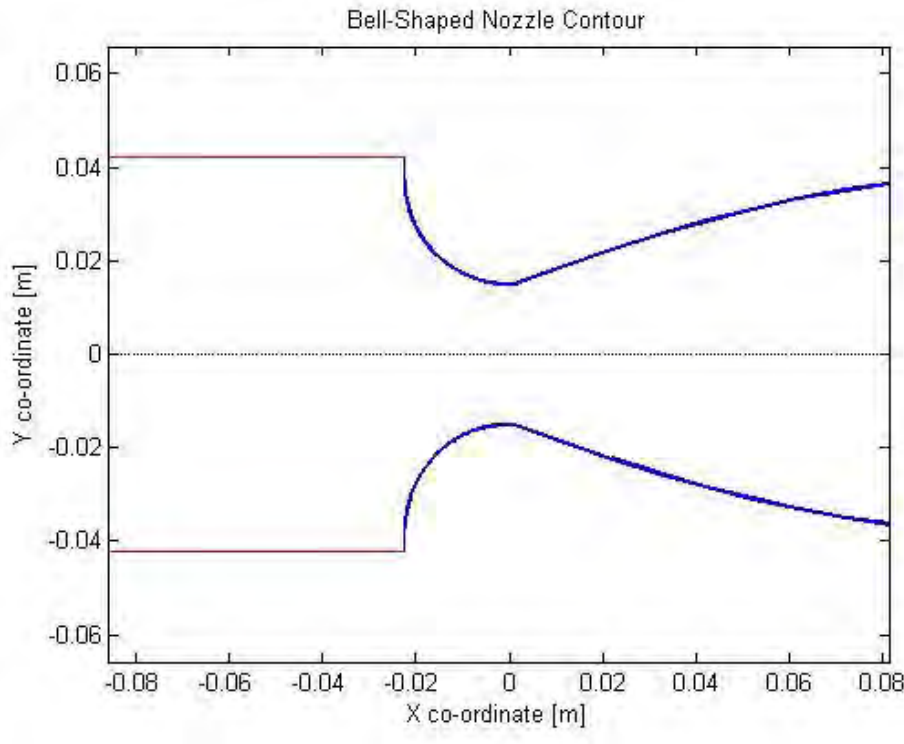
Nozzle throat diameter	Dt	0.029833 m
Nozzle expansion ratio	ExpRat	5.99
Nozzle contraction ratio	ConRat	8
Nozzle contraction angle	Qc	90 deg
Ratio of upstream to throat radius	Rup/Rt	1.5
Ratio of downstream to throat radius	Rd/Rt	0.382
Nozzle Type	Conical-Shaped Nozzle	
Nozzle half cone angle	Alp_c	15 deg

### \*\*\*\* OUTPUTS \*\*\*\*

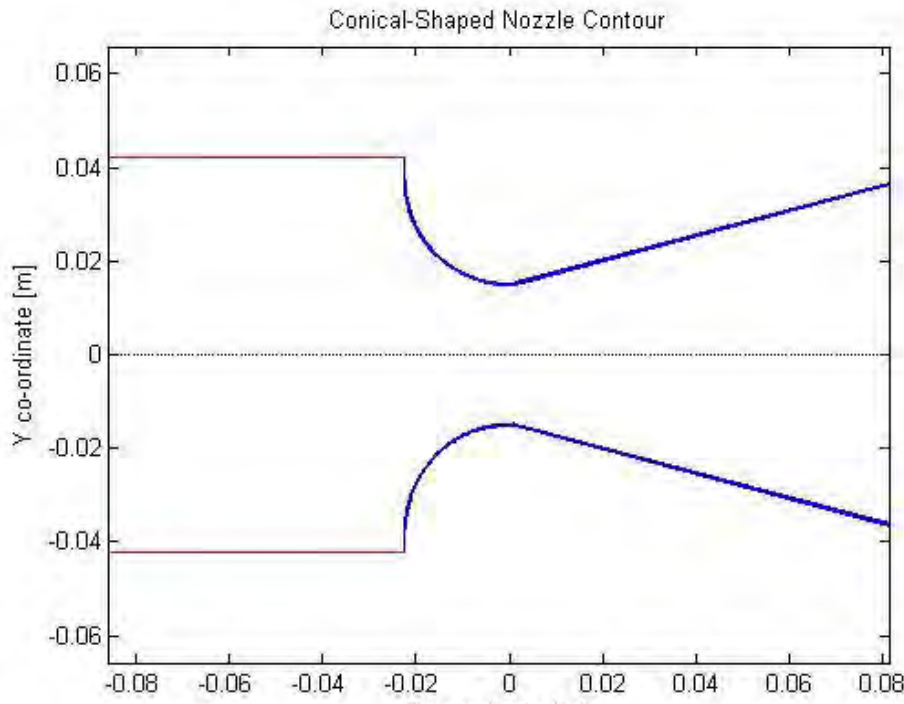
Chamber radius	Rni	0.04219 m
Nozzle throat radius	Rt	0.014916 m
Nozzle exit radius	Re	0.036507 m
Nozzle upstream radius	Rup	0.022375 m
Nozzle downstream radius	Rd	0.005698 m
Nozzle length from inlet to throat plane	Lni	0.022375 m
Length from contraction angle position to throat plane	Lcx	0.022375 m
Radius of contraction angle position to throat plane	Hcx	0.037291 m
Nozzle total length from throat to exit plane	Lne	0.081328 m
Nozzle conical length	Lc	0.079854 m
Conical nozzle correction factor	lambda_c	0.982963

### \*\*\*\* Divergent Contour Co-ordinate \*\*\*\*

X co-ordinate [m]	Y co-ordinate [m]
0.001474777	0.015110652
0.081328297	0.036507338



(a)



(b)

Figure E.2 Graphical output of test run (a) Bell-shaped, and (b) Conical-shaped.

## **APPENDIX F**

### **Phoenix-1A Propulsion System Design**

## Appendix F.1

### Fuel Grain and Nozzle Designs

Table F.1 PV-1 motor fuel grain and nozzle designs for various altitudes.

		Design 1			Design 2		
INPUTS: FUEL GRAIN AND NOZZLE DESIGNS	Altitude	m	0		1000		
	Thrust	N	4250				
	OF		6	7	8	6	7
	$P_c$	bar	40				
	$P_a$	bar	1.01325		0.8987		
	$D_{p,i}$	m	0.05				
	$a$		0.000155				
	$n$		0.5				
	$\eta_{eff}$	%	100				
	Flow Composition		Equilibrium				
OUTPUTS: FUEL GRAIN AND NOZZLE DESIGNS	Burn Time	s	20				
	$P_{1st}$		0.9931	0.9938	0.9945	0.9942	0.9947
	$P_{2nd}$		0.2383	0.2314	0.2227	0.2216	0.2150
	$P_{3rd}$		0.0253	0.0253	0.0253	0.0225	0.0225
	$c^*$	m/s	1609.6	1619.6	1610.4	1609.6	1619.6
	$C_F$		1.5037	1.5187	1.5364	1.5202	1.5359
	$\varepsilon_r$		5.5129	5.7683	6.1099	5.9973	6.2788
	$D_t$	m	0.02999	0.02985	0.02967	0.02983	0.02968
	$D_e$	m	0.07042	0.07168	0.07335	0.07305	0.07437
	$\dot{m}_{ox,p}$	kg/s	1.5051	1.5112	1.5268	1.4887	1.4950
	$\dot{m}_{f,p}$	kg/s	0.2508	0.2159	0.1906	0.2481	0.2136
	$\dot{m}_{noz}$	kg/s	1.7559	1.7279	1.7177	1.7369	1.7085
	$L_g$	m	0.4001	0.3437	0.3023	0.3980	0.3418
	$D_g$	m	0.1402	0.1404	0.1407	0.1399	0.1400
	$V_{f,i}$	$m^3$	0.00539	0.00464	0.00410	0.00533	0.00459
				0.00406			

Table F.1 PV-1 motor fuel grain and nozzle designs for various altitudes.

	$M_{f,i}$	kg	5.0169	4.3197	3.8171	4.9625	4.2713	3.7721			
			Design 3			Design 4					
DESIGNS	Altitude	m	2000			3000					
	Thrust	N	4250								
	OF		6	7	8	6	7	8			
	$P_c$	bar	40								
	$P_a$	bar	0.7949			0.7009					
	$D_{p,i}$	m	0.05								
	$a$		0.0000155								
	$n$		0.5								
	$\eta_{eff}$		100								
	Flow Composition		Equilibrium								
OUTPUTS: FUEL GRAIN AND NOZZLE DESIGNS	Burn Time	s	20								
	$P_{1st}$		0.9951	0.9956	0.9961	0.9959	0.9963	0.9968			
	$P_{2nd}$		0.2054	0.1993	0.1914	0.1899	0.1841	0.1768			
	$P_{3rd}$		0.0199	0.0199	0.0199	0.0175	0.0175	0.0175			
	$c^*$	m/s	1609.6	1619.6	1610.4	1609.6	1619.6	1610.4			
	$C_F$		1.5364	1.5529	1.5727	1.5525	1.5697	1.5906			
	$\varepsilon_r$		6.5401	6.8509	7.2657	7.1509	7.495	7.953			
	$D_t$	m	0.02967	0.02952	0.02933	0.02952	0.02936	0.02916			
	$D_e$	m	0.07589	0.07725	0.07906	0.07894	0.08037	0.08224			
	$\dot{m}_{ox,p}$	kg/s	1.4730	1.4786	1.4916	1.4578	1.4628	1.4748			
	$\dot{m}_{f,p}$	kg/s	0.2455	0.2112	0.1864	0.2429	0.2089	0.1843			
	$\dot{m}_{noz}$	kg/s	1.7186	1.6898	1.6780	1.7007	1.6717	1.6591			
	$L_g$	m	0.3959	0.3399	0.2988	0.3938	0.3381	0.2971			
	$D_g$	m	0.1396	0.1397	0.1399	0.1393	0.1394	0.1396			
	$V_{f,i}$	$m^3$	0.00528	0.00454	0.00401	0.00522	0.00449	0.00396			
	$M_{f,i}$	kg	4.9102	4.2246	3.7289	4.8592	4.1794	3.6			

## Appendix F.2

### PV-1 Motor Design

Table F.2 PV-1 motor selected design 2 for optimum nozzle expansion at 1000 m altitude.

Selected Design 2			
INPUTS: HRPC	$M_{N_2O}$	kg	30
	$M_{He}$	kg	0.004
	$T_{T,i}$	K	298
	$V_{T,i}$	$m^3$	0.043
	Opt. Nozzle Atm. Pres.	bar	0.8987 (1000 m altitude)
	$C_{d,l}$		0.8
	$C_{d,g}$		0.5
	$D_{inj}$	m	0.002
	$N_{inj}$		17
	$P_{loses}$	bar	5
	$V_{f,c}$	kg/m <sup>3</sup>	0.002867
	$\eta_{eff}$		95
	Nozzle Shape		Bell-shaped
	$\lambda$		0.9829
	$P_a$	bar	0.7009 (mid-altitude)      1.01325 (sea-level)
Liquid Burnout			
OUTPUTS: HRPC	$t_b$	s	19.814      19.814
	$M_{f,i}$	kg	6.379
	$M_{f,f}$	kg	1.664
	$\langle \dot{m}_{ox,t} \rangle$	kg/s	1.359      1.359
	$\langle \dot{m}_{f,t} \rangle$	kg/s	0.238      0.238
	$\langle \dot{m}_t \rangle$	kg/s	1.598      1.598
	$\langle \dot{m}_{noz} \rangle$	kg/s	1.597      1.597
	$\langle G_{ox,p} \rangle$	kg/(m <sup>2</sup> s)	222.03      222.03
	$\langle \dot{r} \rangle$	m/s	0.00218      0.00218

Table F.2 PV-1 motor selected design 2 for optimum nozzle expansion at 1000 m altitude.

OUTPUTS: HRPC	< OF >		5.699	5.699
	< $P_c$ >	bar	34.716	34.717
	< $P_e$ >	bar	0.7694	0.7694
	< $V_e$ >	m/s	2392.9	2392.7
	< $V_{exh}$ >	m/s	2289.1	2206.4
	< $c^*$ >	m/s	1518.9	1518.9
	< $C_F$ >		1.507	1.452
	< $F$ >	N	3659.8	3528.9
	< $F_{vac}$ >	N	3953.6	3953.6
	< $F_{mom}$ >	N	3631.2	3631.2
	< $I_{sp}$ >	s	233.3	225.9
	< $I_{vac}$ >	s	252.3	252.3
	< $I_t$ >	Ns	72515.8	69922.1
Gaseous Burnout at 25 s				
OUTPUTS: HPC	$t_b$	s	25	
	$M_{f,i}$	kg	6.379	
	$M_{f,f}$	kg	1.074	
	< $\dot{m}_{ox,t}$ >	kg/s	1.143	1.143
	< $\dot{m}_{f,t}$ >	kg/s	0.212	0.212
	< $\dot{m}_t$ >	kg/s	1.355	1.355
	< $\dot{m}_{noz}$ >	kg/s	1.355	1.355
	< $G_{ox,p}$ >	kg/(m <sup>2</sup> s)	180.22	180.22
	< $\dot{r}$ >	m/s	0.00187	0.00187
	< OF >		5.084	5.084
	< $P_c$ >	bar	29.152	29.152
	< $P_e$ >	bar	0.6485	0.6485
	< $V_e$ >	m/s	2308.2	2308.2
	< $V_{exh}$ >	m/s	2094.6	1962.9
	< $c^*$ >	m/s	1467.1	1467.1
	< $C_F$ >		1.414	1.319
	< $F$ >	N	3025.9	2895

Table F.2 PV-1 motor selected design 2 for optimum nozzle expansion at 1000 m altitude.

<b>OUTPUTS: HRPC</b>	$\langle F_{vac} \rangle$	N	3319.7	3319.7
	$\langle F_{mom} \rangle$	N	3047.9	3047.9
	$\langle I_{sp} \rangle$	s	213.5	200.1
	$\langle I_{vac} \rangle$	s	243.7	243.7
	$\langle I_t \rangle$	Ns	75648.3	72375.5

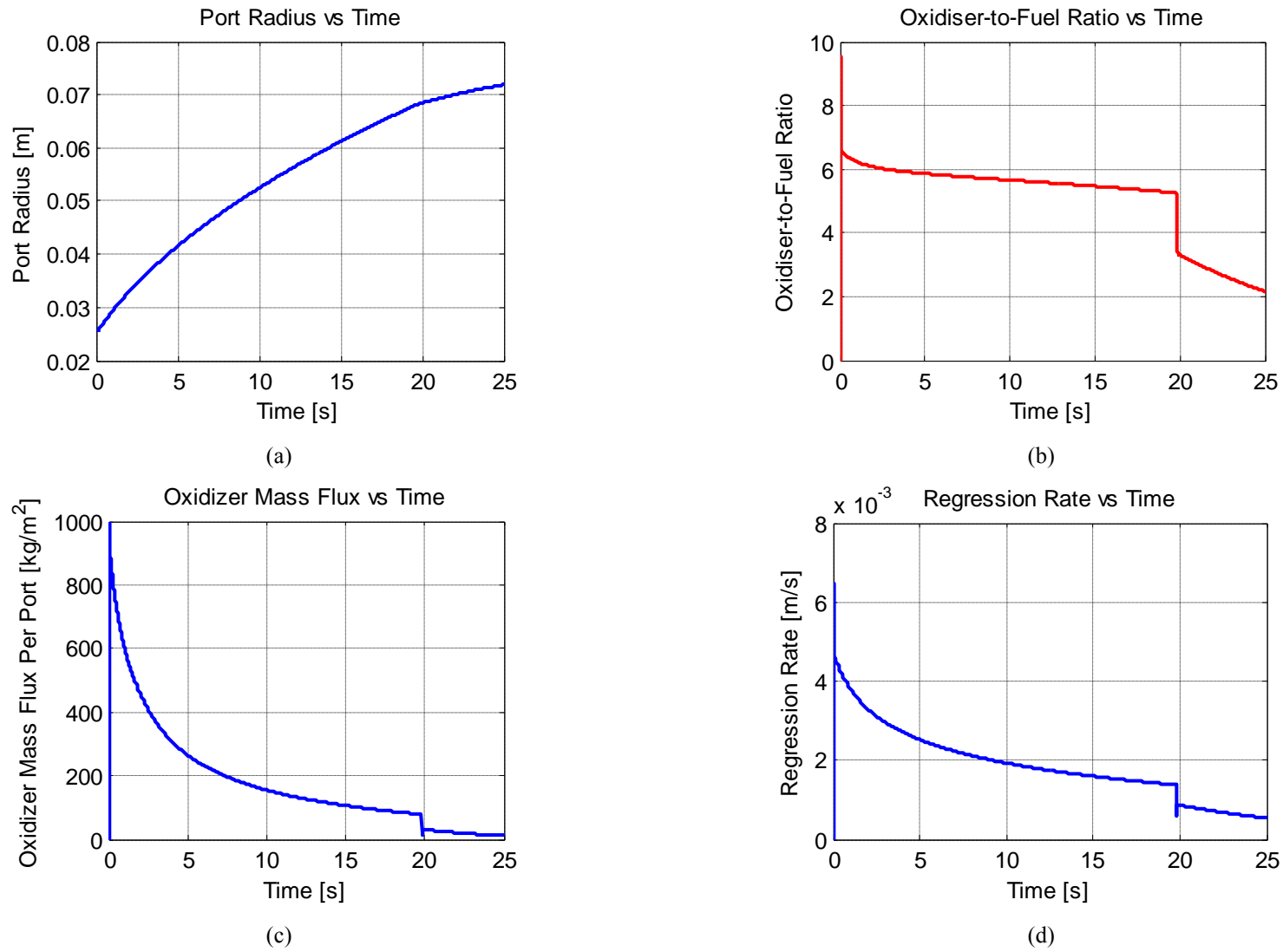
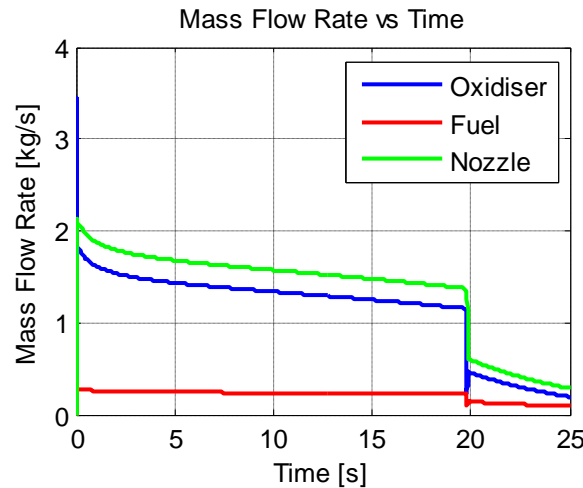
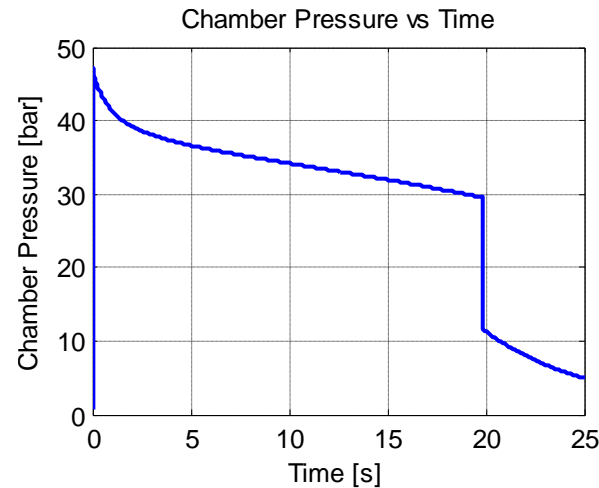


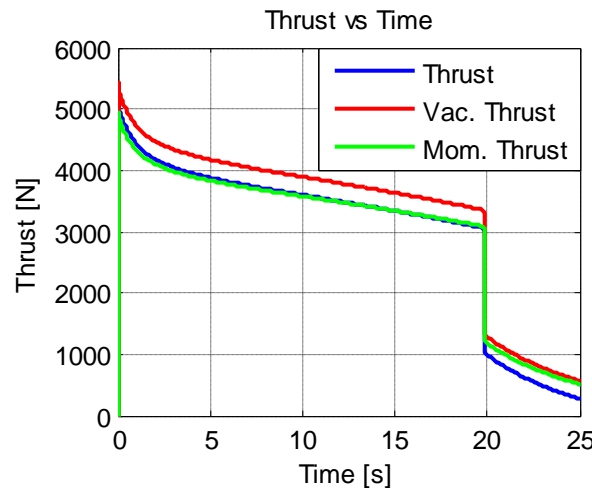
Figure F.1 PV-1 hybrid rocket motor performance at atmospheric pressure of 0.7009 bar (mid-altitude), including gaseous blowdown: (a) Port radius, (b) Oxidiser-to-fuel ratio, (c) Oxidiser mass flux, and (d) Regression rate.



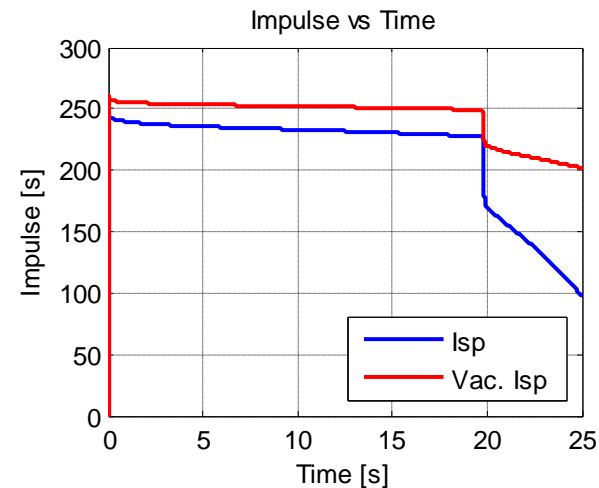
(e)



(f)

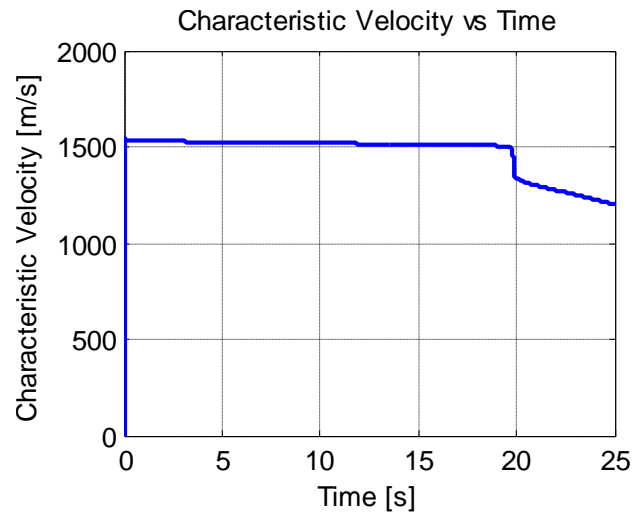


(g)

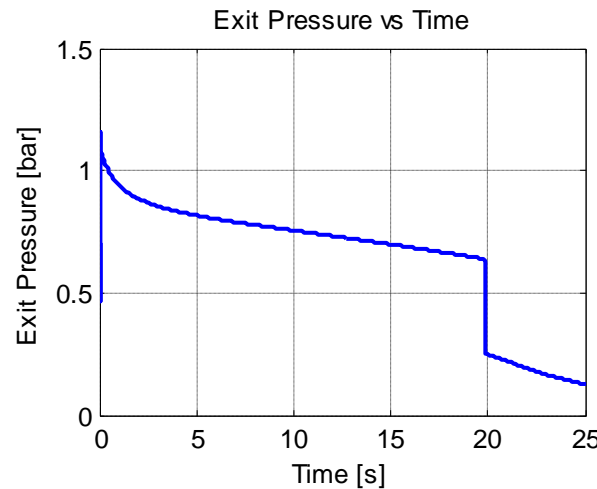


(h)

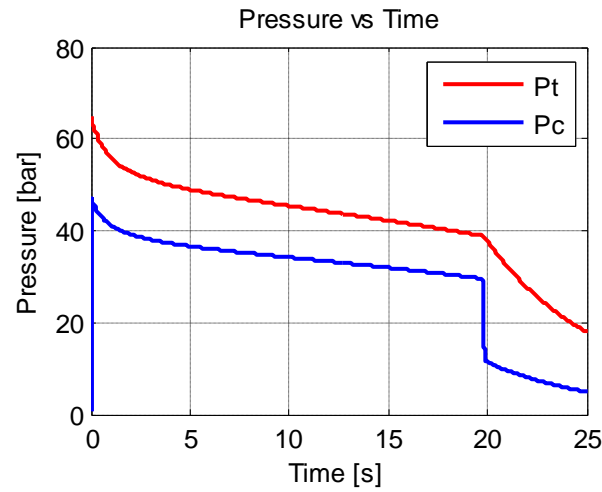
Figure F.1 PV-1 hybrid rocket motor performance at atmospheric pressure of 0.7009 bar (mid-altitude), including gaseous blowdown: (e) Mass flow rate, (f) Chamber pressure, (g) Thrust, and (h) Impulse.



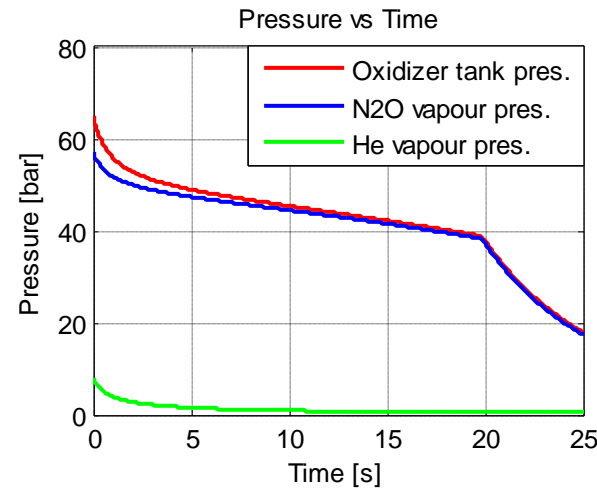
(i)



(j)

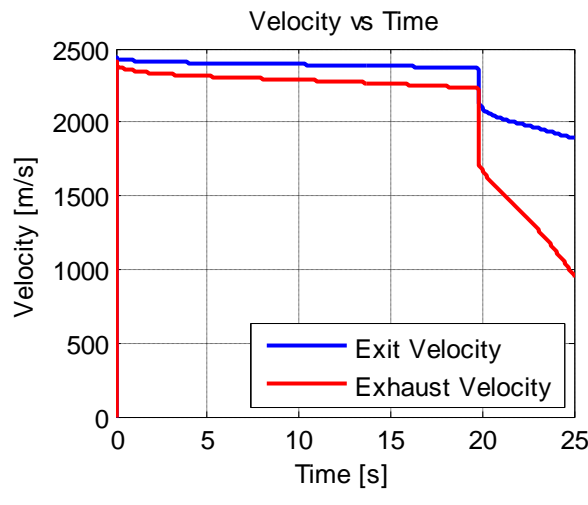


(k)

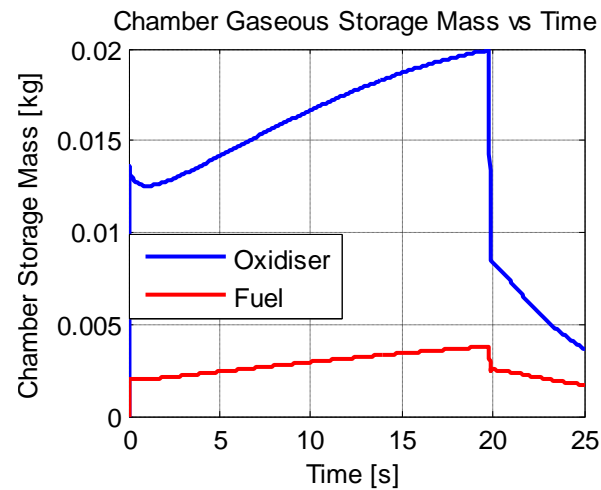


(l)

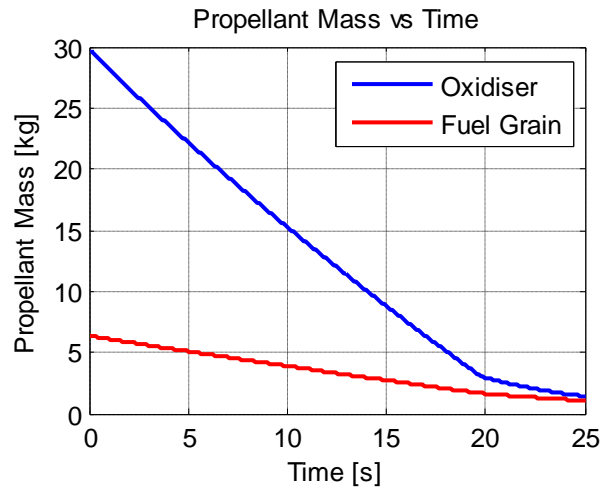
Figure F.1 PV-1 hybrid rocket motor performance at atmospheric pressure of 0.7009 bar (mid-altitude), including gaseous blowdown: (i) Characteristic velocity, (j) Nozzle exit pressure, (k) Tank and chamber pressures, and (l) Tank pressures.



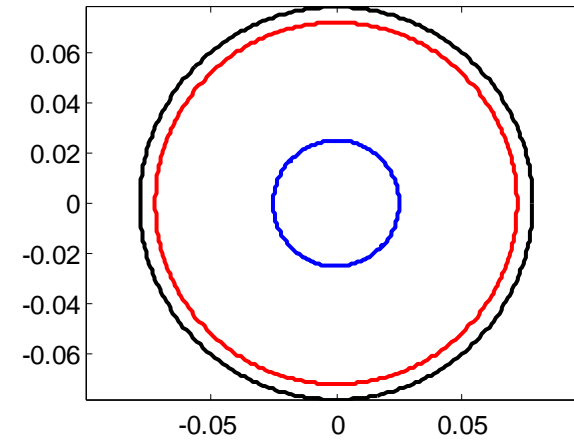
(m)



(n)



(o)

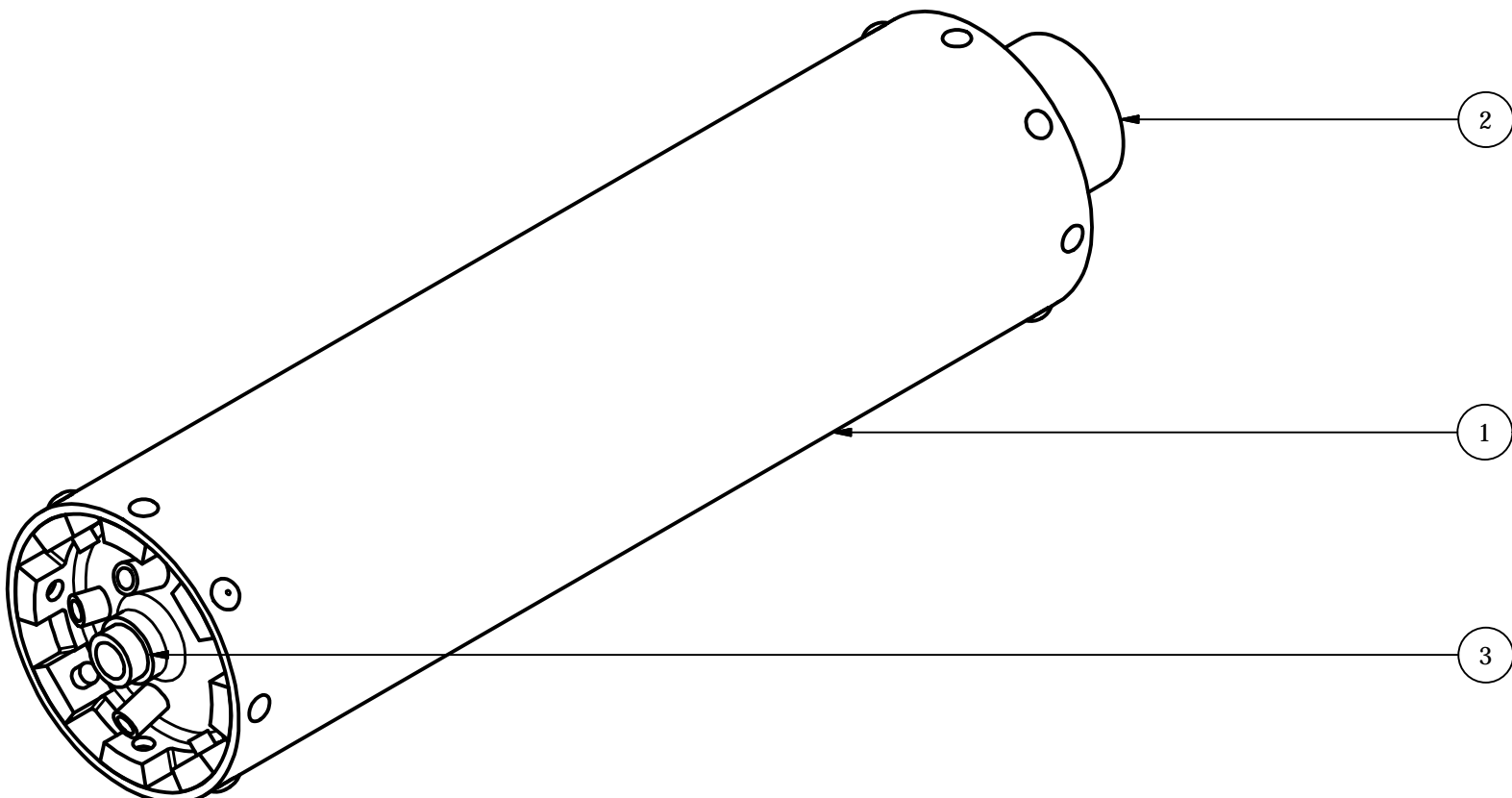


(p)

Figure F.1 PV-1 hybrid rocket motor performance at atmospheric pressure of 0.7009 bar (mid-altitude), including gaseous blowdown: (m) Nozzle gas velocity, (n) Chamber gaseous mass storage, (o) Propellant masses, and (p) Fuel grain 2D representation.

## **APPENDIX G**

### **PV-1 Motor Drawings**



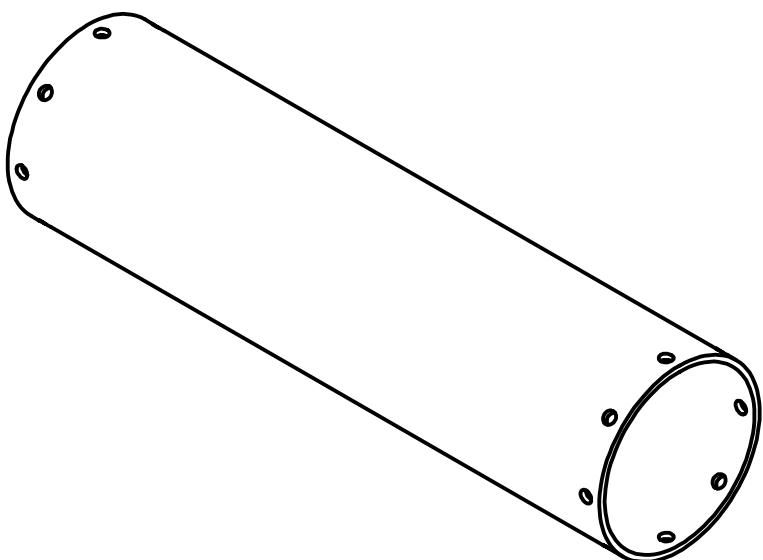
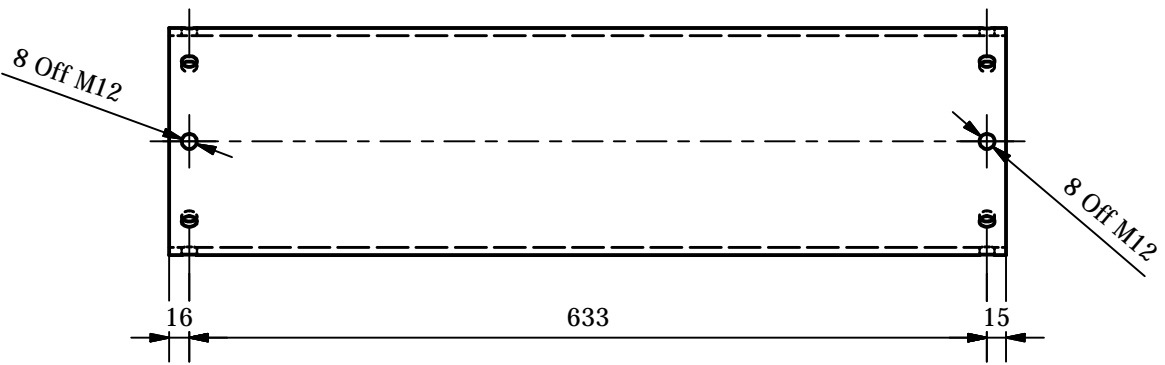
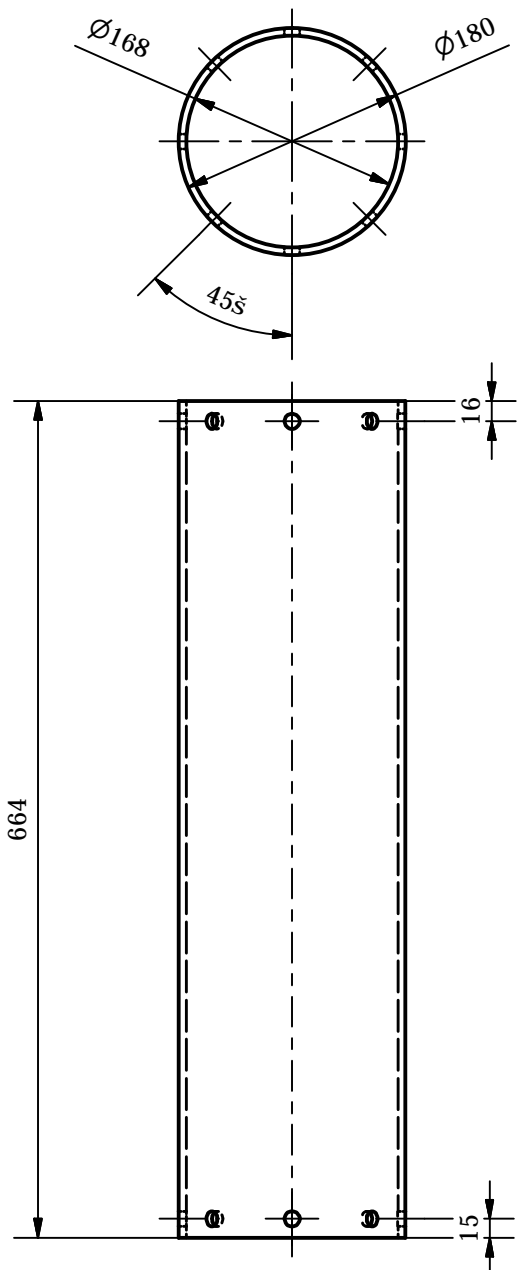
PARTS LIST				
ITEM	QTY	PART NUMBER	DESCRIPTION	
1	1	Chamber Casing	Aluminium 6082-T6	
2	1	Nozzle Retainer	Stainless Steel 431	
3	1	Injector Bulkhead	Stainless Steel 431	



School of Mechanical  
Engineering

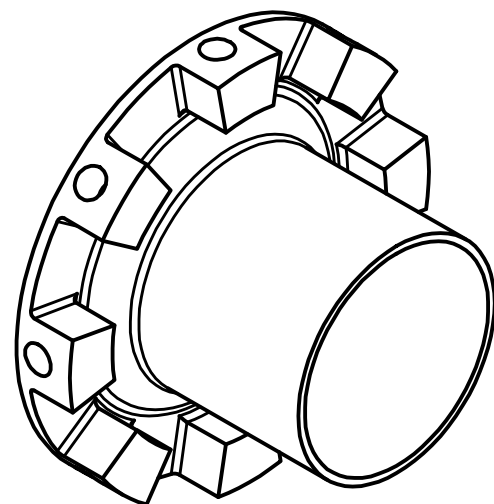
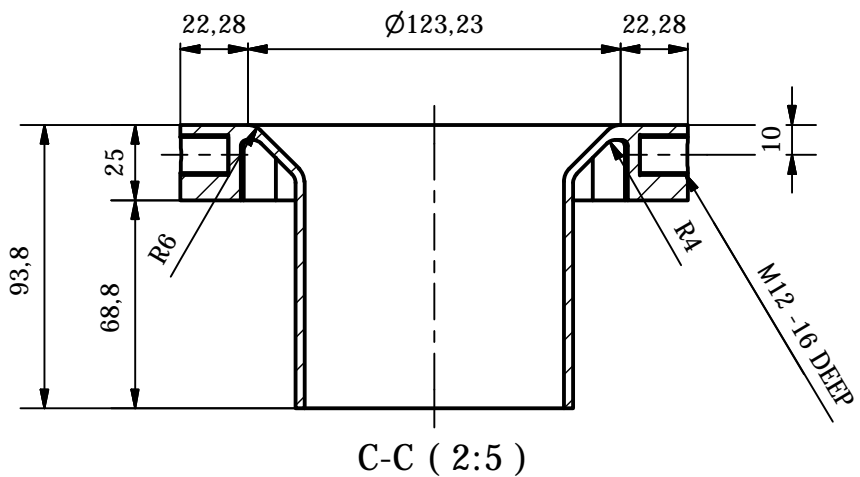
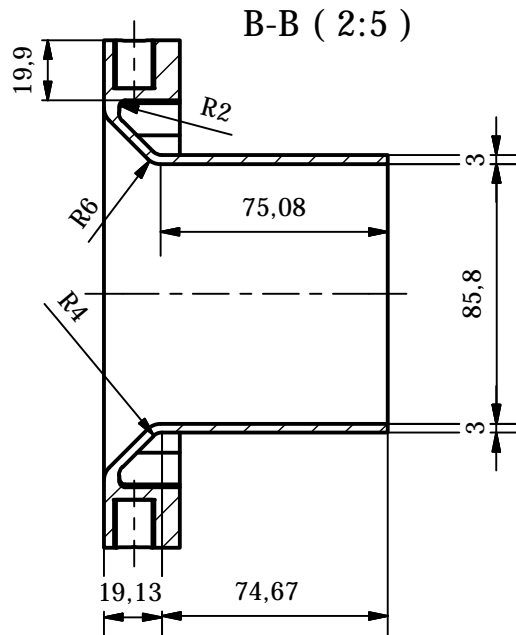
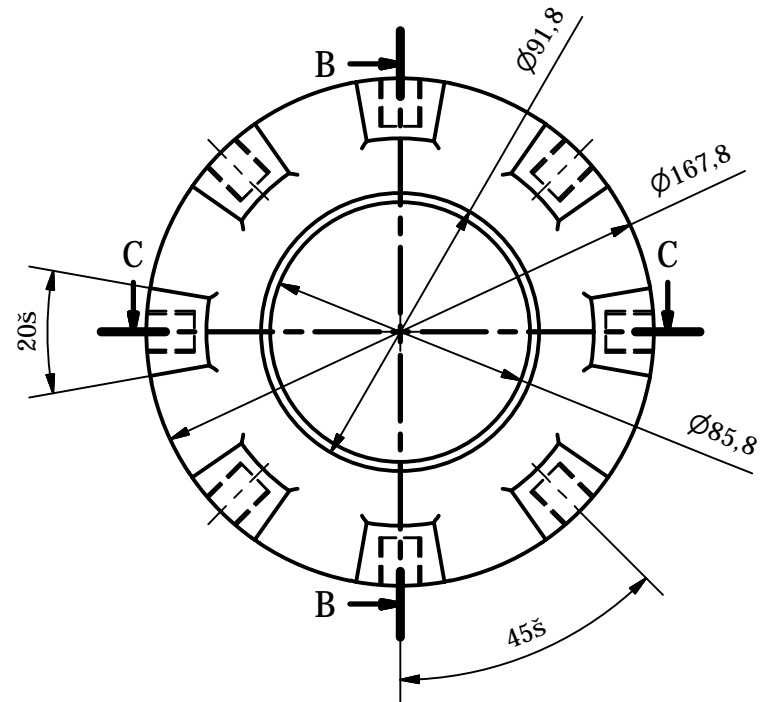
PROJECT SUPERVISOR	DATE	CHECKED	SCALE 1:4	UNITS : mm	PROJECT Phoenix-1A Hybrid Rocket	NO.
W'SHOP TECHNICIAN			STUDENT NAME	Bernard Genevieve		
TECHNICAL OFFICER			E-MAIL	206504262@stu.ukzn.ac.za		



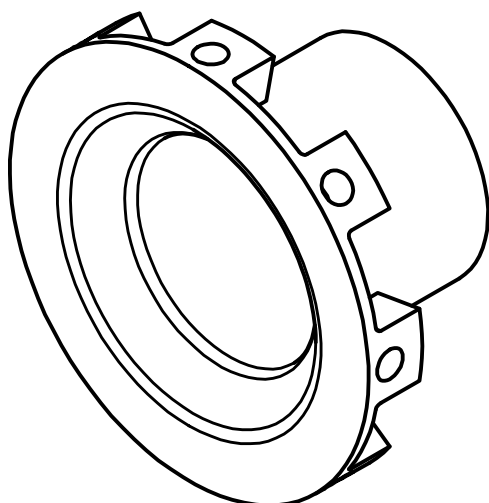
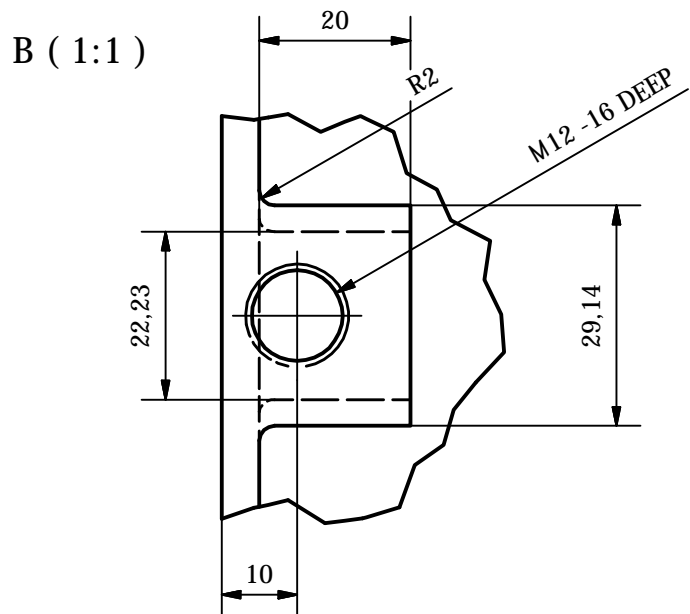
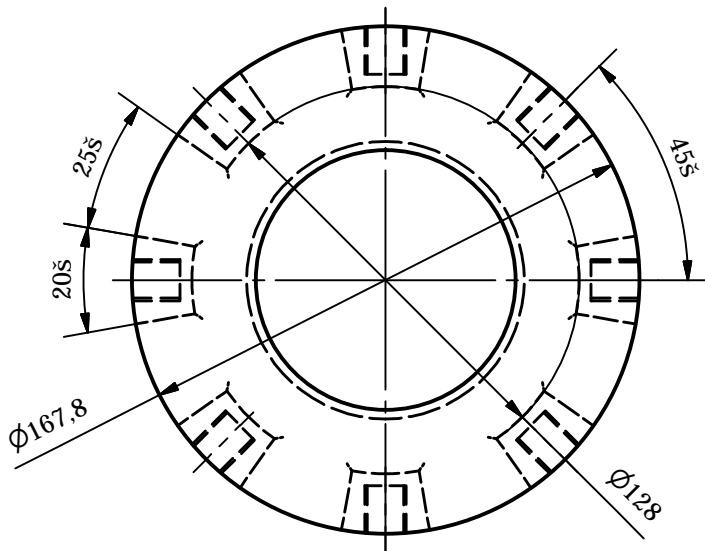
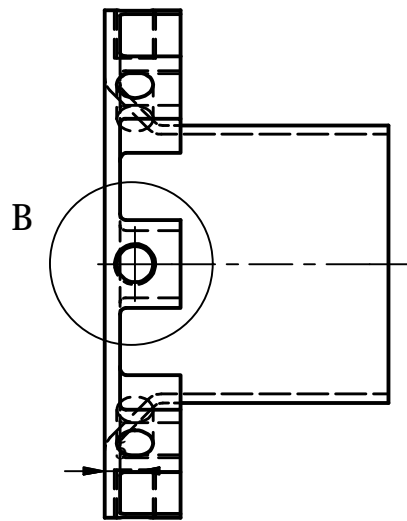


School of Mechanical  
Engineering

PROJECT SUPERVISOR	DATE	CHECKED	SCALE 1:6	UNITS : mm	PROJECT	NO.
				STUDENT NAME Bernard Genevieve	Phoenix-1A Hybrid Rocket	1
W'SHOP TECHNICIAN				E-MAIL 206504262@stu.ukzn.ac.za		
TECHNICAL OFFICER				TEL NO.	TITLE Chamber Casing	



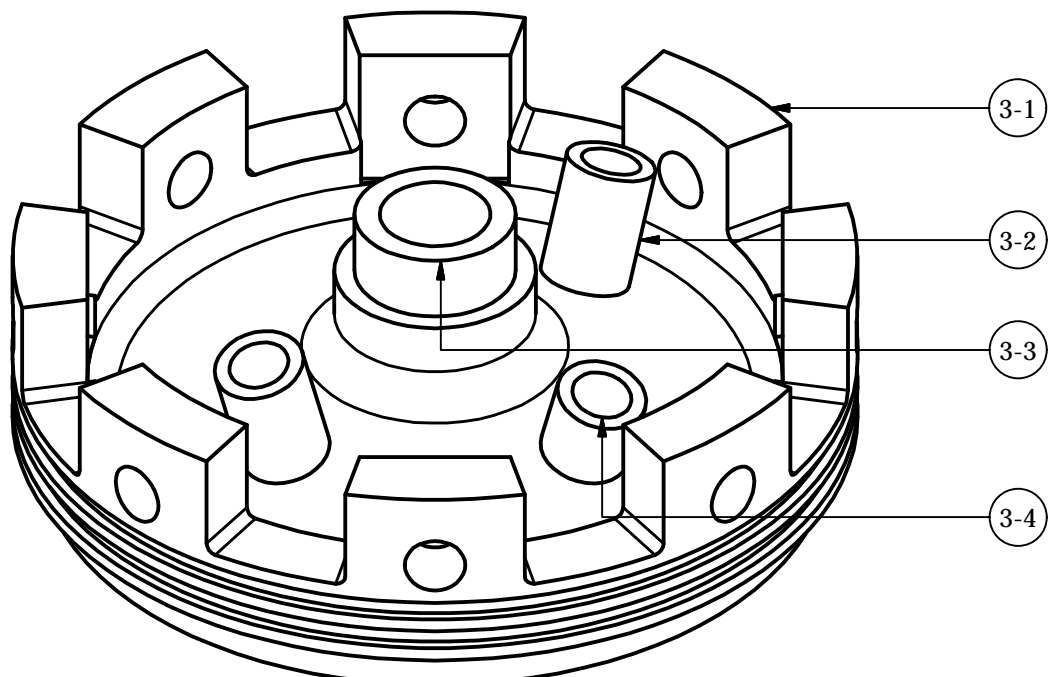
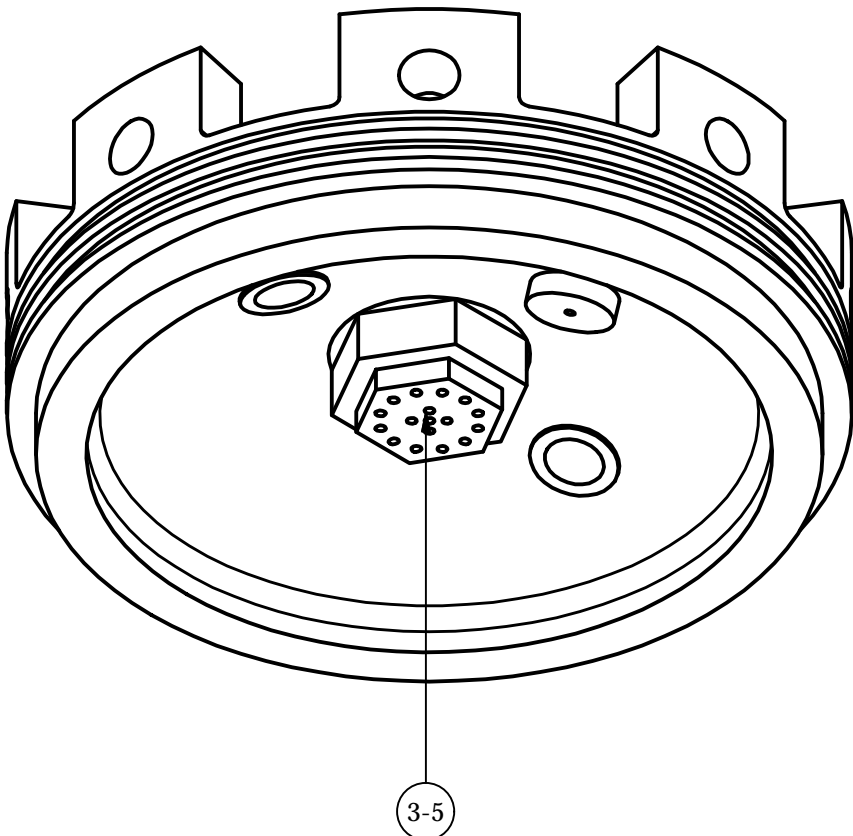
School of Mechanical  
Engineering



School of Mechanical  
Engineering

PROJECT	Phoenix-1A Hybrid Rocket	NO.
PROJECT SUPERVISOR	Bernard Genevieve	2
WSHOP TECHNICIAN	E-MAIL 206504262@stu.ukzn.ac.za	
TECHNICAL OFFICER	TEL NO.	
TITLE	Nozzle Retainer	





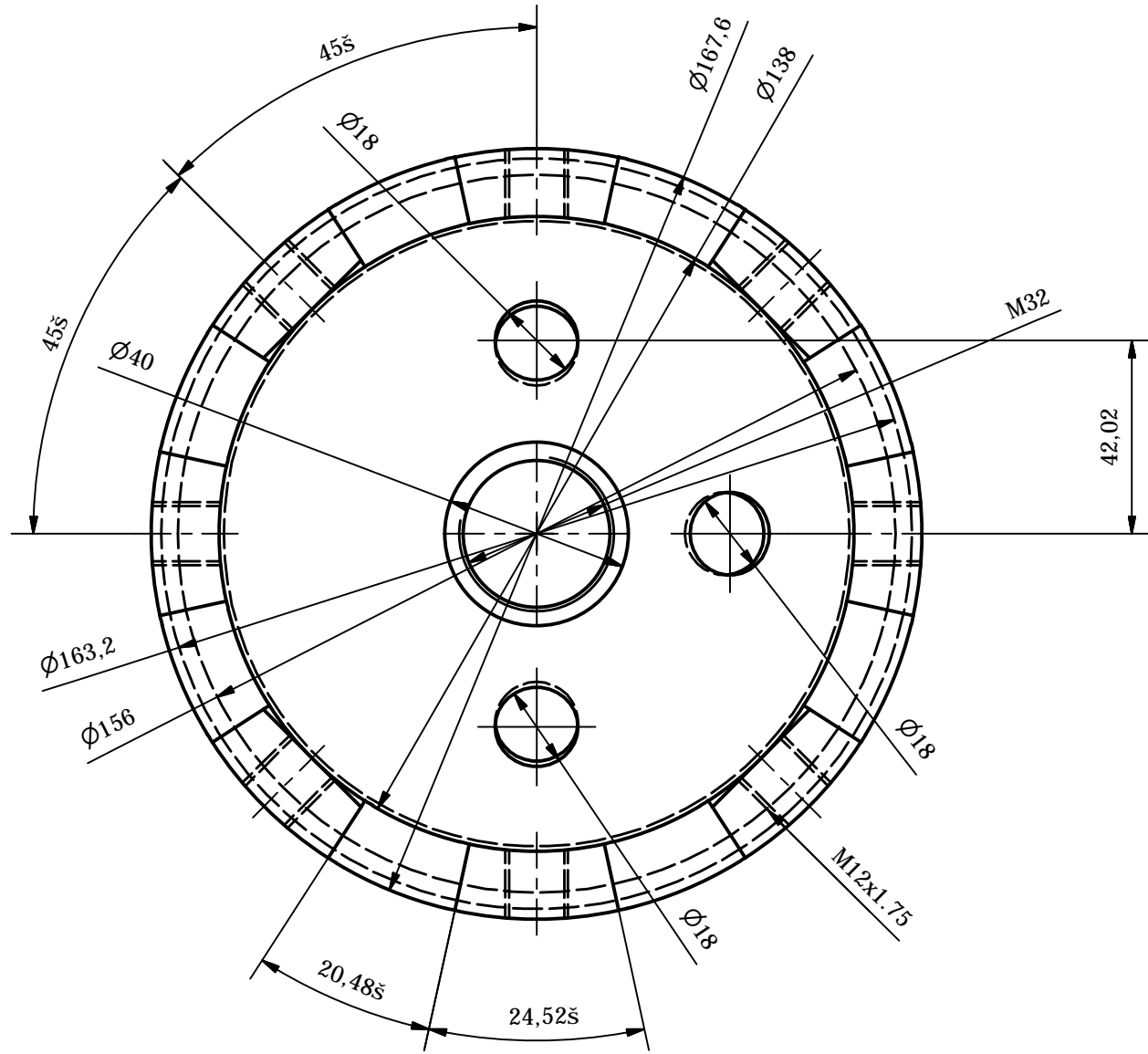
## PARTS LIST

ITEM	QTY	PART NUMBER	DESCRIPTION
3-1	1	Injector Bulk Head	Stainless Steel 431
3-2	2	Igniter Housing	Stainless Steel 431
3-3	1	Injector Manifold	Stainless Steel
3-4	1	Pressure Sensor Housing	Stainless Steel 431
3-5	2	Injector	Stainless Steel



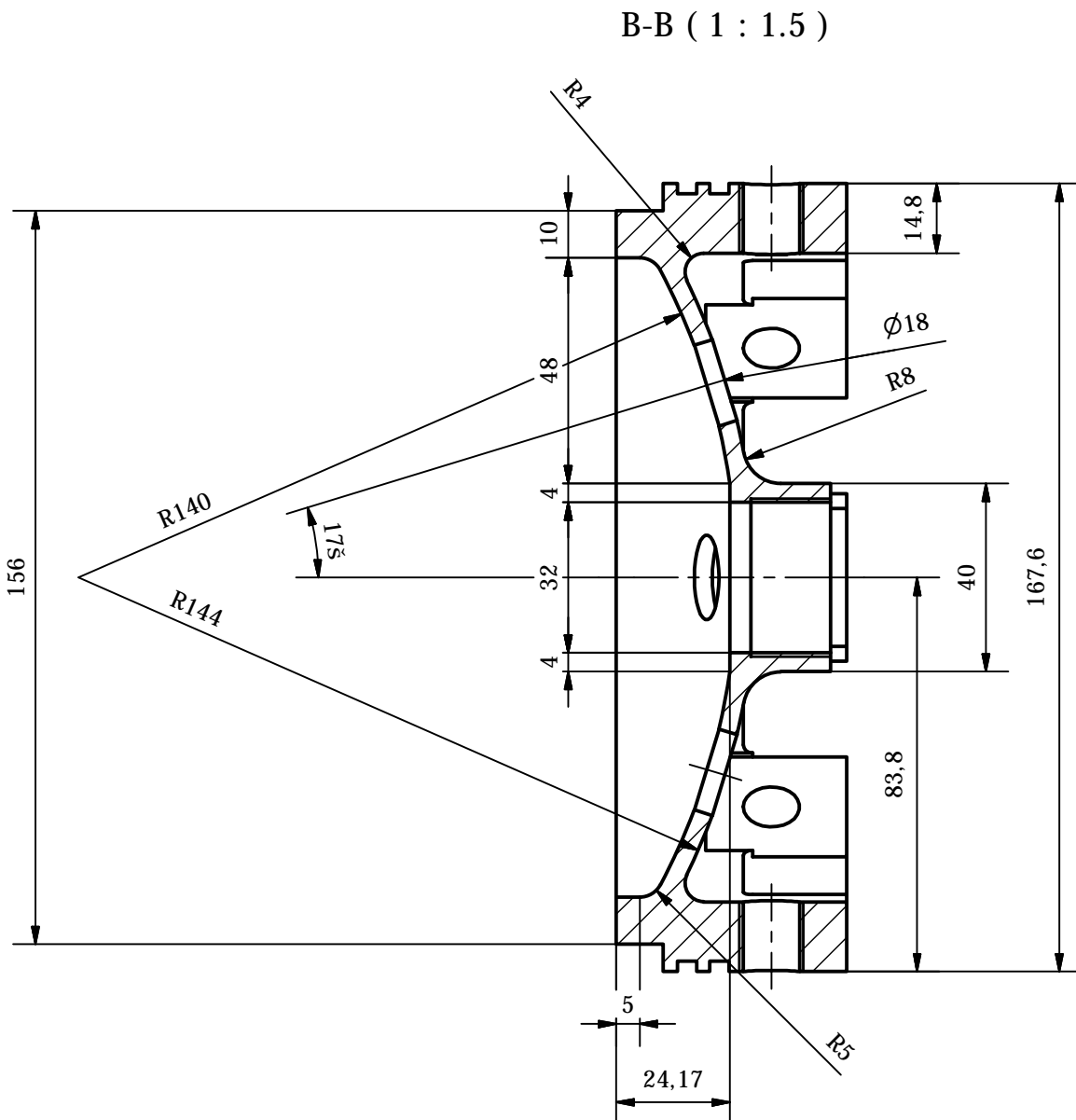
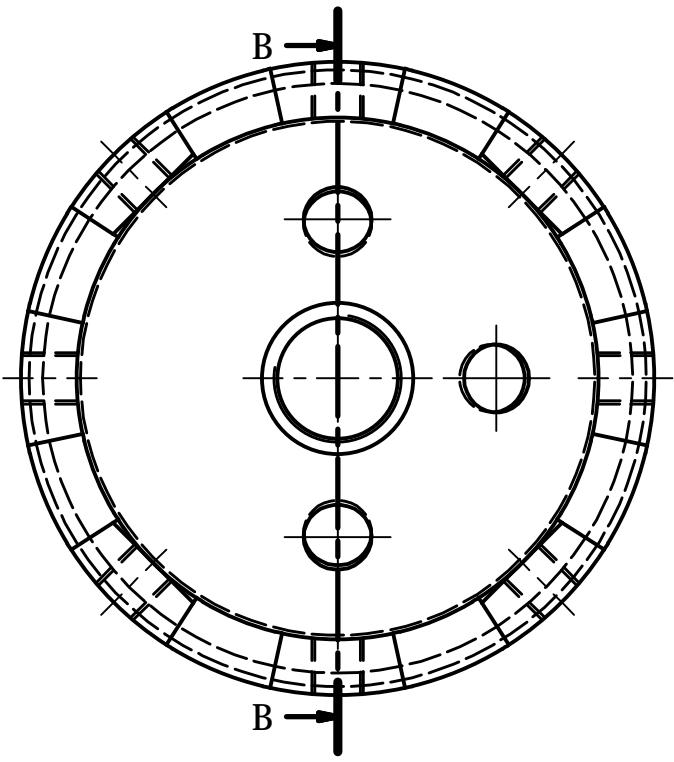
School of Mechanical  
Engineering

PROJECT SUPERVISOR	DATE	CHECKED	SCALE 2:3	UNITS : mm	PROJECT Phoenix-1A Hybrid Rocket	NO. 3		
W'SHOP TECHNICIAN			STUDENT NAME Bernard Genevieve					
TECHNICAL OFFICER			E-MAIL 206504262@stu.ukzn.ac.za					
			TEL NO.		TITLE Injector Bulkhead Assembly			



School of Mechanical  
Engineering

PROJECT SUPERVISOR		DATE	CHECKED	SCALE 2:3	UNITS : mm	PROJECT Phoenix-1A Hybrid Rocket	NO. 3-1
				STUDENT NAME	Bernard Genevieve		
				E-MAIL	206504262@stu.ukzn.ac.za		
				TEL NO.			

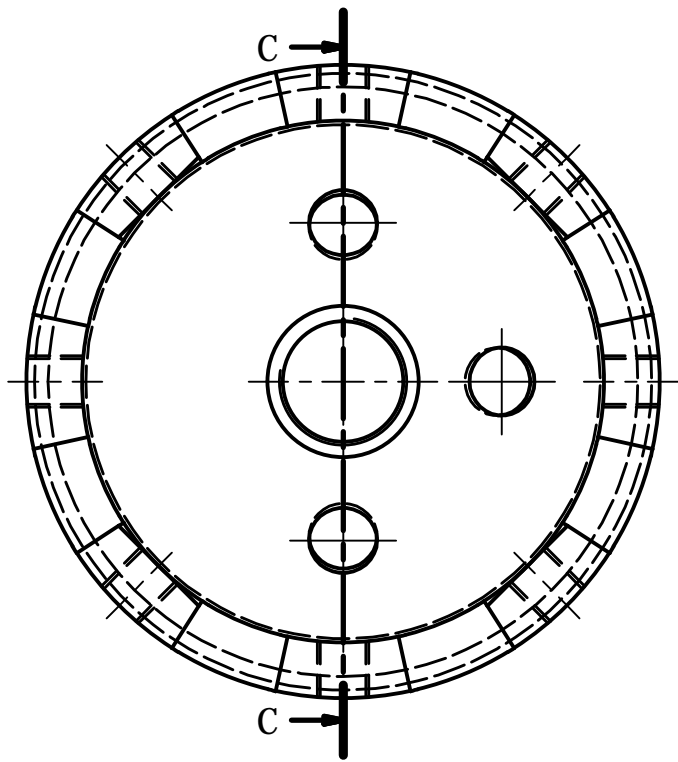


B-B ( 1 : 1.5 )

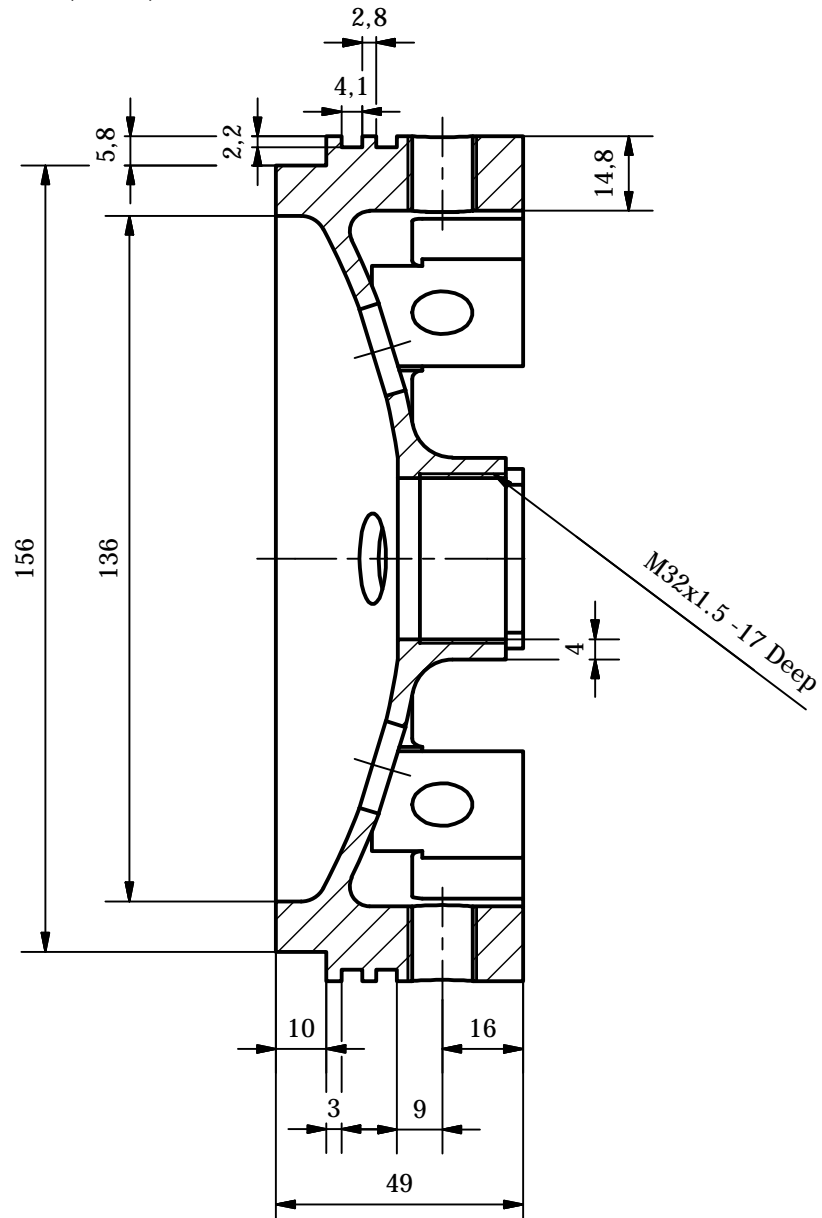


School of Mechanical  
Engineering

	DATE	CHECKED	SCALE 1:2	UNITS : mm	PROJECT	NO.
PROJECT SUPERVISOR				STUDENT NAME Bernard Genevieve	Phoenix-1A Hybrid Rocket	3-1
WSHOP TECHNICIAN				E-MAIL 206504262@stu.ukzn.ac.za		
TECHNICAL OFFICER				TEL NO.	TITLE Injector Bulkhead	



C-C ( 2:3 )



School of Mechanical  
Engineering

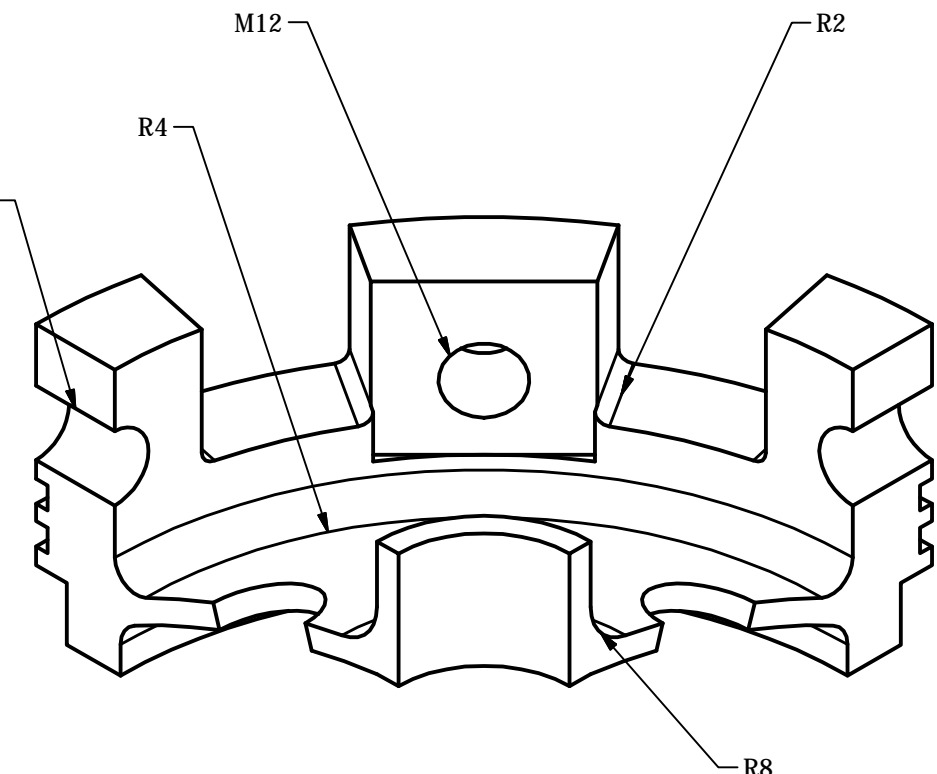
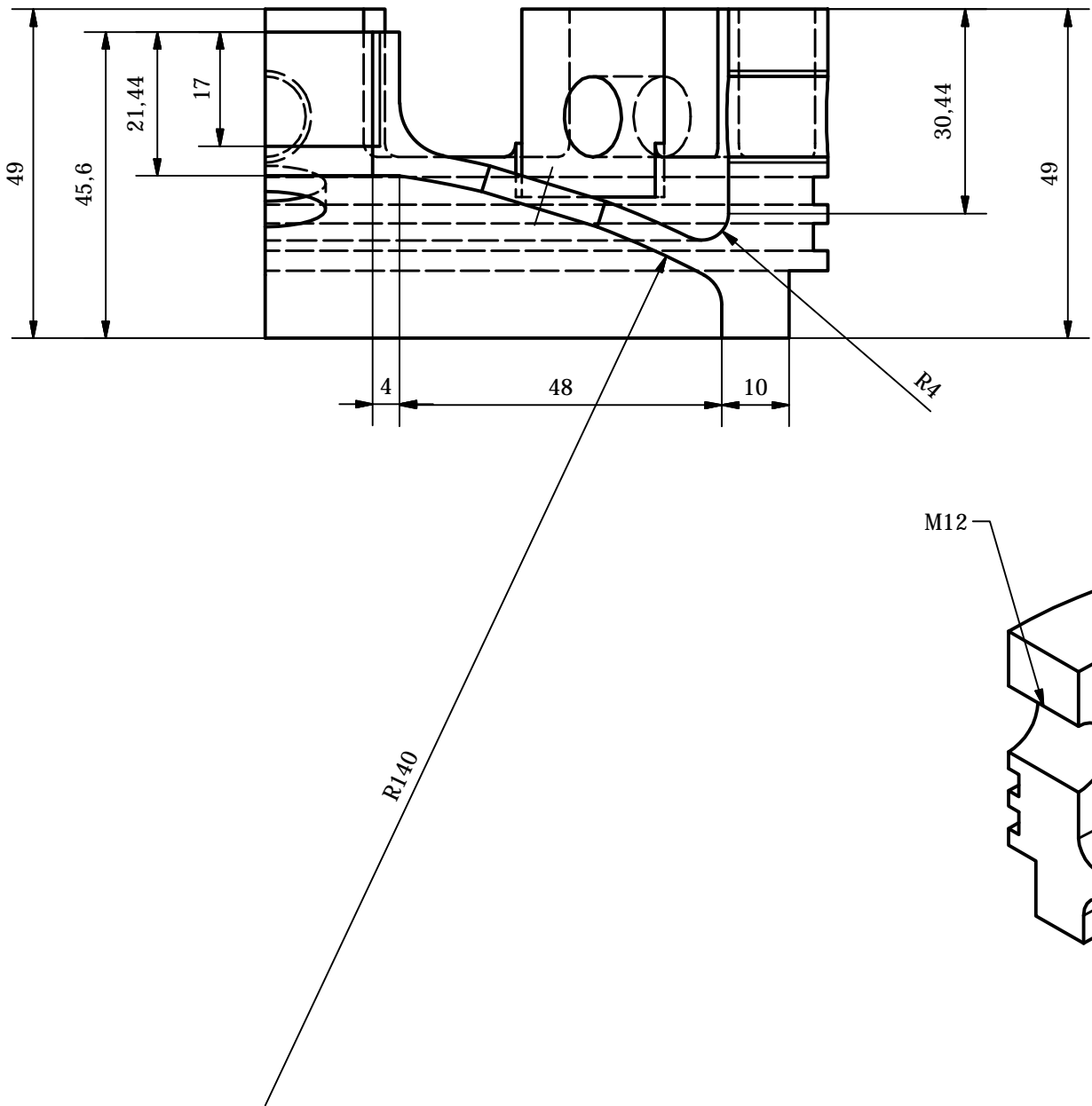
	DATE	CHECKED	SCALE 1:2	UNITS : mm
PROJECT SUPERVISOR			STUDENT NAME	Bernard Genevieve
W'SHOP TECHNICIAN			E-MAIL	206504262@stu.ukzn.ac.za
TECHNICAL OFFICER			TEL NO.	

PROJECT  
Phoenix-1A Hybrid Rocket

NO.  
3-1

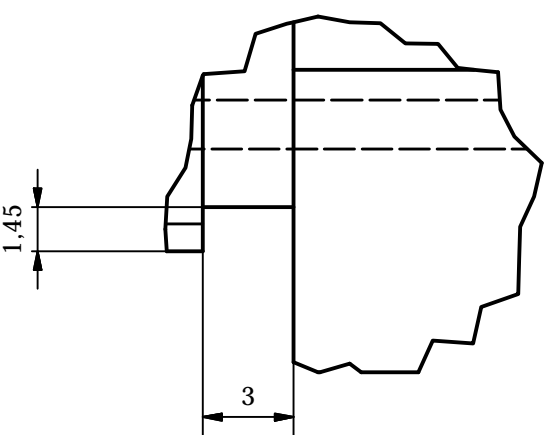
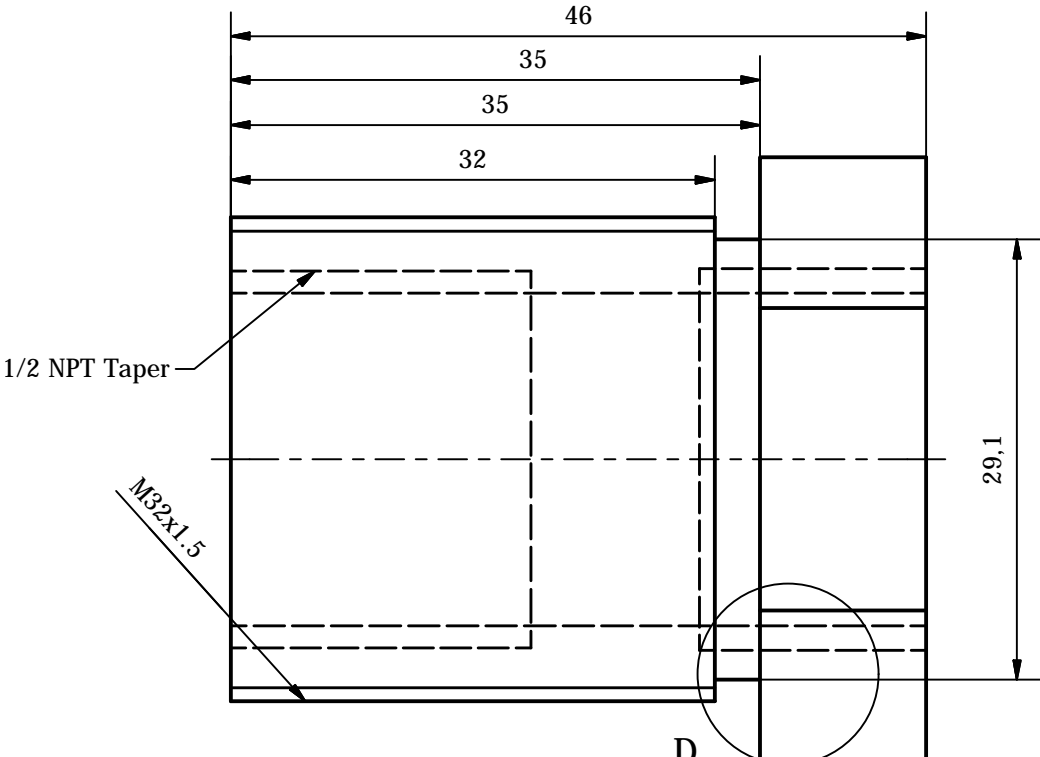
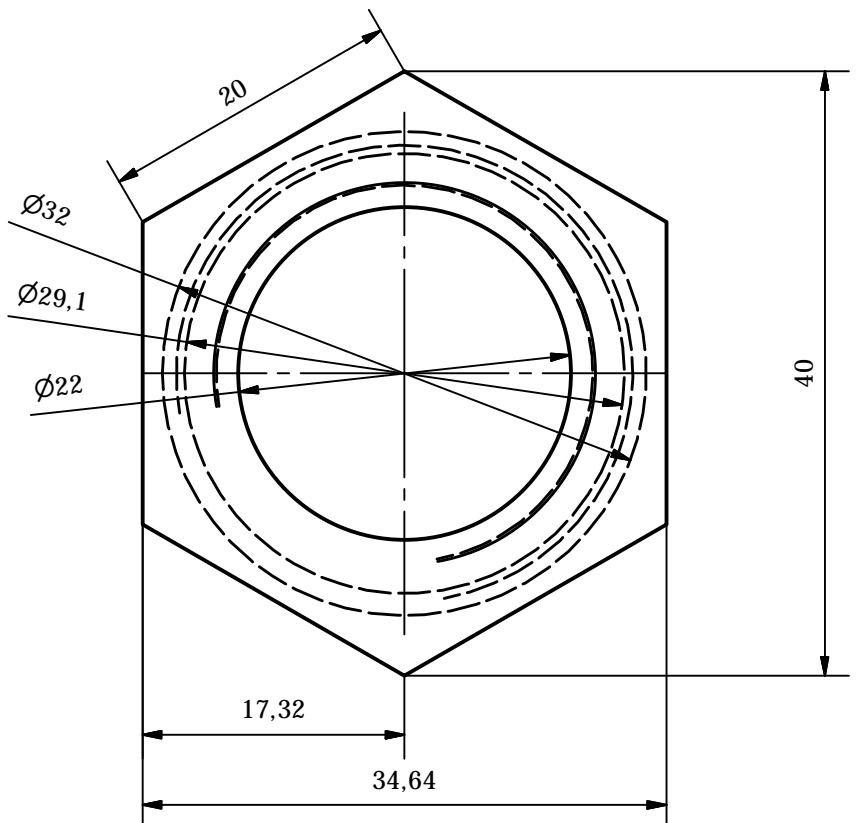
TITLE  
Injector Bulkhead



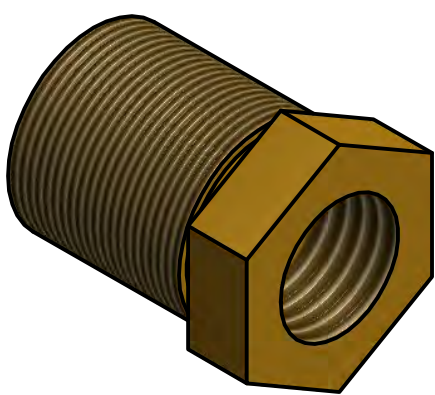


School of Mechanical  
Engineering

PROJECT SUPERVISOR	DATE	CHECKED	SCALE 1:1	UNITS : mm	PROJECT	NO.
				STUDENT NAME Bernard Genevieve	Phoenix-1A Hybrid Rocket	3-1
WSHOP TECHNICIAN			E-MAIL	206504262@stu.ukzn.ac.za		
TECHNICAL OFFICER			TEL NO.		TITLE	

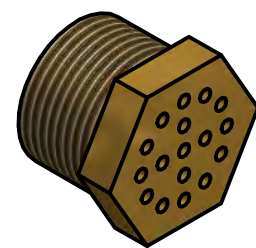
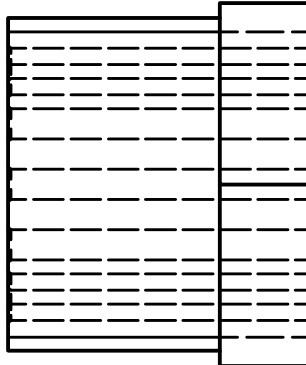
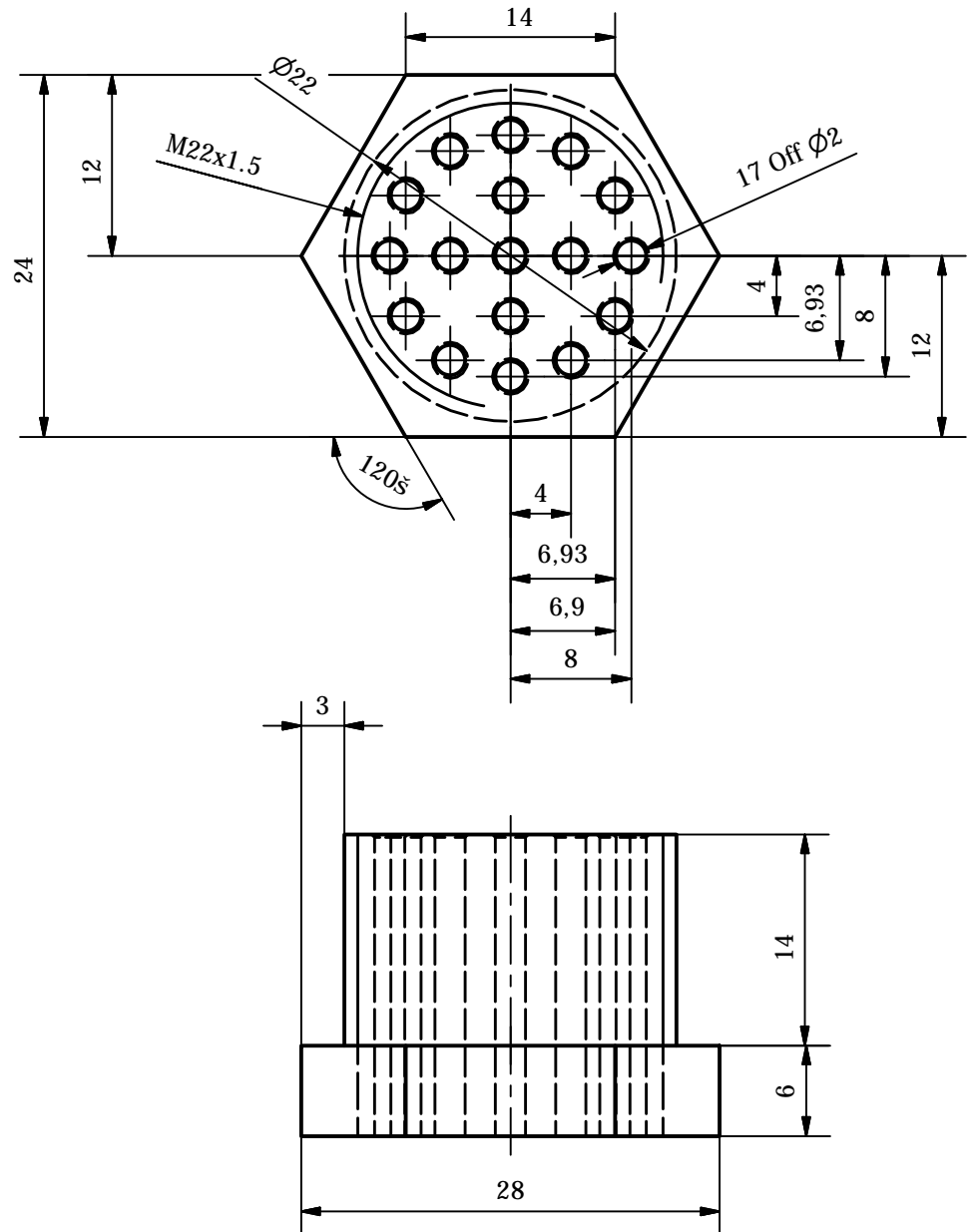


D ( 4: 1 )



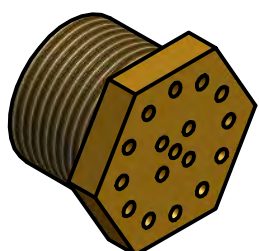
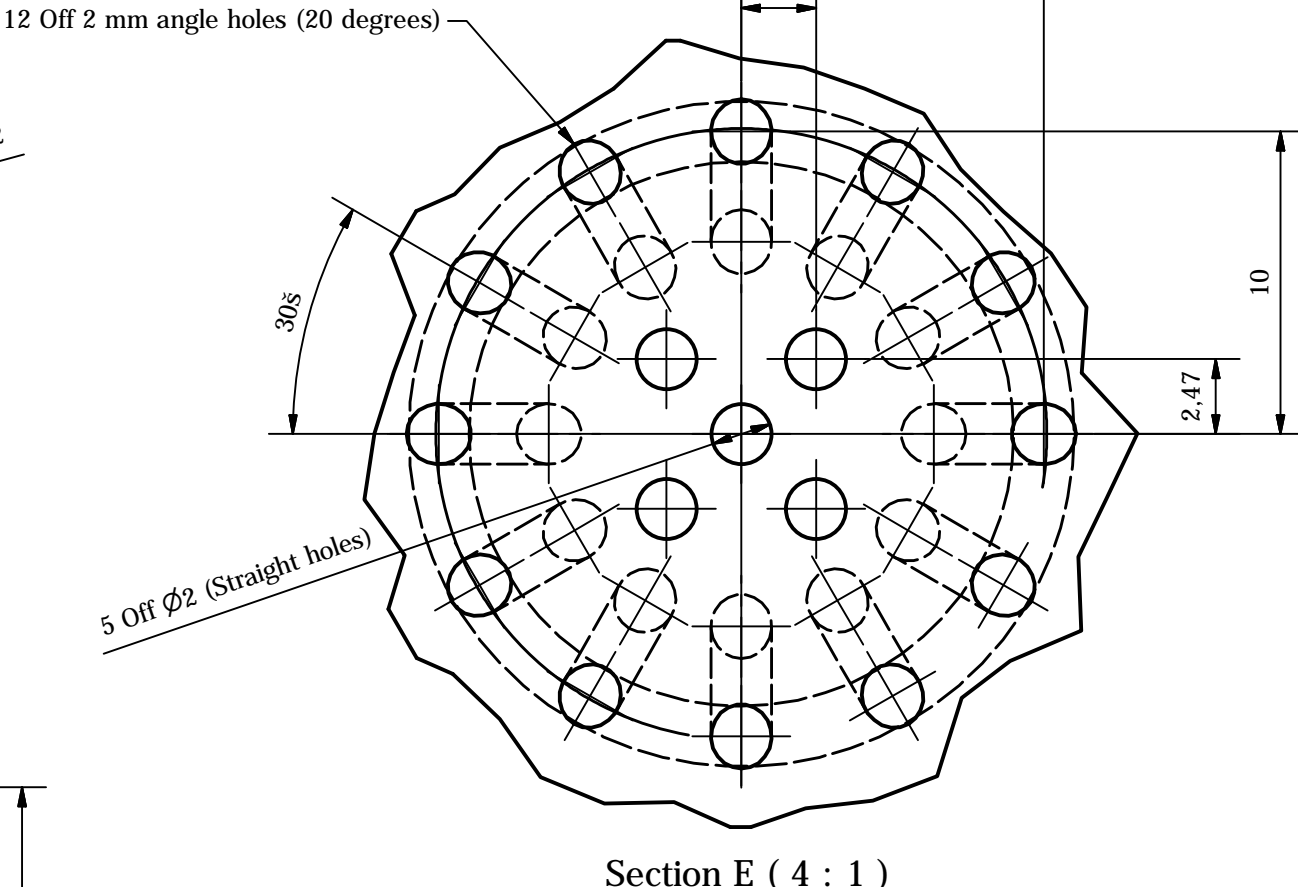
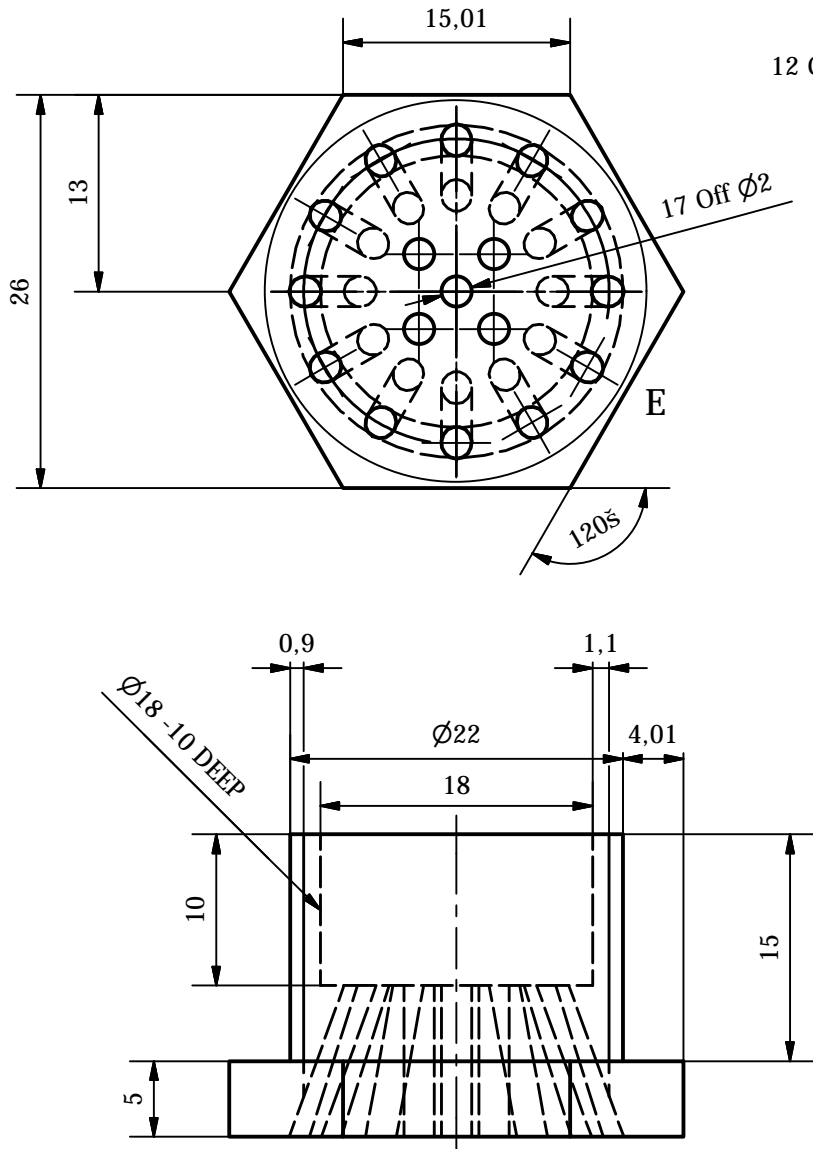
School of Mechanical  
Engineering

PROJECT SUPERVISOR	DATE	CHECKED	SCALE 2:1	UNITS : mm	PROJECT Phoenix-1A Hybrid Rocket	NO. 3-3
W'SHOP TECHNICIAN				STUDENT NAME Bernard Genevieve	E-MAIL 206504262@stu.ukzn.ac.za	
TECHNICAL OFFICER				TEL NO.	TITLE Injector Manifold	



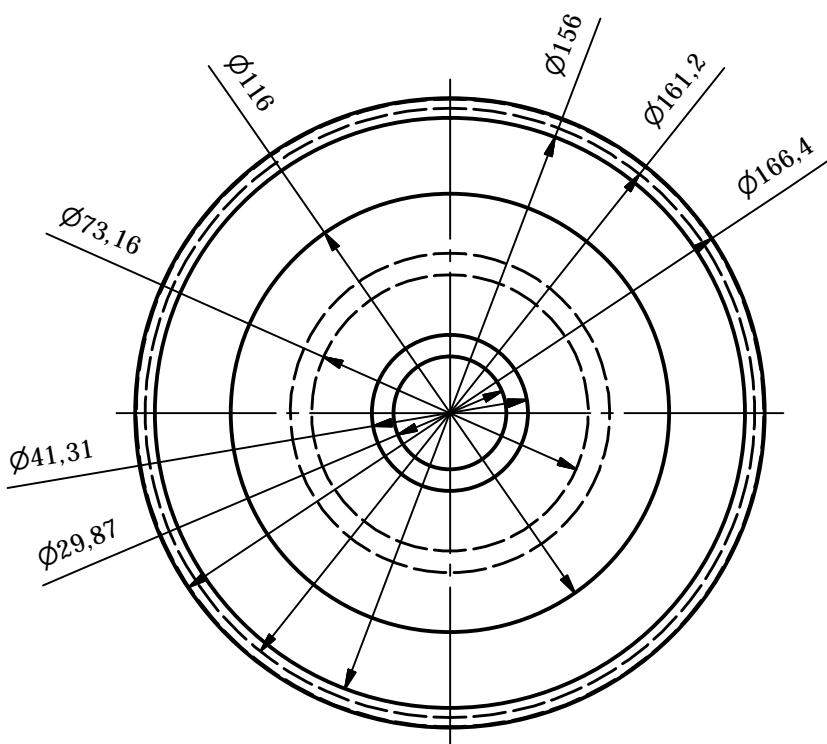
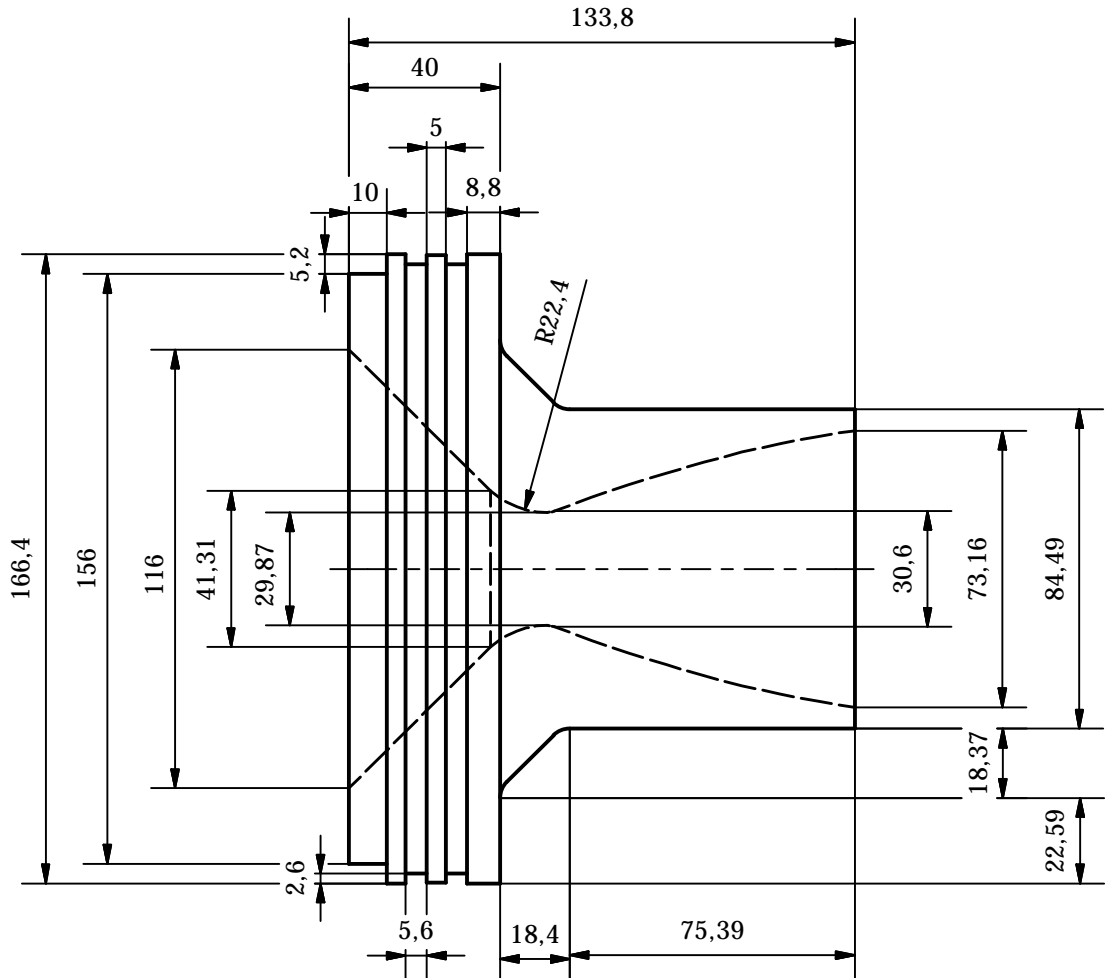
School of Mechanical  
Engineering

PROJECT SUPERVISOR	DATE	CHECKED	SCALE 2:1	UNITS : mm	PROJECT Phoenix-1A Hybrid Rocket	NO. 3-5
W'SHOP TECHNICIAN			E-MAIL 206504262@stu.ukzn.ac.za			
TECHNICAL OFFICER			TEL NO.		TITLE Axial/Straight Injector	



School of Mechanical  
Engineering

PROJECT SUPERVISOR	DATE	CHECKED	SCALE 2:1	UNITS : mm	PROJECT Phoenix-1A Hybrid Rocket	NO. 3-5
W'SHOP TECHNICIAN				STUDENT NAME Bernard Genevieve	E-MAIL 206504262@stu.ukzn.ac.za	
TECHNICAL OFFICER				TEL NO.	TITLE Impinging Injector	



School of Mechanical  
Engineering

PROJECT SUPERVISOR	DATE	CHECKED	SCALE 1:2	UNITS : mm	PROJECT	NO.
				STUDENT NAME Bernard Genevieve	Phoenix-1A Hybrid Rocket	4
W'SHOP TECHNICIAN				E-MAIL 206504262@stu.ukzn.ac.za		
TECHNICAL OFFICER				TEL NO.	TITLE Nozzle	

## **APPENDIX H**

### **PV-1 Motor Structural Design**

## Appendix H.1

### Chamber Casing Wall-Thickness Design

Design calculation for chamber casing wall-thickness using the following specifications:

1. Chamber pressure:  $P_c = 4 \text{ MPa}$ .
2. Safety factor:  $S_f = 3$ .
3. Design pressure:  $P_d = S_f P_c = 12 \text{ MPa}$ .
4. Aluminium yield strength:  $(\sigma_y)_{Al} = 260 \text{ MPa}$ .
5. Casing inner radius:  $r_i = 0.084 \text{ m}$ .

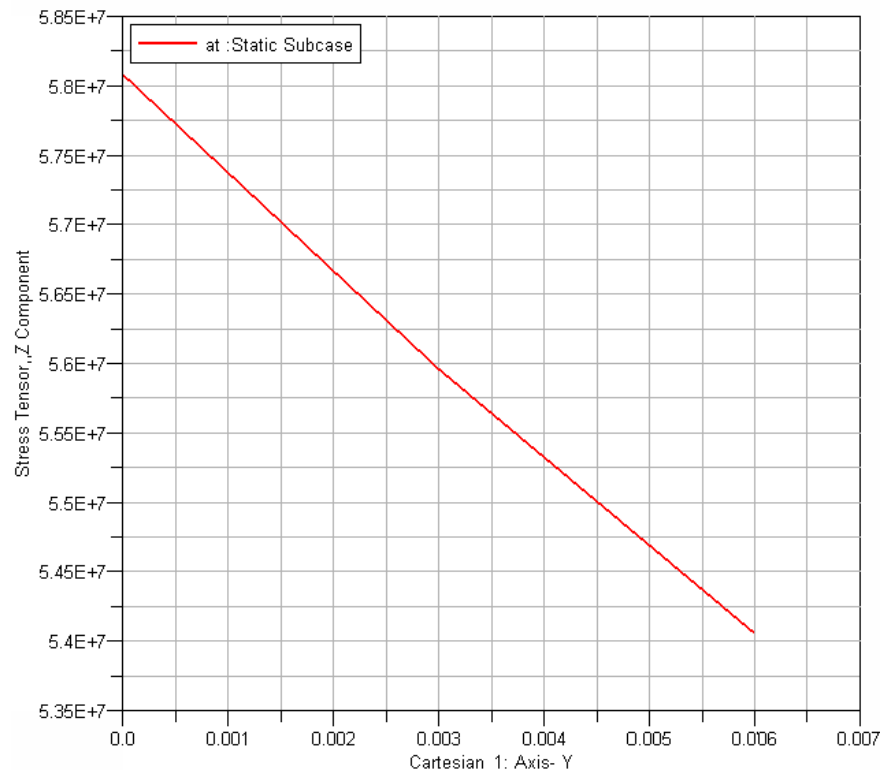
Using Equation 6.5, the required thickness is given as:

$$t = \left[ \frac{0.084^2(1+(260/12))}{(260/12)-1} \right]^{0.5} - 0.084 = 0.004 \text{ m}$$

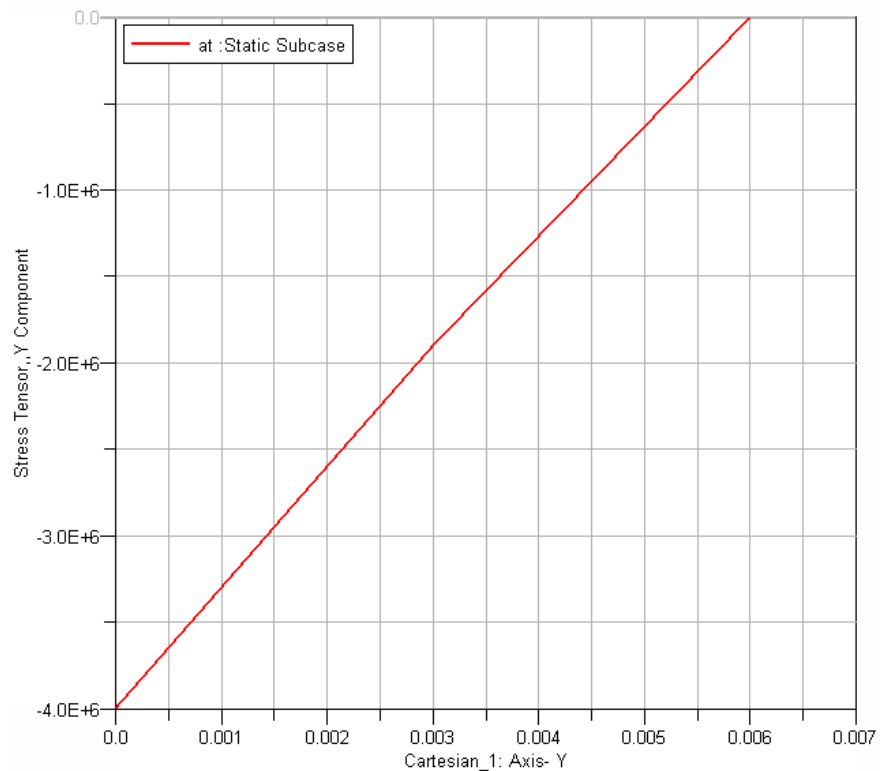
A finite element analysis was performed on the combustion chamber casing. Table H.1 and Fig. H.1 show the stress distributions.

Table H.1 Finite element analysis of chamber casing.

Inputs				
<b>Chamber Pressure</b>	$P_c$	MPa	4	
<b>Aluminium Yield Strength</b>	$\sigma_y, Al$	MPa	260	
<b>Aluminium Young's Mod.</b>	$E_{Al}$	GPa	70	
<b>Aluminium Poisson's Ratio</b>	$\nu_{Al}$		0.35	
<b>Casing Inner Radius</b>	$r_i$	m	0.084	
<b>Casing Outer Radius</b>	$r_o$	m	0.09	
Outputs				
			<b>Inner Radius</b>	<b>Outer Radius</b>
			Cal.	FEA
<b>Hoop Stress</b>	$\sigma_h$	MPa	58.069	58.07
<b>Radial Stress</b>	$\sigma_r$	MPa	-4	-4
			54.069	54.7
			0	0



(a)



(b)

Figure H.1 FEA of chamber casing: (a) Hoop stress, and (b) Radial stress

Table H.2 Failure modes of chamber casing at bolt joints for a 6 mm wall-thickness.

Failure Mode	Chamber Pressure [bar]			
	40		60	
	Value [MPa]	Safety Factor	Value [MPa]	Safety Factor
Tensile	31.48	8.3	47.22	5.5
Compressive	153.94	1.7	230.91	1.1
Double Shear	57.73	3.6	86.59	2.4

## Appendix H.2

### PV-1 Nozzle: Bell-Shaped Contour Design

\*\*\*\*\*

#### Nozzle Design Contour

\*\*\*\*\*

#### \*\*\*\* INPUTS \*\*\*\*

Nozzle throat diameter	Dt	0.029831093 m
Nozzle expansion ratio	ExpRat	5.9973
Nozzle contraction ratio	ConRat	15.08
Nozzle contraction angle	Qc	44.92 deg
Ratio of upstream to throat radius	Rup/Rt	1.5
Ratio of downstream to throat radius	Rd/Rt	0.382
Nozzle Type	Bell-Shaped Nozzle	
Nozzle parabola inlet angle	Qn	20.75 deg
Nozzle parabola exit angle	Qe	7.5 deg
Nozzle fractional length	Lf	1
Nozzle half cone angle	Alp_c	15 deg

#### \*\*\*\* OUTPUTS \*\*\*\*

Chamber radius	Rni	0.057921505 m
Nozzle throat radius	Rt	0.014915547 m
Nozzle exit radius	Re	0.036527257 m
Nozzle upstream radius	Rup	0.02237332 m
Nozzle downstream radius	Rd	0.005697739 m
Nozzle length from inlet to throat plane	Lni	0.052375261 m
Length from contraction angle position to throat plane	Lcx	0.015798221 m
Radius of contraction angle position to throat plane	Hcx	0.021446466 m
Nozzle total length from throat to exit plane	Lne	0.081406122 m
Nozzle parabolic bell length	Lc	0.079387464 m

#### \*\*\*\* Divergent Contour Co-ordinate \*\*\*\*

X co-ordinate [m]	Y co-ordinate [m]
0.002018658	0.015285129
0.012018658	0.018955386
0.022018658	0.022378405
0.032018658	0.025537191
0.042018658	0.028412707
0.052018658	0.030983518
0.062018658	0.033225338
0.072018658	0.035110471
0.081406122	0.036527257